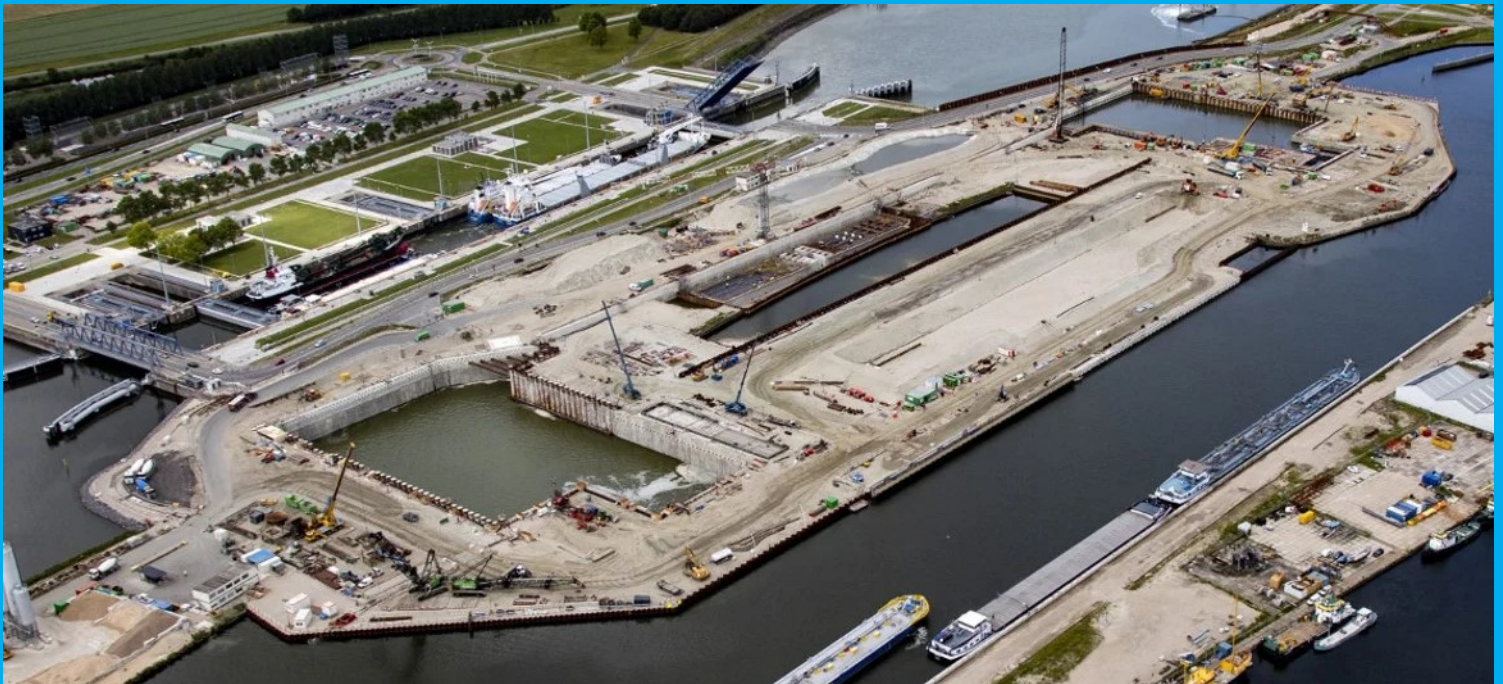


# MSc Thesis

## Back analysis of deep excavation for the New Terneuzen Lock

D. Pavlakis





# Back analysis of deep excavation for the New Terneuzen Lock

*An investigation conducted using a Python-Plaxis  
application and monitoring data from the field*

by

**Dimitrios Pavlakis**

to obtain the degree of Master of Science at the Delft University of Technology,

to be defended publicly on Tuesday November 29, 2022 at 08:30 AM.

Student number: 5379482  
Project duration: January 16, 2022 - November 29, 2022  
Thesis committee: Dr. ir. M. Korff, TU Delft, Chair supervisor  
Dr. ir. C. van Mai, TU Delft, Supervisor  
Ir. T. Nijssen, BAM, Supervisor  
Ir. A. Verweij, Arcadis, Supervisor



An electronic version of this thesis is available at <http://repository.tudelft.nl/>.



---

# Abstract

The case study of the outer lock head of the New Terneuzen Lock is considered to investigate the behavior of the Boom Clay and to develop an automated method for improving the deformation predictions in a deep excavation format. The initiative to perform this study was the uncertainty in modeling the Boom Clay behavior during the design and the over-predictions of the combi wall deformations in the aftermath. The problem has been attributed to the constitutive soil model and soil properties used for that layer.

In the context of this thesis a Python - PLAXIS application has been developed, which facilitates an iterative method to determine the real soil properties of the Boom Clay layer based on inclinometer measurements of the wall throughout the construction stages. The monitoring data present the reality; hence the safety factors had to be filtered out of the design for the comparison with them to be applicable. Therefore, the mean (most probable) soil properties have been recalculated, and the as-build external loads, aquifer heads, structural elements, and phasing have been deciphered to create the Mean model. Using the Mean model, the most appropriate constitutive model and drainage conditions for the Boom Clay are determined. It has been concluded that the Hardening Soil small strain is the most appropriate constitutive model. Using the Mean model as initial input and the constitutive model conclusions, an iterative process on the relevant soil properties has been conducted to reach  $\pm 10\%$  convergence with the corresponding monitoring deformations. The Fine Tuned model uses the soil properties derived by the iterative method to represent reality with the highest accuracy and reaches, on average, 45 % more precision on the prediction of the deformation in comparison to the monitoring data than the Mean model.

Using the Fine Tuned model, sensitivity analysis of the wall to Boom Clay's soil properties is performed. It revealed that  $\phi'$  had the highest impact relative to the other properties. Scenarios with thinner Boom Clay layers have been tested due to the relevant wedging geometry it follows in the project location. Additionally, the Fine Tuned model has been used to improve the prediction of future stages with data derived from earlier monitoring. The example studied was able to improve the prediction by 87 % in comparison to the initial design. In comparing the Design model with the Fine Tuned model, a problem with the anchor wall behavior is discovered that is attributed to the inability of PLAXIS to consider the shaft friction of the anchor rods. The Fine Tuned model, in combination with the fixity solution, allowed for an improvement in deformation accuracy of up to 95 %.

It is concluded that the actual design, despite over-predicting its deformations, produced a retaining wall validated by the Fine Tuned model. It is suggested that the Python Application should be used alongside the traditional designing process and in site engineering to reduce the risk by simulating the actual behavior and limits of the retaining wall.



---

# Acknowledgements

This report presents the work carried out by D. Pavlakis, student of the master Civil Engineering track Geo-Engineering at the Technical University of Delft. The work was established by a cooperation between the University of Delft and the companies BAM and Arcadis. It was completed under the section Geo-engineering, Department of Civil Engineering at the TU Delft.

I want to express my gratitude to Mandy Korff, Cong van Mai from TU-Delft, Thomas Nijssen from BAM, and Ad Verweij from Arcadis for their expert guidance and supervision during my graduation project. I would also like to thank Christian Rash and other colleagues from the companies for their continuous support, expert advice, and constructive comments on my work. BAM is acknowledged for providing the necessary software licenses, and both companies for allowing the use of the data from the project.

Last but not least, a massive thank you goes to my parents for their unlimited support and never-ending love. They were always on my side, showing me the way to become a better person and equipping me with virtues and values that will accompany me throughout my life. To my brother, Aggelos, who always knew how to make me feel better and always believed in me. Also, an immense thank you goes to Irene and my friends for believing in me and making this journey more beautiful. Finally, to my grandfather, Dimitris, a role model of mine, who sadly passed away during my studies, to whom I also dedicate my graduation thesis.

*Dimitris Pavlakis*  
*Delft, November 2022*





# Contents

<b>Abstract</b>	<b>i</b>
<b>List of Figures</b>	<b>vi</b>
<b>List of Tables</b>	<b>x</b>
<b>1 Introduction</b>	<b>2</b>
1.1 Project Description . . . . .	2
1.2 Problem Description . . . . .	3
1.3 Research Questions and Objectives . . . . .	4
1.4 Method of Approach . . . . .	5
1.5 Thesis Outline . . . . .	6
<b>2 Model Description</b>	<b>8</b>
2.1 Parameter Determination - Theoretical Background . . . . .	8
2.1.1 CPT correlations . . . . .	8
2.1.2 Linear Regression . . . . .	9
2.1.3 Mean values determination . . . . .	10
2.1.4 Hardening Soil Small Strain Constitutive Model . . . . .	12
2.2 Parameter Determination - Application . . . . .	24
2.2.1 Soil Layer L05 . . . . .	25
2.2.2 Soil Layer L07 . . . . .	27
2.2.3 Soil Layer L08, L10, L12 . . . . .	28
2.2.4 Soil Layer L09 & L11 . . . . .	30
2.2.5 Soil Layer L15 . . . . .	31
2.2.6 Soil Layer L16 . . . . .	36
2.2.7 Soil Layer L17 . . . . .	38
2.2.8 Soil Layer L18 . . . . .	39
2.2.9 Soil Layer L19 . . . . .	40
2.2.10 Soil Layer LX02 and LX01 . . . . .	40
2.3 Parameter Overview . . . . .	42
2.4 Parameter Determination of Structural Elements . . . . .	43
2.4.1 Combi Wall . . . . .	43
2.4.2 Anchor Wall . . . . .	45
2.4.3 Anchor Rod . . . . .	46
2.5 Construction Phases . . . . .	46
2.6 External Load Investigation . . . . .	47
2.7 Head Determination of the Aquifers . . . . .	48
2.8 Monitoring . . . . .	50
2.8.1 Inclinerometers . . . . .	50
2.8.2 Total Stations - Offset wall movement investigation . . . . .	50
<b>3 Python Application</b>	<b>53</b>

3.1	General Structure . . . . .	53
3.2	Introduction and Main Menu . . . . .	54
3.3	Monitoring Interpretation . . . . .	55
3.4	PLAXIS Output . . . . .	57
3.5	Model and Monitoring Comparison . . . . .	59
3.6	Sensitivity Analysis . . . . .	60
3.6.1	Run Iterations . . . . .	60
3.6.2	Interpretation of Iterations . . . . .	61
3.7	Phase Investigation . . . . .	64
3.8	Purpose and Limitations . . . . .	65
<b>4</b>	<b>Model Application and Investigation</b>	<b>66</b>
4.1	Boom Clay - Constitutive Model Investigation . . . . .	66
4.1.1	Boom Clay Location . . . . .	66
4.1.2	Lab Test Investigation . . . . .	67
4.1.3	Literature Investigation . . . . .	68
4.1.4	Constitutive model application and Comparison . . . . .	71
4.1.5	Summary and Discussion . . . . .	74
4.2	Fine Tuned Model . . . . .	74
4.2.1	Soil Properties Adjustment . . . . .	74
4.2.2	Phase 13 - Investigation . . . . .	77
4.2.3	Summary and discussion . . . . .	79
4.3	Sensitivity Analysis . . . . .	81
4.3.1	Methodology . . . . .	81
4.3.2	Investigation . . . . .	86
4.3.3	Summary and Discussion . . . . .	92
4.4	Impact of the Boom Clay Thickness . . . . .	93
4.4.1	Undrained versus Drained modeling . . . . .	94
4.4.2	Thickness Investigation . . . . .	95
4.4.3	Summary and discussion . . . . .	97
4.5	Model Prediction . . . . .	98
4.5.1	Investigation . . . . .	99
4.5.2	Summary and discussion . . . . .	101
4.6	Design Improvement . . . . .	102
4.6.1	Improvement of the Design Model with the Fine Tuned model. . . . .	102
4.6.2	<i>Fixed</i> versus <i>Free</i> approach retaining wall modeling . . . . .	103
4.6.3	Potential solution with shaft friction on the anchor rods . . . . .	104
4.6.4	Effects of the fixity methods to the safety of the combi wall . . . . .	109
4.6.5	Summary and discussion . . . . .	109
<b>5</b>	<b>Conclusions and Recommendations</b>	<b>111</b>
5.1	Conclusions . . . . .	111
5.2	Recommendations . . . . .	116
	<b>References</b>	<b>118</b>
	<b>Appendices</b>	<b>120</b>
<b>A</b>	<b>References to codes</b>	<b>121</b>
A.1	Table 2.b - NEN9997 . . . . .	121
A.2	Table 9.b - NEN9997 . . . . .	122
A.3	Table 3.1 - CUR 2003 - 7 . . . . .	122

<b>B</b>	<b>Soil Investigation</b>	<b>123</b>
B.1	Soil Cross Section . . . . .	123
B.2	Oedometer Test - Lab report . . . . .	124
B.3	Triaxial Test - Lab Report . . . . .	127
B.4	Soil Parameter Determination - Unit Weight . . . . .	129
B.5	Soil Parameter Determination - Small Strain . . . . .	130
<b>C</b>	<b>Construction Phases</b>	<b>132</b>
C.1	PLAXIS mesh . . . . .	132
C.2	PLAXIS input screenshots . . . . .	132
C.3	CAD drawings . . . . .	135
<b>D</b>	<b>Project Loads</b>	<b>142</b>
<b>E</b>	<b>Aquifer Heads</b>	<b>145</b>
<b>F</b>	<b>Boom Clay Lab Tests</b>	<b>146</b>
F.1	Samples Location . . . . .	146
F.2	Stiffness Determination Methodology . . . . .	146
F.3	Stiffness Determination of the Samples . . . . .	148
<b>G</b>	<b>Small Strain Parameter Determination</b>	<b>153</b>
G.1	Small Strain Correlations . . . . .	153
G.2	Small Strain effect on all the soil layers . . . . .	154
<b>H</b>	<b>Python Application</b>	<b>157</b>
H.1	Python Libraries used . . . . .	157
H.2	Monitoring Input File Structure . . . . .	158
H.3	Plaxis Model Input File Structure . . . . .	159
H.4	Plaxis - Python Remote Connection Instructions . . . . .	162
H.5	Sensitivity Analysis File Structure . . . . .	162
<b>I</b>	<b>Extra Material Chapter 4</b>	<b>165</b>
I.1	Bentonite effect to the stiffness of the combi wall . . . . .	165
I.2	Fully Undrained approach . . . . .	167
I.3	Design Improvement . . . . .	168
I.4	Horizontal Effective stress . . . . .	172

# List of Figures

1.1.1	Top view of the project area that represents the previous and current situation of the Locks in the Gent-Terneuzen canal (SSV-RAP-163-C project report). . . . .	2
1.1.2	3D impression of the construction pit of the outer head (SSV-RAP-163-C project report). . . . .	3
1.4.1	Models . . . . .	5
1.5.1	Thesis flow chart . . . . .	7
2.1.1	Non-normalized CPT Soil Behaviour Type chart (Robertson, 2010 [29]). . . . .	9
2.1.2	Positive and Negative correlation between the Independent and Dependent variable in linear regression. . . . .	10
2.1.3	Visual description of all the properties of the linear regression method. . . . .	10
2.1.4	Normal distribution . . . . .	11
2.1.5	Derivation of MIT stress field and the stress path as the locus of stress points. (Lambe, 1991 [21]). . . . .	13
2.1.6	Derivation of shear strength parameters from $K_f$ line with cohesion intercept. (Lambe, 1964 [20]). . . . .	14
2.1.7	Idealized relation for dilatancy angle, $\psi$ , from triaxial test results (Vermeer & de Borst, 1984 [33]). . . . .	16
2.1.8	Axial strain vs volumetric strain plots to investigated the dilation/compression of dense and loose sand (Lee, 1965 [22]) . . . . .	16
2.1.9	Resulting strain curve for a standard drained triaxial test when including dilatancy cut-off (Brinkgreve et al., 2011 [10]). . . . .	17
2.1.10	Logarithmic relationship of void ratio with loading and unloading, expressed with the parameters $(\lambda - \kappa)$ and $(C_c - C_s)$ . . . . .	19
2.1.11	Stiffness properties for the hardening soil small strain model. . . . .	20
2.1.12	Deviatoric versus axial strain plot resulting from a triaxial compression test at two different confining stress (Brinkgreve et al., 2011 [10]). . . . .	22
2.1.13	Graphical visualization of the hyperbolic model in deviatoric vs strain space (Brinkgreve et al., 2011 [10]). . . . .	23
2.1.14	Comparison of the correlations between $E_{dyn}/E_{stat}$ and $E_{stat}$ according to Alpan, 1970 [1], DGGT (2001) and by Benz & Vermeer, 2007 [7] [after Wichtmann & Triantafyllidis (2009)]. . . . .	23
2.2.1	Phase Comparison Tab of Python Application. . . . .	25
2.2.2	Oedometers stiffness from the 3 samples at Layer L07. . . . .	28
2.2.3	Linear regression for the undrained triaxial lab test on samples with high relative density for L08, L10 & L12 layers at 2 % strain. . . . .	29
2.2.4	Linear regression for the undrained triaxial lab test on samples from all the thickness of L15 layer at 2 % strain. . . . .	32
2.2.5	Linear regression for the undrained triaxial lab test on samples at 2 m intervals of L15 layer at 2 % strain. . . . .	32
2.2.6	Linear regression for the undrained triaxial lab test on samples at 2 m intervals of L15 layer at 2 % strain. . . . .	33

2.2.7	Relationship of vertical effective stress $\sigma'_v$ and cone resistance $q_c$ for Ticino sand (Baldi et al., 1986 [5]) . . . . .	37
2.4.1	Sheet pile cross-section. . . . .	43
2.4.2	Top view of the combi wall of cross-section L01b (units in m). . . . .	43
2.4.3	Top view of the combi-wall indicates the calculated area for the bentonite outside the pile. . . . .	45
2.4.4	Sheet pile cross-section. . . . .	45
2.6.1	Top view of the outer lock head with reference dimensions. [Google Maps] . . . . .	48
2.7.1	Aquifer representation at the location of cross-section L01b under investigation. . . . .	49
2.8.1	Rotation of the global RD coordinate system to a local x-y coordinate system. . . . .	50
2.8.2	Representation of the pile behaviour, with fixed tip (green) and without fixed tip (red). . . . .	51
2.8.3	Rotation of the global RD coordinate system to a local x-y coordinate system. . . . .	52
3.2.1	Python Application . . . . .	55
3.3.1	Monitoring Tab of Python Application . . . . .	56
3.3.2	Plot toolbar . . . . .	56
3.4.1	Output Tab of Python Application . . . . .	57
3.4.2	Output Library - Tree List . . . . .	58
3.4.3	Output Tab of Python Application . . . . .	58
3.5.1	Comparison Tab of Python Application. . . . .	59
3.5.2	Monitoring and model deformations comparison for three construction phases. . . . .	60
3.6.1	Sensitivity Tab of Python Application . . . . .	61
3.6.2	Sensitivity Library - Tree List . . . . .	62
3.6.3	Interpretation of Iterations Tools . . . . .	62
3.6.4	Resulting plots form the "Rate of Change" tool of the sensitivity analysis tab of the Python Application. . . . .	63
3.6.5	3D plots from the "3D - Plot" tool of the sensitivity analysis tab of the Python Application. . . . .	64
3.7.1	Phase Comparison Tab of Python Application. . . . .	65
4.1.1	Boom Clay locations in the Netherlands (a) and in Belgium (b). . . . .	67
4.1.2	Axial stress $p$ vs axial strain $\epsilon$ plot for the oedometer test on Boom Clay sample B2 - St.10. . . . .	68
4.1.3	Investigation of Milioritsas, 2014 [25] to the triaxial test of Deng et al., 2011 [13] regarding the best constitutive model to simulate the Boom Clay behavior. . . . .	69
4.1.4	Investigation of Milioritsas, 2014 [25] to the oedometer test of Deng et al., 2011 [13] regarding the best constitutive model to simulate the Boom Clay behavior. . . . .	70
4.1.5	Strain level depending on the structure type (Atkinson and Salfors, 1991 [3]). . . . .	70
4.1.6	Small Strains . . . . .	71
4.1.7	Comparison of constitutive soil models for the Boom Clay. . . . .	73
4.2.1	Moments and Forces of the Fine Tuned model for five construction phases. . . . .	75
4.2.2	Shear surface between soil and sheet piling. (de Gijt and Broeken, 2013 [15]) . . . . .	75
4.2.3	Comparison of the wall deformations when the Mean and Fine Tuned models are used. . . . .	76
4.2.4	Comparison of the wall deformations when the mean and Fine Tuned properties are used. . . . .	77
4.2.5	Cement bentonite levels for each construction phase. . . . .	78
4.2.6	Influence of bentonite for Phase 13. . . . .	78
4.2.7	Summary of potential reasons for the difference in deformations of the model and monitoring for Phase 13. . . . .	79
4.2.8	Comparison of the monitoring measured deformations with the predicted deformations of the Fine Tuned model for five construction phases. . . . .	80
4.3.1	Riemann sums method for the calculation of the area below a curve. . . . .	83

4.3.2	Example for the calculation of the area between two curves using the Riemann method.	84
4.3.3	Example for the explanation of methodology.	85
4.3.4	Example data and the corresponding linear correlation between two variables.	86
4.3.5	Deformation rate of change due to different $E_{50}^{ref}$ , $\phi'$ and $c'$ values of the Boom Clay for construction phases 8 to 13. The blue shaded area is the $\pm 30\%$ change from the base value.	88
4.3.6	Moments of the combi-wall for all the scenarios of parameters $E_{50}^{ref}$ , $\phi'$ and $c'$ for Phase 11.	89
4.3.7	Overview plots of the effects the $E_{50}^{ref}$ scenarios have on the deformations of the wall.	91
4.3.8	Overview plots of the effects the $\phi'$ scenarios have on the deformations of the wall.	91
4.3.9	Overview plots of the effects the $c'$ scenarios have on the deformations of the wall.	92
4.3.10	Tornado plot for the percentage of deformation change caused by 30 % change of the soil parameters for the Boom Clay layer.	93
4.4.1	Top view of the outer lock head in the new Terneuzen lock. [Design Documents]	94
4.4.2	Soil cross section at the area of the outer head of the New Terneuzen Lock. [Design Documents]	94
4.4.3	Soil cross-section and pumping test of the Boom Clay from the Antwerp trial pit. [de Nijs et al., 2015 [28]]	95
4.4.4	Comparison of partially undrained and drained Fine tuned model for 3 phases.	96
4.4.5	Deformation comparison for different Boom Clay thicknesses in partial undrained and drained Boom Clay conditions.	97
4.4.6	Percentage increase in deformations when transitioning from Partiality Undrained to Fully Drained Boom Clay for different thicknesses.	98
4.5.1	Comparison of the initial, base and improved model predictions for Phases 8 and 11.	101
4.6.1	Anchor rod - shaft friction	104
4.6.2	Deformations and moments comparison of the Design and Fine Tuned model with the <i>Free</i> , the <i>Fixed</i> and the <i>Shaft</i> approaches at the anchor level of the combi wall, for Phases 8.	106
4.6.3	Deformations and moments comparison of the Design and Fine Tuned model with the <i>Free</i> , the <i>Fixed</i> and the <i>Shaft</i> approaches at the anchor level of the combi wall, for Phases 11.	107
4.6.4	Deformations and moments comparison of the Design and Fine Tuned model with the <i>Free</i> , the <i>Fixed</i> and the <i>Shaft</i> approaches at the anchor level of the combi wall, for Phases 13.	108
5.1.1	<i>Explanatory plots</i>	112
E.0.1	Aquifer heads from the field. [Project Data]	145
F.1.1	Locations of the boreholes.	146
F.2.1	Triaxial and Oedometer lab test output plots.	148
F.2.2	Oedometer lab test output process.	148
F.3.1	Deviatoric stress $q$ versus vertical strain $\epsilon$ for the four Boom Clay triaxial samples under three confining stresses each.	151
F.3.2	Axial stress $p$ versus Strain $\epsilon$ for the four oedometer tests on the Boom Clay samples.	152
G.1.1	Different methods to calculate the small strain parameters.	153
G.2.1	Comparison of the wall deformations derived with Alpan's, Benz & Vermeer's and average small strain methods.	156
H.2.1	Monitoring Input File	158
H.3.1	Plaxis Model Input File - Soil Properties Section	159

H.3.2	Plaxis Model Input File - Borehole Section . . . . .	159
H.3.3	Plaxis Model Input File - Heads Section . . . . .	159
H.3.4	Plaxis Model Input File - Plates Section . . . . .	160
H.3.5	Plaxis Model Input File - Node to Node Section . . . . .	160
H.3.6	Plaxis Model Input File - Fixed End Anchors Section . . . . .	160
H.3.7	Plaxis Model Input File - Phases Section . . . . .	161
H.3.8	Plaxis Model Input File - Soil Stresses Section . . . . .	161
H.4.1	Remote Connection Instructions . . . . .	162
H.5.1	Sensitivity Analysis File Structure . . . . .	162
H.5.2	Structure of the # Parameter variation Log excel file from the sensitivity analysis of the python application. . . . .	163
H.5.3	Run excel file structure from the sensitivity analysis of the python application. . . . .	164
I.1.1	Investigation of the effect of the bentonite to the horizontal deformations of the combi wall for four contraction phases. . . . .	166
I.2.1	Partially vs fully undrained Boom Clay conditions for the construction Phases 8, 11 and 13. . . . .	167
I.3.1	Deformations comparison for the Design, Mean and Fine Tuned models for the three anchor rod assumption (free, fixed, shaft friction) for four construction phases. The corresponding monitoring deformations are also included. . . . .	168
I.3.2	Moments comparison for the Design, Mean and Fine Tuned models for the three anchor rod assumption (free, fixed, shaft friction) for four construction phases. . . . .	169
I.3.3	Force Q comparison for the Design, Mean and Fine Tuned models for the three anchor rod assumption (free, fixed, shaft friction) for four construction phases. . . . .	170
I.3.4	Force N comparison for the Design, Mean and Fine Tuned models for the three anchor rod assumption (free, fixed, shaft friction) for four construction phases. . . . .	171
I.4.1	Horizontal effective stress $\sigma'_{xx}$ for the Design and Fine Tuned model under the three different fixity approaches. . . . .	172
I.4.2	Unity check excel example. . . . .	173

# List of Tables

2.1.1	Parameters summary for the Hardening Soil Small Strain constitutive model. . . . .	13
2.1.2	Values of Poisson's ratio $\nu$ . . . . .	15
2.1.3	Values of Poisson's ratio $\nu$ . . . . .	16
2.1.4	Typical values of dilation angle for different materials (Vermeer & de Borst, 1984 [33]).	17
2.1.5	Wall friction angle determination with the relative wall roughness (NEN9997, table 9b). . . . .	18
2.2.1	Description of soil layers of cross section L01b. . . . .	24
2.2.2	Stress profile along the depth for the cross-section L01b. . . . .	25
2.2.3	Average effective friction angle and effective cohesion for layers L08, L10 & L12 at 2 % strain. . . . .	29
2.2.4	Strength parameters of the boom clay layer after the linear regression in 2m intervals.	33
2.2.5	calculation of the undrained shear strength using 3 different correlation methods. . .	34
2.2.6	Calculation of the oedometer stiffness $E_{oed}$ and the unloading/reloading stiffness $E_{ur}$ using the method of Christian and Nielsen. . . . .	35
2.2.7	Saturated and dry unit weight for the sand layers LX01 and LX02. . . . .	41
2.3.1	Mean and design soil properties used in the PLAXIS models. . . . .	42
2.4.1	Properties of the different pipe sections from the combi wall of cross-section L01b. .	43
2.4.2	Dimensions of the sheet pile AZ 46-700. . . . .	43
2.4.3	Properties for each section of the retaining wall used in the model. . . . .	45
2.4.4	Dimensions of the sheet pile AZ 26-700. . . . .	45
2.4.5	Properties for the anchor wall AZ 26-700 of this model. . . . .	46
2.5.1	Summary of the phases used in the PLAXIS model and of the corresponding dates. .	47
2.6.1	Summary of the locations and the value of the loads applied to each phase. . . . .	48
2.7.1	Aquifer heads in [m] for every phase inside and outside the excavation pit. . . . .	49
2.8.1	Summary of the monitoring measurements that correspond to the constructions phases. . . . .	51
2.8.2	Transformation of the RD coordinates to the local x-y coordinate system and comparison with the inclinometer deformations for cross-section L01b. . . . .	52
4.1.1	Summary of the stiffness properties derived by the lab tests on four boom clay samples.	68
4.1.2	Summary of the input soil parameters for the different constitutive models of the Boom Clay. . . . .	72
4.1.3	Area difference in $m^2$ , calculated using Riemann sums, of the models from the corresponding monitoring data for five phases. . . . .	73
4.2.1	Comparison of the soil properties between mean and fine tuned model. . . . .	76
4.2.2	Percentage difference deformations from the monitoring measured deformations. .	77
4.3.1	Interdependent Parameters . . . . .	82
4.3.2	Summary of the scenarios investigated for the three soil properties of Boom Clay. . .	87
4.3.3	Correlations for each construction phase and each soil property under investigation for the Total and Truncated sample. . . . .	90
4.3.4	Statistical description of the truncated and total ranges for Phase 8 and 11. . . . .	90
4.4.1	Area in $m^2$ from the monitoring data of the Partially undrained Boom Clay model and the fully drained Boom Clay model. . . . .	97



4.5.1	Boom Clay properties for the initial, base and improved model in drained and undrained conditions. . . . .	100
4.5.2	Area difference between the three models deformations from the monitoring deformations, for Phase 8 and Phase 11. . . . .	100
4.6.1	Summary of the area difference in $m^2$ of the three models with the three anchor simulations for the five construction phases of the project that are monitored. . . . .	105
4.6.2	Unity check of the combi wall for the Design and Fine Tuned model over the different fixity methods of the combi wall at the anchor level. . . . .	110
B.4.1	Statistical profile for the dry and saturated unit weight of layer L05. . . . .	129
B.4.2	Statistical profile for the dry and saturated unit weight of layer L07. . . . .	129
B.4.3	Statistical profile for the dry and saturated unit weight of layer L08, L10 & L12. . . . .	129
B.4.4	Statistical profile for the dry and saturated unit weight of layer L09 & L11. . . . .	129
B.4.5	Statistical profile for the dry and saturated unit weight of layer L15. . . . .	129
B.4.6	Statistical profile for the dry and saturated unit weight of layer L16. . . . .	129
B.4.7	Statistical profile for the dry and saturated unit weight of layer L17. . . . .	130
B.4.8	Statistical profile for the dry and saturated unit weight of layer L18. . . . .	130
B.5.1	Calculation of small strain shear stiffness $G_0^{ref}$ for soil layers L05a and L05b using Alpan, 1970 [1] and Benz & Vermeer, 2007 [7] methods. . . . .	130
B.5.2	Calculation of small strain shear stiffness $G_0^{ref}$ for layer L07 using Alpan, 1970 and Benz & Vermeer, 2007 [7] methods. . . . .	130
B.5.3	Calculation of small strain shear stiffness $G_0^{ref}$ for the layer L08 with Alpan, 1970 and Benz & Vermeer, 2007 [7] methods. . . . .	130
B.5.4	Calculation of small strain shear stiffness $G_0^{ref}$ for layer L09 with Alpan, 1970 and Benz & Vermeer, 2007 [7] methods. . . . .	131
B.5.5	Calculation of small strain shear stiffness $G_0^{ref}$ for layer L15 with Alpan, 1970 and Benz & Vermeer, 2007 methods. . . . .	131
B.5.6	Calculation of small strain shear stiffness $G_0^{ref}$ for layer L16 with Alpan, 1970 and Benz & Vermeer, 2007 methods. . . . .	131
B.5.7	Calculation of small strain shear stiffness $G_0^{ref}$ for layer L17 with Alpan, 1970 and Benz & Vermeer, 2007 methods. . . . .	131
B.5.8	Calculation of small strain shear stiffness $G_0^{ref}$ for Alpan, 1970 and Benz & Vermeer, 2007 methods. . . . .	131
F.1.1	Lab tests for the Boom Clay layer. . . . .	147
E.3.1	Effective cell pressures used for the triaxial tests of the four Boom Clay samples. . . . .	149
E.3.2	Secant stiffness $E_{50}$ calculation for Boom Clay sample B2 - St.10. . . . .	149
E.3.3	Secant stiffness $E_{50}$ calculation for Boom Clay sample B2 - St.12. . . . .	150
E.3.4	Secant stiffness $E_{50}$ calculation for Boom Clay sample B2 - St.17. . . . .	150
E.3.5	Secant stiffness $E_{50}$ calculation for Boom Clay sample B2 - St.19. . . . .	150
E.3.6	Summary of the oedometer stiffness $E_{oed}$ and the unloading reloading stiffness $E_{ur}$ derived from the oedometer tests of the four Boom Clay samples. . . . .	152
G.2.1	$G_0^{ref}$ determination for all the soil layers of cross-section L01b using Alpan's, Benz & Vermeer's methods and the average. . . . .	154
G.2.2	$\gamma_{0.7}$ small strain parameters determination for all soil layers of cross-section L01b using Alpan's, Benz & Vermeer's method and the average. . . . .	155
I.1.1	Properties for each section of the retaining wall without bentonite consideration. . . . .	165
I.1.2	Area change in $m^2$ for the case on Bentonite and no bentonite in comparison to the corresponding monitoring deformations for 5 construction phases. . . . .	165

# Introduction

## 1.1 Project Description

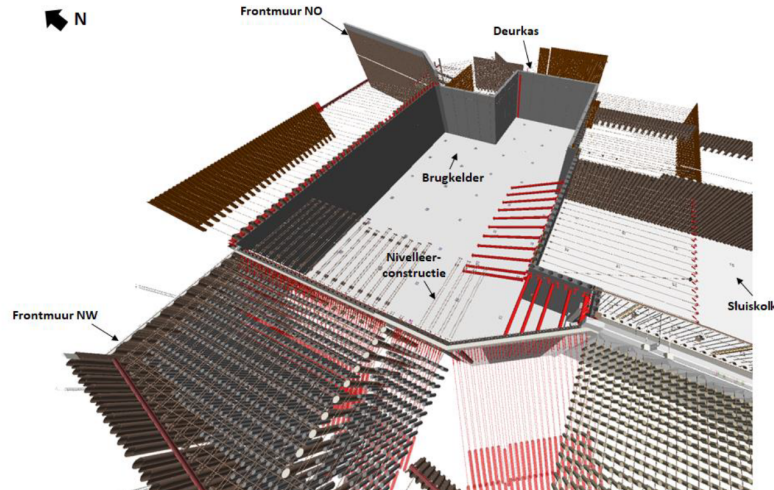
Terneuzen is a city in the southwestern Netherlands, in the province of Zeeland. This city, together with Vlissingen, host the third-largest port of the Netherlands, after those of Rotterdam and Amsterdam, and is located on a vital shipping route, the Ghent – Terneuzen Canal. The pre-existing locks, “Oost sluis”, “West sluis” and “Midden Sluis” was causing a bottleneck because the traffic from Ghent and Terneuzen ports had increased over the years. A new lock had to be constructed for this issue to be resolved. The “Nieuwe Sluis” lock has replaced the smaller “Midden Sluis” lock and is located in between the other two, as indicated in Figure 1.1.1. It aims to increase the capacity, allow larger vessels to sail to the ports, and facilitate the economic growth of the Flemish regions.

“New Terneuzen Lock” is a complex project with many phases and is expected to be completed in 2023. The area underwent a complete reshaping to host the new lock. Figure 1.1.1 shows the previous situation with faded shapes. Some operations included constructing a 427 m x 55 m lock chamber, two lock heads (inner and outer) with two gate doors on each, two bascule bridges, and adjustment of the primary and regional flood defenses. Additionally, adjustment of the road network of the area, deepening the “Buitenhaven” and constructing various service buildings were necessary.



**Figure 1.1.1:** Top view of the project area that represents the previous and current situation of the Locks in the Gent-Terneuzen canal (SSV-RAP-163-C project report).

The current thesis will focus on a small yet vital part of the “New Terneuzen Lock,” the deep excavation of the outer head. Its location is indicated with a red rectangular in Figure 1.1.1. A representation of the excavation pit that will host the lock doors is shown in Figure 1.1.2. It is a complicated excavation reaching the - 22 m NAP. The retaining elements consist of Diaphragm Walls that are 1.5 m thick and reach a depth of NAP -45 m. Additionally, combi-walls have been used for the parts of the excavation pit that will eventually be removed to open the passage to the canal. To stabilize the walls, anchors, struts, and an underwater concrete floor have been used; those elements are shown in Figure 1.1.2.



**Figure 1.1.2:** 3D impression of the construction pit of the outer head (SSV-RAP-163-C project report).

The soil profile encountered at the outer head mainly consists of Anthropogenic and Silt deposits, Holocene Overburden, the First Aquifer sand package, a Boom Clay layer, and the Second Aquifer sand package. Special attention will be given to the behavior of the Boom Clay layer.

## 1.2 Problem Description

Besides the great importance in the region’s economic growth, the "New Terneuzen Lock" is part of the primary defense of the Netherlands against flooding. Such a project’s construction phase must follow strict schedules and meet very high safety standards. Failure in most deep excavation projects is also connected with severe implications. Such a case would compromise the safety of the construction personnel and cause extended damage to the surroundings. Hence, dealing with uncertainties regarding the prediction of the behavior of the construction pit and the appropriate design is vital.

Nowadays, the design of such projects is mainly performed with the aid of 2D or 3D Finite Element Method Programs. Even though these programs are state of the art, they heavily rely on the user’s input to simulate reality. Unfortunately, there are two sources of uncertainty, the first being the uncertainty of the geological conditions. Even though the in-situ and lab tests technology has improved immensely over the years, it cannot give 100 % certainty about underground conditions. It still relies on incremental soil testing throughout the construction site and assumptions of the conditions in between. Additionally, the lab testing on samples from the site has to deal with potential disturbance of the samples during extraction and transportation and testing under different surrounding conditions than the actual site. The constitutive models are the second category that imposes uncertainties in using finite element programs. Those models represent a mathematical framework to describe the material’s mechanical behavior. The tool describes the material’s responses to differ-

ent mechanical and loading conditions, which provide the stress-strain relations to formulate the governing equations (Buljak & Ranzi, 2021) [11].

Such a problem existed with a particular layer relevant to the retaining wall, the Boom Clay. It had a predominant role in the behavior of the wall, but the lab testing performed was inconclusive. Due to uncertainties regarding its behavior, a rather simplistic constitutive model was used, the Mohr-Coulomb. In the aftermath, it was found that the finite element design of the wall overpredicted the deformations for most of the construction phases.

Safety factors are being implemented to overcome the uncertainties mentioned above that are predominant in the geotechnical field. Moreover, a common approach from the designers of a project is to assume, most often than not, the most unfavorable conditions, such as drained soil layers. This combination often leads to projects that are overdesigned. On the one hand, this improves overall safety, but on the other hand, the cost increases immensely and on some occasions is why projects never materialize. Hence, it is essential to increase our confidence in the input parameters and investigate the true behavior of the Boom Clay layer.

### 1.3 Research Questions and Objectives

This thesis will have two main objectives to investigate the abovementioned uncertainties. The first is to investigate the most appropriate constitutive model to simulate the behavior of Boom Clay in a deep excavation format. The Boom Clay has been chosen because it is the most challenging layer this construction site had and created the most uncertainties for the designers at the time. Additionally, questions regarding the influence of the layer thickness and its behavior under drained or undrained conditions will be researched. The second goal is to utilize the monitoring data from this construction project to improve the design model. The monitoring data provide us with the actual situation, and a perfect design should have the same behavior, but this is hardly the case. Thus, this thesis constructed and used a Python Application to help the designer adjust the input parameters to the Finite Element models to close the gap between the actual deformations and the design predictions by taking advantage of data from the actual situation.

Ultimately, the Application will work as a central hub that allows the designer to interpret the monitoring and the design with many tools. It aims to complement conventional designs. It could be used in projects as the monitoring data are being created to allow the designers to make adjustments to achieve better accuracy and reduce risk. Furthermore, it could be a valuable tool for site engineering because it could create opportunities for savings by providing a better understanding of the behavior of the structure and the modeling of it. All in all, this tool captures the essence of the observational method (Nicholson et al., 1999 [27]) and could benefit projects that are designed following this strategy.

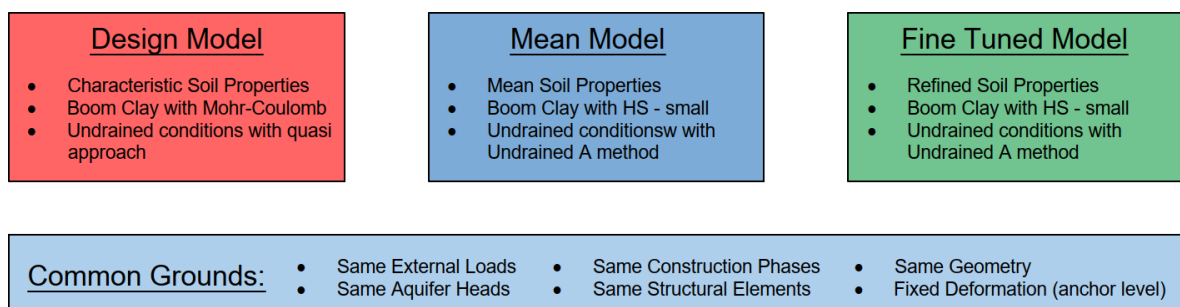
To satisfy these objectives, the following research questions will be answered.

1. *Which constitutive soil model approaches more accurately the behavior of Boom Clay and how is it compared with the one used in the design?*
2. *What is the sensitivity of the retaining wall to the different soil properties of the Boom Clay?*
3. *What is the effect of the boom clay thickness on the deformations and safety of the retaining wall, with special attention to the consideration of drained or undrained behaviour?*
4. *Is there an improvement in the accuracy of the prediction of the following construction stages by updating the parameters of the previous stages with an iterating process?*

5. *How can the current design be improved using the iterating method with the python application and monitoring data during the construction of the project? Are these benefits worth the extra analysis on top of the conventional design?*

## 1.4 Method of Approach

This thesis will work with three models to answer all the research questions and make the necessary comparisons. The models have been analyzed using the finite element program PLAXIS 2022. Figure 1.4.1 presents a short description of the three models. Additionally, a flow chart in Figure 1.5.1 has been constructed that describes the operations performed in the present document. Each operation is accompanied by a link to the corresponding section in the report.



**Figure 1.4.1:** Models

### Preparation Section

The preparation section consists of operations in oval shapes. In this section, all the necessary data for constructing the Design and Mean models are derived. The geometry, external loads, aquifer heads, construction phases, and dates have been created following the actual data from the construction of the project. Additionally, for all the models investigated in this thesis, the deformations of the combi wall at the anchor level have prescribed horizontal movement in PLAXIS. The deformation at that level follows the movement indicated by the corresponding inclinometers. This convention allows the reduction of the variables, essentially overcoming a design problem with the anchor system and focusing on the Boom Clay area where the interest lies. In the end, the effect of this assumption will also be discussed. So far, all these data will be common for both Design and Mean models to be comparable.

The actual difference between the models will be in the geotechnical aspect. For the Design model, the soil properties from the actual design have been used, hence the characteristic values. Similarly, the constitutive model and undrained approach of the actual design are being used. Furthermore, the mean (most probable) soil properties, free of safety factors, had to be derived for constructing the Mean model. A more sophisticated and appropriate soil constitutive model had to be used for the Boom Clay. Therefore, literature research and investigation have been performed to determine the constitutive model. This also answers the first research question. The last part of the preparation section is the process of monitoring data. In this thesis, the deformations are provided by inclinometers and total stations that have been used to include potential offset movement of the wall.

### Iterative Process

The following section is the iterative process that utilizes Python-Plaxis capabilities and monitoring

to produce the Fine Tuned model. This model aims to derive the actual soil properties of particular layers using the monitoring data and an iterative process. The initial input starts from the soil properties used in the Mean model, the Plaxis performs the calculation of the model, and a python script (Output Collector) collects the results and organizes them in a custom library. Then these results are compared with the corresponding monitoring deformations using several tools of the python application like the monitoring script, the comparison script, and the phase comparison script. The user decides if each phase's convergence of the monitoring and model deformations is acceptable. If there is no convergence, the input values change at a rate determined by the sensitivity analysis conducted with the python application, and the loop restarts. If there is a convergence, the Fine Tuned model is derived, and the actual soil properties have been deciphered. Because the comparison is deterministic, the limit to consider convergence has been set to a 10 % total deformation difference.

### Model Comparison

When all three models are derived, they are used to answer the remaining research questions (Yellow Section). The models are compared and used for parametric analysis in combination with the Python Application to produce the necessary results.

## **1.5 Thesis Outline**

Based on the previously described objectives, the outline of the thesis is structured as presented below:

In *Chapter 2 (Model Description)*, the necessary investigation to gather all the information needed for the three previously mentioned models will be made. Therefore, the mean soil properties, the construction phases, the structural elements properties, the actual loads, and aquifer heads will be derived. Furthermore, the available monitoring data will be analyzed and matched with the corresponding construction phases. The chapter also includes all the necessary theoretical background needed.

In *Chapter 3 (Python Application)*, the construction, functions, and use instructions of the python application will be discussed.

In *Chapter 4 (Model Application and Investigation)*, the models and applications described in the previous chapters will be used to answer all the research questions.

*Chapter 5 (Conclusions & Recommendations)* summarizes the report's findings and suggests topics for future study.

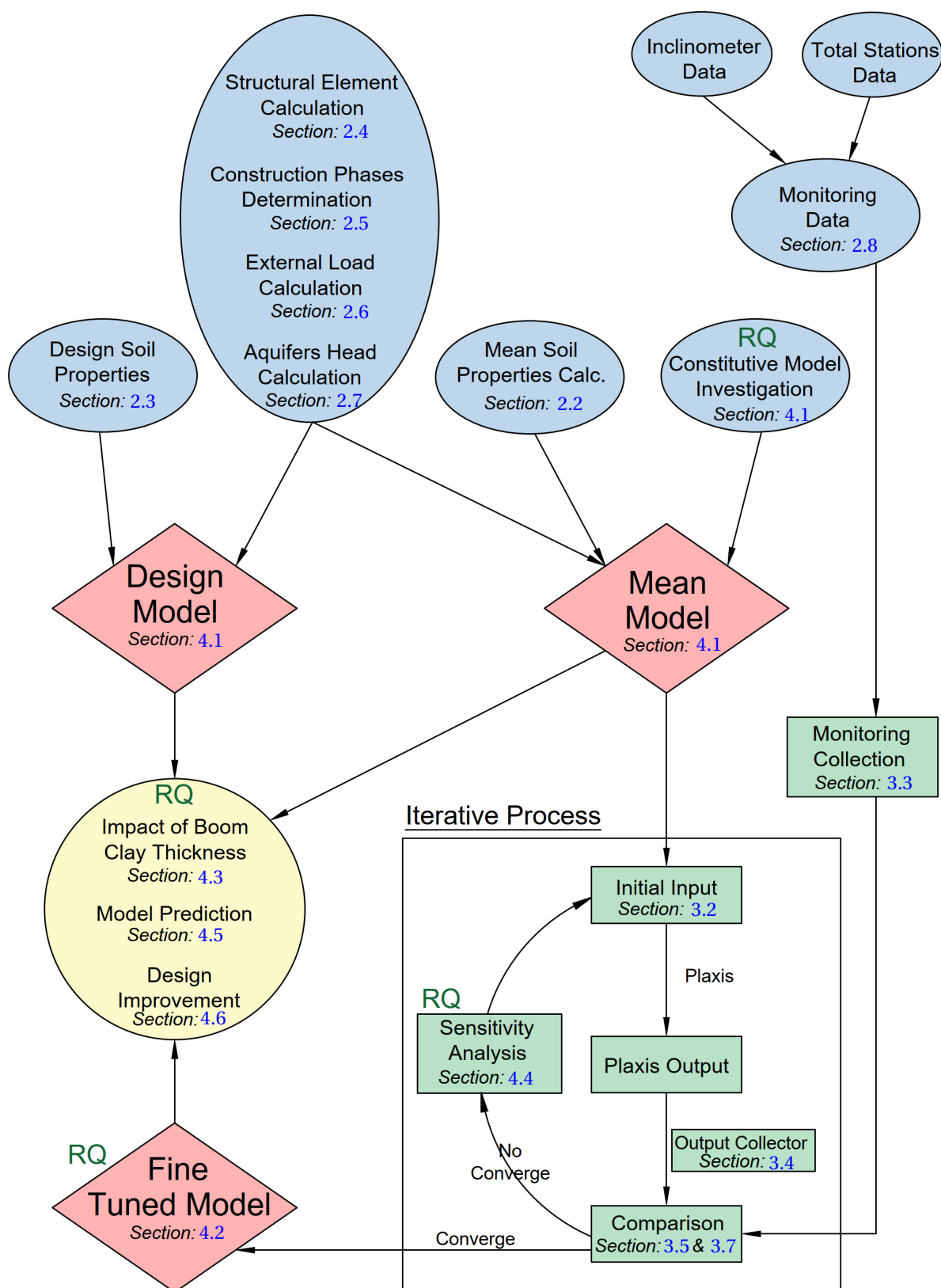


Figure 1.5.1: Thesis flow chart

## Model Description

In this chapter, all the necessary information for constructing the Mean model will be derived. Such information is the soil parameters that describe all the layers, the structural elements, the construction phases, the external loads, and the aquifer heads. Additionally, the monitoring methods for the present excavation are discussed and processed.

### 2.1 Parameter Determination - Theoretical Background

#### 2.1.1 CPT correlations

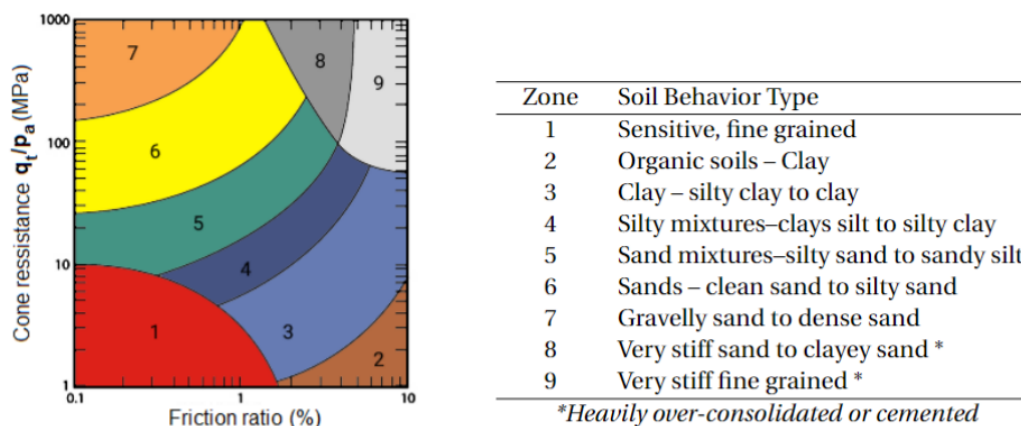
In the Netherlands, it is common practice to derive the soil properties from CPTs using cone resistance  $q_c$  correlations whenever soil lab tests are unavailable. The measured quantities of a normal CPT or a CPT with pore pressure measurements CPTu are:

- $q_c$  = Cone resistance
- $F_s$  = Sleeve friction
- $R_f$  = Friction ratio ( $f_s / q_c$ )
- $P_w$  = Pore pressures (applicable only for CPTu)

All the other properties that describe a soil layer can be derived using these measured values using correlations. Such properties are the secant Young's modulus stiffness at 50 %  $E_{50}$ , the undrained shear strength  $S_u$ , the relative density  $D_r$ , the permeability  $k$ , and the effective friction angle  $\phi'$ . When interpreting the CPT data, the most common correlations and methodology originate from Robertson, 2010 [29]. It is based on the normalized cone resistance ( $q_t / p_a$ ) and the friction ratio  $R_f$ . As seen in Figure 2.1.1, Robertson has considered nine representative areas within which the most common soil types can be categorized.

The vertical axis is the normalized cone resistance, and it is the ratio of the corrected cone resistance values,  $q_t$  (Equation 2.1.1), over the atmospheric pressure  $p_a$  that is considered equal to 100 kPa. The horizontal axis is the friction ratio  $R_f$ , which is the ratio between sleeve friction  $f_s$  and the normalized cone resistance  $q_t$ , given by Equation 2.1.2. The unit weight of the soil  $\gamma$  in relation to the unit weight of water  $\gamma_w$  is determined by Equation 2.1.2. Where  $u_2$ : Pore pressure [kPa],  $\gamma_w$ : Unit weight of water (=10 kN/m<sup>3</sup>),  $A_{tip}$ : The area of the cone and  $P_a$ : Atmospheric pressure (=100 kPa)





**Figure 2.1.1:** Non-normalized CPT Soil Behaviour Type chart (Robertson, 2010 [29]).

$$q_t = q_c - u_2 * (1 - A_{tip}) \quad (2.1.1)$$

$$R_f = f_s / q_t \quad (2.1.2)$$

$$\gamma / \gamma_w = 0.27 * (\log(R_f)) + 0.36 * (\log(q_t / p_a)) + 1.236 \quad (2.1.3)$$

### Table 2.b

The NEN 9997 provides a table that uses the cone resistance  $q_c$  from CPT tests as a first entry. This table is widely used across the Netherlands because it contains most soil layers and allows soil parameter derivation using  $q_c$  correlations. However, using this table in most cases will lead to conservative values. The table and its notes are presented in Appendix A.

### 2.1.2 Linear Regression

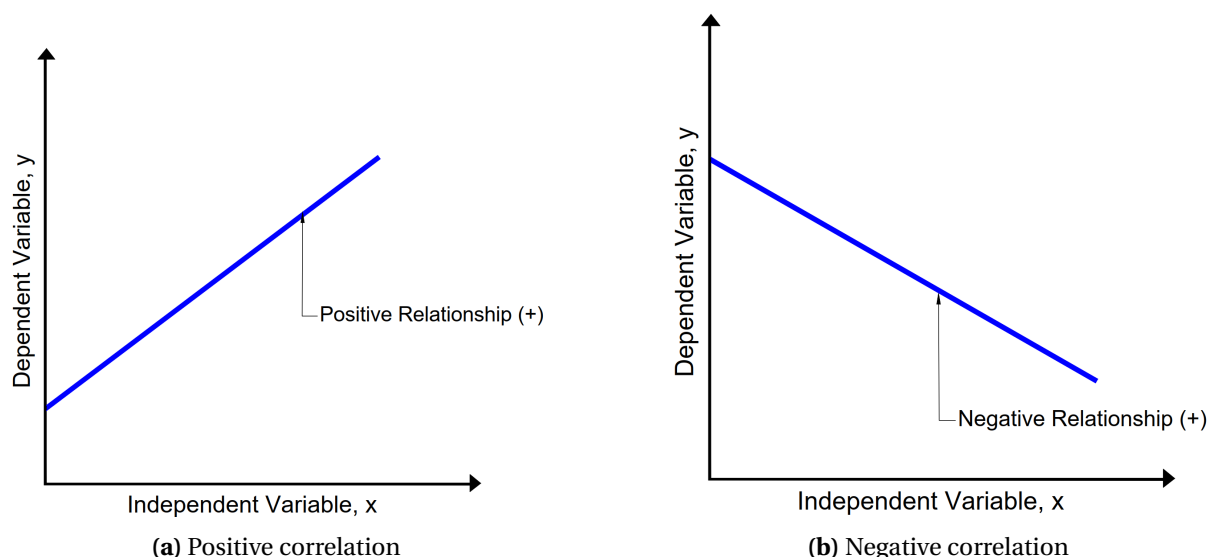
This section explains the linear regression method since it is a tool that will be used to determine the average values of effective friction angle  $\phi'$  and effective cohesion  $c'$  from multiple tests.

Linear regression is a statistical tool that models the relationship between a scalar response and a variable. Therefore, there are two variables, the independent on axis  $x$  and the dependent on axis  $y$ . In this case, the independent variable is the Deviatoric Stress  $q'$  applied by the triaxial apparatus, and the dependent variable will be the Mean Effective Stress  $p'$ .

Suppose the independent variable increases and, as a result, the dependent variable is also increasing. In that case, there is a positive relationship, Figure 2.1.2a. Contrary, when the independent variable increases and, as a result, the dependent variable decreases, there is a negative relationship, Figure 2.1.2b. When testing samples in an Undrained Triaxial Test, the correlation is always positive; hence by increasing the deviatoric stress, the effective stress is also increasing.

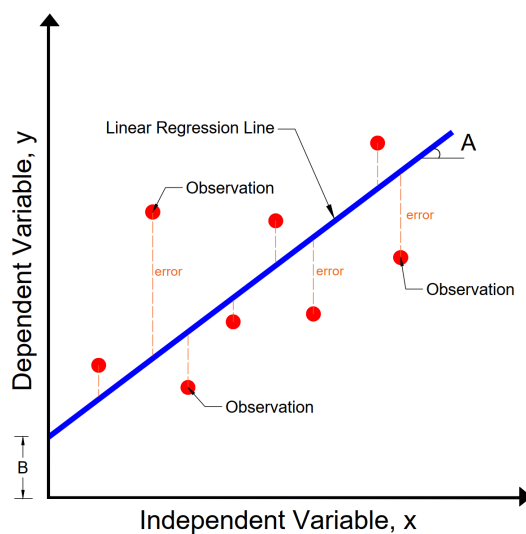
The purpose of the linear regression line is to fit all the observations as well as possible by keeping the straightness and only adjusting the height and inclination, and it is based on the least square's method. Therefore, Equation 2.1.4 can be derived that contains these parameters. The constant A is the inclination of the line, and the constant B is the height or the location where the line intercepts the Y axis,  $x$  is the independent variable, and  $y$  is the dependent variable.

$$y = A * x + B \quad (2.1.4) \quad \phi' = \tan^{-1}(A) \quad (2.1.5)$$



**Figure 2.1.2:** Positive and Negative correlation between the Independent and Dependent variable in linear regression.

Eventually, it tries to minimize the difference between the estimated and actual values. The actual value is the observation, and the estimated value is the cross-section of the linear regression line and the vertical line originating from the observation. This difference is called "error". Hence, adjusting the constant A and B tries to make the errors for all the observations as small as possible. The above parameters are depicted in Figure 2.1.3.



**Figure 2.1.3:** Visual description of all the properties of the linear regression method.

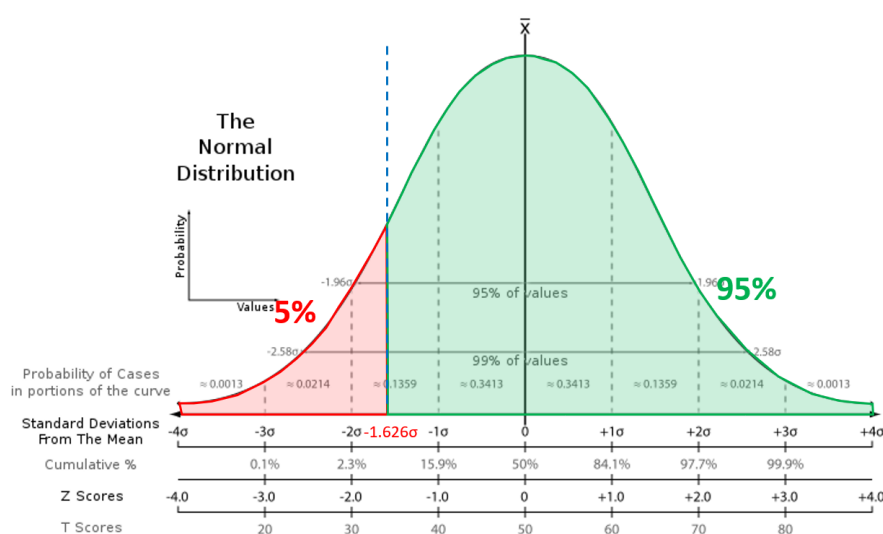
### 2.1.3 Mean values determination

The New Terneuzen Lock, as well as the Dutch geotechnical engineering and design practice in general, are based on NEN 9997-1. In the absence of more detailed lab test data, the parameters are generally determined from table 2.b of the NEN 9997-1 document (Appendix A), using as input the data from CPT in situ testing. For instance, this approach was deemed necessary for determining the soil parameters for the sand and peat layers in the current project.

As mentioned in the notes of [table 2.b](#) for gravel, sand, and to a limited extent for loam and heavily sandy clay, the parameters  $q_c$ ,  $E_{100}$ ,  $\phi'$ ,  $c'$  and the compression parameters,  $C'p$ ,  $C_c/(1 + e_0)$  and  $C_{sw}/(1 + e_0)$  have been standardized for effective vertical ground stress  $\sigma_v'$  of 100 kPa. Therefore, the  $q_c$  measured in the field must also be normalized to that effective stress. Equation 2.1.6 is being used for that purpose.

$$q_{c,table} = q_{c,measured} * (100/\sigma_v')^{0.67} \quad (2.1.6)$$

The values derived from [table 2.b](#) are characteristic values for a vertical effective stress level of 100 kPa. Therefore, the values are increased and decreased depending on the contribution of the parameter to achieve 95 % safety. However, in the present thesis, the results are intended to be compared with real monitoring data from the field. Therefore, the main focus will be on the values closer to reality, the mean (most probable) values. Hence a conversion from characteristic to mean values is needed.



**Figure 2.1.4:** Normal distribution

To perform this conversion, the row that indicates the coefficient of variation  $V$  for [table 2.b](#) for each parameter is used. The assumption that the soil parameters follow a normal distribution is also made. As it can be seen in [Figure 2.1.4](#), the Gaussian bell is divided into parts based on standard deviations ( $-4\sigma$ ,  $-3\sigma$ , ...,  $+3\sigma$ ,  $+4\sigma$ ), and the area of each sector represents the probability of a case belonging there. The entire area of the bell has a probability of 1 to occur. Hence, to find the 95 % reliability, sections of the curve are subtracted until 0.95 probability for a case to occur is reached. When the parameter examined positively affects the project's safety, the 95 % value (characteristic) exists on the left side of the curve. Hence a value lower than the actual is considered. On the other hand, when the parameter examined harms the project's safety, the 95 % value (characteristic) exists on the right side of the bell. Hence the negative effect is amplified. Theoretically, the most probable value exists in the middle of the bell and is the closest to reality.

For instance, the effective friction angle  $\phi'$  is considered. Generally, it is safer to consider a lower value of  $\phi'$  than to overestimate it at a project. Hence, the characteristic value of friction angle belongs on the left side of the bell. Therefore, to find the 5 % (red area in [Figure 2.1.4](#)) that needs to be removed, each section's percentage is added until it reaches 0.05. The relevant sections are:

- Section 1:  $[-4\sigma, -3\sigma]$  with probability 0.0013

- Section 2:  $[-3\sigma, -2\sigma]$  with probability 0.0214
- Section 3:  $[-2\sigma, -1\sigma]$  with probability 0.1395

The sum of sections 1 and 2 is 0.0227; hence,  $0.05 - 0.0227 = 0.0273$  still needs to be removed. Therefore, only a part of section 3 needs to be removed to reach the 0.05 value. This value is derived with linear interpolation.

$$\begin{array}{rcl} \text{At } -2 * \sigma & \rightarrow & 0 \\ \text{At } -Y * \sigma & \rightarrow & 0.0273 \\ \text{At } -1 * \sigma & \rightarrow & 0.1359 \\ \hline & & Y = -1.6255 \end{array}$$

This Y value shows the distance from the mean  $\mu$  value that 95 % exists in terms of standard deviation  $\sigma$ . Therefore, the equations that correlate a parameter's mean and characteristic values are 2.1.7 and 2.1.8 for positive and negative effects, respectively.

$$\text{Positive effect: } X_{characteristic} = X_{mean} - 1.6255 * \sigma \quad (2.1.7)$$

$$\text{Negative effect: } X_{characteristic} = X_{mean} + 1.6255 * \sigma \quad (2.1.8)$$

The variation coefficient is expressed by Equation 2.1.9.

$$V = \frac{\sigma}{X_{mean}} \quad (2.1.9)$$

Finally, given the fact that the table gives  $X_{characteristic}$  and  $V$ , by using the equations 2.1.7 or 2.1.8 with 2.1.9 the  $X_{mean}$  parameter can be derived.

#### 2.1.4 Hardening Soil Small Strain Constitutive Model

This paragraph will analyze all the methods used to derive the soil parameters relevant to the Hardening soil small strain constitutive model. A model that is being used to simulate the behaviour of all the soil layers of the project in a finite element environment. The relevant parameters are summarized in Table 2.1.1.

##### Effective Friction Angle $\phi'$ and Effective Cohesion $c'$

The calculation of strength parameters in this thesis often is performed through Undrained Triaxial Tests in three different confining stresses for each. Most commonly, there is a plethora of lab tests for each soil layer; hence, the linear regression method is used to take them all into account and derive the most representative values for the strength parameters. The parameters change is depending on the strain percentage. Therefore, for the sake of uniformity and following the suggestions of the CUR code for deep excavations, the  $\tau$ - $s$  space is constructed for 2 % strain of the sample.

In a lab environment or the field, a soil specimen is subjected to a load; as a result, it experiences changes in the stress state. The stress state of a sample can be fully described by three perpendicular principal stresses  $\sigma_1, \sigma_2, \sigma_3$ , and the pore pressure  $u$ . One of the most common ways to represent

**Table 2.1.1:** Parameters summary for the Hardening Soil Small Strain constitutive model.

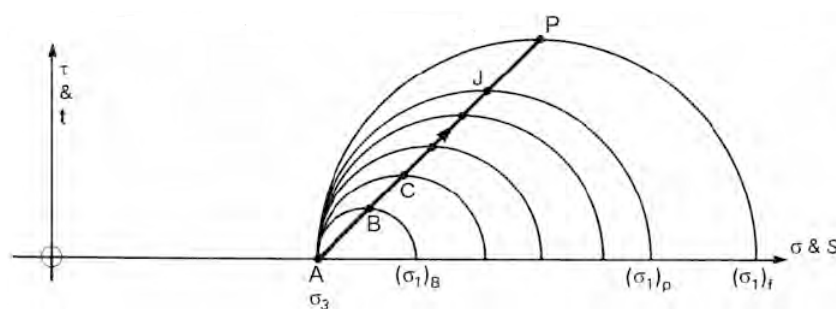
N.	Parameters	Description
1	$c'$	Effective Cohesion
2	$\phi'$	Effective Friction Angle
3	$\nu_{ur}$	Poisson's ratio in unloading / reloading
4	$\psi$	Dilatancy angle
5	$K_0^{nc}$	Stress ratio $\sigma'_{xx}/\sigma'_{yy}$ in 1D primary compression
6	$E_{Oed}^{ref}$	Tangent stiffness from oedometer test at $p_{ref}$
7	$E_{ur}^{ref}$	Reference stiffness in unloading / reloading
8	$E_{50}^{ref}$	Secant stiffness from triaxial test at reference pressure
9	$m$	Rate of stress dependency in stiffness behavior
10	$p_{ref}$	Reference pressure
11	$R_f$	Failure ratio
12	$G_0^{ref}$	Reference shear stiffness at small strains
13	$\gamma_{0.7}$	Shear strain at which $G$ has reduced to 72.2 %

the stress state of a soil sample is the MIT stress path developed by Professor T. W. Lambe [21]. The parameters  $s$  and  $\tau$  have been derived by Atkinson and Bransby, 1978 [4]. and are described by the Equations 2.1.10 and 2.1.11, respectively.

$$s = (\sigma_1 + \sigma_3)/2 \quad (2.1.10)$$

$$\tau = (\sigma_1 - \sigma_3)/2 \quad (2.1.11)$$

During a compression test, the vertical stress  $\sigma_1$  increases. Hence, the Mohr circles have an increasing radius in Figure 2.1.5. The A-B-C-J-P is the sample's stress path until failure, where the Mohr circle touches the failure envelope. An advantage is that by using stress path points, the circles are replaced.



**Figure 2.1.5:** Derivation of MIT stress field and the stress path as the locus of stress points. (Lambe, 1991 [21]).

Through the stress path, the derivation of shear strength parameters is possible. Figure 2.1.6 shows line H-P as the failure line at the peak deviator stress. Although the inclination and interception of the y-axis of this line do not give the effective friction angle  $\phi'$  and effective cohesion  $c'$  of the sample, the transformation is possible. The equations that compare the  $K_f$  - line with the tangent failure are 2.1.12 and 2.1.13.



Bowles E. 1968, [9] suggests that a more representative undrained poisson ratio for fine-grained soil would be 0.15 and for coarse-grained material 0.2.

To conclude, the suggestions of Bowles will be used since they agree with the Plaxis Manual of Brinkgreve et al., 2011 [10] and have been used by the present design, which will be convenient for comparison purposes in a later stage. Specifically for the soil layer L15, the Boom Clay, the undrained Poisson's ratio  $\nu_{ur}$  will be considered equal to 0.3 according to findings of the Oosterweelverbinding Rechteroever Integral project parameter determination report, which has a similar soil profile as the current project in Terneuzen. Poisson's ratio takes the values depicted in Table 2.1.2.

**Table 2.1.2:** Values of Poisson's ratio  $\nu$

Soil Type	Poisson's ratio $\nu$ .
Sand	0.2 - 0.3
Clay and Peat	0.3 - 0.45
Clay and peat in undrained conditions	0.5

### Dilatancy Angle $\psi$

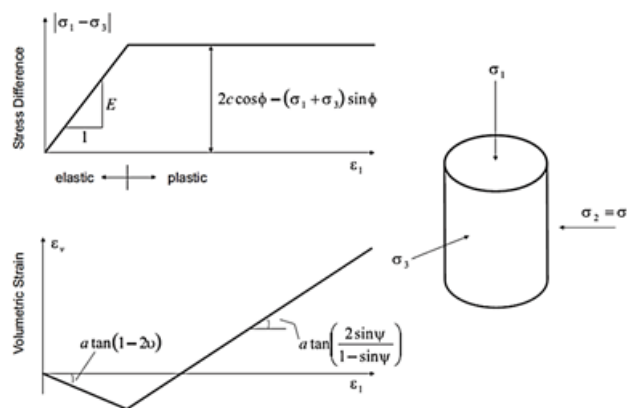
Upon shearing, the soil material dilates or contracts depending on its initial density configuration; this behavior is described by the dilatancy angle,  $\psi$ . Essentially as has been described by Steven F. Bartlett, 2011 [6], the angle of dilation controls an amount of plastic volumetric strain developed during plastic shearing and is assumed constant during plastic yielding. Typically, the dilatancy angle is determined from triaxial tests directly. For instance, Figure 2.1.7 by Vermeer & de Borst, 1984 [33] shows that the dilation angle can be found using the axial strain vs volumetric strain plot. The lower curve shows that after a small amount of compaction, the sample dilates, after which it comes into a state in which the volumetric strain does not change anymore. The latter coincides with the final failure state and is called Critical State.

When the dilatancy angle is 0 it translates to volume preservation while shearing. Clay soils typically observe such behavior, whether normally consolidated or slightly over-consolidated. For sands and coarse-grained material, the dilation angle depends on the internal friction angle. The dilatancy angle  $\psi$  can be expressed following Schanz and Vermeer's, 1996 [31] Equation 2.1.16. Where  $\phi_f$  is the friction angle at failure,  $\psi_{cv}$  is the critical state or constant volume friction angle, and  $\psi_f$  is the dilatancy angle at failure.

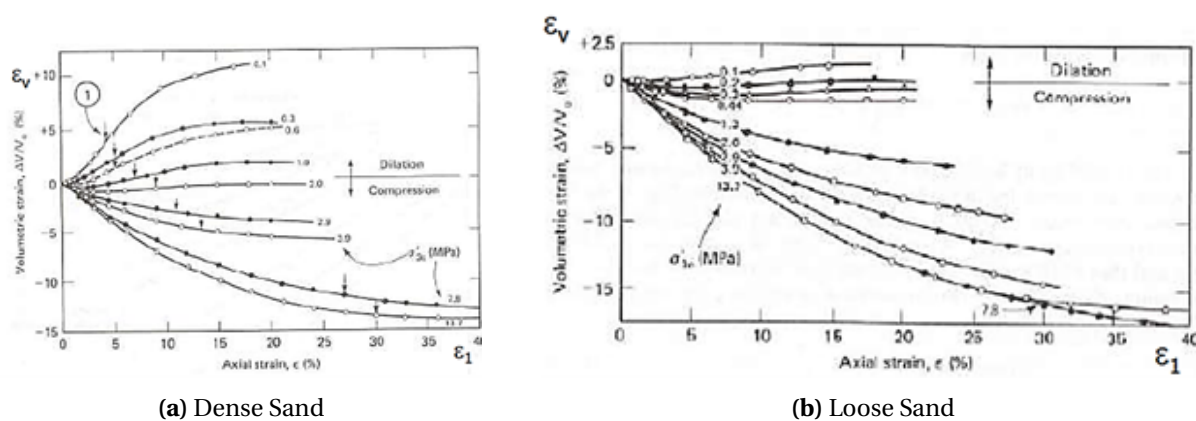
$$\sin(\psi_f) = \frac{\sin(\phi_f) - \sin(\phi_{cv})}{1 - \sin(\phi_f) * \sin(\phi_{cv})} \quad (2.1.16)$$

Additionally, it was found by Lee, 1965 [22] that the dilatancy also depends on the confining pressure. It can be seen in Figure 2.1.8a for dense sand and Figure 2.1.8b for loose sand that for the small confining pressure, the sample dilates, and if the confining pressure is increased a lot, the dense soil starts to behave as soft soil and only compacts. One possible explanation for this 'suppression of dilatancy' is the effect of 'grain crushing'.

Since lab tests are not always available to determine the peak and constant friction angle, it is common practice to use some estimations that are summarized in Table 2.1.3. A reasonable estimate for sands states that when the effective friction angle  $\phi'$  of sands is greater than  $30^\circ$ , then the dilatancy angle  $\psi$  can be calculated as  $\psi = \phi' - 30^\circ$ . Although a negative dilation angle is possible, it has been adopted to be considered as 0. Essentially these values are only valid for quartz sands and normally



**Figure 2.1.7:** Idealized relation for dilatancy angle,  $\psi$ , from triaxial test results (Vermeer & de Borst, 1984 [33]).



**Figure 2.1.8:** Axial strain vs. volumetric strain plots to investigate the dilation/compression of dense and loose sand (Lee, 1965 [22])

consolidated or lightly over-consolidated clay. Typical values for dilatancy angles  $\psi$  of materials are given in Table 2.1.4 by Vermeer & de Borst, 1984 [33].

**Table 2.1.3:** Values of Poisson's ratio  $\nu$

Soil Type	Dilatancy Angle $\psi$ .
Sand: $\phi' > 30^\circ$	$\phi' - 30^\circ$
Sand: $\phi' < 30^\circ$	0
Clay and Peat	0

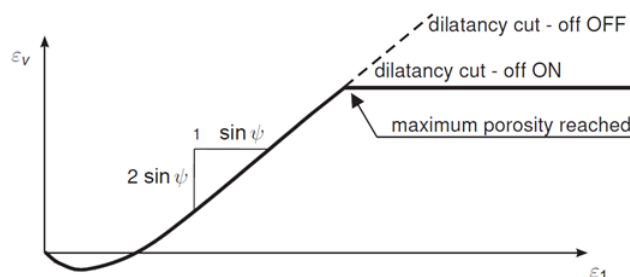
Furthermore, the PLAXIS Manual also suggests the use of Table 2.1.4 for the calculation of dilatancy angle while at the same time raising awareness about the necessity of dilatancy cut-off. As seen from the bottom plot of Figure 2.1.7, soil with a positive dilatancy angle in drained conditions will continue to dilate as long as shear deformation occurs. However, this is unrealistic since the soil will reach a critical state where it will retain a constant volume no matter the shear deformation. Therefore, the Hardening Soil small strain model applies a dilatancy cut-off, that as soon as the volume change results in a state of the maximum void, the dilatancy angle is set back to 0. That behavior is presented in Figure 2.1.9 by PLAXIS Manual of Brinkgreve et al., 2011 [10]. Finally, when dealing with undrained



**Table 2.1.4:** Typical values of dilation angle for different materials (Vermeer & de Borst, 1984 [33]).

Material	Dilation Angle $\psi$ .
Dense Sand	$15^\circ$
Loose Sand	$< 10^\circ$
Normally consolidated clay	$0^\circ$
Granulated and intact marble	$12^\circ - 20^\circ$
Concrete	$12^\circ$

material, the dilatancy angle should equal to 0 because the void ratio remains constant.

**Figure 2.1.9:** Resulting strain curve for a standard drained triaxial test when including dilatancy cut-off (Brinkgreve et al., 2011 [10]).

### Interface $R_{int}$ and Angle of wall friction $\delta$

For models of retaining walls, in PLAXIS, the reduced strength of the soil/construction interface is not described with a wall friction angle  $\delta$  ( $= \phi'_{interface}$ ) but with an interface parameter  $R_{int}$  as given by the Equation 2.1.17. The wall friction angle is generally determined from Table 2.1.5 of NEN9997 code table 9b, Appendix A, or literature references. Theoretically, the wall friction angle  $\delta$  can be determined using a direct shear test, where a characteristic soil sample is sheared along a wall sample. However, given the difficulty and unreliability of this test, this approach is rarely preferred.

$$R_{int} = \frac{\tan(\phi'_{interface})}{\tan(\phi'_{soil})} \quad (2.1.17)$$

PLAXIS calculates the correct shape of the sliding surfaces, which automatically takes into account the required compatibility of the deformation induced by the wall friction angle. As a result, the  $\delta$  can be determined based on the rules valid for curved sliding surfaces. Moreover,  $\delta$  should be maintained at 0 when the adjusted soil to the structure is peat according to code CUR 166.

### Neutral ground pressure coefficient $K_0$

Following the suggestions of the PLAXIS Manual, the neutral ground pressure coefficient was determined using Jaky's, 1944 [18] (Equation 2.1.18), in which  $\phi'$  is the design value of the effective angle of internal friction. The same Equation is used for all cohesive soil materials.

**Table 2.1.5:** Wall friction angle determination with the relative wall roughness (NEN9997, table 9b).

Relative wall roughness	Definition	Wall Angle of friction $\delta$	
		Strain slip circles	Curved slip circles
Toothed	$> 10 * \delta_{10}$	$0.67 * \phi_k'$	$\phi_k'$
Rough / Coarse	$0.5 * \delta_{10} - 10 * \delta_{10}$	$0.67 * \phi_k'$	$\phi_k' - 2.5, \max 27.5$
Half rough	$0.1 * \delta_{10} - 0.5 * \delta_{10}$	$0.33 * \phi_k'$	$0.5 * \phi_k'$
Smooth	$< 0.1 * \delta_{10}$	0	0

$$K_0 = (1 - \sin(\phi)') \quad (2.1.18)$$

For calculations of earth-retaining structures, the value at 2 % strain is used to determine the internal effective friction angle. Finally, the neutral soil pressure coefficient for peat layers equals 0.5.

### Oedometer Stiffness $E_{oed}$ and Unloading/Reloading Stiffness $E_{ur}$

When oedometer lab tests are available for soft soils like clay, the oedometer stiffness can be calculated using the modified compression index  $\lambda^*$  that originates from the Soft Soil constitutive model. Equation 2.1.19 is essentially derived from the relationship with the Cam-clay constitutive model parameter  $\lambda$  divided by the specific volume  $(1+e)$ .

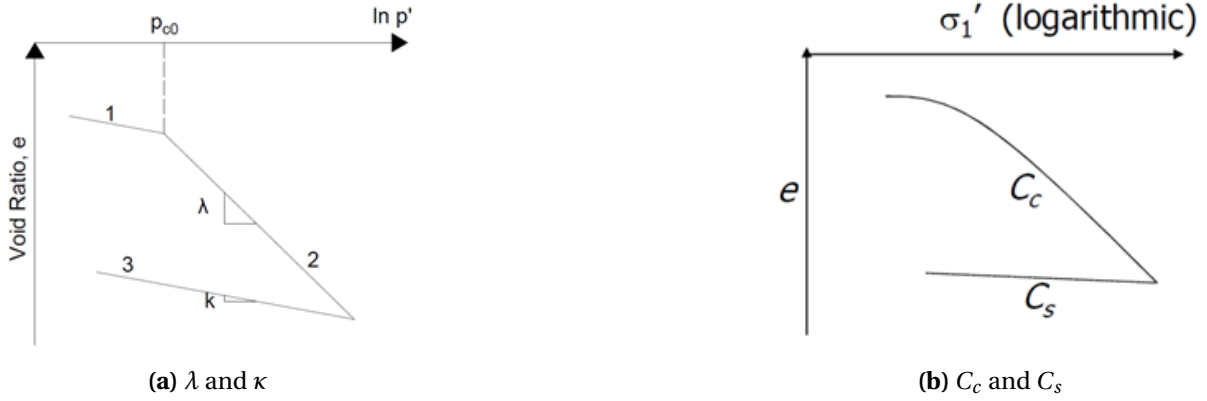
$$\lambda^* = \frac{\lambda}{1+e} \quad (2.1.19)$$

The parameter  $\lambda$  is based on the logarithmic relationship for the change of void ratio in isotropic compression and unloading. Figure 2.1.10a presents an idealized and qualitative version. Section 2 in the figure is the primary loading called Normal Consolidation Line; its starting point is immediately after the pre-consolidation stress  $p_{c0}$ . The rate at which the void ratio changes under compression is given by the parameter  $\lambda$ .  $\lambda$  is essentially the inclination of the line and is also mentioned in literature as a compression index. It is shown that with the load increase, the void ratio is reduced; the higher the  $\lambda$ , the larger the straining. Geometrically, the  $\lambda$  in primary loading can be calculated by Equation 2.1.20.

$$e_0 - e = \lambda * \ln(p'/p_0) \quad (2.1.20)$$

On the other hand, section 1 and section 3 are the reloading and unloading states, respectively. It is shown that these two sections are parallel to each other; hence they have the same inclination. Therefore, whenever the sample is loaded with stress below the pre-consolidation stress  $p_{c0}$ , or it is unloaded, the parameter  $\kappa$  gives the change rate of the void ratio. This parameter is also mentioned in literature as the swelling index. Geometrically, the  $\kappa$  for unloading/reloading can be calculated by Equation 2.1.21.

$$e_0 - e = \kappa * \ln(p'/p_0) \quad (2.1.21)$$



**Figure 2.1.10:** Logarithmic relationship of void ratio with loading and unloading, expressed with the parameters ( $\lambda - \kappa$ ) and ( $C_c - C_s$ ).

An additional method to calculate the modified compression  $\lambda^*$  and swelling  $\kappa^*$  index, according to Bjerrum, 1967 [8], is to relate them with one-dimensional compression index  $C_c$  and swelling index  $C_s$ , respectively. The Equations 2.1.22 and 2.1.23 describe this relationship. The  $\ln(10)$  is used in the Equation because the  $C_c$  and  $C_s$  are based on a  $\log - 10$  scale, as shown in Figure 2.1.10b. Whereas  $\lambda^*$  and  $\kappa^*$  are based on an  $\ln$  scale. The  $C_c$  and  $C_s$  indexes are calculated similarly to  $\lambda$  and  $\kappa$ , as shown in Equations 2.1.24 and 2.1.25 for their respective sectors.

$$\lambda^* = C_c / (\ln(10) * (1 + e)) \quad (2.1.22) \quad \kappa^* = 2 * C_s / (\ln(10) * (1 + e)) \quad (2.1.23)$$

$$C_c = (e_0 - e) / (\log(\sigma'_v / \sigma'_{v0})) \quad (2.1.24) \quad C_s = (e_0 - e) / (\log(\sigma'_v / \sigma'_{v0})) \quad (2.1.25)$$

As a result, according to PLAXIS Manual, when soft soils are considered, the oedometer stiffness can be calculated by the Equation 2.1.26 and the unloading reloading oedometer stiffness from Equation 2.1.27.

$$E_{oed} = \frac{\ln(10) * (1 + e_{ini}) * p}{C_c} \quad (2.1.26)$$

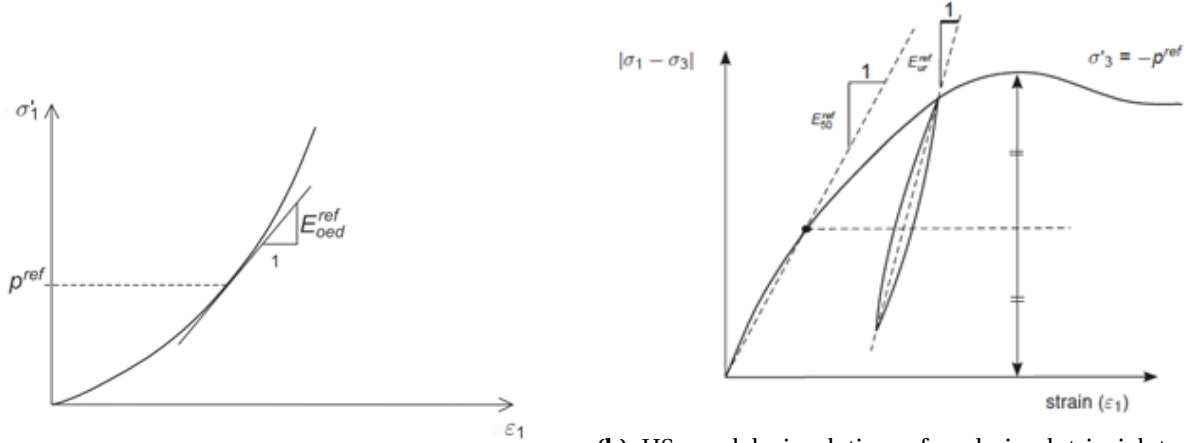
$$E_{ur} = \frac{\ln(10) * (1 + e_{ini}) * (1 + \nu_{ur}) * (1 - 2 * \nu_{ur}) * p}{(1 * \nu_{ur}) * C_s * K_0} \quad (2.1.27)$$

The Poisson's ratio in unloading/reloading  $\nu_{ur}$  according to PLAXIS Manual is equal to 0.2 because, in the Hardening Soil model,  $\nu_{ur}$  is considered a pure elastic parameter. By default, PLAXIS assumes that, on average, the horizontal stress is equal to the vertical stress during unloading/reloading ( $K_0 = 1$ ).

The unloading reloading stiffness  $E_{ur}$  can also be derived by implying an unloading step in a drained triaxial or oedometer apparatus; its behavior is purely elastic. The  $E_{ur}$  is the inclination of the unloading/reloading stress path, as shown in Figure 2.1.11b. The stiffness is stress-dependent; hence the  $E_{oed}$  corresponds to the investigated stress  $p$ . Therefore, to find the reference stiffness  $E_{oed}^{ref}$ , the stress  $p_{ref}$  should be considered, typically 100 kPa. Graphically, the  $E_{oed}$  is the inclination of the tangent at a specific stress level, as shown in Figure 2.1.11a. Similarly, the  $E_{ur}^{ref}$  is the average unloading/reloading stiffness in a triaxial test at a cell pressure  $p_{ref}$ , where unloading is performed just before failure is reached.

$$E_{Oed}^{ref} = \frac{E_{Oed}}{\left( \frac{c * \cos(\phi') - \sigma' * \sin(\phi')}{c * \cos(\phi') + p_{ref} * \sin(\phi')} \right)^m} \quad (2.1.28)$$

$$E_{ur}^{ref} = \frac{E_{ur}}{\left( \frac{\sigma}{p_{ref}} \right)^m} \quad (2.1.29)$$



(a) Determination of the reference oedometer modulus  $E_{Oed}^{ref}$  (Brinkgreve et al., 2011 [10]).

(b) HS model simulation of a drained triaxial test at a cell pressure equal to the reference stress level (Brinkgreve et al., 2011 [10]).

**Figure 2.1.11:** Stiffness properties for the hardening soil small strain model.

### Secant Stiffness $E_{50}$

In reality, the stiffness of soil material is stress-dependent, and the Hardening Soil Small Strain constitutive model allows for the simulation of this behavior by using the secant stiffness  $E_{50}$ . It can be derived from a standard drained triaxial test by plotting the deviatoric stress versus the strain. As indicated in Figure 2.1.13, the secant stiffness is the inclination of the line that connects 50 % of the maximum deviatoric stress and the start of the axis. Similarly, with the different stiffnesses mentioned previously,  $E_{50}$  must be translated at a reference level. Therefore, at a cell pressure equal to the reference stress level  $p_{ref}$ , which typically is 100 kPa, the reference secant stiffness is derived using Equation 2.1.30.

$$E_{50}^{ref} = \frac{E_{50}}{\left( \frac{\sigma}{p_{ref}} \right)^m} \quad (2.1.30)$$

Suppose triaxial tests are unavailable according to the code CUR 2003 – 7, table 3.1, Appendix A. In that case, the  $E_{50}^{ref}$  and  $E_{ur}^{ref}$  can be determined in correlation to the oedometer stiffness, depending on the type of soil they refer to. These correlations are given from the Equations 2.1.31 to 2.1.36.

$$\text{Clay (OCR < 1)} \quad E_{50}^{ref} \approx 2 * E_{Oed}^{ref} \quad (2.1.31)$$

$$E_{ur}^{ref} \approx 5 * E_{50}^{ref} \quad (2.1.32)$$

$$\text{Clay (OCR > 1)} \quad E_{50}^{ref} \approx E_{Oed}^{ref} \quad (2.1.33)$$

$$E_{ur}^{ref} \approx 4 * E_{50}^{ref} \quad (2.1.34)$$

$$\text{Sand (OCR = 1)} \quad E_{50}^{ref} \approx E_{Oed}^{ref} \quad (2.1.35) \quad E_{ur}^{ref} \approx 4 * E_{50}^{ref} \quad (2.1.36)$$

### Stiffness correlations based in $q_c$

However, many times the derivation of the stiffness is only sometimes successful by the lab tests. Therefore, the relevant project's soil stiffness correlation with  $q_c$  is presented in this paragraph.

It is known that undisturbed samples of sandy soil are nearly impossible to be obtained. For a coarse-grained sample to be tested, its in-situ density has to be restored, which requires a special measuring apparatus (the conductivity cone). To overcome this problem, it is common practice to use correlations with the cone resistance to derive the strength parameters. Based on a review of available calibration chamber tests, Lunne and Christophersen, 1983 [24] recommended that the  $E_{oed}$  for NC un-aged and un-cemented predominantly silica sands can be obtained from Equations 2.1.37, 2.1.38 and 2.1.39.

$$E_{oed} = 4 * q_c \text{ (MPa)} \quad \text{for } q_c < 10 \text{ MPa} \quad (2.1.37)$$

$$E_{oed} = 2 * q_c + 20 \text{ (MPa)} \quad \text{for } 10 \text{ MPa} < q_c < 50 \text{ MPa} \quad (2.1.38)$$

$$E_{oed} = 120 \text{ (MPa)} \quad \text{for } q_c > 50 \text{ MPa} \quad (2.1.39)$$

Lunne and Christophersen, 1983 [24] also included OC sands in their study and recommended as a rough guideline to use the Equations 2.1.40 and 2.1.41.

$$E_{oed} = 5 * q_c \text{ (MPa)} \quad \text{for } q_c < 50 \text{ MPa} \quad (2.1.40)$$

$$E_{oed} = 250 \text{ (MPa)} \quad \text{for } q_c > 50 \text{ MPa} \quad (2.1.41)$$

For lightly to highly glauconite sand layers, the correlation of Trofimenkiv given by the Equation 2.1.42 is used.

$$E_{oed} = E_{50} = 3.4 * q_c + 13 \text{ (MPa)} \quad (2.1.42)$$

Finally, the unloading and reloading stiffness for tertiary clay layers can be derived from Equation 2.1.43, according to Lunne and Christophersen, 1983 [24].

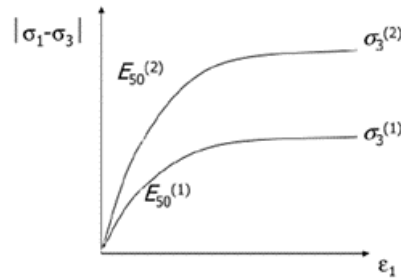
$$E_{ur}^{ref} = 5 * E_{Oed}^{ref} \quad (2.1.43)$$

### Rate of stress dependency $m$

The parameter  $m$  is the stress dependency rate on a material's stiffness. It is determined from two triaxial tests on the same material at different confining pressures, for instance,  $\sigma_3^{(1)}$ , and  $\sigma_3^{(2)}$ . The resulting secant stiffness for each confining pressure would be  $E_{50}^{(1)}$  and  $E_{50}^{(2)}$ , respectively. Equation 2.1.44 gives the power law of that stress dependency and is graphically presented in Figure 2.1.12, according to Brinkgreve et al., 2011 [10].

$$\frac{E_{50}^{(1)}}{E_{50}^{(2)}} = \left( \frac{\sigma_3^{(1)}}{\sigma_3^{(2)}} \right)^m \Rightarrow m = \frac{\ln \left( \frac{E_{50}^{(1)}}{E_{50}^{(2)}} \right)}{\ln \left( \frac{\sigma_3^{(1)}}{\sigma_3^{(2)}} \right)} \quad (2.1.44)$$

If the stress dependency of stiffness cannot be measured from lab tests, the reasonably accurate estimation for sand layers is  $m \approx 0.5$  and for normally consolidated clay layers  $m \approx 1.0$ .



**Figure 2.1.12:** Deviatoric versus axial strain plot resulting from a triaxial compression test at two different confining stress (Brinkgreve et al., 2011 [10]).

### Reference Pressure $p_{ref}$

Since some soil parameters like stiffness are stress-dependent is helpful to translate them into certain stress. The finite element program used in this thesis will be PLAXIS, and according to its manual, the reference stress level pref suggested is 100 kPa or 1 Bar.

### Failure ratio $R_f$

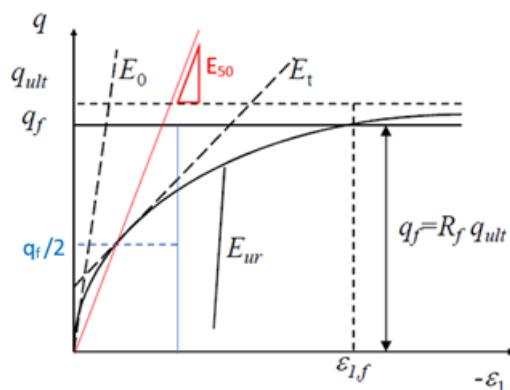
In a hyperbolic model like the Hardening Soil, the principal stress difference can be written as given by the Equation 2.1.46 and is graphically depicted in Figure 2.1.13.

$$q = \frac{-\epsilon_1}{\frac{1}{E_{50}} - \frac{\epsilon_1}{q_{ult}}} \Rightarrow \epsilon_1 = \frac{\frac{q}{E_0}}{1 - \frac{q}{q_{ult}}} \quad (2.1.45)$$

By looking at Equation 2.1.45, it can be seen that when  $q_{ult}$  approaches  $q$ , the denominator of the Equation becomes 0; hence the strains  $\epsilon$  tends to go to infinity. It is reasonable to assume that the deviatoric stress  $q$  has an asymptotic that will never reach because the strains, in reality, can be infinite. However, that does not mean that the sample will not fail at a finite strain level. To overcome this problem, a new failure deviatoric stress  $q_f$  is being defined  $R_f$  times the  $q_{ult}$  level as shown in Equation 2.1.46.

$$R_f = \frac{q_f}{q_{ult}} \quad (2.1.46)$$

The PLAXIS Manual recommends a value of  $R_f$  equal to 0.9, which means the failure level is reduced by 10 %.

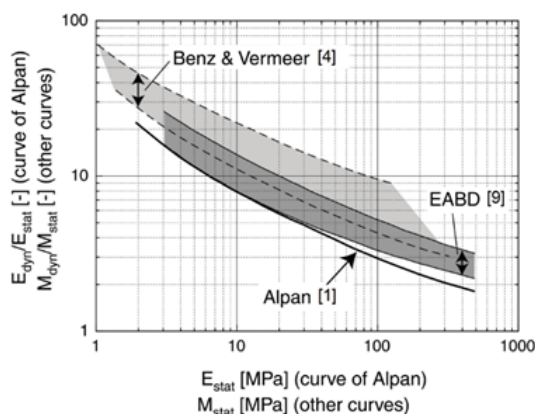


**Figure 2.1.13:** Graphical visualization of the hyperbolic model in deviatoric vs strain space (Brinkgreve et al., 2011 [10]).

### Small Strain Shear Stiffness $G_0^{ref}$ and Shear strain $\gamma_{0.7}$

The small strain shear stiffness  $G_0^{ref}$  and the shear strain at which  $G$  has reduced to 72.2 %  $\gamma_{0.7}$  are parameters exclusive to the small strain variation of the Hardening Soil constitutive model. Due to the absence of experimental data, the determination of  $G_0^{ref}$  and  $\gamma_{0.7}$  is being performed through correlations. Two of the most predominant are those of Alpan, 1970 [1] and Benz & Vermeer, 2007 [7]. However, there needs to be more clarity on what stiffness Alpan refers to when he mentions the static modulus. That has been investigated by both Benz & Vermeer, 2007 [7] and Wichtmann & Triantafyllidis, 2009 [35], who concluded that Alpan's  $E_{stat}$  is the apparent elastic Young's modulus in conventional soil testing. However, both authors found that the stiffness predictions are reasonable if Alpan's correlation is fitted with  $E_{stat} = 3 * E_{50}$ . Additionally, Benz & Vermeer, 2007 [7] provided an alternative correlation between  $M_{dyn}/M_{stat}$  and  $M_{stat}$ . To summarize in the original approach Alpan considers  $E_{stat} = E_{50}$  and Benz & Vermeer  $E_{stat} = E_{ur} = 3 * E_{50}$ .

The correlations Alpan, 1970 [1], Benz & Vermeer, 2007 [7] and Deutsche Gesellschaft für Geotechnik (DGGT), 2001 are presented in Figure 2.1.14, and as it can be seen, there are differences between them, most probably that is due to a different interpretation of  $E_{stat}$ .



**Figure 2.1.14:** Comparison of the correlations between  $E_{dyn}/E_{stat}$  and  $E_{stat}$  according to Alpan, 1970 [1], DGGT (2001) and by Benz & Vermeer, 2007 [7] [after Wichtmann & Triantafyllidis (2009)].

Considering all the investigations above, the  $E_{stat}$  or  $M_{stat}$  are determined from the Equation 2.1.47. The small strain modulus  $G_0$  can be calculated if Poisson's ratio  $\nu$  is known by the Equation 2.1.49 of Wichtmann & Triantafyllidis, 2009 [35], where  $E_0$  is the static Young's modulus at very small strains and is essentially the  $E_{stat}$ . The shear strain  $\gamma_{0.7}$  for which the secant shear modulus is reduced to 70 % of the value  $G_0$  is being calculated using the Equation 2.1.50 of Hardin & Drnevich, 1972 [16]. Where  $c'$  is the drained effective cohesion,  $\phi'$  is the drained effective friction angle,  $K_0$  is the neutral earth pressure coefficient, and  $\sigma_1'$  is the effective vertical stress.

$$E_{stat} = E_{ur} \approx 3 * E_{50} \quad (2.1.47)$$

$$E_0 = \frac{E_{dyn}}{E_{stat}} * E_{ur} \quad (2.1.48)$$

$$G_0 = \frac{E_0}{2 * (1 + \nu)} \quad (2.1.49)$$

$$\gamma_{0.7} = \frac{1}{9 * G_0} * (2 * c' * (1 + \cos(2 * \phi')) + \sigma_1' * (1 + k_0) * \sin(2 * \phi')) \quad (2.1.50)$$

## 2.2 Parameter Determination - Application

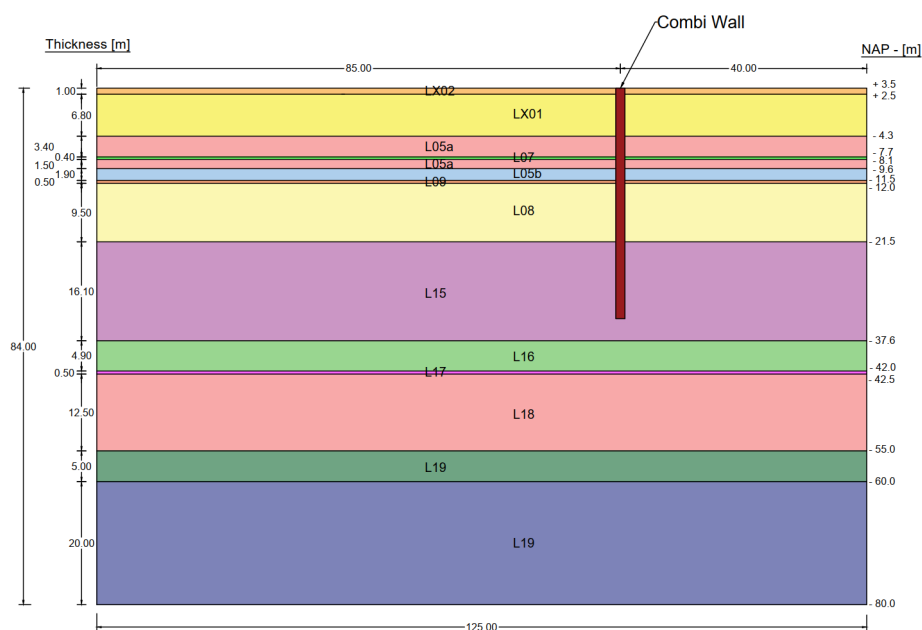
The representative soil profile for this cross-section has been constructed for the design of this project, and it is based on the area's CPT results and boreholes. It is presented in Appendix B, along with the legend that color coordinates the layers. The cross-section L01b consists of 13 different soil layers described in Table 2.2.1 and depicted in Figure 2.2.1. The thickness, unit weights, and stress conditions of the soil layers are presented in Table 2.2.2.

**Table 2.2.1:** Description of soil layers of cross section L01b.

Name	Description	Formation	Geological Era
L05a	Moderately packed sand	Naaldwijk	
L05b	Densely packed sand -	Nieuwkoop	
L07	Clay/Peat	Boxtel	Quaternary Pleistocene (12000 - 2.6 mil. years)
L08	Densely packed sand/ Lightly Silting	Koewacht & Boxtel	
L09	Moderately packed clay or loamy sand	Koewacht & Boxtel	
L15	Boom clay	Rupel	
L16	Lightly glauconitic sand	Tongeren	Tertiary Oligo-Miocene
L17	Clay/ strong silty layer	Tongeren	Pliocene
L18	Tertiary sand	Tongeren	(2.6 - 33.7 mil. years)
L19	Clay/ strong silty layer	Tongeren	
LX01	Backfilled sand (Re: 30 - 40 %)	-	-
LX02	Backfilled sand (Re: 60 - 70 %)	-	-

Similar methodology and references to the design have been used to determine soil parameters for comparison purposes. However, an essential difference from the design is that this thesis will be based on mean values, whereas the design is based on characteristic values. The codes suggest using characteristic values to overcome uncertainty by implementing over-conservatism. Therefore, the parameters that are being chosen are reduced or increased values (depending on the contribution)





**Figure 2.2.1:** Phase Comparison Tab of Python Application.

**Table 2.2.2:** Stress profile along the depth for the cross-section L01b.

Layer	Top	Bot	$\gamma_{dry}$	$\gamma_{sat}$	$\sigma_{v,bot}$	$\sigma_{v,mid}$	$u_{bot}$	$u_{mid}$	$\sigma'_{v,bot}$	$\sigma'_{v,mid}$
LX02	3.5	2.5	18.7	18.7	18.7	9.4	0	0	18.7	9.4
LX01	2.5	-4.3	17.5	17.5	137.4	78.1	68	34	69.4	44.1
L05a1	-4.3	-7.7	10.9	10.9	174.6	156	102	85	72.6	71
L07	-7.7	-8.1	18.6	18.6	182.1	178.3	106	104	76.1	74.3
L05a2	-8.1	-9.6	14.9	14.9	204.3	193.2	121	113.5	83.3	79.7
L05b	-9.6	-11.5	18.6	18.6	239.6	222	140	130.5	99.6	91.5
L09	-11.5	-12	21.0	21.0	250.1	244.8	145	142.5	105.1	102.3
L08	-12	-21.5	18.7	18.7	428.1	339.1	240	192.5	188.1	146.6
L15	-21.5	-37.6	18.5	18.5	726.5	577.3	401	320.5	325.5	256.8
L16	-37.6	-42	19.3	19.2	811.2	768.8	445	423	366.2	345.8
L17	-42	-42.5	19.1	19.1	820.7	815.9	450	447.5	370.7	368.4
L18	-42.5	-55	19.1	19.1	1060	940.3	575	512.5	484.8	427.9
L19	-55	-60	18.6	18.6	1153	1106	625	600	527.9	506.4
L19b	-60	-80	19.1	19.1	1536	1344	825	725	710.5	619.2

to achieve 95 % certainty. On the contrary, this thesis will use mean values (or most probable values) to make the comparison with the monitoring data (real situation) possible.

### 2.2.1 Soil Layer L05

Layer L05 can be subdivided into L05a (moderately packed sand with clay and loam lenses) and L05b (densely packed sand). L05a and L05b occur alternatively over the project area and are locally observed several times over each other. In the present cross-section, the L05a variation of this sandy layer is located in two locations, the «upper» and «lower», as shown in Table 2.2.2. For L05a, the cone

resistance is significantly lower than L05b. For L05a,  $q_c = 7.5$  MPa is assumed as a representative value, and for L05b, a much higher cone resistance is found (15 MPa to 25 MPa).

### Strength Parameters

Because the triaxial tests are not representative for sandy layers generally, the parameters of the sand layers in this project have been derived from the correlations with  $q_c$  of CPTs and table 2b. The sub-layers L05a and L05b have a range of  $q_c$  values [1.5 – 15] kPa and [15 – 25] kPa, respectively. The representative values chosen for layers L05a and L05b are 8.25 kPa and 20 kPa, respectively, which are the median values of each range.

Since the material is coarse-grained, 0 effective cohesion  $c'$  is considered, and the effective friction angle  $\phi'$  is derived from table 2.b, Appendix A. However, table 2.b uses characteristic values and, in the case of the strength parameters, are values that underestimate the capabilities of the soil for safety reasons. Because the present thesis aims to compare with actual monitoring data, the most representative parameters of the soil need to be used, which are the mean values. The derivation of the mean values from table 2.b is explained in Paragraph 2.1.3. Eventually, the effective friction angle given to the L05a and L05b sublayers equals  $29.06^\circ$  and  $37.78^\circ$ , respectively.

### Stiffness Parameters

According to Lunne's and Christophersen's correlation, for normally consolidated and uncemented silica sand layers, the oedometer stiffness can be derived via Equation 2.1.37 and 2.1.38 for L05a and L05b, respectively. The stiffness depends on the stress level; therefore, it is essential to normalize it to a reference stress level using Equation 2.1.28. According to the PLAXIS Manual, the reference stress level  $p_{ref}$  is chosen to be 100 kPa, the effective vertical stress for each layer is given in Table 2.2.2, and the mean strength parameters are being used. Finally, the secant reference stiffness  $E_{50}^{ref}$  and the unloading reloading reference stiffness  $E_{ur}^{ref}$  are derived using Equations 2.1.35 and the 2.1.36, respectively.

### Other Parameters

The dilatancy angle  $\psi$  is calculated according to Table 2.1.3. The undrained Poisson's ratio  $\nu_{ur}$  is equal to 0.20 according to the discussion in Paragraph 2.1.4, and the  $m$  is considered 0.5 for this sandy layer in line with the recommendations of the PLAXIS Manual. Since this material is adjacent to a steel combi wall that generally is regarded as a Rough/coarse surface, the wall angle of friction  $\delta$  from Table 2.1.5 is equal to  $26.56^\circ$  and  $27.50^\circ$  for L05a and L05b, respectively. Therefore, following Equation 2.1.17, the  $R_{int}$  for L05a is equal to 0.8996, and for L05b is equal to 0.6715. The neutral ground pressure coefficient  $K_0^{nc}$  is calculated using Equation 2.1.18 and is equal to 0.514 and 0.387, respectively.

The unit weight of this layer has been derived by examining 39 samples in the lab from various bore-hole locations along the construction area. The average values of  $\gamma_{sat}$  and  $\gamma_{dry}$  are found to be 18.56 and 14.71 kN/m<sup>3</sup>, respectively. The statistical outcome for saturated and dry unit weight is presented in Table B.4.1 (Appendix B.4). The unit weights are valid for both sub-parts of the sand layer L05.

### Small Strain Parameters

The small strain parameters are calculated with Alpan, 1970 [1] and Benz & Vermeer, 2007 [7] methods. The methodology explained in Paragraph 2.1.4 is being used, and the analytical results are presented in Table B.5.1 of Appendix B.5. The average value of these two methods will be considered, leading to  $G_0^{ref}$  equal to 174502 and 231070 kPa for layers L05a and L05b, respectively. Finally, the calculation of the shear strain  $\gamma_{0.7}$  is being performed using Equation 2.1.50 is equal to 0.000097 and 0.000109 for L05a and L05b, respectively.

The Hardening Soil Small Strain constitutive model soil properties for the soil layers L05a and L05b used in the finite element program PLAXIS are summarized in Table 2.3.1.

### 2.2.2 Soil Layer L07

Layer L07 is a clay/peat layer with relatively high cone resistance, located at approximately NAP -9m. The representative  $q_c$  value from the CPTs for this layer is 1.00 MPa. The high cone resistance for the clay/peat layer is due to the small thickness of the layer and the existing sand layer below. Since the CPT cone is being pushed into the ground and given the high differences in stiffness between these two adjacent layers, the cone can sense the sand layer before reaching it. Additionally, limited samples were taken due to the limited layer thickness (< 0.5m).

#### Strength Parameters

As previously mentioned, the limited thickness of the layer and the heterogeneity didn't allow for the collection of samples for lab testing. Therefore, the strength parameters will be derived from table 2.b of NEN9997, Appendix A. The visual inspection of the lab report categorizes the sample as organic clay. However, by taking into consideration the eight lab vane tests that give an average value of undrained shear strength  $s_u$  equal to 56 kPa, the reference oedometer stiffness  $E_{oed}^{ref}$  from the lab tests equal to 1500 kPa and the higher cone resistance  $q_c$  is more appropriate to compare the sample with the table category (Klei à Schoon à Matig). Based on that description, the strength parameters are being derived. As explained in Paragraph 2.1.3, the transformation to mean values has been performed. The derived effective friction angle  $\phi'$  for this layer is equal to  $20.34^\circ$  and the effective cohesion  $c'$  is equal to 6.63 kPa.

#### Stiffness Parameters

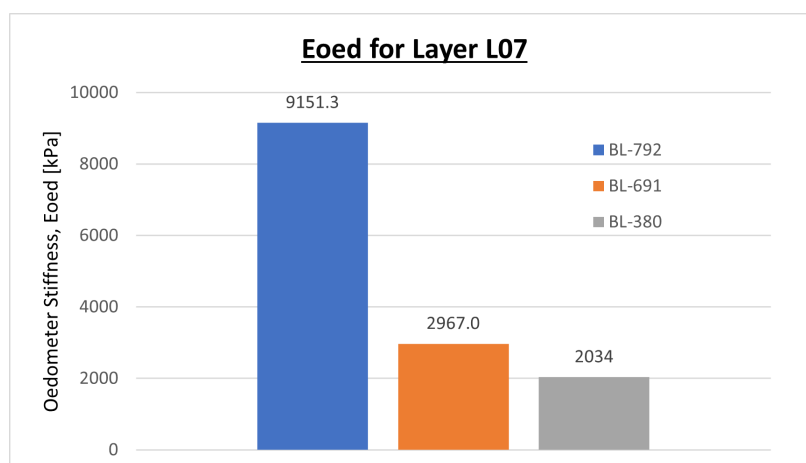
To proceed with the calculation of the stiffnesses, the unloading reloading Poisson's ratio  $\nu_{ur}$  has been considered equal to 0.15 according to Paragraph 2.1.4 and  $K_0 = 1$ , according to PLAXIS Manual instructions. According to literature research, the power for the stress-level dependency of stiffness  $m$  is considered 0.8 for the particular peat layer. Also, the reference stress  $p_{ref}$  is 100 kPa. The  $E_{oed}$  and  $E_{ur}$  were calculated using the 2.1.26, and 2.1.27, respectively, and the stiffnesses at the reference stress are calculated using Equations 2.1.28 and 2.1.29. A representative oedometer report from the lab is presented in Appendix B.

However, as seen in Figure 2.2.2, the oedometer test on the sample from Borehole BL-792 provides high stiffness values. These values are out of the normal range for a clay/peat layer; hence it is being disregarded from the parameter determination values of the present layer. This layer is a neighbor with a sandy layer (L05); thus, the mix between them in the interface can explain this high value.

There are no triaxial tests for this layer to determine the secant stiffness  $E_{50}$ ; hence, it will be derived following the suggestion of Table 3.1 from the CUR 2003-7 code, Appendix A. According to which, the reference secant stiffness can be estimated as two times the reference oedometer stiffness ( $E_{50}^{ref} = 2 * E_{oed}^{ref}$ ).

#### Other Parameters

The dilation angle  $\psi$ , as analyzed in Paragraph 2.1.4, is equal to 0 for this peat/clay layer. Since this material is peat, the wall angle of friction  $\delta$  is considered equal to 0 according to code CUR 166. Therefore, following Equation 2.1.17, the  $R_{int}$  is also equal to 0. The neutral ground pressure coefficient  $K_0^{nc}$  is calculated using Equation 2.1.18 and equals 0.65.



**Figure 2.2.2:** Oedometers stiffness from the 3 samples at Layer L07.

The unit weight of this layer has been derived by examining nine samples in the lab from various borehole locations along the construction area. The average values of  $\gamma_{sat}$  and  $\gamma_{dry}$  are found to be 14.85 and 9.24  $kN/m^3$ , respectively. The statistical outcome for saturated and dry unit weight is presented in Table B.4.2 (Appendix B.4).

#### Small Strain Parameters

The small strain parameters are calculated with Alpan 1970 and Benz & Vermeer, 2007 [7] methods. The methodology explained in Paragraph 2.1.4 is being used, and the analytical results are presented in Table B.5.2 of Appendix B.5. The average value of these two methods will be considered, leading to  $G_0^{ref}$  equal to 21837 kPa. Finally, the calculation of the shear strain  $\gamma_{0.7}$  is performed using Equation 2.1.50 is equal to 0.000886.

The Hardening Soil Small Strain constitutive model properties for the soil layer L07 that will be used in the finite element program PLAXIS are summarized in Table 2.3.1.

### **2.2.3 Soil Layer L08, L10, L12**

The first aquifer sand package, consisting of several soil layers, mainly contains an alternation of free to very close-packed sand layers with a cone resistance of 15 MPa to > 35 MPa (L08, L10, and L12) and moderately packed clay or loamy sand layers (L09 and L11). The layers L08, L10, and L12, will be considered one with common parameters. The representative cone resistance  $q_c$  for these is equal to 25 MPa.

#### Strength Parameters

Layer L08, L10 & L12 have a range of  $q_c$  values [15 – 35]. The representative value chosen for these layers is 25 kPa, the range's median value. CPT correlations and triaxial tests have derived the strength parameters for these layers on selected samples.

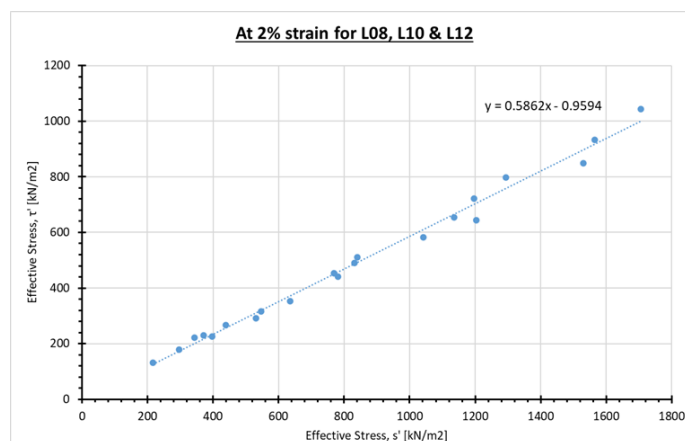
Firstly, during the triaxial tests, the minimum and maximum dry density have been calculated; therefore, the calculation of the relative density is possible using Equation 2.2.1. The tests performed on moderately to tightly packed sand samples were selected to derive realistic strength parameters from the triaxial tests. These samples were expected to show dilative behavior during the test.

$$I_d = \frac{\frac{1}{\gamma_{d,min}} - \frac{1}{\gamma_d}}{\frac{1}{\gamma_{d,min}} - \frac{1}{\gamma_{d,max}}} \quad (2.2.1)$$

By applying the linear regression method as described in Paragraph 2.1.2 on all the selected lab tests for this layer, the average effective friction angle and effective cohesion are being calculated for 2 % strain, according to the recommendation of the CUR code for deep excavations, in Figure 2.2.3 using the Equations 2.1.14 and 2.1.15. The results are summarized in Table 2.2.3.

**Table 2.2.3:** Average effective friction angle and effective cohesion for layers L08, L10 & L12 at 2 % strain.

2 % Strain	Kf-line	Failure Line
Average Effective Friction Angle, $\phi'$ [ $^\circ$ ]	30.38	35.89
Average Effective Cohesion, $c'$ [kPa]	0.00	0.00



**Figure 2.2.3:** Linear regression for the undrained triaxial lab test on samples with high relative density for L08, L10 & L12 layers at 2 % strain.

Additionally, correlations are also being used to confirm the method with the triaxial tests suggested previously. Since the material is coarse-grained, 0 effective cohesion  $c'$  is considered, and the effective friction angle  $\phi'$  is derived from table 2.b, Appendix A. To use the  $q_c$  as import to table 2.b for a sand layer it needs to be standardized for an effective vertical ground stress  $\sigma'_v$  of 100 kPa, as explained in Paragraph 2.1.3. Therefore, Equation 2.1.6 is being used where the  $\sigma'_v$  of the current layer is given in Table 2.2.2. As a result, the input cone resistance  $q_{c,table}$  is equal to 13.06 MPa, and the material is categorized to the section (Zand  $\rightarrow$  Schoon  $\rightarrow$  Matig). However, table 2.b uses characteristic values, and in the case of strength parameters are values that underestimate the capabilities of the soil for safety reasons. The goal of the present thesis is to compare with actual monitoring data the most representative parameters of the soil, which are the mean values, need to be used. The derivation of the mean values from table 2.b is explained in Paragraph 2.1.3. Eventually, the effective friction angle given to the layers L08, L10 & L12 equals  $37.78^\circ$ .

To conclude, the method with the triaxial test on selected samples gave an effective friction angle of  $35.90^\circ$ , and the method of correlations gave an effective friction angle of  $37.78^\circ$ . That outcome

confirms that choosing the samples with higher relative density was the correct way to get representative parameters for the layer. Otherwise, by incorporating the weaker zones' samples, the linear regression method provided a negative cohesion of -32 kPa.

### Stiffness Parameters

According to Lunne's and Christophersen's correlation, the oedometer stiffness can be derived via Equation 2.1.38 for the present layer for normally consolidated and uncemented silica sand layers. The stiffness depends on the stress level; therefore, it is essential to normalize it to a reference stress level using Equation 2.1.28. According to the PLAXIS Manual, the reference stress level is chosen to be 100 kPa, the effective vertical stress for each layer is given at Table 2.2.2, and the mean strength parameters are being used. Finally, the secant reference stiffness  $E_{50}^{ref}$  and the unloading reloading reference stiffness  $E_{ur}^{ref}$  are derived using the Equations 2.1.28 and the 2.1.29, respectively.

### Other Parameters

The dilatancy angle  $\psi$  is calculated according to Table 2.1.3, the undrained Poisson's ration  $\nu_{ur}$  is equal to 0.15 according to the discussion in Paragraph 2.1.4. The  $m$  is considered 0.5 for this sandy layer in line with the recommendations of the PLAXIS Manual. Since this material is adjacent to a steel combi wall that is regarded as a Rough/coarse surface, the wall angle of friction  $\delta$  from Table 2.1.5 equals  $27.50^\circ$ . Therefore, following Equation 2.1.17, the  $R_{int}$  for this layer is equal to 0.6715. The neutral ground pressure coefficient  $K_0^{nc}$  is calculated using Equation 2.1.18 and is equal to 0.3873.

The unit weight of this layer has been derived by examining 56 samples in the lab from various bore-hole locations along the construction area. The average values of  $\gamma_{sat}$  and  $\gamma_{dry}$  are found to be 18.74 and  $15.55 \text{ kN/m}^3$ , respectively. The statistical outcome for saturated and dry unit weight is presented in Table B.4.3 (Appendix B.4).

### Small Strain Parameters

The small strain parameters are calculated with Alpan's 1970 and Benz & Vermeer's, 2007 [7] methods. The methodology explained in Paragraph 2.1.4 is being used, and the analytical results are presented in Table B.5.3 of Appendix B.5. The average value of these two methods will be considered, leading to  $G_0^{ref}$  equal to 232511 kPa. Finally, the shear strain  $\gamma_{0.7}$  is calculated using Equation 2.1.50 and is equal to 0.00017.

The Hardening Soil Small Strain constitutive model properties for the soil layer L08 that will be used in the finite element program PLAXIS are summarized in Table 2.3.1.

## **2.2.4 Soil Layer L09 & L11**

The soil layers L09 & L11 are also part of the first aquifer. They consist of moderately packed clay or loamy sand layers with cone resistances between 1.5 MPa and 12.5 MPa. The layers L09 and L11 will be regarded as one, and they will have common parameters. The representative cone resistance  $q_c$  for these is equal to 7 MPa.

### Strength Parameters

Because the results from the triaxial tests are not representative for sandy layers generally, it has been chosen to determine the strength parameters for these layers through correlations with  $q_c$  of CPTs and table 2b. The cone resistance  $q_c$  for these two layers has a range of values [1.5 – 12.5] kPa.

To use the  $q_c$  as import to table 2.b for a sand layer it needs to be standardized for an effective vertical

ground stress  $\sigma'_v$  of 100 kPa, as explained in Paragraph 2.1.3. Therefore, Equation 2.1.6 is used where the  $\sigma'_v$  of the present layer is given in Table 2.2.2. As a result, the input cone resistance  $q_{c, table}$  is equal to 4.54 MPa, and the material is categorized to the section (Zand à Sterk silting, kleig). However, table 2.b uses characteristic values, and in the case of the strength parameters are values that underestimate the capabilities of the soil for safety reasons. Since the goal of the present thesis is to compare with actual monitoring data, the most representative parameters of the soil need to be used, which are the mean values. The derivation of the mean values from table 2.b is explained in Paragraph 2.1.3. Eventually, the effective friction angle given to the layers L09 & L11 equals  $31.97^\circ$ . Since the material is coarse-grained, 0 effective cohesion  $c'$  is considered.

### Stiffness Parameters

According to Lunne's and Christophersen's correlation, the oedometer stiffness can be derived via Equation 2.1.37 for the present layer for normally consolidated and uncemented silica sand layers. The stiffness depends on the stress level; therefore, it is essential to normalize it to a reference stress level using Equation 2.1.28. According to the PLAXIS Manual, the reference stress level is chosen to be 100 kPa, the effective vertical stress for each layer is given at Table 2.2.2, and the mean strength parameters are being used. Finally, the secant reference stiffness  $E_{50}^{ref}$  and the unloading reloading reference stiffness  $E_{ur}^{ref}$  are derived using the Equations 2.1.28 and the 2.1.29, respectively.

### Other Parameters

The dilatancy angle  $\psi$  is calculated according to Table 2.1.3, the undrained Poisson's ration  $\nu_{ur}$  is equal to 0.15 according to the discussion in Paragraph 2.1.4, and the  $m$  is considered 0.5 for this sandy layer in line with the recommendations of the PLAXIS Manual. Since this material is adjacent to a steel combi wall that is generally considered a Rough/coarse surface, the wall angle of friction  $\delta$  from Table 2.1.5 equals  $27.50^\circ$ . Therefore, following Equation 2.1.17, the  $R_{int}$  for this layer is equal to 0.834. The neutral ground pressure coefficient  $K_0^{nc}$  is calculated using Equation 2.1.18 and is equal to 0.4705.

The unit weight of this layer has been derived by examining 16 samples in the lab from various bore-hole locations along the construction area. The average values of  $\gamma_{sat}$  and  $\gamma_{dry}$  are found to be 18.53 and 14.66 kN/m<sup>3</sup>, respectively. The statistical outcome for saturated and dry unit weight is presented in Table B.4.4 (Appendix B.4).

### Small Strain Parameters

The small strain parameters are calculated with Alpan's, 1970 and Benz & Vermeer's, 2007 [7] methods. The methodology explained in Paragraph 2.1.4 is being used and the analytical results are presented in Table B.5.4 of Appendix B.5. The average value of these two methods will be considered, leading to  $G_0^{ref}$  equal to 137586 kPa. Finally, the calculation of the shear strain  $\gamma_{0.7}$  is performed using Equation 2.1.50 is equal to 0.000206.

The Hardening Soil Small Strain constitutive model properties for the soil layers L09 & L11 that will be used in the finite element program PLAXIS are summarized in Table 2.3.1.

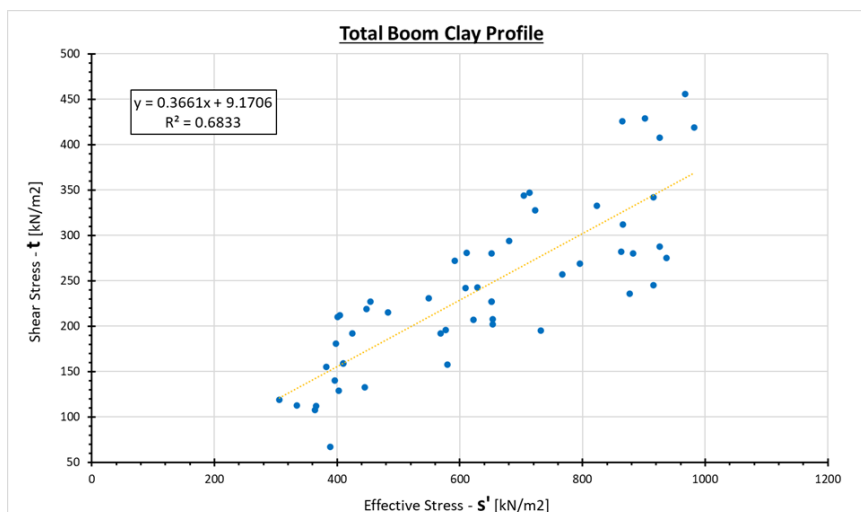
## 2.2.5 Soil Layer L15

### Strength Parameters

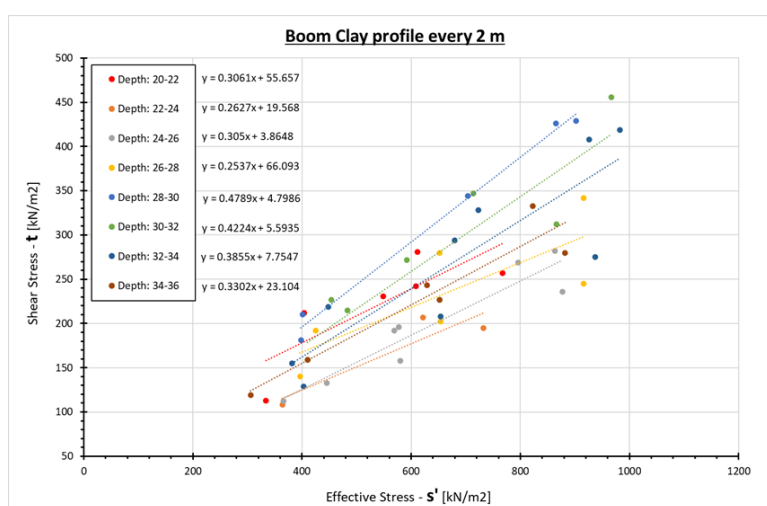
Similarly to the previous soil layers, the results from the triaxial tests will be summarized using the linear regression method described in paragraph 2.1.2. To begin with, all 18 undrained triaxial tests

at three cell pressure conditions each have been included in Figure 2.2.4, but the results are questionable. Although the derived effective friction angle  $\phi'$  is  $20.11^\circ$  and the effective cohesion  $c'$  is 9.77 kPa. The observations are spread apart, and the error parameter  $R^2$  depicts the linear regression line's low fitting accuracy, equal to 0.683. The perfect fitting of the line would have an  $R^2$  equal to 1, and any result over 0.95 is considered a reasonably accurate prediction.

An investigation has been conducted to determine if the boom clay layer can be subdivided into smaller sublayers. According to the present design, the top 5 m of the Boom Clay layer have slightly lower cone resistance  $q_c$  than the rest of the layer. To achieve that, the layer has been divided into 2 m intervals, and the corresponding undrained triaxial tests have been plotted. The results are summarized in Table 2.2.4 and Figure 2.2.6.



**Figure 2.2.4:** Linear regression for the undrained triaxial lab test on samples from all the thickness of L15 layer at 2 % strain.



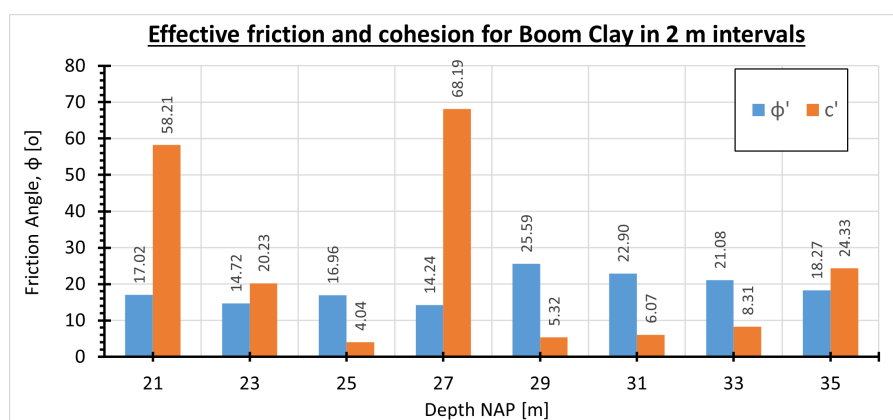
**Figure 2.2.5:** Linear regression for the undrained triaxial lab test on samples at 2 m intervals of L15 layer at 2 % strain.

By processing the data in Figure 2.2.6, no depth trend can be observed. Additionally, although the effective friction angle  $\phi'$  tends to have relatively reasonable values, the effective cohesion  $c'$  presents high variation. Since those two parameters are interdependent in the way they have been derived,



**Table 2.2.4:** Strength parameters of the boom clay layer after the linear regression in 2m intervals.

Depth	Middle	$A_{val}$	$B_{val}$	$\theta$	$\tau_0$	$\phi'$	$c$
20 - 22	21.00	0.3061	55.657	17.02	55.66	17.02	58.21
22 - 24	23.00	0.2627	19.568	14.72	19.57	14.72	20.23
24 - 26	25.00	0.3050	3.8650	16.96	3.87	16.96	4.04
26 - 28	27.00	0.2537	66.093	14.24	66.09	14.24	68.19
28 - 30	29.00	0.4789	4.7990	25.59	4.80	25.59	5.32
30 - 32	31.00	0.4224	5.5940	22.90	5.59	22.90	6.07
32 - 34	33.00	0.3855	7.7550	21.08	7.76	21.08	8.31
34 - 36	35.00	0.3302	23.104	18.27	23.10	18.27	24.33
Average						18.85	24.34

**Figure 2.2.6:** Linear regression for the undrained triaxial lab test on samples at 2 m intervals of L15 layer at 2 % strain.

the cohesion's uncertainty also affects the effective friction angle. This variation could be due to disturbed samples, common among Boom Clay samples because they tend to swell.

Finally, the calculation of the properties from table 2.b of NEN9997, Appendix A, has been attempted. The (Klei à Schoon à Vast) has been chosen given that the representative cone resistance of this layer is equal to 4.5 MPa. Additionally, using three correlation methods for calculating the undrained shear strength of the Boom Clay from another project will allow estimating if the values belong to the aforementioned table 2.b category.

The first method is from Carpentier, 1982 [12] and refers to a project from Kontich in Belgium in the general vicinity of the new Terneuzen lock. It calculates the undrained shear strength using a correlation with the depth from the surface, as shown in Equation 2.2.2. The second method is from the Oosterweel connection in Antwerp and uses Equation 2.2.3 to calculate the undrained shear strength in correlation with depth. The third method is a correlation from Lunne et al. 1997 [23] and is given by Equation 2.2.4, where  $N_k$  is an empirical cone factor ranging from 13 to 24,  $q_c$  is the cone resistance, and  $\sigma'v$  is the effective vertical stress. This method will use the mean value of  $N_k$ , the representative cone resistance  $q_c$  for this layer, and the effective stress from the middle of the layer given in Table 2.2.2. The results of the calculation are presented in Table 2.2.5.

$$c_u = 6.4 * h + 81.4 \quad (2.2.2)$$

$$c_u = 2.5 * h + 172.2 \quad (2.2.3)$$

$$c_u = \frac{q_c - \sigma'_v}{N_k} \quad (2.2.4)$$

**Table 2.2.5:** calculation of the undrained shear strength using 3 different correlation methods.

	Top	Bottom	Average	Units
Method 1	219	322	270	kPa
Method 2	226	266	270	kPa
Method 3		207		kPa
Total Average		241		kPa

The category of table 2b chosen is (Klei à Schoon à Vast) and corresponds to the undrained shear strength of 100 to 200 kPa. Since the cone resistance for this layer is in the upper end, the 200 kPa is considered more representative of layer L15. However, table 2.b uses characteristic values, and they need to be transformed to mean values to be compared with the correlation of Table 2.2.5, using the method explained in Paragraph 2.1.3. Hence the mean  $c_u$  that table 2b gives is 265 kPa, which is reasonably close to the average values from the correlations. That confirms that the selection of (Klei → Schoon → Vast) category to represent the Boom Clay is justified.

To conclude, the lab tests give an average effective friction angle  $\phi'$  and effective cohesion  $c'$  of  $18.85^\circ$  and 24.34 kPa, respectively. On the other hand, table 2b gives values of  $\phi'$  and  $c'$  equal to  $24.41^\circ$  and 18.55 kPa. It is clear that with the given data, there is no definitive answer; hence the values from table 2b will be used to align with the present design's approach. Later, this thesis will focus on determining the correct parameters of Boom Clay using the monitoring data from the field.

#### Stiffness Parameters

To proceed with the calculation of the stiffnesses, the unloading reloading Poisson's ratio  $\nu_{ur}$  has been considered equal to 0.30 according to Paragraph 2.1.4 and  $K_0 = 1$ , according to PLAXIS Manual instructions. According to literature research, the power for the stress-level dependency of stiffness  $m$  is considered 0.8 for the particular clay layer. Finally, the reference stress  $p_{ref}$  is 100 kPa. The  $E_{oed}$  and  $E_{ur}$  have been calculated using Equations 2.1.26 and 2.1.27, respectively, and the stiffnesses at the reference stress are calculated using Equations 2.1.28 and 2.1.29. A representative oedometer report from the lab is given in Appendix B. From the nine oedometer tests performed on samples of layer L15, the average  $E_{oed}^{ref}$  and  $E_{ur}^{ref}$  are equal to 4119 kPa and 11689 kPa, respectively.

However, these values are very low compared to stiffnesses found in the literature for the boom clay. According to the reports from the lab tests facility, the clay samples were disturbed because once they were removed from the plastic pipe, they experienced expansion (swelling). To prove it, the undrained triaxial tests on the boom clay samples were examined. When attempting to back figure the strength ratio  $m$  using Equation 2.1.44 on the same boom clay samples tested under different cell pressures, the results deviated on some occasions up to 90 % from the expected value of 0.8. This is a good indication that the samples were highly disturbed. Therefore, using these lab tests to derive the stiffness parameters for the present layer is not representative.

To overcome this obstacle and derive the stiffness parameters, they used the correlations performed by Christian and Nielsen. This approach calculates the stiffness of the Boom Clay based on its depth from the surface  $d$  and the effective vertical stress  $\sigma'_{av}$ . This method has been produced by fitting measurements from a trial pit on a similar soil profile to the Terneuzen project. The calculation

of the oedometer stiffness  $E_{oed}$  and the unloading reloading stiffness  $E_{ur}$  is given by Equations 2.2.5 and 2.2.6, respectively. The Boom Clay layer spans from -21.5 m to -37.5 m NAP, and the calculation of the stiffness for 0.5-meter intervals is presented in Table 2.2.6.

$$E_{oed} = (50 + 2 * d) * \sigma'_v \quad (2.2.5)$$

$$E_{ur} = (75 + 5 * d) * \sigma'_v \quad (2.2.6)$$

**Table 2.2.6:** Calculation of the oedometer stiffness  $E_{oed}$  and the unloading/reloading stiffness  $E_{ur}$  using the method of Christian and Nielsen.

Depth [NAP] m	$\sigma'_v$ kPa	d m	A -	C -	$E_{oed}$ kPa	$E_{ur}$ kPa
-21.5	276	28.2	216	106.4	29315	59511
-22	280	28.7	218.5	107.4	30075	61187
-22.5	285	29.2	221	108.4	30845	62885
-23	289	29.7	223.5	109.4	31623	64605
-23.5	294	30.2	226	110.4	32411	66348
-24	298	30.7	228.5	111.4	33207	68114
-24.5	303	31.2	231	112.4	34013	69902
-25	307	31.7	233.5	113.4	34828	71713
-25.5	312	32.2	236	114.4	35651	73546
-26	316	32.7	238.5	115.4	36484	75402
-26.5	321	33.2	241	116.4	37326	77281
-27	325	33.7	243.5	117.4	38176	79182
-27.5	330	34.2	246	118.4	39036	81105
-28	334	34.7	248.5	119.4	39905	83052
-28.5	339	35.2	251	120.4	40783	85021
-29	343	35.7	253.5	121.4	41670	87012
-29.5	348	36.2	256	122.4	42566	89026
-30	352	36.7	258.5	123.4	43470	91062
-30.5	357	37.2	261	124.4	44384	93122
-31	361	37.7	263.5	125.4	45307	95203
-31.5	366	38.2	266	126.4	46239	97314
-32	370	38.7	268.5	127.4	47180	99454
-32.5	375	39.2	271	128.4	48131	101623
-33	379	39.7	273.5	129.4	49090	103821
-33.5	384	40.2	276	130.4	50058	106048
-34	388	40.7	278.5	131.4	51035	108294
-34.5	393	41.2	281	132.4	52021	110559
-35	397	41.7	283.5	133.4	53016	112843
-35.5	402	42.2	286	134.4	54021	115146
-36	406	42.7	288.5	135.4	55034	117467
-36.5	411	43.2	291	136.4	56056	119806
-37	415	43.7	293.5	137.4	57088	122163
-37.5	420	44.2	296	138.4	58128	124538
Average					42975	78318

The stiffness depends on the stress level; therefore, it is important to normalize it to a reference stress level using Equation 2.1.28. According to the PLAXIS Manual, the reference stress level is chosen to be 100 kPa, the effective vertical stress for each layer is given in Table 2.2.2, and the mean strength parameters are being used. Finally, the secant reference stiffness  $E_{50}^{ref}$  and the unloading reloading reference stiffness  $E_{ur}^{ref}$  are derived using Equations 2.1.35 and the 2.1.36, respectively. To determine the secant stiffness  $E_{50}$ , table 3.1 from the CUR 2003-7 code, Appendix A, is used. The reference

secant stiffness can be estimated equal to the reference oedometer stiffness ( $E_{50}^{ref} = E_{oed}^{ref}$ ) for an over-consolidated clay.

#### Other Parameters

The dilatancy angle  $\psi$  is calculated according to Table 2.1.3, the undrained Poisson's ratio  $\nu_{ur}$  is equal to 0.30 according to the discussion in Paragraph 2.1.4, and the  $m$  is considered 0.8 for this clay layer in line with the recommendations of the PLAXIS Manual. Since this material is adjacent to a steel combi wall that is regarded as a Rough/coarse surface, the wall angle of friction  $\delta$  from Table 2.1.5 equals  $21.91^\circ$ . Therefore, following Equation 2.1.17, the  $R_{int}$  for this layer is equal to 0.886. The neutral ground pressure coefficient  $K_0^{nc}$  is calculated using Equation 2.1.18 and is equal to 0.587.

The unit weight of this layer has been derived by examining 32 samples in the lab from various bore-hole locations along the construction area. The average values of  $\gamma_{sat}$  and  $\gamma_{dry}$  are found to be 19.25 and  $15.18 \text{ kN/m}^3$ , respectively. The statistical outcome for saturated and dry unit weight is presented in Table B.4.5 (Appendix B.4).

#### Small Strain Parameters

The small strain parameters are calculated with Alpan's 1970 and Benz & Vermeer's 2007 methods. The methodology explained in Paragraph 2.1.4 is being used, and the analytical results are presented in Table B.5.5 of Appendix B.5. The average value of these two methods will be considered, leading to  $G_0^{ref}$  equal to 80897 kPa. Finally, the shear strain  $\gamma_{0.7}$  is calculated using Equation 2.1.50, equal to 0.00065.

The Hardening Soil Small Strain constitutive model properties for the soil layer L15 that will be used in the finite element program PLAXIS are summarized in Table 2.3.1.

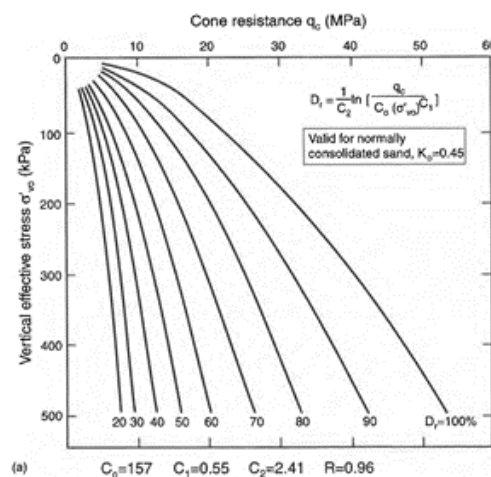
### **2.2.6 Soil Layer L16**

The soil layer L16 is part of the second aquifer. It is lightly glauconitic sand, and its cone resistance  $q_c$  ranges between 8 MPa and 25 MPa. The representative cone resistance  $q_c$  for these is equal to 16.5 MPa.

#### Strength Parameters

As shown in Table 2.2.2, this layer is located very deep, and the effective vertical stress  $\sigma'_v$  in the middle of the layer at -46.5 m equals 440 kPa. Under these conditions, the conversion of the cone resistance using Equation 2.1.6 is not representative. Therefore, the correct category of table 2.b is selected through the relative density. Using the correlation from Baldi et al. 1986 shown in Figure 2.2.7 with Equation 2.2.7, the relative density  $D_r$  for this layer equals 54.2 %. Following note (b) of table 2.b, Appendix A, for relative density  $Re = 54.2 \%$ , the soil belongs to the medium density (Matig) category of sand.

However, table 2.b uses characteristic values, and in the case of the strength parameters are values that underestimate the capabilities of the soil for safety reasons. Since the goal of the present thesis is to compare with actual monitoring data, the most representative parameters of the soil need to be used, which are the mean values. The derivation of the mean values from table 2.b is explained in Paragraph 2.1.3. Eventually, the effective friction angle given to layer L16 equals  $37.78^\circ$ . Since the material is coarse-grained, 0 effective cohesion  $c'$  is considered.



**Figure 2.2.7:** Relationship of vertical effective stress  $\sigma'_v$  and cone resistance  $q_c$  for Ticino sand (Baldi et al., 1986 [5])

$$D_r = \frac{1}{C_2} * \ln \left( \frac{q_c}{C_0 * \sigma'_{v0} C_1} \right) \quad (2.2.7)$$

### Stiffness Parameters

According to the Trofimenkov correlation, the oedometer stiffness can be derived via Equation 2.1.42 for the present layer for lightly to highly glauconitic sand layers. This correlation yields the best results for tertiary sandy soils in Flanders. The stiffness depends on the stress level; therefore, it is essential to normalize it to a reference stress level using Equation 2.1.28. According to the PLAXIS Manual, the reference stress level is chosen to be 100 kPa, the effective vertical stress for each layer is given in Table 2.2.2, and the mean strength parameters are being used. Finally, the secant reference stiffness  $E_{50}^{ref}$  and the unloading reloading reference stiffness  $E_{ur}^{ref}$  are derived using Equations 2.1.28 and the 2.1.29, respectively.

### Other Parameters

The dilatancy angle  $\psi$  is calculated according to Table 2.1.3, the undrained Poisson's ration  $\nu_{ur}$  is equal to 0.20 according to the discussion in Paragraph 2.1.4, and the  $m$  is considered 0.5 for this sandy layer in line with the recommendations of the PLAXIS Manual. Since this material is adjacent to a steel combi wall that is regarded as a Rough/coarse surface, the wall angle of friction  $\delta$  from Table 2.1.5 equals  $27.50^\circ$ . Therefore, following Equation 2.1.17, the  $R_{int}$  for this layer is equal to 0.6715. The neutral ground pressure coefficient  $K_0^{nc}$  is calculated using Equation 2.1.18 and is equal to 0.3873.

The unit weight of this layer has been derived by examining 28 samples in the lab from various bore-hole locations along the construction area. The average values of  $\gamma_{sat}$  and  $\gamma_{dry}$  are found to be 19.13 and 15.53  $kN/m^3$ , respectively. The statistical outcome for saturated and dry unit weight is presented in Table B.4.6 (Appendix B.4).

### Small Strain Parameters

The small strain parameters are calculated with Alpan's 1970 and Benz & Vermeer's 2007 methods. The methodology explained in Paragraph 2.1.4 is being used, and the analytical results are presented in Table B.5.6 of Appendix B.5. The average value of these two methods will be considered, leading to  $G_0^{ref}$  equal to 183956 kPa. Finally, the calculation of the shear strain  $\gamma_{0.7}$  is performed using Equation

2.1.50 is equal to 0.000357.

The Hardening Soil Small Strain constitutive model properties for the soil layer L16 that will be used in the finite element program PLAXIS are summarized in Table 2.3.1.

## 2.2.7 Soil Layer L17

Due to the deep position of this clay strong silty layer, there are no available samples to test in the lab. This layer is part of the second aquifer, and the parameters for this layer will be determined through correlations using the CPT data. The cone resistance  $q_c$  ranges between 4 MPa and 7 MPa. The representative cone resistance  $q_c$  for these is equal to 5.5 MPa.

### Strength Parameters

Since this is a clay layer with relatively high cone resistance  $q_c$ , the (Klei à Schoon à Vast) category of the table has been chosen. The upper limit of this category will represent the reality more accurately since the cone resistance is almost double the recommended for this category. However, table 2.b uses characteristic values, and in the case of the strength parameters are values that underestimate the capabilities of the soil for safety reasons. Since the goal of the present thesis is to compare with actual monitoring data, the most representative parameters of the soil need to be used, which are the mean values. The derivation of the mean values from table 2.btable 2.b is explained in Paragraph 2.1.3. Eventually, the effective friction angle  $\phi'$  and the effective cohesion  $c$  given to layer L17 equal  $26.16^\circ$  and 17.44 kPa, respectively.

### Stiffness Parameters

According to table 2b, the representative stiffness after the translation into a mean value as described in Paragraph 2.1.3 equals 11630 kPa. The stiffness depends on the stress level; therefore, it is important to normalize it to a reference stress level using Equation 2.1.28. According to the PLAXIS Manual, the reference stress level is chosen to be 100 kPa, the effective vertical stress for each layer is given in Table 2.2.2, and the mean strength parameters are used. According to Lunne's and Christophersen's correlation, for tertiary clay layers like L17, the unloading reloading stiffness  $E_{ur}^{ref}$  can be derived from Equation 2.1.43. Finally, the secant reference stiffness  $E_{50}^{ref}$  is derived using Equation 2.1.33.

### Other Parameters

The dilatancy angle  $\psi$  is calculated according to Table 2.1.3, the undrained Poisson's ratio  $\nu_{ur}$  is equal to 0.20 according to the discussion in Paragraph 2.1.4, and the  $m$  is considered as 0.8 for this sandy layer in line with the recommendations of the PLAXIS Manual. Since this material is adjacent to a steel combi wall that is regarded as a Rough/coarse surface, the wall angle of friction  $\delta$  from Table 2.1.5 equals  $23.66^\circ$ . Therefore, following Equation 2.1.17, the  $R_{int}$  for this layer is equal to 0.892. The neutral ground pressure coefficient  $K_0^{nc}$  is calculated using Equation 2.1.50 and is equal to 0.5592.

The unit weight of this layer has been derived by examining three samples in the lab from various borehole locations along the construction area. The average values of  $\gamma_{sat}$  and  $\gamma_{dry}$  are found to be 19.13 and 15.60  $kN/m^3$ , respectively. The statistical outcome for saturated and dry unit weight is presented in Table B.4.7 (Appendix B.4).

### Small Strain Parameters

The small strain parameters are calculated with Alpan's 1970 and Benz & Vermeer's 2007 methods. The methodology explained in Paragraph 2.1.4 is being used, and the analytical results are presented in Table B.5.7 of Appendix B.5. The average value of these two methods will be considered, leading to

$G_0^{ref}$  equal to 108989 kPa. Finally, the calculation of the shear strain  $\gamma_{0.7}$  is performed using Equation 2.1.50 is equal to 0.00064.

The Hardening Soil Small Strain constitutive model properties for the soil layer L17 that will be used in the finite element program PLAXIS are summarized in Table 2.3.1.

## 2.2.8 Soil Layer L18

The soil layer L18 is a deep over consolidated tertiary sand layer that is part of the second aquifer and is located from -42.5 m to -55 m. It presents very high cone resistance ranging from 25 to 50 MPa. As a representative  $q_c$  value, the mean 37.5 MPa has been chosen.

### Strength Parameters

For the current layer, there is no available lab testing; therefore, the strength parameters will be derived from correlations with CPT data and the use of table 2.b, Appendix A. As shown in Table 2.2.2, this layer is located very deep, and the effective vertical stress  $\sigma'_v$  in the middle of the layer at -55.45 m equals 518 kPa. Under these conditions, the conversion of the cone resistance using Equation 2.1.6 is not representative. Therefore, the correct category of table 2.b is selected through the relative density. Using the correlation from Baldi et al. 1986 shown in Figure 2.2.7 with Equation 2.2.7, the relative density  $D_r$  for this layer is equal to 84.57 %. Following note (b) of table 2.b, A, for relative density  $Re = 84.57 \%$ , the soil belongs to the high density (Vast) category of sand.

However, table 2.b uses characteristic values, and in the case of the strength parameters are values that underestimate the capabilities of the soil for safety reasons. Since the goal of the present thesis is to compare with actual monitoring data, the most representative parameters of the soil need to be used, which are the mean values. The derivation of the mean values from table 2.b is explained in Paragraph 2.1.3. Eventually, the effective friction angle given to layer L18 equals  $43.60^\circ$ . Since the material is coarse-grained, 0 effective cohesion  $c'$  is considered.

### Stiffness Parameters

According to Lunne's and Christophersen's correlation, the oedometer stiffness can be derived for over-consolidated tertiary sand layers via Equation 2.1.40. The stiffness depends on the stress level; therefore, it is important to normalize it to a reference stress level using Equation 2.1.28. According to the PLAXIS Manual, the reference stress level is chosen to be 100 kPa, the effective vertical stress for each layer is given in Table 2.2.2, and the mean strength parameters are used. Finally, the secant reference stiffness  $E_{50}^{ref}$  and the unloading reloading reference stiffness  $E_{ur}^{ref}$  are derived using Equations 2.1.28 and the 2.1.29, respectively.

### Other Parameters

The dilatancy angle  $\psi$  is calculated according to Table 2.1.3, the undrained Poisson's ration  $\nu_{ur}$  is equal to 0.20 according to the discussion in Paragraph 2.1.4, and the  $m$  is considered 0.5 for this sandy layer in line with the recommendations of the PLAXIS Manual. Since this material is adjacent to a steel combi wall that is generally considered a Rough/coarse surface, the wall angle of friction  $\delta$  from Table 2.1.5 equals  $27.50^\circ$ . Therefore, following Equation 2.1.17, the  $R_{int}$  for this layer is equal to 0.547. The neutral ground pressure coefficient  $K_0^{nc}$  is calculated using Equation 2.1.50 and is equal to 0.31.

The unit weight of this layer has been derived by examining nine samples in the lab from various borehole locations along the construction area. The average values of  $\gamma_{sat}$  and  $\gamma_{dry}$  are found to be 18.61 and 15.21  $kN/m^3$ , respectively. The statistical outcome for saturated and dry unit weight is

presented in Table B.4.8 (Appendix B.4).

### Small Strain Parameters

The small strain parameters are calculated with Alpan's 1970 and Benz & Vermeer's 2007 methods. The methodology explained in Paragraph 2.1.4 is being used, and the analytical results are presented in Table B.5.7 of Appendix B.5. The average value of these two methods will be considered, leading to  $G_0^{ref}$  equal to 343152 kPa. Finally, the calculation of the shear strain  $\gamma_{0.7}$  is performed using Equation 2.1.50 is equal to 0.00023.

The Hardening Soil Small Strain constitutive model properties for the soil layer L18 that will be used in the finite element program PLAXIS are summarized in Table 2.3.1.

### **2.2.9 Soil Layer L19**

Layer L19 is a clay, strong silty layer, but there are no available samples to test in the lab. This layer is part of the second aquifer, and the parameters for this layer will be determined through correlations using the CPT data. The cone resistance  $q_c$  ranges between 4.5 MPa and 10 MPa. The representative cone resistance  $q_c$  for these is equal to 7 MPa. Eccentrically, layer L19 is, in reality, L17 repeating itself in a higher depth. Therefore, similar parameters will be considered.

The Hardening Soil Small Strain constitutive model for the soil layers L19 that will be used in the finite element program PLAXIS is summarized in Table 2.3.1.

### **2.2.10 Soil Layer LX02 and LX01**

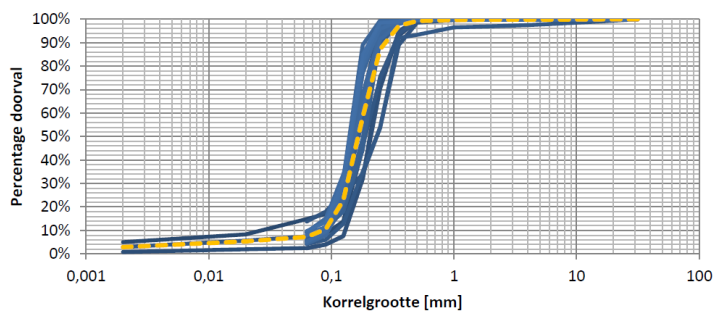
Both sand layers have been extracted from the same project's outer harbor, and quartz is their main mineral. The layer LX02 is a backfilled layer comprised of uniform fine sand placed above water with a relative density  $Re$  between 60 % and 70 %. This layer will replace the excavated soil to place the laying anchors between the anchor and combi walls. The layer LX01 is a sand fill used to create the land in the north section of the outer excavation pit. It has been placed underwater with no compaction; hence it has a lower density than LX02 at  $Re$ , between 30 % and 40 %. After the placement of the sands, CPTs were performed to confirm the properties of the manufactured layers. The cone resistance  $q_c$  for LX02 and LX01 is 7.5 MPa and 5.0 MPa, respectively.

### Strength Parameters

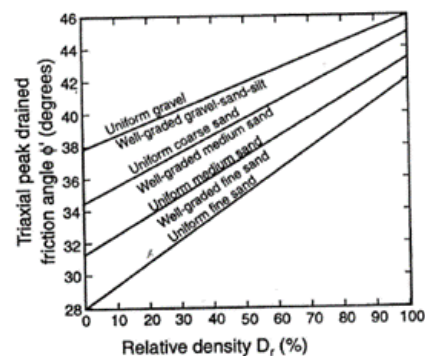
At the in-situ location of the sand, wells were drilled to determine the grain distribution of the sand. The result was an average fine particle content of 7.2 %, and the distribution is presented in Figure 2.2.8a. As shown in the figure, the sand is uniformly distributed. Additionally, some fine particles will be washed away when dredging and reusing the material. Therefore, it is described as uniform fine sand, and the effective friction angle is derived through the correlation on Schmertmann 1978, Figure 2.2.8b. For the layer LX02 with an average relative density  $D_r$  equal to 65 %, the effective friction angle  $\phi'$  is  $37.5^\circ$ . Similarly, layer LX01 with average relative density  $D_r$  equal to 35 %, the effective friction angle  $\phi'$  is  $33.5^\circ$ . Since the material is coarse-grained, 0 effective cohesion  $c'$  is considered.

Knowing the effective friction angle and the cone resistance for the two sand layers, the unit weights are derived using table 2.b, A. To use the  $q_c$  as import to table 2.b for a sand layer, it needs to be standardized for an effective vertical ground stress  $\sigma'v$  of 100 kPa, as explained in Paragraph 2.1.3. Therefore, Equation 2.1.6 is being used where the  $\sigma'v$  of the current layer is given in Table 2.2.2. Table 2.2.7 gives the derived unit weights.





(a) In-situ grain distribution for the sand layers LX02 and LX01.

(b) Relative density versus peak effective friction angle  $\phi'$  for different types of sand [Schmertmann (1978)].**Table 2.2.7:** Saturated and dry unit weight for the sand layers LX01 and LX02.

	LX01	LX02	
$\gamma_{dry}$	19	17	$kN/m^3$
$\gamma_{sat}$	20	18	$kN/m^3$

### Stiffness Parameters

The odometer stiffness at a reference level of 100 kPa was determined for the backfill sand layers with Equation 2.2.8. Finally, the secant reference stiffness  $E_{50}^{ref}$  and the unloading reloading reference stiffness  $E_{ur}^{ref}$  are derived by using Equations 2.1.35 and the 2.1.36, respectively.

$$E_{oed}^{ref} = R_e * 60 \text{ MPa} \quad (2.2.8)$$

### Other Parameters

The dilatancy angle  $\psi$  is calculated according to Table 2.1.3, the undrained Poisson's ration  $\nu_{ur}$  is equal to 0.20 according to the discussion in Paragraph 2.1.4, and the  $m$  is considered 0.5 for this sandy layer in line with the recommendations of the PLAXIS Manual. Since this material is adjacent to a steel combi wall that is regarded as a Rough/coarse surface, the wall angle of friction  $\delta$  from Table 2.1.5 equals  $27.50^\circ$ . Therefore, following Equation 2.1.17, the  $R_{int}$  for LX02 and LX01 is 0.6784 and 0.7865, respectively. The neutral ground pressure coefficient  $K_0^{nc}$  is calculated using Equation 2.1.50 and is equal to 0.3912 for LX02 and 0.4481 for LX01.

### Small Strain Parameters

The small strain parameters are calculated with Alpan's 1970 and Benz & Vermeer's 2007 methods. The methodology explained in Paragraph 2.1.4 is being used, and the analytical results are presented in Table B.5.8 of Appendix B.5. The average value of these two methods will be considered, leading to  $G_0^{ref}$  equal to 269750 and 155750 kPa for LX02 and LX01, respectively. Finally, the calculation of the shear strain  $\gamma_{0.7}$  is performed using Equation 2.1.50 is equal to 0.000023 and 0.0001 for LX02 and LX01, respectively.

The Hardening Soil Small Strain constitutive model properties for the soil layers LX02 and LX01 that will be used in the finite element program PLAXIS are summarized in Table 2.3.1.

## 2.3 Parameter Overview

**Table 2.3.1:** Mean and design soil properties used in the PLAXIS models.

<b>Mean</b>	Model	Drainage	$\gamma_{sat}$	$\gamma_{dry}$	$\phi'$	$c'$	$\psi$	$E_{50}^{ref}$	$E_{Oed}^{ref}$	$E_{ur}^{ref}$	$\nu_{ur}$	$m$	$G_0^{ref}$	$\gamma_{07}$	$R_{int}$	POP
LX02	HSS	Drained	20.00	18.71	37.50	0.00	7.5	39000	39000	156000	0.20	0.5	208000	2.3E-05	0.678	0
LX01	HSS	Drained	19.00	17.00	33.50	0.00	2.6	21000	21000	84000	0.20	0.5	112000	1.0E-04	0.787	0
L05a	HSS	Drained	18.56	18.56	29.10	0.00	0.0	30348	30348	125000	0.20	0.5	174502	1.0E-04	0.899	10
L07	HSS	Drained	14.85	14.85	20.30	6.63	0.0	2703	1729	5410	0.15	0.8	21837	8.9E-04	0.250	10
L05b	HSS	Drained	21.00	21.00	37.80	0.00	7.8	46214	46214	184856	0.20	0.5	231070	1.1E-04	0.672	10
L09	HSS	Drained	18.74	18.74	32.00	0.00	2.0	20285	20285	81140	0.15	0.5	137586	2.1E-04	0.834	10
L08	HSS	Drained	18.53	18.53	37.80	0.00	7.8	43127	43127	172508	0.15	0.5	232511	1.7E-04	0.578	10
L15	HSS	Drained	19.25	19.25	24.40	18.55	0.0	23199	23199	46400	0.30	0.8	80897	6.5E-04	0.886	550
L16	HSS	Drained	19.13	19.13	37.80	0.00	7.8	32947	32947	131789	0.20	0.5	183956	3.6E-04	0.672	550
L17	HSS	Drained	19.13	19.13	26.20	17.40	0.0	11626	11626	58128	0.20	0.8	108989	6.4E-04	0.892	550
L18	HSS	Drained	18.61	18.61	43.60	0.00	13.6	61600	53000	123266	0.20	0.5	343152	2.3E-04	0.547	550
L19	HSS	Drained	19.13	19.13	26.20	17.44	0.0	11626	11626	58128	0.20	0.8	108989	7.5E-04	0.892	550
Gravel	HSS	Drained	20.00	20.00	35.00	0.00	5.0	40000	29330	160000	0.20	0.5	83250	1.4E-04	0.743	0
L15b	HSS	Undra. A	19.25	19.25	24.40	18.55	0.0	23199	23199	46400	0.30	0.8	80897	6.5E-04	0.886	550

<b>Design</b>	Model	Drainage	$\gamma_{sat}$	$\gamma_{dry}$	$\phi'$	$c'$	$\psi$	$E_{50}^{ref}$	$E_{Oed}^{ref}$	$E_{ur}^{ref}$	$\nu_{ur}$	$m$	$G_0^{ref}$	$\gamma_{07}$	$R_{int}$	POP
LX02	HSS	Drained	20.00	18.00	38.50	0.00	5.5	39000	39000	156000	0.20	0.5	165800	1.0E-04	0.506	0
LX01	HSS	Drained	19.00	17.00	33.50	0.00	2.6	21000	21000	84000	0.20	0.5	112000	1.0E-04	0.550	0
L05a	HSS	Drained	18.50	18.50	27.50	0.00	0.0	30000	30000	120000	0.20	0.5	137500	1.0E-04	0.699	10
L07	HSS	Drained	13.20	13.20	20.00	5.00	0.0	1500	2300	5550	0.15	0.8	28200	2.0E-05	0.250	10
L05b	HSS	Drained	18.50	19.00	38.50	0.00	5.5	30000	50000	200000	0.20	0.5	192500	1.0E-04	0.458	10
L09	HSS	Drained	20.00	18.00	28.30	0.00	0.0	20000	20000	80000	0.15	0.5	111300	1.0E-04	0.675	10
L08	HSS	Drained	20.00	18.00	35.80	0.00	2.8	50000	50000	200000	0.15	0.5	200900	1.0E-04	0.506	10
L15	MC	Drained	19.00	19.20	22.00	15.00	0.0	E = 52000			0.30	0.8	-	-	0.901	550
L16	HSS	Drained	19.50	19.50	32.60	0.00	1.1	50000	50000	200000	0.20	0.5	192500	1.0E-04	0.570	550
L17	HSS	Drained	19.60	19.60	25.00	15.00	0.0	20000	20000	100000	0.20	0.8	122900	2.0E-05	0.781	550
L18	HSS	Drained	20.00	18.00	38.20	0.00	5.5	120000	120000	360000	0.20	0.5	306000	1.0E-04	0.463	550
L19	HSS	Drained	19.60	19.60	30.00	15.00	0.0	20000	20000	100000	0.20	0.8	122900	2.0E-05	0.630	550
Gravel	HSS	Drained	20.00	20.00	35.00	0.00	5.0	40000	29330	160000	0.20	0.5	83250	1.4E-04	0.743	0

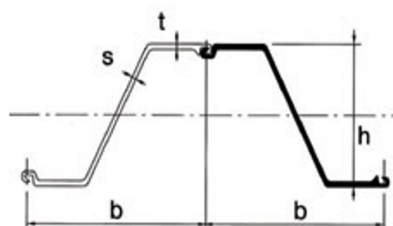
## 2.4 Parameter Determination of Structural Elements

### 2.4.1 Combi Wall

The retaining wall for cross-section L01b is a combi wall placed in a trench prefilled with cement bentonite. For the combi wall to be simulated in PLAXIS, the equivalent stiffness of the pipes, sheet piles, and cement bentonite have been considered. For efficiency purposes, the pipes are different sections welded together with various thicknesses. Table 2.4.1 summarizes the four different sections. The sheet pile between two consecutive pipes consists of two AZ 46-700 parts with steel quality S390GP. The properties of such a sheet pile are given in Figure 2.4.1 and Table 2.4.2.

**Table 2.4.1:** Properties of the different pipe sections from the combi wall of cross-section L01b.

Section	Steel	External Diameter [mm]	Thickness [mm]	Length [mm]	Location NAP
1	S460	1420	15.7	5.5	[+5.00 , -0.50]
2	S460	1420	27.7	11.5	[-0.50 , -12.0]
3	S460	1420	25.8	11.5	[-12.0 , -23.5]
4	S460	1420	15.7	5.5	[-23.5 , -34.0]

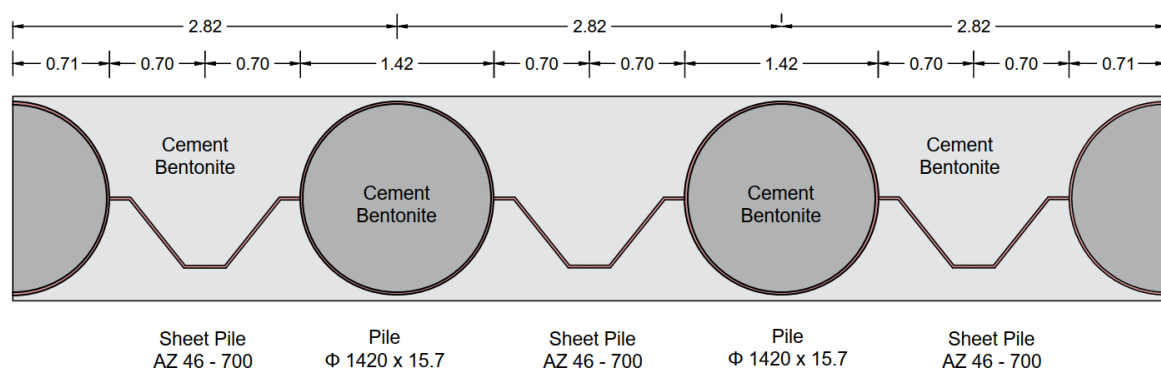


**Figure 2.4.1:** Sheet pile cross-section.

Parameter	Value	Unit
b	700	mm
h	501	mm
t	20	mm
s	16	mm

**Table 2.4.2:** Dimensions of the sheet pile AZ 46-700.

Lastly, the cement bentonite is presented both outside and inside the piles. The top view of the retaining wall is given in Figure 2.4.2.



**Figure 2.4.2:** Top view of the combi wall of cross-section L01b (units in m).

The properties of the combi wall have been collected from the as-built drawings of the project. The plates that simulate the wall in the finite element program use the elastic material type, and the most important properties that need to be determined are the  $EA$  and  $EI$ . The modulus of elasticity for the steel structural elements is considered  $E = 2.1 * 10^8 \text{ kN/m}^2$ . For the steel pipe, the area of the ring  $A$

is given by Equation 2.4.1, where  $D$  is the external diameter and  $d$  is the internal diameter. Therefore,  $EA$  can be derived by multiplying the area of the pile with the modulus of elasticity. The moment of inertia in both directions ( $I_x$  and  $I_y$ ) of the pile is the same and is given by Equation 2.4.2, where  $t$  is the thickness of the pipe wall. Therefore, the flexural rigidity  $EI$  can be derived by multiplying the modulus of elasticity with the moment of inertia. The unit weight of steel  $\gamma_{steel}$  is taken as  $7850 \text{ kg/m}^3$ ; hence the unit weight per meter  $w$  is given by Equation 2.4.3, where  $g$  is the gravity acceleration. The piles are not continuous throughout the length of the wall, but they repeat themselves with a center-to-center distance of 2.82 m. The values of  $EA$ ,  $EI$ , and  $w$  are divided by the center-to-center distance to obtain the correct properties for the model. Similarly, the properties of the sheet piles are calculated using the values from the manufacturer. The final values for the present wall are summarised in Table 2.4.3.

$$A_{ring} = \frac{\pi}{4} * (D^2 - d^2) \quad (2.4.1)$$

$$I_x = I_y = \frac{\pi}{64} * D^4 - ((D - (2 * t))^4) \quad (2.4.2)$$

$$w = A_{ring} * \gamma_{steel} * g \quad (2.4.3)$$

As described previously, the cement bentonite exists inside and outside the piles. The modulus of elasticity for bentonite is considered  $E = 5 * 10^5 \text{ kN/m}^2$ . The area occupied by the bentonite inside the pile is given by Equation 2.4.4, where  $d$  is the internal diameter of the pile. Therefore  $EA$  can be derived by multiplying the area of the pile with the modulus of elasticity. The moment of Inertia for both directions is the same and given by Equation 2.4.5. Therefore, the flexural rigidity  $EI$  can be derived by multiplying the modulus of elasticity with the moment of inertia. The unit weight of the bentonite is  $\gamma_{bentonite} = 13.5 \text{ kN/m}^3$ ; hence the weight per meter  $w$  is given by Equation 2.4.6, where  $g$  is the gravity acceleration. Similarly, with the piles, the values of  $EA$ ,  $EI$ , and  $w$  are divided by the center-to-center distance to obtain the correct properties for the model. The parameters are summarized in Table 2.4.3.

$$a = \frac{\pi * d^2}{4} \quad (2.4.4)$$

$$I_x = I_y = d^4 \pi / 64 \quad (2.4.5)$$

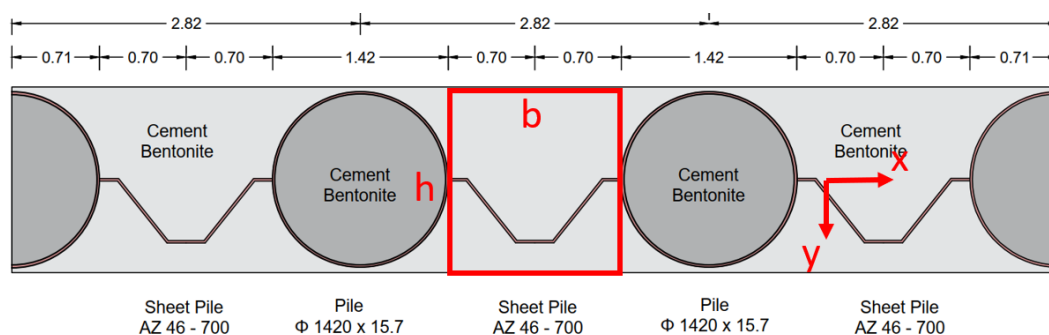
$$w_{bentonite} = a * \gamma_{bentonite} * g \quad (2.4.6)$$

Regarding the bentonite outside of the pile, the relevant area is the one between two piles. For simplification purposes, it has been regarded as rectangular with the width of the trench and the length of the distance between the piles. For instance, this area is represented by the red rectangular in Figure 2.4.3. Even though the area occupied by the sheet pile is included inside, it is considered insignificant. The area for the outside bentonite is given by Equation 2.4.7. Therefore,  $EA$  can be derived by multiplying the area of the pile with the modulus of elasticity. Because direction  $y$  and direction  $x$  are not the same, the  $I_y$  is different from  $I_x$  in this case. Suppose the wall direction is considered as  $x$ . In that case, the relevant moment of inertia for retaining the excavation pit is the  $I_x$  and is given by Equation 2.4.8. Therefore, the flexural rigidity  $EI$  can be derived by multiplying the modulus of elasticity with the moment of inertia. The weight per meter  $w$  is given by Equation 2.4.9 where  $g$  is the gravity acceleration. Similarly, the values of  $EA$ ,  $EI$ , and  $w$  are divided by the center-to-center distance to obtain the correct properties for the model. The parameters are summarized in Table 2.4.3.

$$A_{outside,ben} = b * h \quad (2.4.7)$$

$$I_x = (b * h^3) / 12 \quad (2.4.8)$$

$$w_{bentonite} = A_{outside,ben} * \gamma_{bentonite} * g \quad (2.4.9)$$



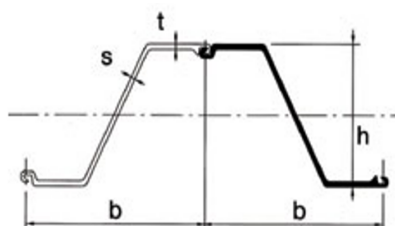
**Figure 2.4.3:** Top view of the combi-wall indicates the calculated area for the bentonite outside the pile.

**Table 2.4.3:** Properties for each section of the retaining wall used in the model.

Section	Par.	Unit	Pipe	Sheet Pile	Inner Bentonite	Outer Bentonite	Total
Section 1	W	kN/m/m	1.90	0.77	7.11	9.86	19.65
	EA	kN/m/m	5190463	2110113	268436	372340	7941352
	EI	kN*m <sup>2</sup> /m	1279467	85914	32341	69814	1467535
Section 2	W	kN/m/m	3.31	0.77	6.87	9.86	20.81
	EA	kN/m/m	9022620	2110113	259311	372340	11764385
	EI	kN*m <sup>2</sup> /m	2187158	85914	30180	69814	2373065
Section 3	W	kN/m/m	3.09	0.77	6.91	9.86	20.63
	EA	kN/m/m	8415208	2110113	260758	372340	11158419
	EI	kN*m <sup>2</sup> /m	2045379	85914	30517	69814	2231623
Section 4	W	kN/m/m	1.90	-	7.11	9.86	18.88
	EA	kN/m/m	5190463	-	268436	372340	5830000
	EI	kN*m <sup>2</sup> /m	1279467	-	32341	69814	1380000

## 2.4.2 Anchor Wall

The anchoring system for the cross-section under investigation uses layered anchors. Therefore, it consists of a system of anchor walls and anchor rods. The anchor wall at this location is AZ 26-700 sheet pile with S390 GP steel quality and 16 m length [3, -13] m NAP. The properties of the sheet pile are given in Table 2.4.4.



**Figure 2.4.4:** Sheet pile cross-section.

Parameter	Value	Unit
b	700	mm
h	460	mm
t	12.2	mm
s	12.2	mm
A	187	cm <sup>2</sup> /m
I <sub>y</sub>	59720	cm <sup>4</sup> /m

**Table 2.4.4:** Dimensions of the sheet pile AZ 26-700.

The properties of the sheet pile wall have been collected from the as-built drawings of the project. The plates that simulate the wall in PLAXIS use the elastic material type, and the most important properties that need to be determined are the  $EA$  and  $EI$ . The modulus of elasticity for the steel structural elements is considered  $E = 2.1 * 10^8 \text{ kN/m}^2$ . Therefore, the flexural rigidity  $EI$  can be derived by multiplying the modulus of elasticity with the moment of inertia  $I_y$ . The  $EA$  is derived by multiplying the cross-section area of the sheet with the modulus of elasticity. The unit weight of steel  $\gamma_{steel}l$  is taken as  $7850 \text{ kg/m}^3$ ; hence the unit weight per meter  $w$  is given by Equation 2.4.10, where  $g$  is the gravity acceleration. In this case, the wall is continuous, so there is no need to divide the values by center-to-center distance. The properties of the anchor wall are summarized in Table 2.4.5.

$$w_{bentonite} = A_{sheet} * \gamma_{steel} * g \quad (2.4.10)$$

**Table 2.4.5:** Properties for the anchor wall AZ 26-700 of this model.

	<b>W</b>	<b>EA</b>	<b>EI</b>
	<i>kN/m/m</i>	<i>kN/m/m</i>	<i>kN * m<sup>2</sup>/m</i>
Anchor Wall	1.47	3927000	125400

### 2.4.3 Anchor Rod

According to the final drawings, the anchor rods used in the cross-section under investigation are M110 / 106 with steel quality ASF500. The anchor rod has a length of 45 m and spanning between the combi wall and the anchor wall at a depth of 0 m NAP. The center-to-center distance between them is 2.58 m. They are pre-stressed at 400 kN, and in the finite element program PLAXIS, they are simulated with the node-to-node element type. The node-to-node elements use the elastoplastic material type, and the most important property that needs to be determined is the  $EA$ . The modulus of elasticity for the steel structural elements is considered  $E = 2.1 * 10^8 \text{ kN/m}^2$ . The area of the rod is  $\frac{\pi * D^2}{4}$  and is multiplied by the modulus of elasticity to derive the  $EA$ . The value of  $EA$  is divided by the center-to-center distance to obtain the correct properties for the model, and it is equal to  $773525 \text{ kN/m/m}$ .

## 2.5 Construction Phases

This section discusses the construction phases used in the PLAXIS model. Thirteen construction stages comprise the model. Firstly a short description of each phase is given. The phase and the construction dates are summarised in Table 2.5.1. A screenshot from PLAXIS input and a CAD figure is given for each construction phase in Appendix C.

Phase 1: The excavation for the installation of the anchor wall is performed. Phase 2: The area between the anchor wall and the combi-wall is excavated until -0.5 m NAP. Phase 3: The soil is replenished with the material LX02 until the level of the anchor rod at 0 m NAP. Phase 4: The anchor rod is installed and pre-tensioned at 400 kN. Phase 5: Replenished with the material LX02 up to the surface at +3.5 m NAP. Phase 6: The water table inside the excavation pit is lowered to -15 m NAP to allow for dry excavation. Phase 7: The level of the excavation pit is lowered to -6 m NAP with dry excavation methods. Phase 8: The level of the excavation pit is lowered to -11 m NAP with dry excavation methods. Phase 9: The excavation pit is refilled with water up to 0 m NAP to allow for wet

excavation. Phase 10: The level of the excavation pit is lowered to -17 m NAP with wet excavation methods. Phase 11: The level of the excavation pit is lowered to -22 m NAP with wet excavation methods. Phase 12: 0.5 m of gravel is placed underwater, and then 1 m of the underwater concrete floor (UWC) without tension piles is poured inside the excavation pit. Phase 13: The UWC floor is hardened and worked as a beam, then the excavation pit is set dry.

**Table 2.5.1:** Summary of the phases used in the PLAXIS model and of the corresponding dates.

Phase	Description	End of Phase
Phase 0	Initial Phase	-
Phase 1	Anchor wall excavation	-
Phase 2	Excavation for anchor rod installation	-
Phase 3	Replenish with soil to anchor level	-
Phase 4	Installation and pre-tension of the anchors	-
Phase 5	Replenish with soil to surface level	-
Phase 6	Lower water level in pit to -15m NAP	-
Phase 7	Dry excavation to -6m NAP	22-01-2020
Phase 8	Dry excavation to -11m NAP	27-01-2020
Phase 9	Submerge pit to 0m NAP	08-02-2020
Phase 10	Wet excavation to -17m NAP	30-04-2020
Phase 11	Wet excavation to -22m NAP	25-06-2020
Phase 12	Dumping gravel and pouring UWC	07-08-2020
Phase 13	Set excavation dry	10-09-2020

## 2.6 External Load Investigation

This section describes the external loads used in the PLAXIS model. Figure 2.6.1 has been taken from Google Maps to present a reference for the dimensions and allow the visualization of where the loads are being applied.

The external loads applied to the project influence the deformations. Therefore it is important for the loads to accurately describe the actual conditions that took place during the construction of the excavation pit. Unfortunately, there was no accurate log of the timeline and machinery involved in the project. The best way to trace the information needed is through regular drone footage. Using these videos, the loads for the excavation pit were derived, and the corresponding picture for the construction phase is given in Appendix D. The loads have been implemented from the suggestions of professional engineers because the exact determination of them is impossible with the available data. Behind the anchor wall from the initial phase, there is a road that allows the entrance to the project. Hence a 10 kPa load has been considered for the project. The load conditions until stage 6 are not very relevant since the pit excavation has not started yet. Table 2.6.1 presents the load locations and values derived from the project's photos and videos for every construction phase.



**Figure 2.6.1:** Top view of the outer lock head with reference dimensions. [Google Maps]

**Table 2.6.1:** Summary of the locations and the value of the loads applied to each phase.

Phase	Load Position	Load Value	Picture	Picture Date
0	x: [-85, -60]	10 kPa	Picture 1	09-09-2019
1	x: [-85, -60]	10 kPa	-	-
2	x: [-85, -60]	10 kPa	-	-
3	x: [-85, -60]	10 kPa	-	-
4	x: [-85, -60]	10 kPa	Picture 2	23-10-2019
5	x: [-85, -60]	10 kPa	-	-
6	x: [-85, -60]	10 kPa	-	-
7	x: [-85, -60]	10 kPa	Picture 3	17-01-2020
8	x: [-85, -60]	10 kPa	Picture 3	17-01-2020
9	x: [-85, -60], [-40, -3]	10, 12 kPa	Picture 4	10-02-2020
10	x: [-85, -60], [-40, -13], [-13, -3], [-3, -1]	10, 10, 5, 12 kPa	Picture 5	23-04-2020
11	x: [-85, -60], [-40, -13], [-13, -3], [-3, -1]	10, 10, 5, 12 kPa	Picture 6	26-06-2020
12	x: [-85, -60], [-40, -13], [-13, -3], [-3, -1]	10, 10, 5, 12 kPa	Picture 7	20-08-2020
13	x: [-85, -60], [-40, -13], [-13, -3], [-3, -1]	10, 10, 5, 12 kPa	Picture 8	19-10-2020

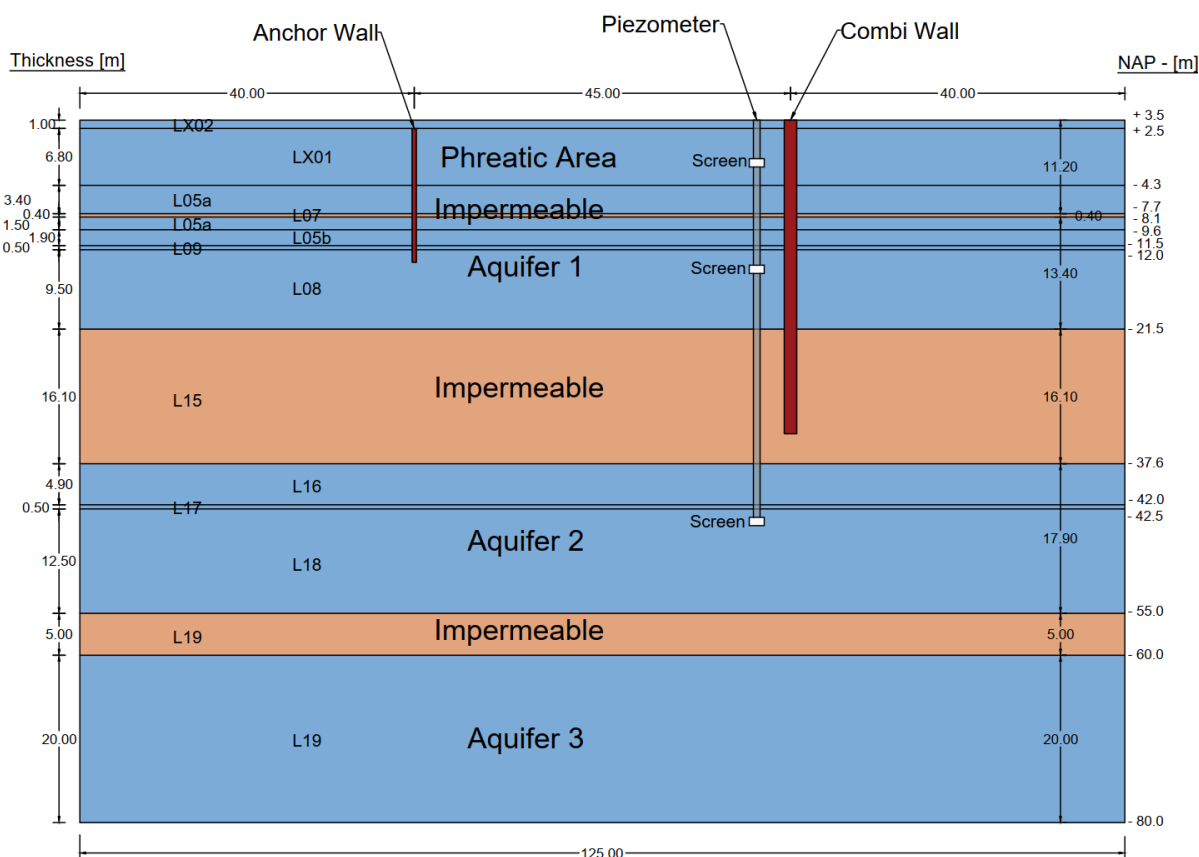
## 2.7 Head Determination of the Aquifers

The project contains three aquifers and the phreatic area as shown in Figure 2.7.1. Piezometers have determined the aquifer heads. The piezometer is placed right behind the wall and has screens in the Phreatic Area, Aquifer1, and Aquifer 2. The third Aquifer maintains a stable head throughout all the construction phases and is monitored by deeper piezometers in other project locations. The aquifers are divided by three Impermeable layers L07, L15, and L19. In the PLAXIS model, the impermeable layers use the interpolation method for head determination.

Different piezometers determine the water level inside the excavation pit. Aquifers 2 and 3 always have the same head inside and outside the excavation. However, Aquifer 1 and the Phreatic area are interrupted by the impermeable combi-wall. Depending on the construction phase, the head inside and outside the excavation differs. An overview of the heads for all aquifers, for every construction phase inside and outside the excavation pit, is given in Table 2.7.1. The values that have been chosen



correspond to the moment the inclinometer measurement has been performed. This is important because the head significantly influences the deformations of the wall. In that way, the deformations of the model are compared with the monitored deformations. Appendix E presents the continuous measurements of the piezometer for all the aquifers.



**Figure 2.7.1:** Aquifer representation at the location of cross-section L01b under investigation.

**Table 2.7.1:** Aquifer heads in [m] for every phase inside and outside the excavation pit.

P.	Outside of Excavation				Inside of Excavation			
	Phre.	Aq.1	Aq.2	Aq.3	Phre.	Aq.1	Aq.2	Aq.3
Phase 0	2.30	1.20	1.2	0.68	2.30	1.20	1.20	0.68
Phase 1	-1.52	-0.50	0.62	0.68	2.30	1.20	0.62	0.68
Phase 2	-1.52	-0.50	0.62	0.68	2.30	1.20	0.62	0.68
Phase 3	-1.52	-0.50	0.62	0.68	2.30	1.20	0.62	0.68
Phase 4	-1.52	-0.50	0.62	0.68	2.30	1.20	0.62	0.68
Phase 5	-1.52	-0.50	0.62	0.68	2.30	1.20	0.62	0.68
Phase 6	-1.52	-0.50	0.62	0.68	-15.0	-15.0	0.62	0.68
Phase 7	-1.52	-1.50	0.40	0.68	-15.0	-15.0	0.40	0.68
Phase 8	-1.52	-5.00	-6.25	0.68	-15.0	-15.0	-6.25	0.68
Phase 9	-1.52	-5.00	-11.5	0.68	0.00	0.00	-11.5	0.68
Phase 10	-1.38	-3.50	0.30	0.68	0.00	0.00	0.30	0.68
Phase 11	-1.38	-3.50	0.30	0.68	0.00	0.00	0.30	0.68
Phase 12	-0.80	-2.00	-12.0	0.68	0.00	0.00	-12.0	0.68
Phase 13	-0.80	-1.00	-12.0	0.68	-	-	-12.0	0.68

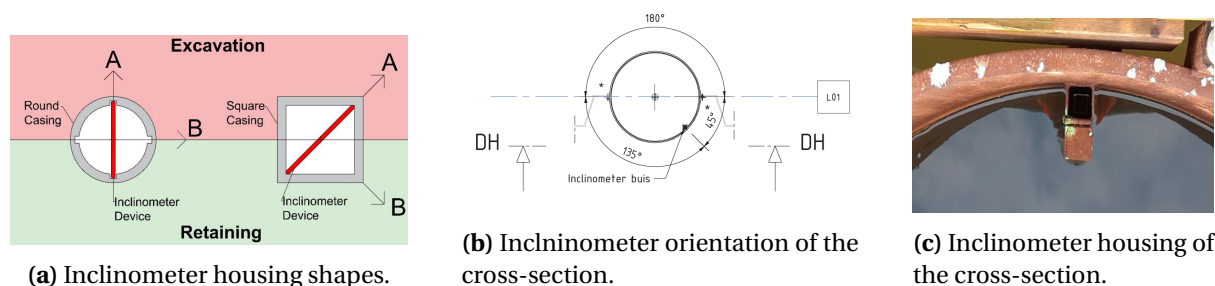
## 2.8 Monitoring

This section will discuss the monitoring methods applied to the excavation pit and the way that has been utilized in the present thesis to improve the model.

### 2.8.1 Inclinometers

The excavation pit's primary monitoring is performed with inclinometers on the retaining wall. An inclinometer measures the horizontal deformations in two perpendicular axes in one pass. To perform the measurement, the inclinometer is put into the inclinometer housing. The housing of an inclinometer can be a circular or a square tube, as shown in Figure 2.8.1a. Often the housing is placed in such a way that does not allow the inclinometer to measure the deformations of the wall directly. This scenario is depicted in Figure 2.8.1a at the square tube, where the inclinometer (red line) measures the deformations at an angle. In that case, a correction for the angle should be applied.

In the specific cross-section under investigation, the housing is a square steel tube (Figure 2.8.1c) welded in the piles and is placed at a  $45^\circ$  angle as shown in Figure 2.8.1b. Every wall of the excavation is being monitored from multiple inclinometers frequently. However, for the monitoring deformations to be compared with the model deformations, they must represent the same conditions. Therefore, the completion date of the construction phase has been matched with a measurement performed after that date but before other construction operations. Table X summarizes the monitoring dates that have been used for every phase. Some of the phases do not have an inclinometer measurement, or they are not under investigation. An assumption that is being made is that the correction angle is correct and remains the same throughout all the construction stages. An investigation of the effects of different correction angles is made in Appendix X.



**Figure 2.8.1:** Rotation of the global RD coordinate system to a local x-y coordinate system.

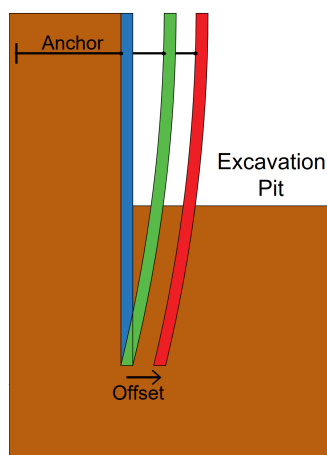
### 2.8.2 Total Stations - Offset wall movement investigation

An additional monitoring method that has been used for the deformation of the wall is the total stations. Total stations are devices that measure the coordinates of a point on the wall. The purpose is to confirm whether the pile is shifted in one direction. This offset movement cannot be seen from the inclinometer measurements since they measure the deformation of the pile relative to itself. The total station, on the other hand, measures the deformation of a pile relative to a fixed point. This offset behavior of the pile is depicted in Figure 2.8.2, where the red pile does not have a fixed tip, and the green pile has.

Using the coordinates given in Figure 2.8.3a for points a, b, c, and d, the corner of the retaining wall is created in Figure 2.8.3b. The orientation of the corner is based on the RDx-RDy coordinate system.

**Table 2.8.1:** Summary of the monitoring measurements that correspond to the constructions phases.

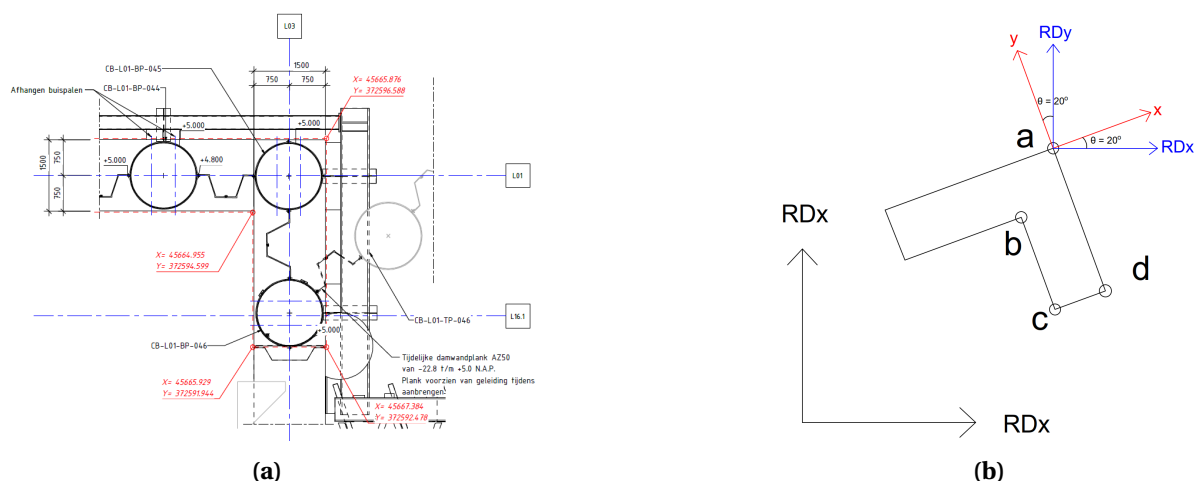
Phase	Description	End of construction	Inclinometer measur.
0.	Initial Phase	-	-
1.	Anchor wall excavation	-	-
2.	Excavation for anchor rods	-	-
3.	Replenish with soil to anchor	-	-
4.	Installation of anchors	-	-
5.	Replenish with soil to surface	-	-
6.	Lower water in pit to -15m NAP	-	-
7.	Dry excavation to -6m NAP	-	-
8.	Dry excavation to -11m NAP	27-01-2020	29-01-2020
9.	Submerge pit to 0m NAP	08-02-2020	10-02-2020
10.	Wet excavation to -17m NAP	30-04-2020	08-05-2020
11.	Wet excavation to -22m NAP	25-06-2020	30-06-2020
12.	Dumping gravel & pouring UWC	-	-
13.	Set excavation dry	10-09-2020	11-09-2020

**Figure 2.8.2:** Representation of the pile behaviour, with fixed tip (green) and without fixed tip (red).

However, a local coordinate system is being used that considers  $x$  as the direction of the wall and  $y$  as the direction of the excavation. The red axis system depicts the local system in Figure 2.8.3b. The RD and local system have  $\vartheta = 20.15^\circ$  difference. Therefore, the total station RD coordinated to be used needs to be rotated by  $\theta$ . The rotation is performed using the transformation matrix, Equation 2.8.1.

$$\begin{pmatrix} x \\ y \end{pmatrix} = \begin{bmatrix} \cos(\theta) & -\sin(\theta) \\ \sin(\theta) & \cos(\theta) \end{bmatrix} * \begin{pmatrix} RDx \\ RDy \end{pmatrix} \quad (2.8.1)$$

In Table 2.8.2, the columns  $RDx$  and  $RDy$  present the exact coordinates received from the total station measurement at each date. Using Equation 2.8.1, the RD coordinates are rotated to the local ( $x$ - $y$ ) coordinate system. The  $dx$  and  $dy$  columns provide the distance of the measuring point on each date from the original position on 11/20/2019. The columns  $dx$  and  $dy$  give the movement of the measuring point from the original position in the  $x$  and  $y$  system, with ( $y$ ) being the excavation direction and ( $x$ ) the L01 wall direction. The negative symbol (-) indicates movement toward the ex-



**Figure 2.8.3:** Rotation of the global RD coordinate system to a local x-y coordinate system.

cavation pit, and the positive (+) is away from the excavation pit, as shown in the red axis system in Figure 2.8.3b. The measuring point is located at the top of the combi wall piles at +4 m NAP. The next column provides the cumulative deformation, monitored from the inclinometer, relative to the same base measuring date as the total stations (11/20/2019). The measurements from both methods were taken on the same dates, and the comparison was performed for the same NAP level. Finally, the last column calculates the difference in mm between the two methods for each date. This difference is the offset movement of the pile.

In the present case the previously calculated offset ( $\delta$ ) has considered and the pile for the corresponding phase has been moved as shown in Figure 2.8.2. The  $\delta$  is used to add or subtract from the corresponding cumulative inclinometer deformations of the entire wall.

**Table 2.8.2:** Transformation of the RD coordinates to the local x-y coordinate system and comparison with the inclinometer deformations for cross-section L01b.

$\theta$	RDx	RDy	RDx	RDy	dx	dy	Incl.	Differ
20.1537	-	-	rot (x)	rot (y)	[m]	[m]	[mm]	[mm]
11/20/2019	45653.718	372590.781	171230.737	334048.180	0.0000	0.0000	0	0
01/22/2020	45653.738	372590.782	171230.756	334048.174	0.0188	-0.0058	1.40	4.449
01/29/2020	45653.733	372590.776	171230.750	334048.170	0.0124	-0.0099	6.00	3.862
02/10/2020	45653.734	372590.774	171230.750	334048.168	0.0126	-0.0121	9.60	2.484
03/19/2020	45653.739	372590.767	171230.752	334048.160	0.0149	-0.0204	12.70	7.678
04/06/2020	45653.737	372590.770	171230.751	334048.163	0.0140	-0.0169	9.50	7.373
04/22/2020	45653.737	372590.770	171230.751	334048.163	0.0140	-0.0169	8.40	8.473
05/08/2020	45653.731	372590.772	171230.746	334048.167	0.0091	-0.0129	9.50	3.428
06/10/2020	45653.733	372590.772	171230.748	334048.167	0.0110	-0.0136	9.00	4.617
07/02/2020	45653.735	372590.769	171230.749	334048.163	0.0118	-0.0171	11.10	6.022
07/31/2020	45653.739	372590.781	171230.757	334048.173	0.0197	-0.0072	11.70	-4.465
08/11/2020	45653.732	372590.766	171230.745	334048.161	0.0080	-0.0189	20.90	-1.995
09/04/2020	45653.731	372590.754	171230.740	334048.150	0.0029	-0.0298	28.00	1.826
09/06/2020	45653.729	372590.759	171230.740	334048.156	0.0027	-0.0244	29.50	-5.057
09/07/2020	45653.729	372590.748	171230.736	334048.145	-0.001	-0.0348	28.70	6.069
09/09/2020	45653.730	372590.748	171230.737	334048.145	-0.000	-0.0351	27.80	7.314
09/11/2020	45653.733	372590.748	171230.740	334048.144	0.0027	-0.0361	24.70	11.448
09/15/2020	45653.731	372590.750	171230.739	334048.147	0.0015	-0.0336	25.90	7.681
10/15/2020	45653.731	372590.740	171230.735	334048.137	-0.002	-0.0430	34.40	8.569

# 3

## Python Application

In this chapter, the Python Application constructed for the present thesis's realization will be discussed. The purpose of this application is to create a central Hub that allows the users to do the following operations:

- PLAXIS model build and mesh creation
- Process and Interpretation of the monitoring data
- PLAXIS results collection and creation of custom libraries
- Comparison of monitoring and PLAXIS deformations
- Sensitivity Analysis creation and interpretation
- Phase comparison of PLAXIS calculations in conjunction with monitoring

The extensiveness and the diversity of the initial python code ( $\approx 7000$  lines) made its use challenging for the users. Therefore, the decision has been made to host the code in a Graphical User Interface (GUI) environment. The application used the programming language Python 3.9 in the Anaconda Navigator environment, and for the GUI, the basic Tkinter package has been used (Moore, 2018) [26]. The functions, capabilities, and libraries of the application will be explained in the following sections.

### 3.1 General Structure

For the application to function needs to follow a fundamental structure. Firstly, the code with the name "Python Application.py" needs to be run in a python language interpreter. Also, the latest version of many universally available libraries must be imported/installed. Additionally, a specialized library for the Python-PLAXIS connection is required that is available when the PLAXIS finite element program is installed, called "plxscripting.easy". The necessary libraries are described in Appendix H. Two files accommodate the code. The first is the "Input" file containing the monitoring and PLAXIS model Excel files. The second folder is the "Settings" folder which includes icons and information the application requires, and the users do not need to interact with it.

Every wall of the outer lock head excavation is monitored by multiple inclinometers that measure the horizontal deformations in two perpendicular directions. The measurements are performed in

an interval of 0.5 m for the entire length of the wall. The data can be translated into Absolute, Cumulative, and Incremental deformations. The precise date and time of the measurement are also being logged. This significant amount of data is being stored in a custom excel file following a specific format that allows the code to read it. Additionally, the pile offset derived from the total station process is listed in this file. The Excel program has been chosen for data storage because it is widely used and accepted. It has been formatted to allow the users to easily add the new measurements produced by the project's surveyors. Appendix H provides screenshots of the excel format from the monitoring data. Each Excel file corresponds to the measurement of a specific inclinometer of the project.

The structure of the PLAXIS model Excel file is given in Appendix H and contains in a specific format the following information:

- Soil Properties
- Borehole information
- Flow Conditions
- Plates Information
- Node to Node elements information
- Fixed end anchors information
- Names of construction phases
- Stress conditions of the soil layers

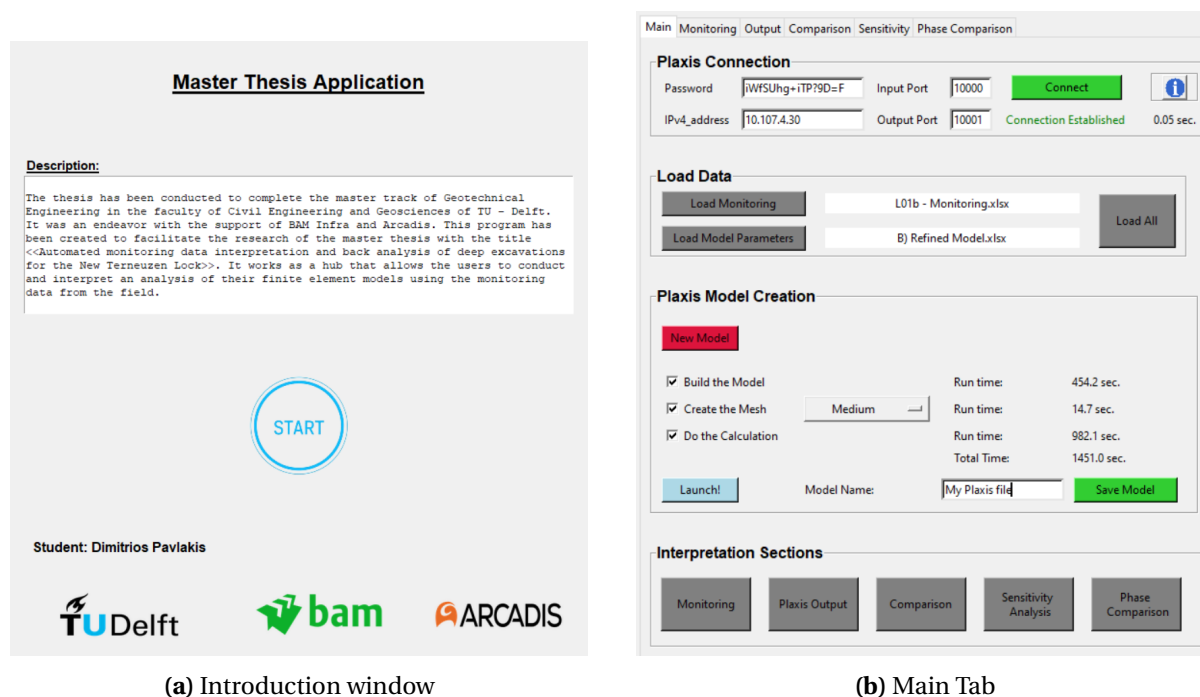
## 3.2 Introduction and Main Menu

Initially, the users are greeted with an introduction Tkinter window, as shown in Figure 3.2.1a. The introduction window contains information about the application's purpose and credits for its creation. By pressing the "Start" button, the users can access the main Tab of the Application (Figure 3.2.1b).

It starts with the "Main Tab", which allows the users to browse through all the windows of the application. The navigation is performed by the TAB ribbon at the top of the window or the Buttons at the bottom ("Interpretation Sections") with the corresponding names. Every Tab has a "<- Go Back" button that allows the users to return to the main Tab.

The "Plaxis Connection" section allows the application to remotely connect to the finite element program PLAXIS, even if it runs on a separate server. The firewall of the PLAXIS program hosting server needs to allow access to both the input and output of PLAXIS for communication with the application to be successful. The connection can be established by filling the input boxes of "Password," "IPv4-address", "Input Port," and "Output Port" and pressing the green button "Connect." To make the application user-friendly an info mark has been added that, when pressed, provides step-by-step instructions for completing the previously mentioned entry boxes (Appendix H). The message "Connection Established" and the time needed will appear if the connection is successful. The code will remember the last entries to speed up the process.

The "Load Data" section is responsible for loading the necessary information for the code to run. The "Load Monitoring" and "Load Model Parameters" buttons give access to a file explore browsing window where the users can find and load the corresponding excel files. The selected files' names



(a) Introduction window

(b) Main Tab

Figure 3.2.1: Python Application

will appear next to the buttons. The latest files will instantly load if the desired files are selected from a previous session by clicking the "Load All" button.

The "Plaxis Model Creation" section allows the users to create the model in the finite element program. The back end code contains a function that uses the `plxscripting.easy` library to create the complete model. This function draws information from the PLAXIS model excel file. The advantage of making the model through coding is when the model needs to be tested multiple times under different conditions. For instance, when the users want to change the head conditions of an aquifer in PLAXIS, they have to adjust the head in every polygon of the Aquifer manually. In the code, they can decide the new head value, and the code will do the tedious and time-consuming process automatically. Several instances provide time-effective solutions in the model built through coding that ultimately make the investigation more effective.

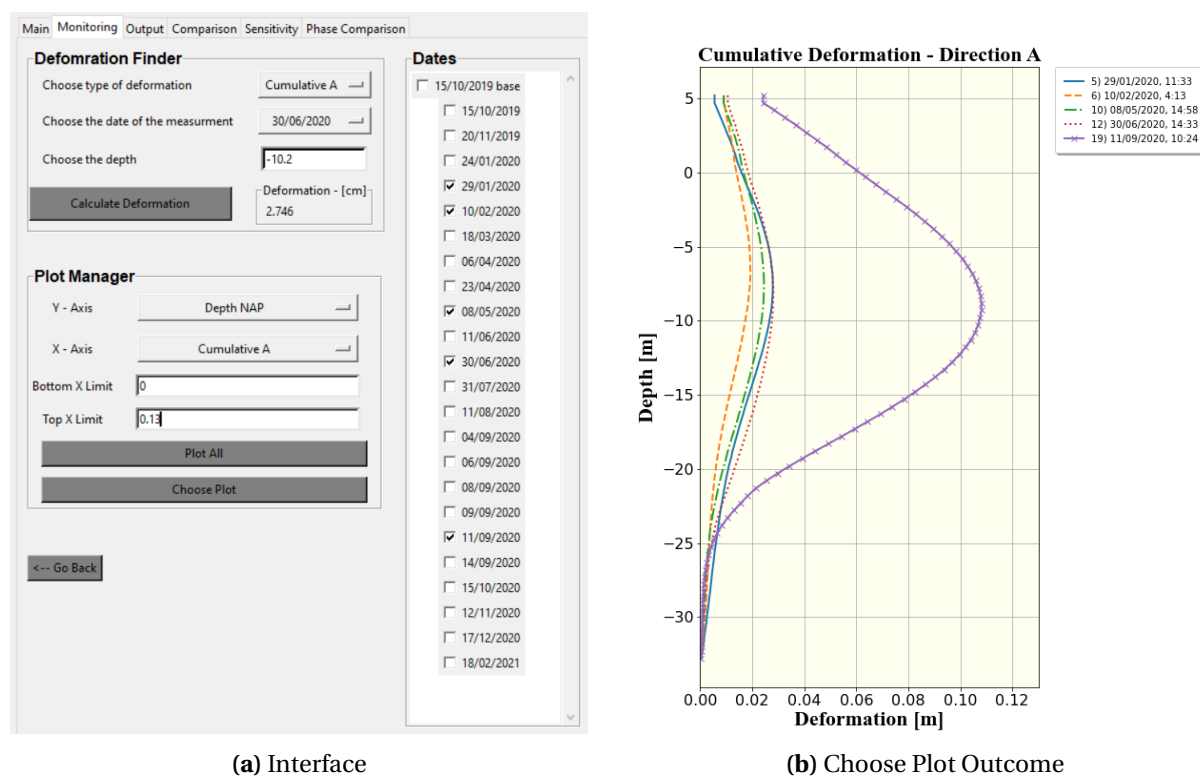
The red button "New Model" lets users clear the PLAXIS input section. The possibilities the code offers are to "Build the Model," to "Create the Mesh," and to "Do the Calculation." The users must decide in which actions are interested in by ticking the corresponding checkboxes. If the creation of a mesh is desired, its density can be chosen by the drop-down menu. Once all the above decisions have been made by clicking the blue button "Launch," the operations are performed in PLAXIS. When the processes in PLAXIS are completed, the required time for each is printed in seconds, and the users can name and save the Plaxis File using the green button "Save Model."

### 3.3 Monitoring Interpretation

A great amount of monitoring information accommodates complicated projects like the New Terneuzen Lock. Every wall of the outer lock head excavation is monitored by multiple inclinometers that measure the horizontal deformations. Therefore, a monitoring excel file is created for each measuring location, as shown in Appendix H. In this thesis, the project's cross-section and inclinometer L01b is being used. The application users can access and interpret all the monitoring data in an organized

and effective manner.

Figure 3.3.1 shows the interface from the monitoring interpretation section of the application. Once the monitoring file is loaded, the users can utilize this section to interpret the monitoring data. It consists of three sections the Deformations finder, the Plot manager, and the Date section. The Deformation finder allows the users to find the exact deformation of the wall at any date and depth. There are three types of deformations (Absolute, Cumulative, Incremental) in both the excavation (A) and wall (B) direction. Then from a drop-down menu, the date of measurement is chosen, and in the input box, any depth is given. Even though the inclinometer measurements are every 0.5 m, the code uses linear interpolation to produce the deformations requested in depths between those values.



(a) Interface

(b) Choose Plot Outcome

**Figure 3.3.1:** Monitoring Tab of Python Application

The users with Plot Manager can plot the deformations from all the dates using the button "Plot All" or choose specific dates from the "Dates" section by ticking the corresponding checkboxes and clicking the "Choose Plot" button. Additionally, they can choose the type of deformation plotted on the X-axis. The Y axis can be set to present depth from the surface or in a NAP base. Finally, they can determine the bottom and top limits of the X-axis for a better presentation of the results. For instance, Figure 3.3.1b presents the generated plot when the actions shown in the interface section (Figure 3.3.1a) are made.

Every plot the Python Application produces is accommodated with the toolbar shown in Figure 3.3.2. On the left side, there are options to manipulate the plot, like zooming and panning. On the right side, the coordinates of the mouse on the graph are given. These coordinates are adjusted based on the axis plotted each time.



**Figure 3.3.2:** Plot toolbar



### 3.4 PLAXIS Output

The Output section of the application is shown in Figure 3.4.1. The primary purpose of it is the collection and interpretation of the PLAXIS output. The users can collect the desired data when the PLAXIS calculations are complete, and the PLAXIS output program is open. By selecting in the "Plaxis Output" section the option "Load data from model" and clicking the button "Load Output," the code will loop throughout all the construction phases calculated and store the data in a custom library. This application has been constructed to interpret the behavior of a vertical retaining structure. It focuses on the deformations in both directions, the moments, and the forces applied to the wall. The custom library is a three-dimensional python list; its layers are explained in Figure 3.4.2. The users can save the output in an excel file by pressing the blue button "Refresh" and then by giving a name to the file and pressing the green button "Save in Excel." Moreover, the users can load previously saved output excel files by selecting the "Load data from excel" option and pressing the "Load Output" button. This method saves much memory because by focusing on the data of interest, the  $\approx 500$  MB PLAXIS saves are replaced by  $\approx 150$  KB excel files.

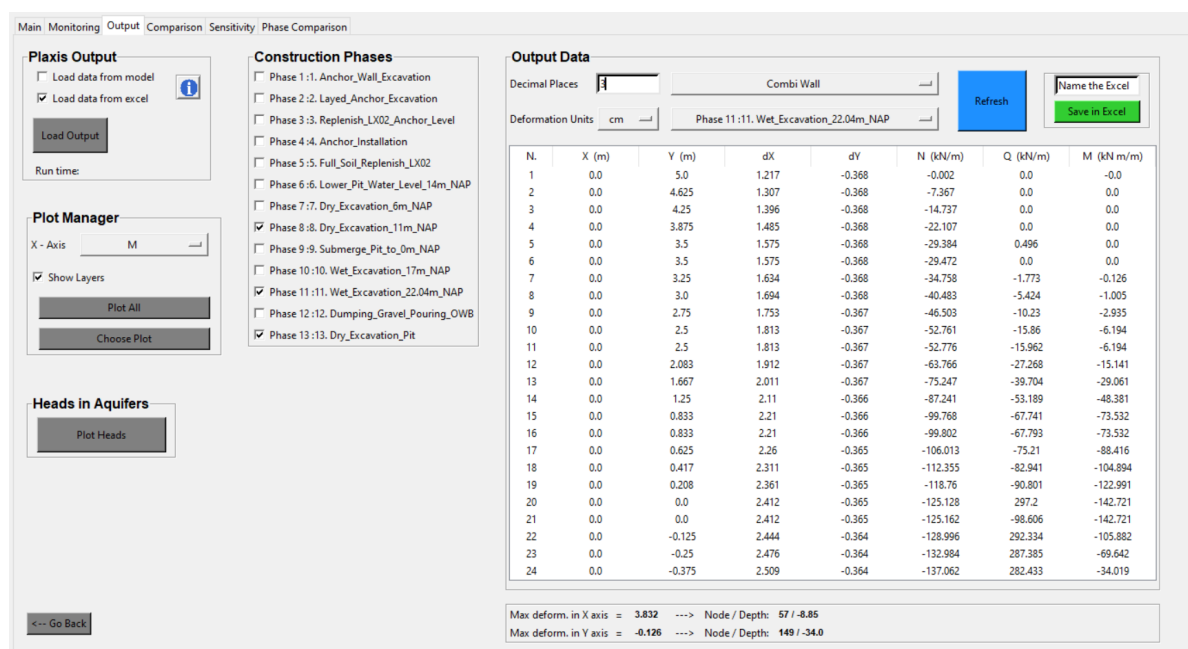


Figure 3.4.1: Output Tab of Python Application

Once the data are loaded, the users have several tools to interpret the results. Firstly, from the "Plot Manager" section, the results are plotted. They can decide on the type of plotted data from the dropdown menu (Deformations, Forces, Moments). These data can be plotted either for all the construction phases by clicking the "Plot All" button or for selected phases from the "Construction Phases" section and the "Choose Plot" button. Finally, there is the choice to include dashed lines for soil layers boundaries in the plot for better interpretation. For instance, Figure 3.4.3a has been created by selecting the moments for phases 8, 11, and 13 along with the soil layer boundaries.

The data can also be accessed in a table format from the "Output Data" section. The options given to the users are the construction phase that wants to investigate and the units and decimal places for the deformation values. The table presents the data from every node used to simulate the wall in the finite element program. Finally, the button "Plot Heads" allows the users to plot the evolution of the aquifer heads for every construction phase (Figure 3.4.3b).

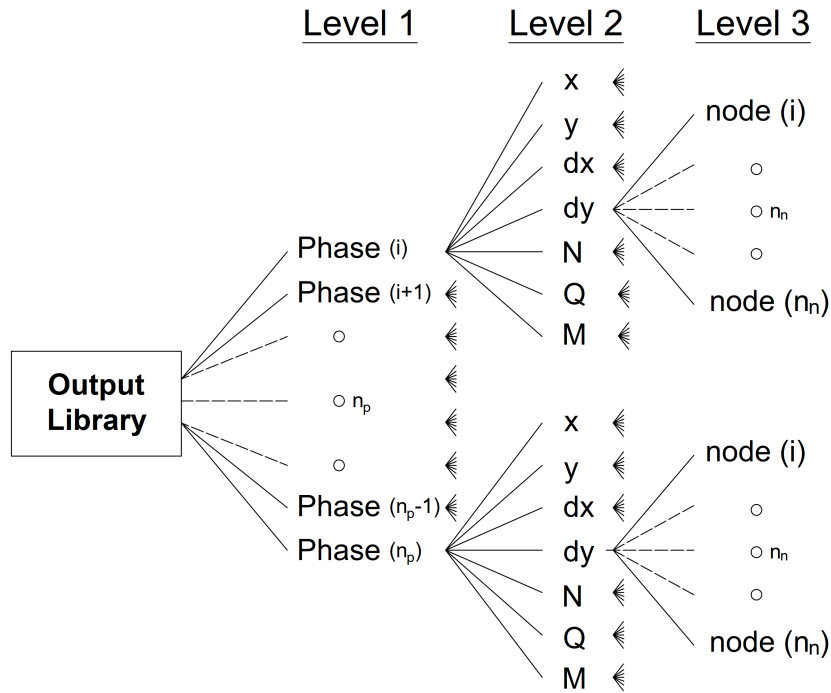


Figure 3.4.2: Output Library - Tree List

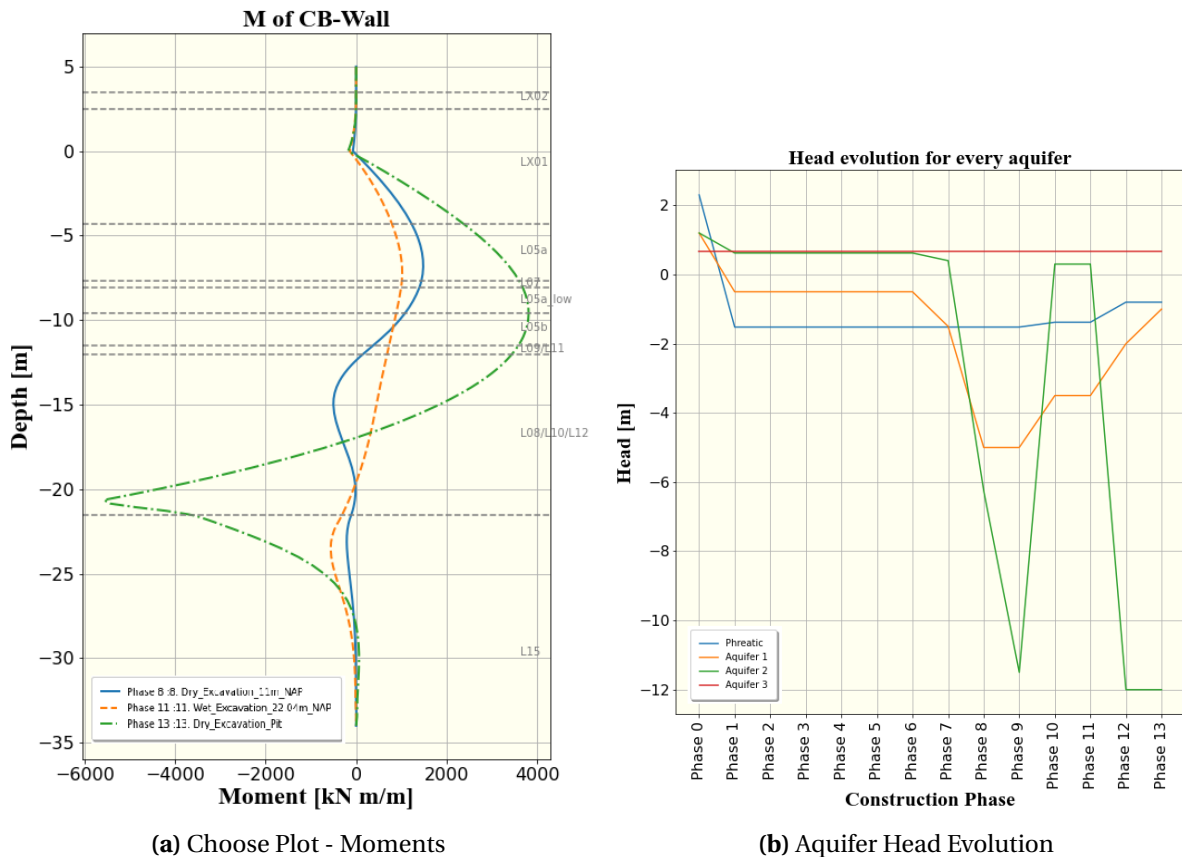


Figure 3.4.3: Output Tab of Python Application

### 3.5 Model and Monitoring Comparison

In the Comparison Tab, the monitoring and the model deformations are compared. To begin with, the users from the "Plaxis Output" section can load the desired excel file, as discussed in the previous paragraph. Once the data have been loaded, the "Plot Comparison Menu" section appears. Every construction phase is loaded, and choose date option is given for each phase. First, the users choose the desired phases by ticking the checkbox; then, they correspond the selected phases with the comparable monitoring measurement from the drop-down menu. If the Monitoring Excel file loaded previously includes total station information, the option "Consider Offset" will appear.

The actions the users can make after the selection of the data is to plot the deformation comparison by using the button "Create Plot" or see the data in the "Data Comparison" section by clicking the button "Load ."For instance, the plot produced for the selection shown in Figure 3.5.1 is given in Figure 3.5.2. Each color represents a construction phase, the dashed lines are the monitoring deformations, and the continuous lines are the model deformations. The difference between sub-figure a and b is the offset of the monitoring data due to information derived by the total stations. When the offset is not used, the monitoring deformations always start from the (0, 0) location.

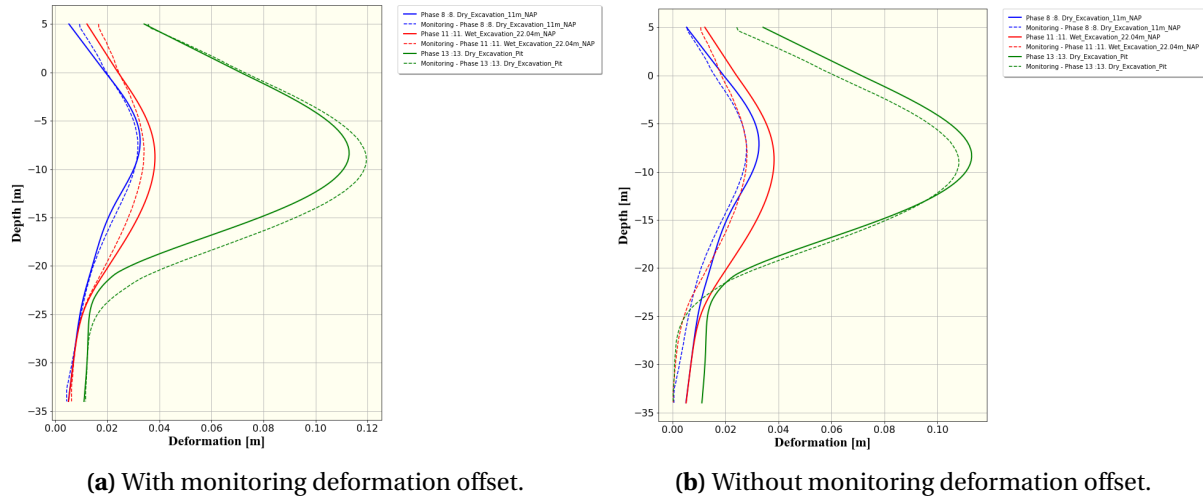
When the table in the section "Data Comparison" is loaded, the users can decide between the chosen construction phases from the drop-down menu and press the "Refresh" button to create the data. The information provided represents each wall node from the finite element program. Finally, the "Export to Excel" button allows the users to save in an excel the data given in the table for every construction phase selected.

The screenshot shows the 'Comparison' tab of a software application. It features three main panels:

- Plaxis Output:** Contains two checkboxes: 'Load data from model' (unchecked) and 'Load data from excel' (checked). Below them is a 'Load Output' button.
- Plot Comparison Menu:** Includes a 'Create Plot' button and a 'Consider Offset' checkbox (checked). Below is a table with 13 rows, each representing a construction phase. Each row has a checkbox, a phase description, and a 'Choose Date' dropdown menu. Phases 11 and 13 are selected.
- Data Comparison:** Contains a 'Decimal Places' input field (set to 3), a 'Load' button, and a 'Name the Excel' input field. Below this is a 'Deformation Units' dropdown (set to 'cm'), a 'Refresh' button, and an 'Export to Excel' button. At the bottom is a table with 24 rows of data.

N.	Depth (m)	dX_Design (cm)	dX_Mon. (cm)	Difference (cm)	Difference (%)
1	5.0	1.217	1.662	-0.445	-36.534
2	4.625	1.307	1.676	-0.369	-28.233
3	4.25	1.396	1.743	-0.347	-24.862
4	3.875	1.485	1.811	-0.325	-21.897
5	3.5	1.575	1.886	-0.311	-19.776
6	3.5	1.575	1.886	-0.311	-19.776
7	3.25	1.634	1.941	-0.307	-18.777
8	3.0	1.694	1.98	-0.286	-16.905
9	2.75	1.753	2.015	-0.262	-14.933
10	2.5	1.813	2.058	-0.245	-13.534
11	2.5	1.813	2.058	-0.245	-13.534
12	2.083	1.912	2.133	-0.221	-11.573
13	1.667	2.011	2.207	-0.196	-9.736
14	1.25	2.11	2.265	-0.155	-7.336
15	0.833	2.21	2.316	-0.106	-4.801
16	0.833	2.21	2.316	-0.106	-4.801
17	0.625	2.26	2.344	-0.084	-3.717
18	0.417	2.311	2.378	-0.067	-2.901
19	0.208	2.361	2.411	-0.05	-2.109
20	0.0	2.412	2.444	-0.032	-1.337
21	0.0	2.412	2.444	-0.032	-1.337
22	-0.125	2.444	2.464	-0.02	-0.82
23	-0.25	2.476	2.484	-0.008	-0.313
24	-0.375	2.509	2.506	0.003	0.123

Figure 3.5.1: Comparison Tab of Python Application.



**Figure 3.5.2:** Monitoring and model deformations comparison for three construction phases.

### 3.6 Sensitivity Analysis

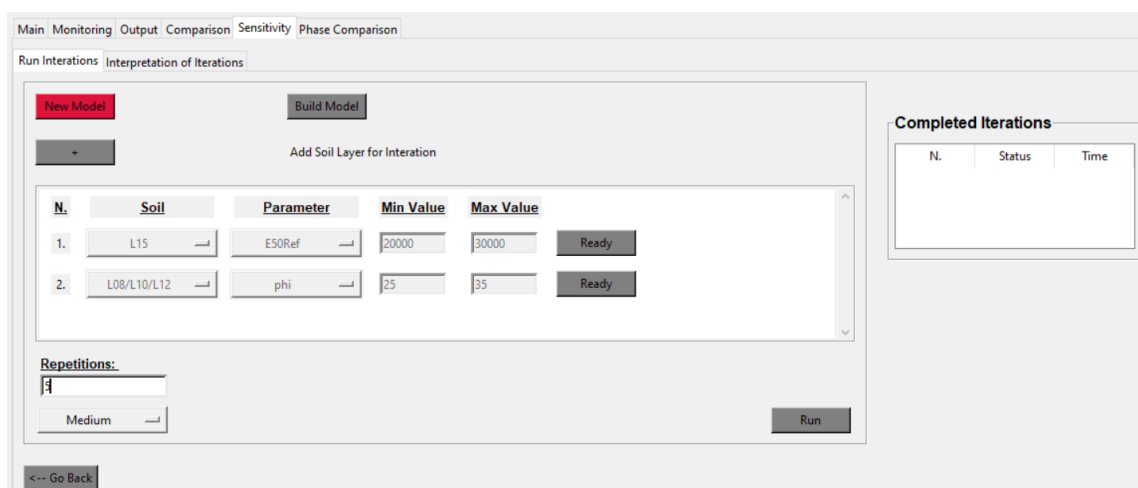
This application section allows the users to perform sensitivity analysis for the soil layer of the project under investigation. The Sensitivity Tab is divided into two sections, the "Run Iterations" section (Figure 3.6.1a) and the "Interpretation of Iterations" section (Figure 3.6.1b).

#### 3.6.1 Run Iterations

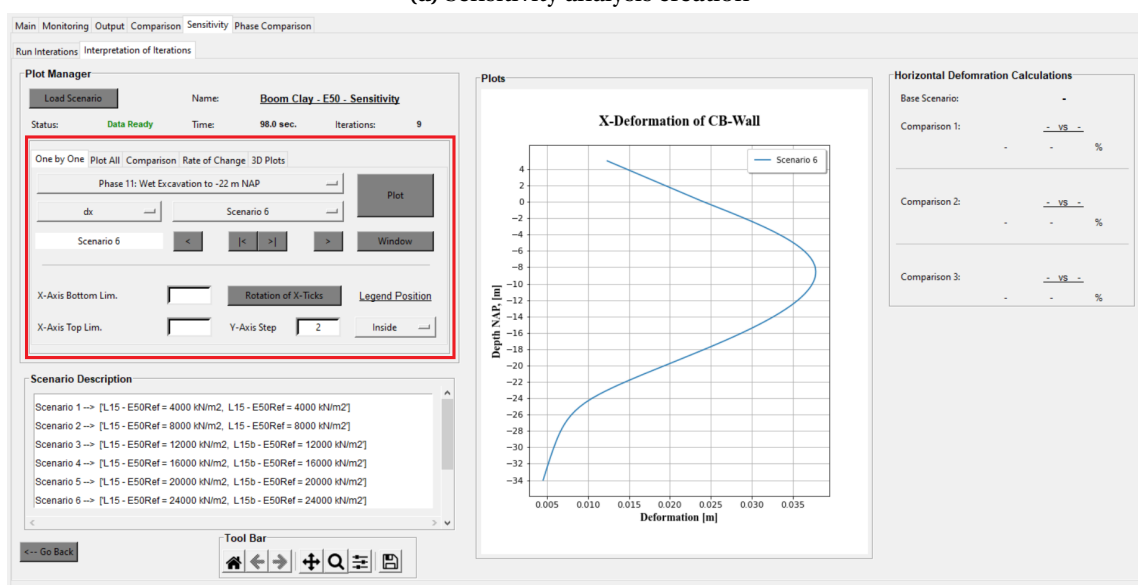
The first window is responsible for the conduction of the sensitivity analysis. Firstly, the model has to be constructed in PLAXIS input with the buttons "New Model" and "Build Model" as explained in section 3.2. Then by pressing the "+" button, an investigation line appears that requires as an input the soil layer, the soil parameter, and the minimum/maximum value this parameter has to range within. The "Ready" button must be pressed when all the information has been entered. Following the same process, the users can enter as many investigations as desired. The next step is to type the number of repetitions needed in the entry box. This number represents how many complete models will run in the PLAXIS application. The range of each parameter is divided by this number to define what value it will have in every repetition. For instance, in Figure 3.6.1a, two investigations will run simultaneously in every repetition. The investigation one changes the stiffness  $E_{50}^{ref}$  of soil layer L15 from  $20000 \text{ kN/m}^2$  to  $30000 \text{ kN/m}^2$ . Because the repetitions decided are 5, and the step derived from Equation 3.6.1 is  $2000 \text{ kN/m}^2$ , the parameter values will be  $[20000, 22000, \dots, 28000, 30000]$ . Every investigation will share the same range; therefore, in this example, layer L08 will take the following effective friction angle values  $[25, 27, \dots, 33, 35]$ . The drop-down menu can determine the mesh density.

$$Step = \frac{Max\ Value - Min\ Value}{Repetitions} \quad (3.6.1)$$

The code will create a folder named "Sensitivity Analysis," which will store the analysis. The files within are excel files called "# Parameter variation Log," whose purpose is to summarise the research performed. Additionally, it provides all the properties the soil layers had in each repetition and the construction phases used. The structure of this file can be found in Appendix H. Furthermore, "Run



(a) Sensitivity analysis creation



(b) Sensitivity analysis interpretation

**Figure 3.6.1:** Sensitivity Tab of Python Application

i" excel files are created to store the library of Figure 3.4.2 for each iteration. The users are advised to organize these files in a different spot because once a new sensitivity analysis is initiated, the "Sensitivity Analysis" Folder is cleared.

Lastly, the "Completed Iterations" table will show the time needed for each iteration completed in the PLAXIS program. To conclude, the code automatically creates scenarios, runs them, and saves them in a custom library. This tool improves efficiency and provides users with various investigation combinations. In the next paragraph, the tool for the interpretation of this analysis will be discussed.

### 3.6.2 Interpretation of Iterations

This section is responsible for interpreting the sensitivity analysis and providing many tools for the users to use. In Figure 3.6.1b, four sections are disguised, the "Plot Manager," the "Scenario Description," the "Plots," and the right side where information from each tool is printed. To begin with,

the parts that remain constant for all the tools are the section "Plots," where the plots from all the tools are depicted, and the section " Scenario Description," which describes what each scenario represents. For instance, in Figure 3.6.1b, the secant stiffness  $E_{50}^{ref}$  of the soil layers L15 and L15b is changing with a step of  $4000 \text{ kN/m}^2$  and each iteration is matched with a scenario.

The first step the users have to do is to load the sensitivity investigation by pressing the button "Load Scenario." A file explorer browser will open that can be used to navigate to the folder location the users saved the analysis. This loading process can take several minutes depending on the size of the sensitivity analysis,  $\approx 11$  seconds for each iteration. Once the loading process is complete, the name, status, iteration numbers, and time needed will be printed in the application. The code uses a similar structure for the sensitivity library as the one used previously in the output library (Figure 3.4.2) but with one more dimension. The sensitivity analysis library now contains four layers and is presented in Figure 3.6.2.

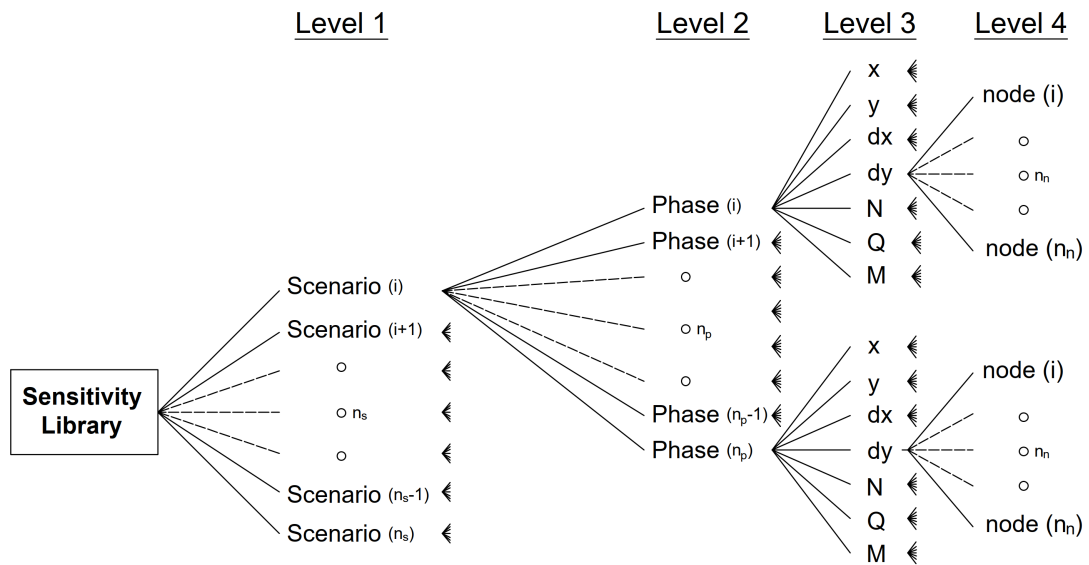


Figure 3.6.2: Sensitivity Library - Tree List

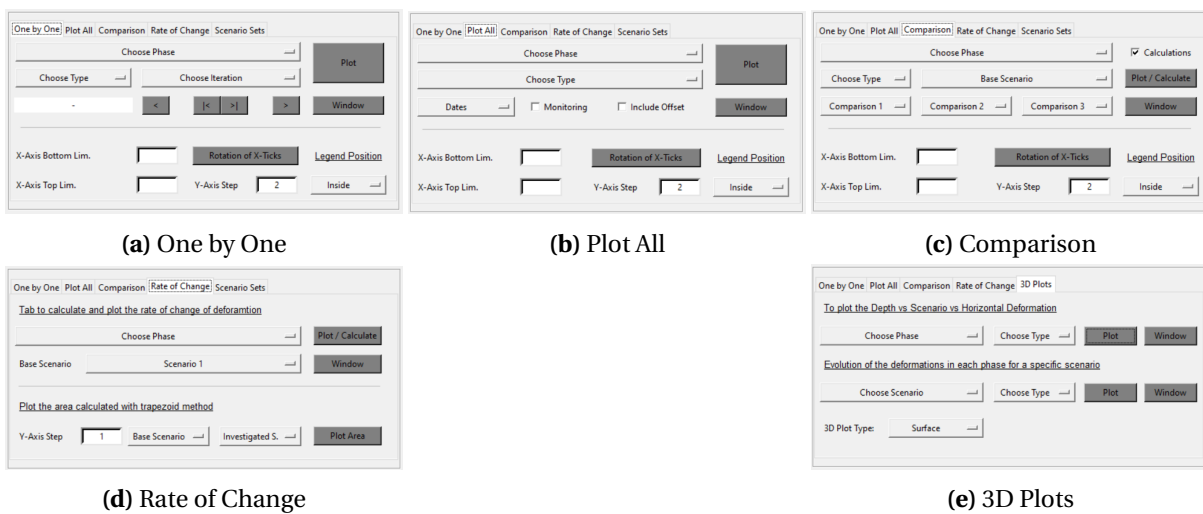


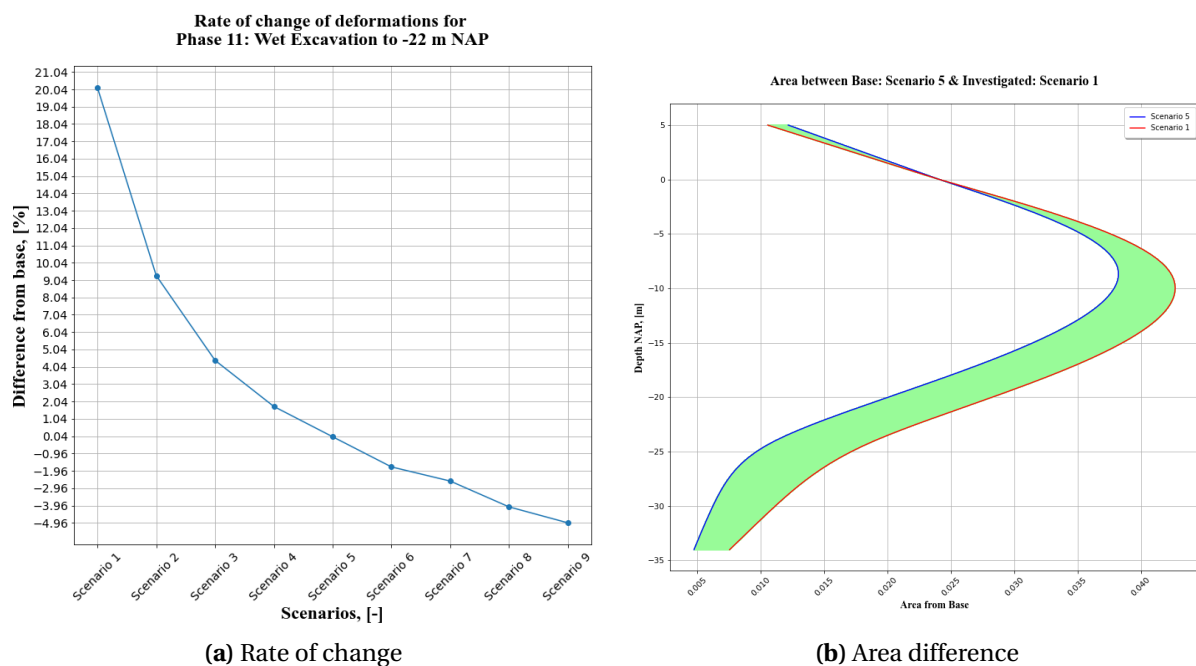
Figure 3.6.3: Interpretation of Iterations Tools

To interpret the analysis, the users can use the five different tools hosted in the red rectangular of

Figure 3.6.1b. These five tools are presented in Figure 3.6.3 and will be discussed briefly. Starting with the "One by One" tool (Figure 3.6.3a) has the purpose of plotting the results of each scenario separately. The users can choose the construction phase, the type of information (deformations, moments, forces), and the scenario via the corresponding drop-down menus. The "Plot" button can plot these options, and the figure will appear in the "Plots" section. Additionally, the users can open the plot in a separate pop-up window by pressing the button "Window." This option is helpful for more complicated cases, and the toolbar allows for the printing of the plots. Additionally, the "<, |<, >|" buttons allow the users to navigate between scenarios efficiently. Lastly, the bottom section provides options for axis and legend modifications. Some of the functions discussed are common for most of the five tools.

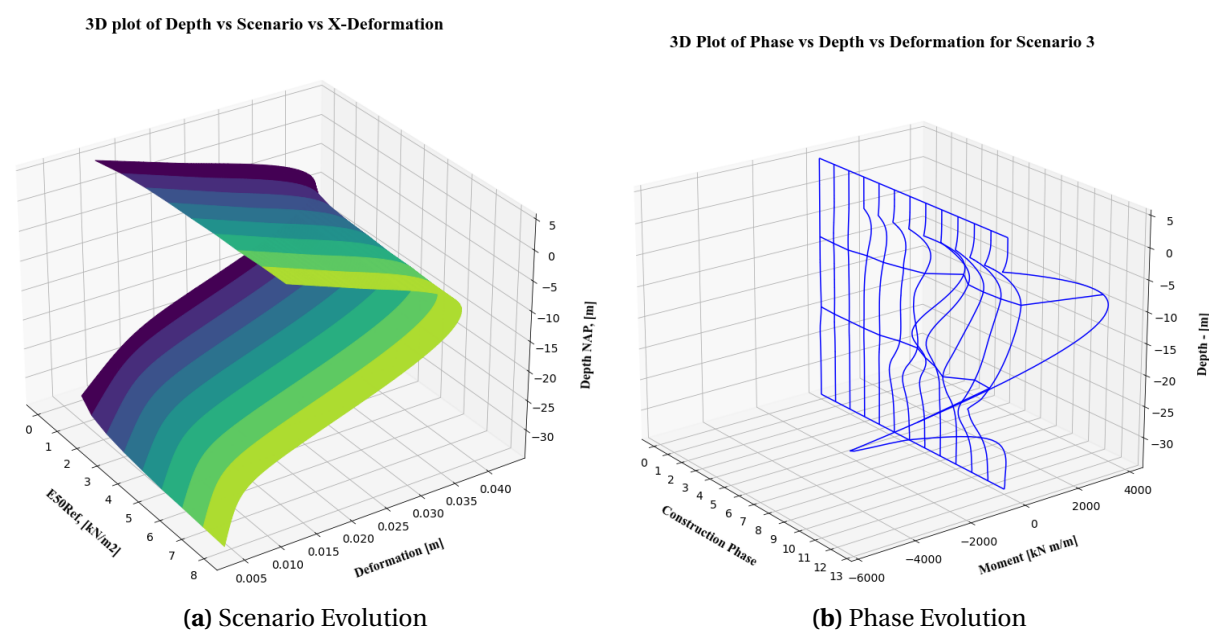
The following tool is the "Plot all" (Figure 3.6.3b) that gives the option to the users to plot every scenario of the sensitivity analysis in a single plot. The input is the construction phase and information type determined by the corresponding drop-down menus. An extra feature here is the option to include the monitoring deformations if applicable. Hence, the sensitivity analysis can relate to actual deformations from the field. The "Comparison" tool (Figure 3.6.3c) allows the users to compare scenarios. The idea is that the designer determines the base scenario used in the project's design and compares it with other fictional scenarios of the sensitivity analysis. If the "Calculations" checkbox is selected, then information regarding the change in deformations between the base and investigated scenarios is given on the right side of the application.

The "Rate of Change" (Figure 3.6.3d) is a unique tool that provides information for the entirety of the sensitivity analysis. The first function requires the construction phase and the base scenario. All the scenarios are compared to the base scenario by the percentage of deformation change. An example result is given in Figure 3.6.4a. The deformation difference between scenarios is calculated using the Riemann method as explained in Paragraph 4.3.1. The creation of the particular plot can take several minutes depending on the size of the sensitivity analysis due to several calculations in the background. Additional information regarding the rate of change plot is given on the right side of the application. The area change with the Riemann method is visualized in the second function of the tool, where the users can choose to plot the area calculated between two scenarios (Figure 3.6.4b).



**Figure 3.6.4:** Resulting plots from the "Rate of Change" tool of the sensitivity analysis tab of the Python Application.

The "3D Plots" (Figure 3.6.3e) is the last tool that allows for the creation of two types of 3D - Plots to summarise the data in an efficient and confined way. The first type plots the Scenarios versus the data type (Deformations, Forces, Moments) versus the wall height for a specific construction phase. Therefore, it represents the evolution of the phase for the different scenarios. For instance, Figure 3.6.5a shows the moments evolution for the different scenarios along the height of the wall for Phase 11. On the other hand, the second type of 3D plots provides the evolution of the scenario for all the construction phases. For example, Figure 3.6.5b shows the evolution of the moments throughout all the construction phases for Scenario 3. Finally, the users can choose between two 3D figure styles (Surface, Wireframe) from the drop-down menu.



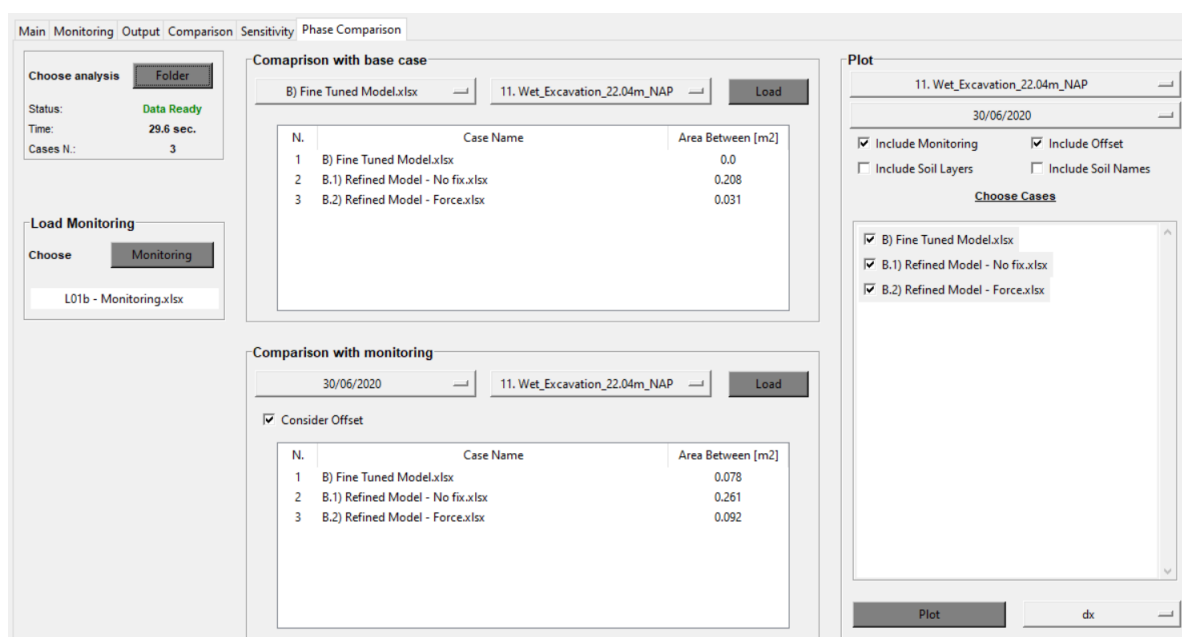
**Figure 3.6.5:** 3D plots from the "3D - Plot" tool of the sensitivity analysis tab of the Python Application.

### 3.7 Phase Investigation

The last Tab of the application is the "Phase Comparison" section (Figure 3.7.1) which allows the users to compare different models per construction phase. To use this tool, the users must put in a folder the models loaded with the output tool or scenarios from the sensitivity analysis. Then the button "Folder" will allow the users to browse to the folder in which the models are saved and load them. When the loading process is complete, information about the status, time, and number of models will appear in the application. If the users desire to compare the monitoring deformations with the model deformations, they have to load also the monitoring excel file using the "Monitoring" button.

There are three functions in this tool that produce results. The first is the "Comparison with the base case," where a base model and the construction phase are chosen via drop-down menus. Then by pressing "Load," the area difference will be calculated for all models from the base model in  $m^2$  units using the Riemann method. The "Comparison with monitoring section" perform the same operation but compares the area difference of every model from the monitoring. The lowest number would indicate a better match with the monitoring deformations; for this section to work along with the construction phase, the users must decide on the monitoring date.





**Figure 3.7.1:** Phase Comparison Tab of Python Application.

Lastly, the different models can be plotted and compared per construction phases along with the monitoring deformations. All the loaded models will appear as checkboxes in the table, and the users can choose the desirable combinations. Additionally, the users can decide between monitoring deformations, data offset, outlines of the layers, and soil layer names. Finally, the type of modeled data can be determined (Deformations, Moments, Forces). To produce the plots in a pop-up window, the button "Plot" need to be clicked.

### 3.8 Purpose and Limitations

The Python Application has been created to facilitate the needs of the present thesis. It allowed the creation and interpretation of many models to determine the correct way of modeling the retaining wall. Ultimately, it aims to be used alongside the conventional design to increase confidence in the original design by modeling the actual conditions as the monitoring data are created. Additionally, its use could be important in site engineering, where the actual conditions of the project have a significant role. The site engineers will have at their disposal a tool that will allow them to conduct efficient research on the true behavior and the actual limits of the retaining structure. Hence, they will be able to solve the problems that arise comprehensively. Furthermore, comparing the original design with the refined design produced by the application during and after the completion of the project creates knowledge that can be used in future projects. Finally, the elaborated comparisons and figures of the application allow for the creation of well-rounded and explanatory reports.

There are limitations in the creation of the present application. Firstly, it has been built in parts depending on the needs of the research questions. Therefore, it didn't follow object-oriented programming. Additionally, a more efficient way of storing data could be created to speed up the code and reduce memory issues. Lastly, the GUI used is relatively basic and old fashioned. Ultimately it can be replaced by more modern versions.

# Model Application and Investigation

## 4.1 Boom Clay - Constitutive Model Investigation

In the current retaining project and others in the general area where the Boom Clay layer is present, there is uncertainty on how it should be modeled. Such uncertainty leads to over-designed or high-risk projects. Therefore, the investigation of its behavior is a priority.

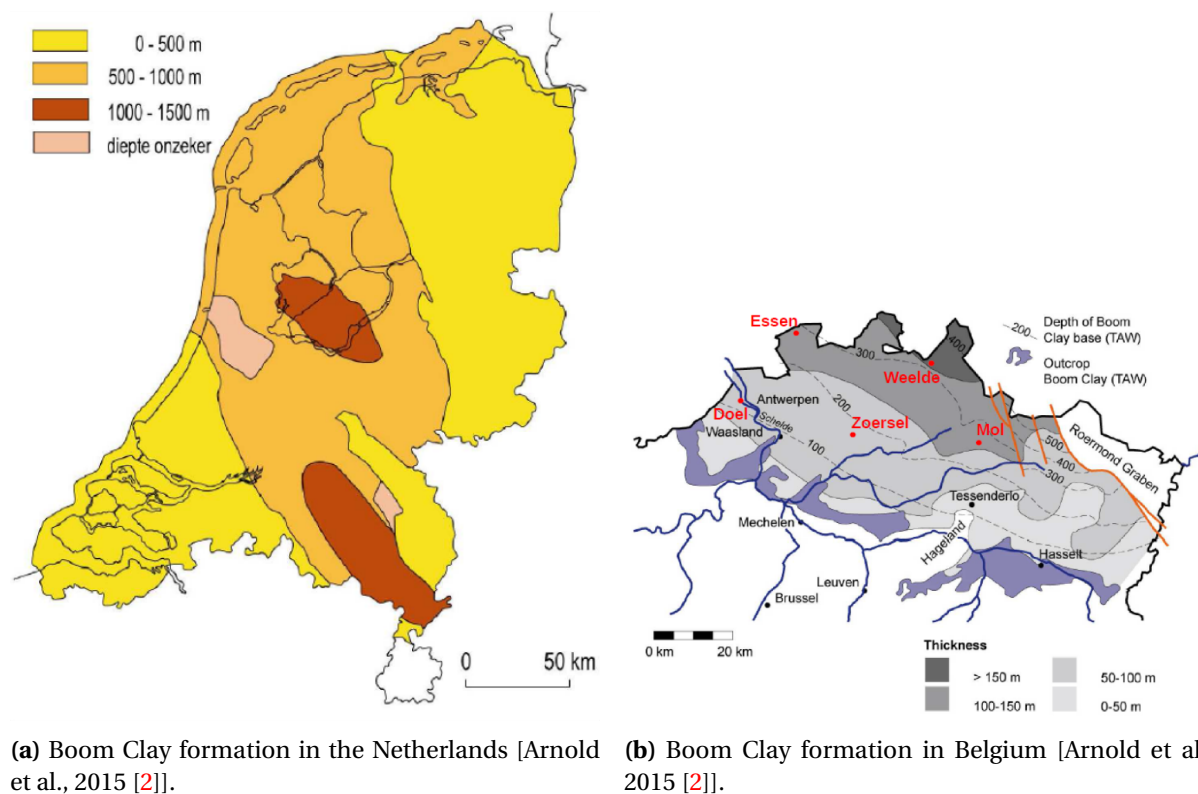
For the Boom Clay, an appropriate constitutive soil model is considered one that can capture the mobilized shear strength and the material stiffness on the corresponding stress level. Specialized soil models at an academic level have been created to model it accurately. However, they are highly complex and require several model inputs derived from sophisticated or costly lab tests.

Because this thesis is based on an actual project, it will focus on the engineering community's well-known and widely accepted constitutive soil models. Models that are applicable in practice because they provide a balance between accuracy and usage difficulty. Specifically, the Hardening Soil (HS) model (Schanz, 1999 [30]), the Hardening Soil Small Strain (HS-small) model (Benz and Vermeer, 2007 [7]), and the Mohr-Coulomb (MC) model are going to be examined. The undrained conditions of the Boom Clay are relevant to this project. Therefore, the effect of the quasi-undrained approach used in the project will also be discussed. For the rest of the models, the Undrained A approach in PLAXIS will be used to simulate the undrained conditions.

The constitutive models are going to be researched through soil tests and literature. Then the most appropriate will be implemented in the PLAXIS models for their behavior to be compared with the monitoring representing reality. Therefore, for the results to be comparable to reality, the mean (most probable) soil properties, calculated in Section 2.2, will be considered for all the layers. The models will be the same except for the modeling method applied to the Boom Clay layer.

### 4.1.1 Boom Clay Location

The Boom Clay is a marine deposit of the Tertiary Rupelian age of the Oligocene epoch ([34]). This layer exists in the Netherlands and the northeast of Belgium, as shown in Figure 4.1.1a and 4.1.1b, respectively. This material is generally considered stiff and lightly over-consolidated (OC) clay. The OC values are due to secondary compression and diagenetic processes and not due to erosion of the overlying strata, according to [17]. Extensive research on the properties of Boom Clay has been conducted by Arnold et al., 2015 [2].



**Figure 4.1.1:** Boom Clay locations in the Netherlands (a) and in Belgium (b).

#### 4.1.2 Lab Test Investigation

The current project is accommodated by many lab tests conducted on Boom Clay samples from boreholes. These boreholes are summarized in Appendix F. The initial plan was the comparison of the lab tests with the lab test facility of the PLAXIS 2D 2022 finite element program under the different constitutive models. The objective was to determine what constitutive soil model better represents the Boom Clay behavior for the retaining structure design. However, high variation of stiffness and unexpected values of rate of stress dependency  $m$  are witnessed. The values of stiffnesses and  $m$  are summarized in Table 4.1.1, and the calculation methods are discussed in Appendix F.

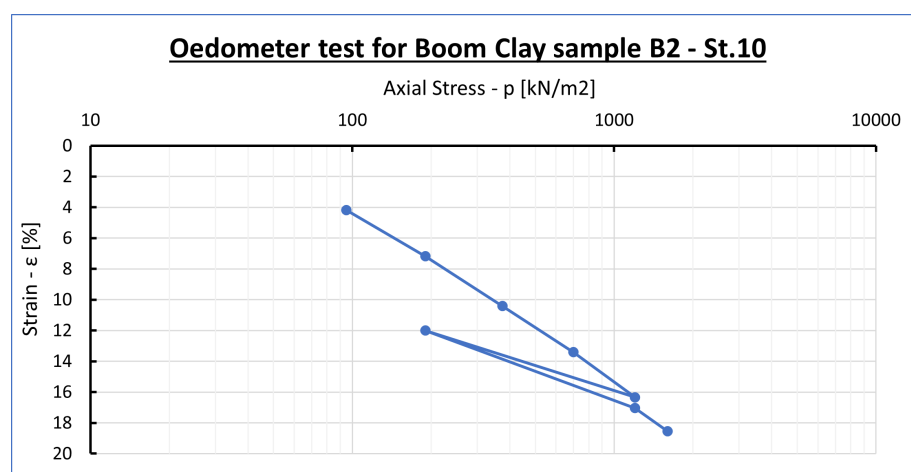
Four soil samples have been chosen where both an undrained triaxial test and an oedometer test have been performed. Each triaxial test has executed under three different confining stresses. Using equation 2.1.44, the  $m$  can be derived for each stress combination of each triaxial test. According to the PLAXIS manual Brinkgreve et al., 2011 [10] and the design, the expected value is 0.8 – 1.0. However, as summarized in Table 4.1.1, not all the  $m$  values agree with the expected range. Eventually, the problem was attributed to disturbed samples. Such a phenomenon is common when it comes to Boom Clay samples due to the swelling effect.

Additionally, the oedometer test of the Boom Clay sample provides very low values of oedometer stiffness  $E_{oed}$ . The results depict a material that is not pre-consolidated, which is not true for this Boom Clay. For instance, Figure 4.1.2 shows axial stress  $p$  versus the vertical strain  $\epsilon$  plot derived by the corresponding oedometer test for the Boom Clay sample B2 – St.10. The plot for the rest samples are given in Appendix F. The pre-consolidation point does not exist; hence, the sample probably has not kept the in-situ conditions.

To conclude, the lab tests for the Boom Clay of the New Terneuzen Lock are not reliable in deriving the soil properties.

**Table 4.1.1:** Summary of the stiffness properties derived by the lab tests on four boom clay samples.

Samples	Param.	Units	Step 1	Step 2	Step 3	m	m
B2 - St.10	$E_{50}^{ref}$	$kN/m^2$	24869	14356	9500	$m_{1-2}$	0.868
	$E_{oed}^{ref}$	$kN/m^2$		3170		$m_{1-3}$	0.707
	$E_{ur}^{ref}$	$kN/m^2$		21660		$m_{2-3}$	0.117
B2 - St.12	$E_{50}^{ref}$	$kN/m^2$	23953	11855	12311	$m_{1-2}$	0.652
	$E_{oed}^{ref}$	$kN/m^2$		3900		$m_{1-3}$	1.008
	$E_{ur}^{ref}$	$kN/m^2$		17600		$m_{2-3}$	1.422
B2 - St.17	$E_{50}^{ref}$	$kN/m^2$	27616	12757	8801	$m_{1-2}$	0.082
	$E_{oed}^{ref}$	$kN/m^2$		6300		$m_{1-3}$	0.076
	$E_{ur}^{ref}$	$kN/m^2$		27300		$m_{2-3}$	0.064
B2 - St.19	$E_{50}^{ref}$	$kN/m^2$	27212	-	13539	$m_{1-2}$	-
	$E_{oed}^{ref}$	$kN/m^2$		3900		$m_{1-3}$	0.681
	$E_{ur}^{ref}$	$kN/m^2$		95300		$m_{2-3}$	-

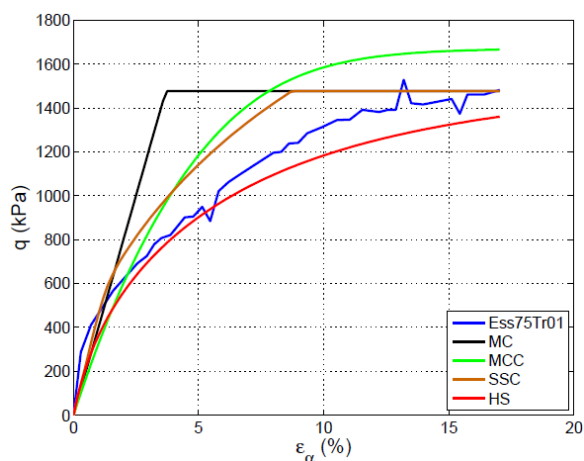
**Figure 4.1.2:** Axial stress  $p$  vs axial strain  $\epsilon$  plot for the oedometer test on Boom Clay sample B2 - St.10.

### 4.1.3 Literature Investigation

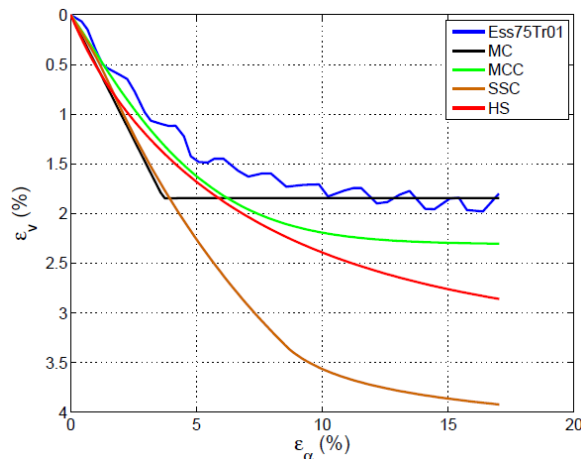
Due to inconclusive results from lab tests on the Boom Clay samples from the New Terneuzen Lock, a literature investigation has been conducted regarding which constitutive models describe its behavior best. Milioritsas, 2014 [25] has conducted similar research examining four constitutive soil models on Boom Clay samples using the lab test facility of the PLAXIS 2D 2011 finite element program (Plaxis, 2011) Brinkgreve et al., 2011 [10]. The constitutive models that have been investigated are the Linear Elastic Perfectly Plastic Mohr-Coulomb (LEPP-MC) model, the Modified Cam-Clay (MCC) model, the Soft Soil-Creep (SS-C) model, and the Hardening Soil (HS) model. The numerical simulation from Milioritsas, 2014 [25] has been performed on three conventional consolidated-drained, strain-controlled triaxial tests on intact Boom Clay cores from the Essen site in Belgium by Deng et al., 2011 [13]. The over-consolidation degree for the Boom Clay samples Ess75Tr01 and Ess75Tr03

was 1.0 and 4.4, respectively.

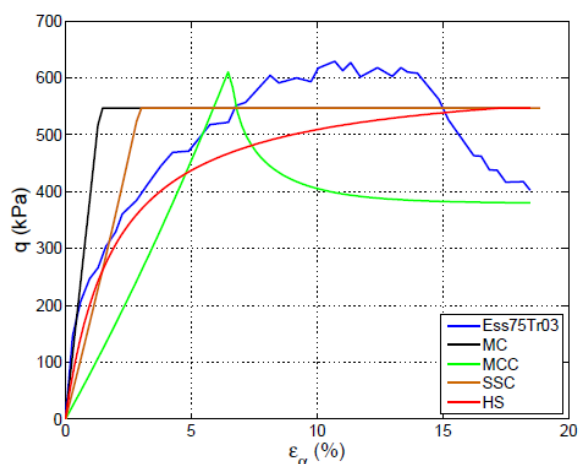
The findings are summarized in Figure 4.1.3 for the triaxial tests and Figure 4.1.4 for the oedometer tests. Figure 4.1.3a and Figure 4.1.3b refer to sample Ess75Tr01, and Figure 4.1.3c and Figure 4.1.3d refer to the sample Ess75Tr03. In each case, the four constitutive models are compared with the Lab Tests (blue line) derived by Deng et al., 2011 [13]. Similarly, for the oedometer test, Figure 4.1.4a, Figure 4.1.4b, and Figure 4.1.4c compare the lab data (blue line) using the constitutive models MCC, SSC, and HS, respectively.



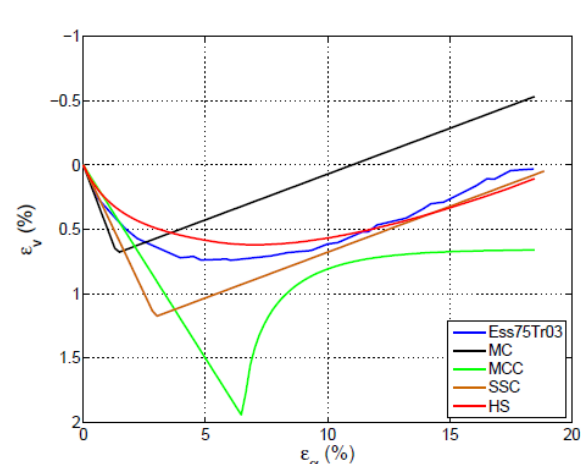
(a) Deviatoric stress  $q$  versus axial strain  $\epsilon_a$  for the numerical simulations of Ess75Tr01 test with four soil models.



(b) Volumetric strains  $\epsilon_v$  versus axial strains  $\epsilon_a$  for the numerical simulations of the Ess75Tr01 test with four soil models.



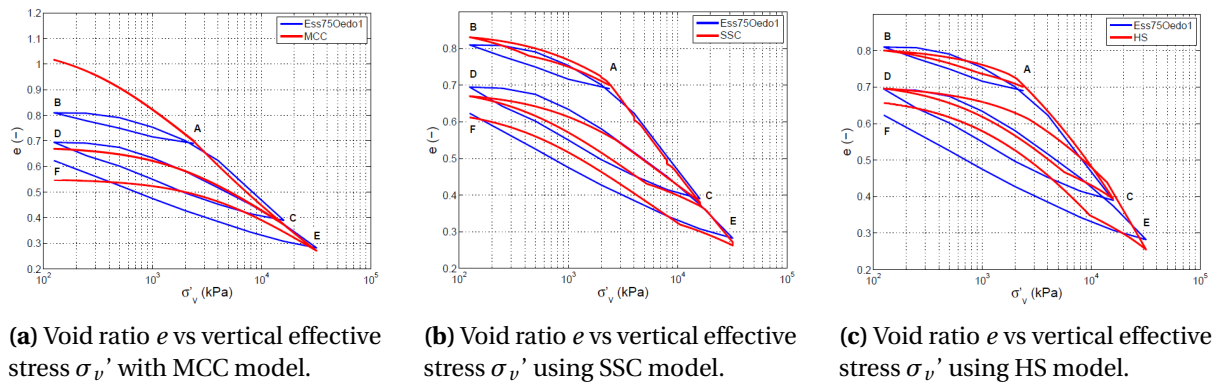
(c) Deviatoric stress  $q$  versus axial strain  $\epsilon_a$  for the numerical simulations of Ess75Tr03 test with four soil models.



(d) Volumetric strains  $\epsilon_v$  versus axial strains  $\epsilon_a$  for the numerical simulations of the Ess75Tr03 test with four soil models.

**Figure 4.1.3:** Investigation of Milioritsas, 2014 [25] to the triaxial test of Deng et al., 2011 [13] regarding the best constitutive model to simulate the Boom Clay behavior.

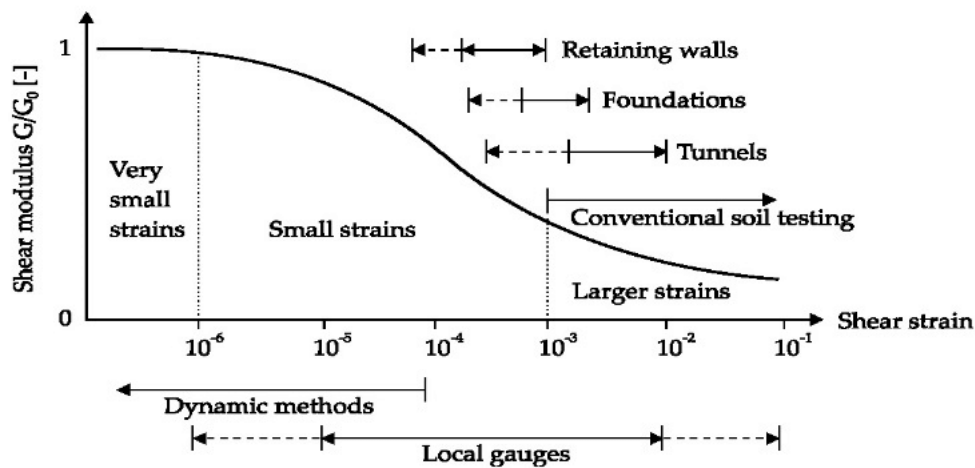
Milioritsas, 2014 [25] concluded that the LEPP-MC model, despite its simplicity and the few input parameters, provides reasonable results, but it could not capture the un-/reloading paths. Another downfall is that it does not hold any memory of the pre-consolidation of the material. Moreover, it is not able to reproduce the strain hardening. The MCC model produces good results for the NC sample, but it does not capture the OC clay's behavior well in the  $\epsilon_a - q$  space. Also, it holds a memory of the pre-consolidation of the soil and has adequate prediction in the oedometer test. The SSC model appeared to underperform in the deviator stress  $q$  versus axial strain  $\epsilon_a$  comparison plots of



**Figure 4.1.4:** Investigation of Milioritsas, 2014 [25] to the oedometer test of Deng et al., 2011 [13] regarding the best constitutive model to simulate the Boom Clay behavior.

the triaxial test but had the best fit for the behavior of the soil in 1-dimensional loading. Finally, the HS model performed the best overall. It captured the soil response for NC and OC conditions fairly well concerning the mobilized shear strength, the change in stiffness, and the non-linearity of Boom Clay. The unloading and reloading cycles in the 1-D compression test are satisfying.

The Hardening Soil model, according to Schanz, 1999 [30], is indeed an appropriate constitutive soil model to simulate the Boom Clay. It captures the plastic compaction in primary loading compression and distinguishes between primary loading and unloading/reloading using compaction (cap) hardening characteristics. Additionally, it considers the decreasing stiffness (increasing plastic shear strain) in deviatoric loading using frictions (or Shear) hardening characteristics. In this project, adding small strains to the Hardening Soil model is useful. Figure 4.1.5 (Atkinson and Salfors, 1991 [3]) represents in the vertical axis the secant shear modulus divided by the small-strain shear modulus  $G_0$ , and in the horizontal axis, the shear strain amplitude on a logarithmic scale. Retaining walls like the present are projects described by small strains.

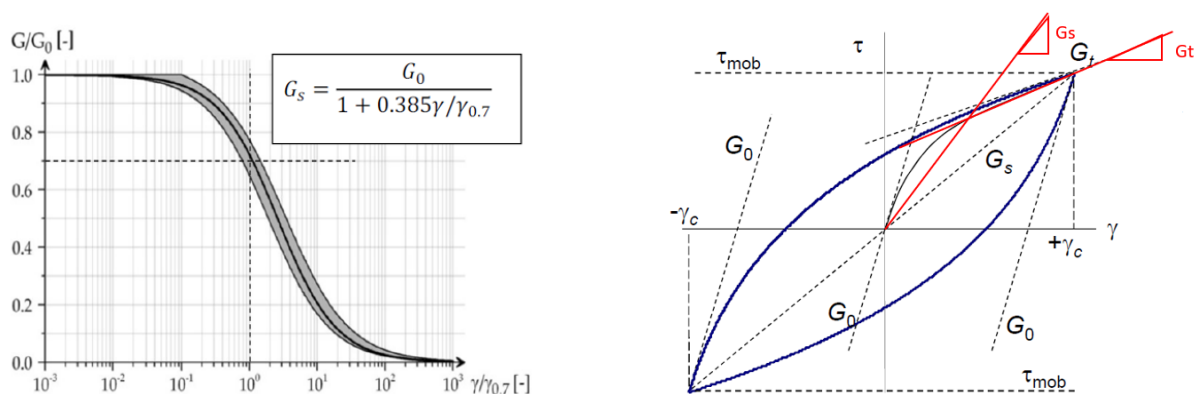


**Figure 4.1.5:** Strain level depending on the structure type (Atkinson and Salfors, 1991 [3]).

Soils tend to be very stiff at very small strains, and the stiffness decreases with the strain level. This can be visualized in a Modulus Reduction Curve by Hardin and Drnevich, 1972 [16] (Figure 4.1.6a), where the secant shear modulus  $G_s$  (or relative secant shear modulus  $G_s/G_0$ ) is plotted as a function of the shear strain  $\gamma$  (or relative shear strain  $\gamma/\gamma_{0.7}$ ) on a log-scale. A key element in the HS-small model with its strain-dependent stiffness formulation is that upon full strain reversal, the stiffness restarts at the small-strain stiffness  $G_0$ . Figure 4.1.6b shows the shear stress  $\tau$  versus the shear strain

$\gamma$  according to the HS-small model. Starting in origin, the initial inclination of the stress-strain curve is equal to the small-strain shear modulus  $G_0$ , but with the increase of stress and strain, the tangential stiffness  $G_t$  decreases. When  $\tau_{mob}$  is reached, which is considered well below failure, the load is reversed, and the initial inclination becomes  $G_0$  again, gradually decreasing until the next load reversal. Therefore, every time the shear direction is reversed, it starts from a small strain stiffness.

The actual project and the construction phases considered in the design model contained unloading and reloading conditions. The monitoring deformations describing the reality include this effect due to changes in load. Such changes are aquifer heads due to pumping or tidal fluctuations, construction phases like submersion of the excavation pit or excavation, and external loads behind the wall. Therefore, the HS-small soil constitutive model is considered the most appropriate to simulate the behavior of the Boom Clay and is expected to produce fewer deformations than the other models.



(a) Modulus reduction curve (Hardin and Drnevich, 1972 [16]).

(b) Stiffness parameters in cyclic shear test (PLAXIS Manual, 2022).

Figure 4.1.6: Small Strains

#### 4.1.4 Constitutive model application and Comparison

An investigation of Boom Clay's constitutive models is conducted to confirm the theoretical conclusions discussed in the previous paragraph. The models that will be discussed in this section follow three conventions. Firstly, all the models will use the mean soil properties and the actual conditions derived in Chapter 2. Additionally, all the soil layers except the Boom Clay will constantly follow the HS-small constitutive model, a convention that has been made for the results to be comparable with the actual design of the project. Then they can be comparable with the monitoring data representing reality and with each other. Secondly, only Boom Clay's constitutive soil model, properties and drainage conditions will be altered each time to investigate the effects and determine the most suitable solution. This decision will be taken based on the Comparison with the monitoring deformations. The third convention is that the deformations of the combi wall at the anchor level will have pre-described movement in PLAXIS based on the inclinometer deformations.

The constitutive soil models investigated for the Boom Clay are the HS-small, the HS, and the Mohr-Coulomb. In the first two models, the stiffness is stress dependent and is described by three different values, the secant stiffness  $E_{50}$ , the oedometer stiffness  $E_{oed}$ , and the un-/reloading stiffness  $E_{ur}$ . On the other hand, the Mohr-Coulomb model uses only one value for the stiffness. Therefore, the model has been used two times, one considering the stiffness  $E'$  equal to the secant stiffness and one considering the stiffness  $E'$  equal to the un-/reloading stiffness. When the Mohr-Coulomb model is chosen, it is common practice to use an average value between the two stiffnesses or the one predominant in the specific construction phase. Therefore, by running the model twice, the lower and

upper end of the spectrum is covered, and any potential combination of stiffnesses is in between those values.

The drainage conditions for the Boom Clay were considered for Phase 9 and after to be undrained. For the models that used the HS constitute soil models, the Undrained A approach has been used. According to the PLAXIS manual, Brinkgreve et al., 2011 [10] "allows PLAXIS to automatically add the stiffness of water to the stiffness matrix to distinguish between effective stresses and (excess) pore pressures (= effective stress analysis)". However, the Mohr-Coulomb constitutive soil models have been analyzed with both the Quasi and Undrained A methods. The Quasi approach has been used in the project's actual design alongside the Mohr-Coulomb constitutive model. It is implemented by setting the drainage conditions of the material to drained and doubling the cohesion. Therefore, six variations of the Boom Clay modeling will be tested, with different combinations of constitutive models, stiffnesses and drainage conditions. Their properties are summarized in Table 4.1.2.

**Table 4.1.2:** Summary of the input soil parameters for the different constitutive models of the Boom Clay.

Model	Drai.	$\phi'$	$c'$	$\nu$	$\nu_{ur}$	$E'$	$E_{50}^{ref}$	$E_{oed}^{ref}$	$E_{ur}^{ref}$	$G_0$	$\gamma_{07}$
Unit	-	$^\circ$	$\frac{kN}{m^2}$	-	-	$\frac{kN}{m^2}$	$\frac{kN}{m^2}$	$\frac{kN}{m^2}$	$\frac{kN}{m^2}$	$\frac{kN}{m^2}$	-
$MC_{(E=E_{50})}$	Und.A	24.4	18.5	0.3	-	23200	-	-	-	-	-
$MC_{(E=E_{ur})}$	Und.A	24.4	18.5	0.3	-	46400	-	-	-	-	-
$MC_{(E=E_{50})}$	Quasi	24.4	37.1	0.3	-	23200	-	-	-	-	-
$MC_{(E=E_{ur})}$	Quasi	24.4	37.1	0.3	-	46400	-	-	-	-	-
$HS_{(E=E_{50})}$	Und.A	24.4	18.5	-	0.3	-	23200	23200	46400	-	-
$HSS_{(E=E_{50})}$	Und.A	24.4	18.5	-	0.3	-	23200	23200	46400	80897	6.5E-4

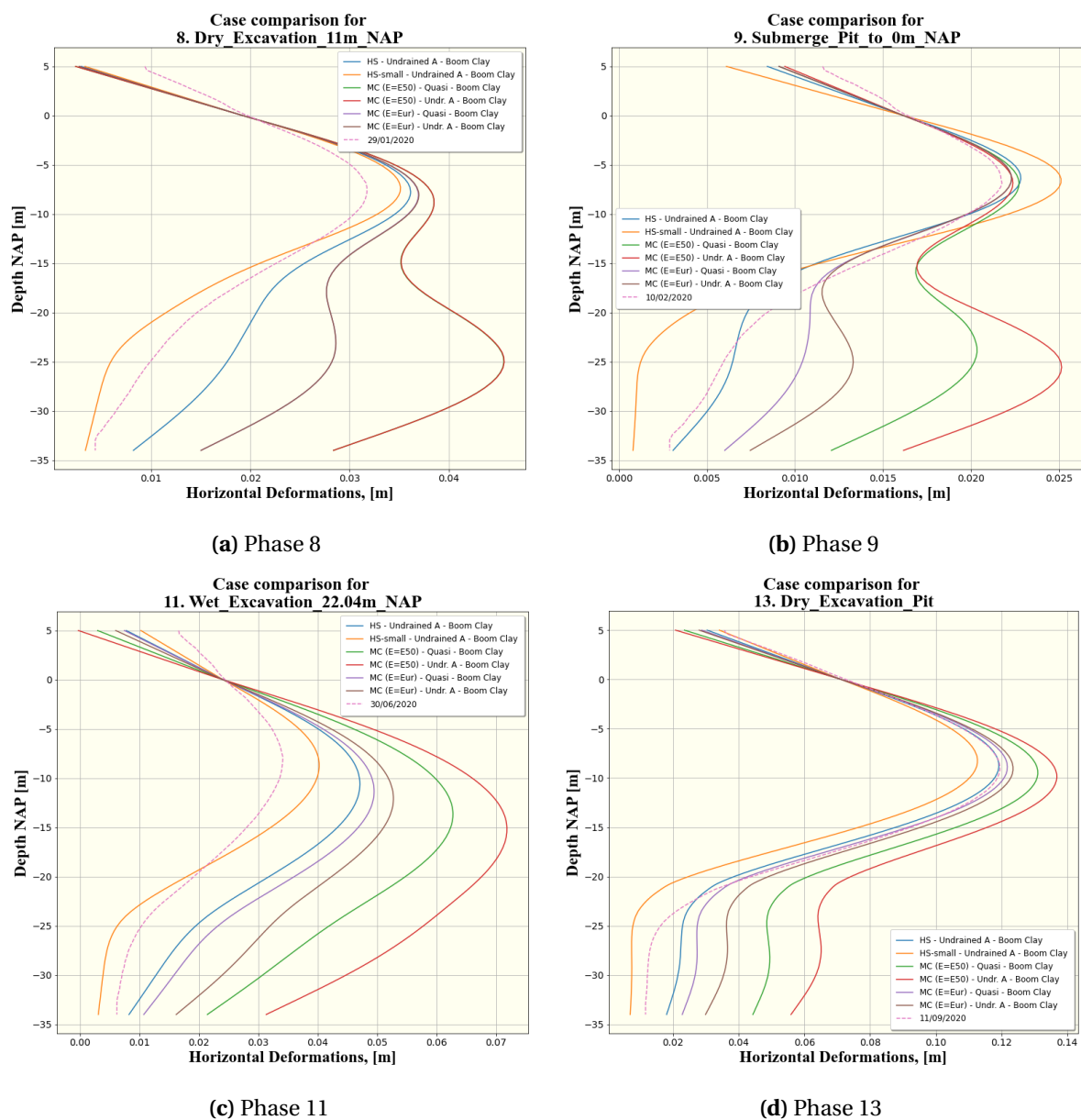
\*Data for undrained Boom Clay. When it is drained for the cohesion is quasi approach is halved.

The Boom Clay layer spans from – 21.5 m NAP to – 37.6 m NAP at cross-section L01b. The investigation has been conducted using the Python application of Chapter 3 and the finite element program PLAXIS.

Figure 4.1.7 depicts the investigation of the Boom Clay constitutive models for four different construction phases that are also represented by inclinometer measurements. The inclinometer measurements each time are depicted with a dashed line. The Hardening Soil models generally have superior accuracy than the Mohr-Coulomb models. The MC model over-predicts the deformations, especially those using the  $E' = E_{50}$  as stiffness. Starting with the difference between Undrained A - Mohr-Coulomb and Quasi-Mohr-Coulomb, it can be noticed that the latter produces a stiffer behavior for the Boom Clay than the former for both stiffness variations. In Figure 4.1.7a, the deformations of the Mohr-Coulomb models match because up to that point, the Boom Clay is considered drained. However, all Mohr-Coulomb methods produce less accurate predictions than the HS models.

On most occasions, the HS-small (orange line) is closer to the monitoring deformations except for the unloading Phase 9, where the HS model (blue line) gives better results. Phase 11 is the most crucial phase for the Boom Clay since it is the only soil layer retaining the wall, and the UWC does not exist yet. So the stiffness and strength of the Boom Clay are dominant for the wall deformations. At that phase, the HS-small model predicts significantly better deformations than the other models. Using the Python Application described in Chapter 3 and the method of Riemann Polygons described in Paragraph 4.3.1, the difference between the models from the monitoring is quantified (Table 4.1.3).





**Figure 4.1.7:** Comparison of constitutive soil models for the Boom Clay.

**Table 4.1.3:** Area difference in  $m^2$ , calculated using Riemann sums, of the models from the corresponding monitoring data for five phases.

Phase	Monit. Date	HS	HS-small	MC-(E <sub>50</sub> )	MC-(E <sub>50</sub> )	MC-(E <sub>UR</sub> )	MC-(E <sub>UR</sub> )
		Undr. A $m^2$	Undr. A $m^2$	Quasi $m^2$	Undr. A $m^2$	Quasi $m^2$	Undr. A $m^2$
Phase 8	29-01-2020	0.179	0.097	0.651	0.651	0.353	0.354
Phase 9	10-02-2020	0.042	0.117	0.234	0.296	0.076	0.111
Phase 10	08-05-2020	0.135	0.087	0.459	0.734	0.192	0.337
Phase 11	30-06-2020	0.349	0.139	0.888	1.220	0.441	0.611
Phase 13	11-09-2020	0.152	0.315	0.679	1.012	0.195	0.340

### 4.1.5 Summary and Discussion

To conclude, the Hardening Small Strain soil constitutive model is chosen to represent the Boom Clay layer because it produces a better prediction of the deformations of the wall. As discussed in Paragraph 2.1.4 for the rest of the layers, several methods exist to determine the small strain parameters  $G_0$  and  $\gamma_{07}$  of the HS-small model. The Hs-small model in Figure 4.1.7 determines the small strain parameters using the average of the two methods. Appendix G describes the investigation of the effect the small strain parameter determination methods have on the deformations of the retaining wall. The Mohr-Coulomb model constantly over-predicts the deformations, but the decision made for the design to use as stiffness  $E'$  the un-/reloading stiffness  $E_{ur}$  and the Quasi approach were assumptions towards the right direction.

## 4.2 Fine Tuned Model

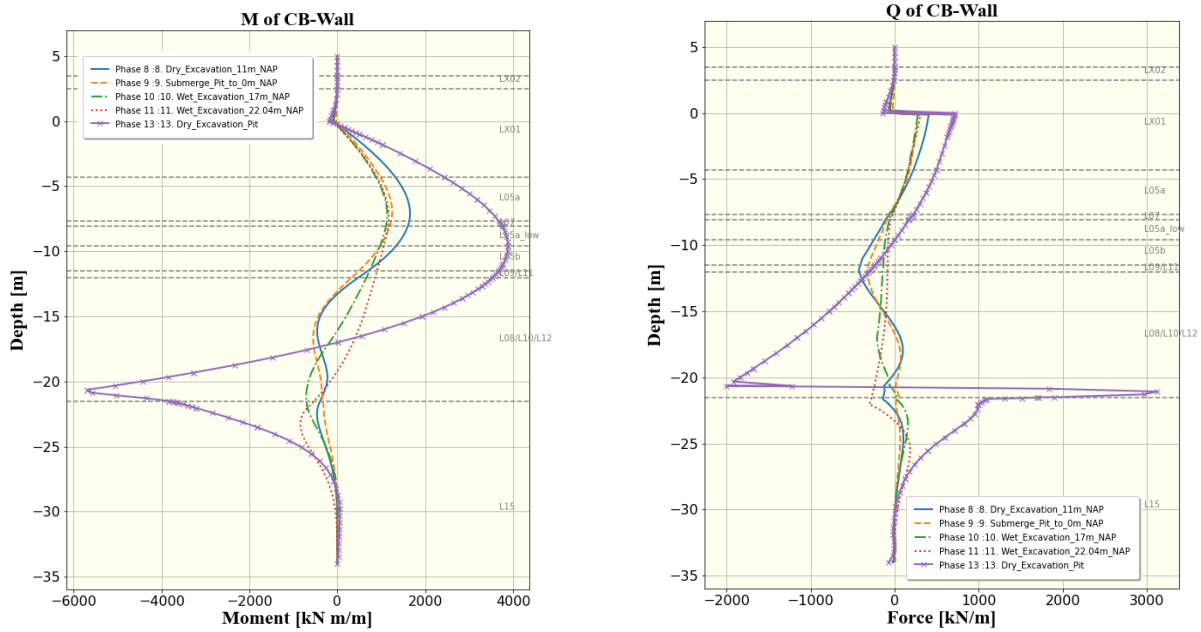
In geotechnical engineering, the soil parameters are uncertain even if an extensive geotechnical investigation is conducted. Therefore, this section will use the fine-tuned model to accurately determine the soil parameters of the impactful layers. The inclinometer deformations accurately represent reality and will be utilized to achieve this. Assuming that all the other aspects of the retaining structure have been modeled with high accuracy and the assumptions represent reality relatively well, the only uncertainty lies in the soil properties. The goal of it is to update the model and the parameters to reach a convergence of the model predictions with the measured deformations. The values that provide a prediction with  $\pm 10\%$  accuracy will be considered as the actual ones, representing the soil layers.

### 4.2.1 Soil Properties Adjustment

The adjusted soil properties will be derived by comparing the deformations of five construction phases each time with the corresponding monitoring deformations. Starting from the mean model described in Chapter 2, the adjustment will be made on the soil layers whose response impacts the wall's deformations. Utilizing the Python Application in Section 3.4, the combi-wall's combined moments and shear forces for the relevant construction phases are plotted in Figure 4.2.1a and Figure 4.2.1b, respectively. The soil properties will change by advising a sensitivity analysis performed on the corresponding soil layer. A preliminary sensitivity investigation of the Boom Clay (L15) and of the Sand (L08) has been performed, before the Fine Tuned analysis. The sensitivity analysis of the Boom Clay is using the Fine Tuned model and is discussed in Section 4.3.

Starting Phase 8 is the end of the dry excavation to -11 m NAP. Figure 4.2.1a shows at that stage that the wall relies on soil layers L15 and L08 on the active side and the soil layer L09 and L05b on the passive side. Therefore, these are the relevant layers whose properties would impact the wall deformations. The layers on the passive side will have a smaller impact than those on the active side. The top layers on the active side do not significantly affect the deformations of the wall. For the following construction phases, the same principle applies as witnessed by Figure 4.2.1a. Hence, the goal is the determination of the soil properties for the previously mentioned soil layers that would provide acceptable results for all the consecutive phases.

The iterative process allowed for a match of at least 10 % between the design and monitoring deformations. A wide range of tools from the Python Application were used for the conduction of the iterative process, as shown in the Flow Chart of Section 1.4. Without the application, this process would be more time and memory-consuming.



(a) Moments of the combi-wall for the five phases based on the mean model.

(b) Horizontal forces of the combi wall for the five phases based on the mean model.

**Figure 4.2.1:** Moments and Forces of the Fine Tuned model for five construction phases.

The changes of the mean model were based on the strength, stiffness properties of the material, and the friction ratio  $R_{inter}$ . The  $R_{inter}$  is derived by Equation 2.1.17 and depends on the effective friction angle  $\phi'$  and the wall friction  $\delta$ . de Gijt and Broeken, 2013 [15] state that research from Deltares concluded that the physical friction angle lies between  $\delta = 2/3\phi'$  and  $\delta = 0.8\phi'$  for the interface between soil and structure. This value would be appropriate for a straight surface, but the present combi-wall consists of piles and Z-type sheet piles. Therefore, the actual surface per m of the wall is larger than the stretch of the wall. Figure 4.2.1 indicates the shear surface between soil and sheet piling with a red line and suggests that only a part of that interface is between steel-soil and the rest is soil-soil. Therefore, according to de Gijt and Broeken, 2013 [15] "Assuming a physical wall friction of  $\delta = 2/3\phi'$  for 1/3 of the stretch one would conclude that no reduction would be necessary. For practical purposes it is advised to use a wall friction ratio of  $R_{int} = 0.8$  to 0.9." Additionally, the present combi-wall has been placed in a trench filled with cement bentonite that assured a perfect connection between soil and steel. For the above reason, the  $R_{int}$  has been chosen to be 0.9 for all the soil layers.

Table 4.2.1 provides the soil properties compared to the mean values that resulted in the best convergence. The results are visualized in Figure 4.2.3 for the important construction phases and compared with the deformations when the mean soil properties are used. The quantified percentage difference from the monitoring measured deformations is shown in Table 4.2.2. The table values are the area between the model and design deformation curves and have been calculated using the Reimann Sums described in Paragraph 4.3.1. The increase in accuracy is at least 25 %, and in some construction, phases reach 65 %.

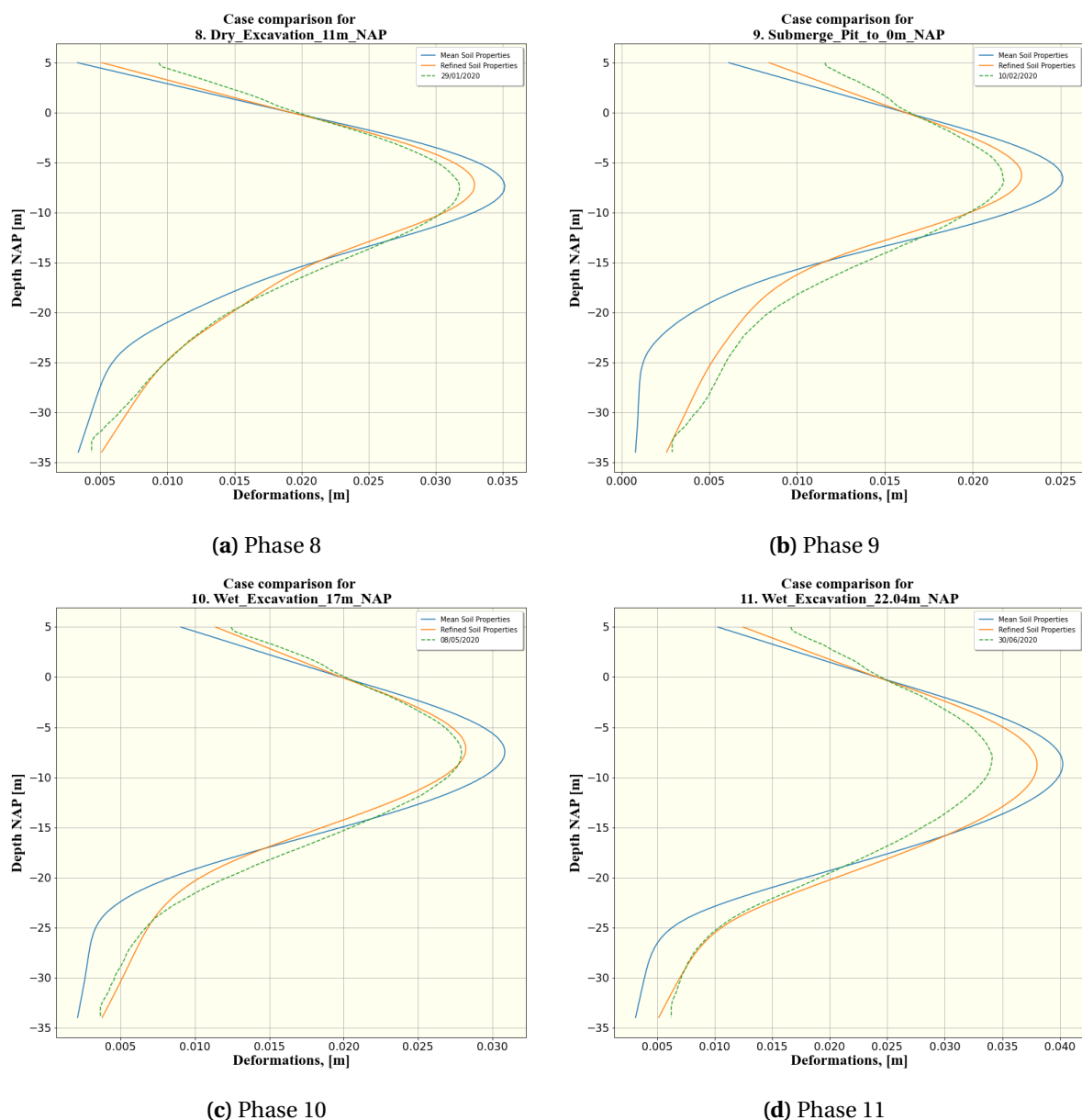


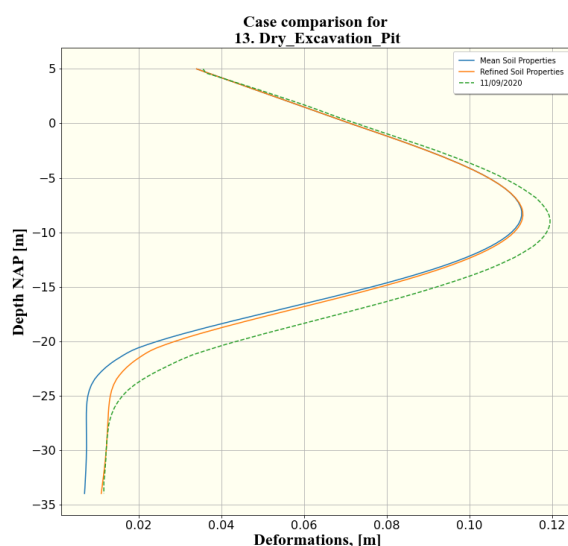
**Figure 4.2.2:** Shear surface between soil and sheet piling. (de Gijt and Broeken, 2013 [15])

$$R_{inter} = \frac{\tan(\delta)}{\tan(\phi')} \quad (4.2.1)$$

**Table 4.2.1:** Comparison of the soil properties between mean and fine tuned model.

Layer	Properties	$\phi'$	$c'$	$E_{50}^{ref}$	$E_{oed}^{ref}$	$E_{ur}^{ref}$	$G_0^{ref}$	$\gamma_{0.7}$
L09	Mean Properties	32.0	0	20285	20285	81140	137586	0.00021
	Fine Tuned Properties	35.0	0	30000	30000	90000	139688	0.000109
L08	Mean Properties	37.8	0	43127	43127	172508	232511	0.00017
	Fine Tuned Properties	42.0	0	60000	60000	180000	223500	0.000097
L15	Mean Properties	24.4	18.55	23199	23199	46400	80897	0.00065
	Fine Tuned Properties	20	16	20000	20000	40000	78462	0.000468

**Figure 4.2.3:** Comparison of the wall deformations when the Mean and Fine Tuned models are used.



(a) Phase 13

**Figure 4.2.4:** Comparison of the wall deformations when the mean and Fine Tuned properties are used.

**Table 4.2.2:** Percentage difference deformations from the monitoring measured deformations.

	Phase 8	Phase 9	Phase 10	Phase 11	Phase 13
Mean Properties	0.178	0.117	0.087	0.139	0.315
Refined Properties	0.133	0.041	0.031	0.075	0.224
Accuracy Improvement	25.3 %	65.0 %	64.4 %	46.0 %	28.9 %

#### 4.2.2 Phase 13 - Investigation

Figure 4.2.4a indicates two potential problems with the deformations. The first and less significant is that Phase 13 underestimates the deformations of the wall. The second is that the bending of the pile happens lower than the location of the underwater concrete (UWC) floor. This is an unexpected situation because normally, the wall bends around the contact location with the much stiffer UWC floor. Therefore, a side investigation has been conducted to decipher this behavior of the wall in Phase 13.

In the previously discussed comparison, all the construction phases consider that the stiffness of the wall is constant throughout all the construction phases. However, this is inaccurate because as the excavation is performed, cement bentonite at the inner side of the excavations is removed from the wall. More specifically, Phase 1 to Phase 6 has all the bentonite. Phase 7 to Phase 11 have inner bentonite removed up to -11 m NAP, where the dry excavation stopped. The cement bentonite was present during the wet excavation because the dredging equipment could not remove it. Before, Phase 12, the bentonite was removed manually up to -22 m NAP for the underwater concrete floor to be in direct contact with the steel combi-wall. The condition of the combi-wall for the different construction phases is visualized in Figure 4.2.5.

As a result, two more scenarios based on the refined model have been created, with the only change on the properties of the combi-wall for Phase 13.

- **Wall Investigation 1:** Considers that the inner part of the bentonite has been removed and excludes it from the parameter determination of the corresponding wall sections.
- **Wall Investigation 2:** Due to the change in loading and movement direction of the wall, the cement bentonite has cracked in all locations; hence, it is not considered for Phase 13.

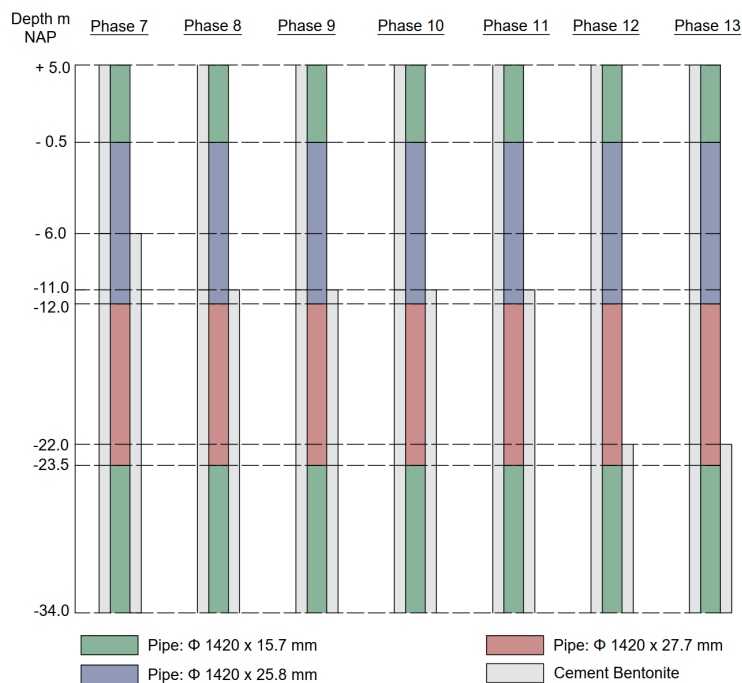


Figure 4.2.5: Cement bentonite levels for each construction phase.

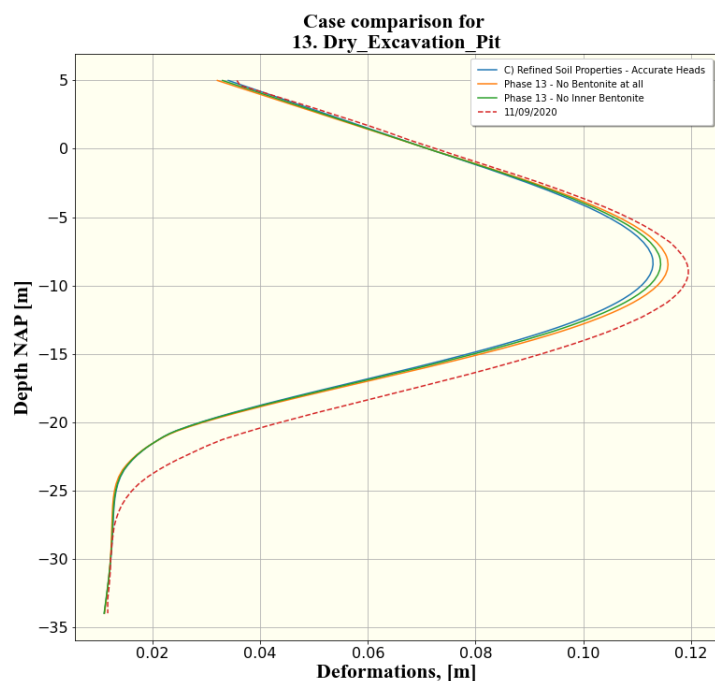
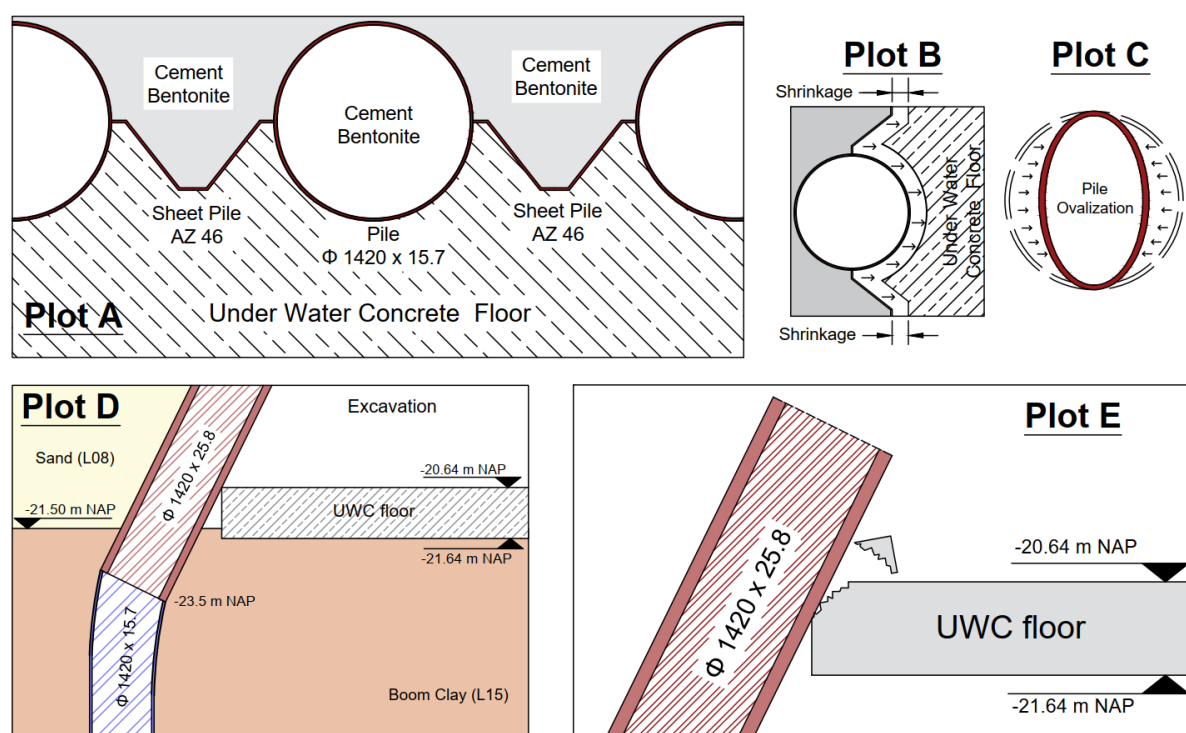


Figure 4.2.6: Influence of bentonite for Phase 13.

Figure 4.2.6 shows that the deformations increase when the cement bentonite is not considered for Phase 13, but the effect is relatively small. An investigation of the bentonite effect for all the monitored construction phases as well as the area change results are given in Appendix I.1. This conclusion was expected because, as Table 2.4.3 shows, the stiffness of the bentonite section is only a fraction of the stiffness generated by the steel sections of the combi wall. However, the difference could be due to reasons the PLAXIS model cannot simulate. The UWC is located from -20.64 m to -21.64 m NAP. When the underwater concrete is poured, it perfectly surrounds the excavation side of the wall. However, while hardening, there is the potential for shrinkage and the formation of a gap between the wall and the UWC floor. During the de-watering of the pit, the wall will first cover this gap and then find resistance from the UWC. As a result, the monitoring deformations could be slightly larger. This effect is visualized in Figure 4.2.7 at Plot B. Another possible explanation is the ovalization of the circular steel pile (Figure 4.2.7 Plot C) while it is being pushed against the much stiffer UWC floor. However, because the pile is surrounded by UWC and has the side sheet piles as shown in Plot A this effect should be minimal. Finally, potential cracking of the edge of the UWC floor (Figure 4.2.7 Plot E) or something unknown that happened in the field could lead to more deformations.

The second problem is that the bending of the pile is happening lower than the location of the UWC floor. A potential explanation for this could be that until -23.5 m NAP, the pile has a thickness of 25.8 mm, and after, it becomes 15.7 mm. Therefore, the stiffer part of the pile could rotate on the floor, and the bending is propagating at the lower part of the pile, which is weaker. This effect is visualized in Figure 4.2.7, Plot D.



**Figure 4.2.7:** Summary of potential reasons for the difference in deformations of the model and monitoring for Phase 13.

### 4.2.3 Summary and discussion

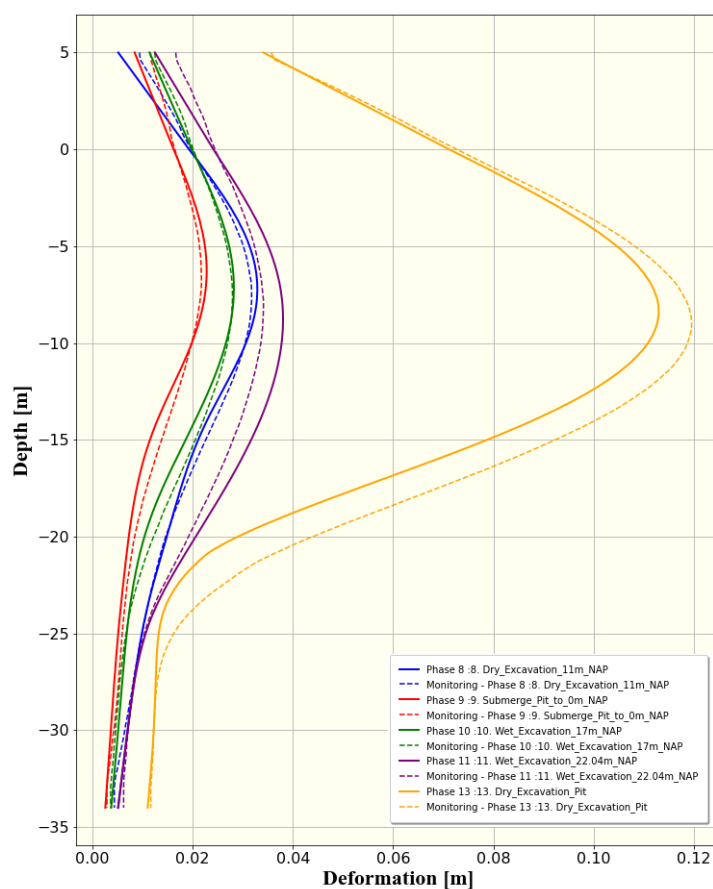
The actual soil properties of the materials influential to the wall deformations have been determined using the monitoring deformations. These soil parameters are summarised in Table 4.2.1. In general,

the soil properties of the Fine Tuned sand layers L08 and L09 have increased compared to the mean values. On the other hand, the soil properties of the Boom Clay L15 have decreased for the Fine Tuned model. Depending on the construction phase, the new deformation predictions are from 25 % to 65 % more accurate than the mean values.

The repetition process to derive the Fine Tuned model has followed the process described in the flow chart of Section 4.5 and utilized the tools of the Python Application (Chapter 3). The altered properties are strength and stiffness. However, better accuracy can be achieved if more parameters are adjusted and more repetitions are performed. Therefore, the accuracy of the new soil properties is heavily impacted by the validity of the assumptions made for the model and the extent of the investigation. This was a limiting factor, but a proposal for further investigation is made in Section 5.2.

Additionally, it has been proven that the wall friction ratio for a combi-wall placed in a cement bentonite-filled trench does not need reduction and can be kept to 0.9 or higher. Some speculations have been made regarding the behavior of the wall around the UWC, but they haven't definitively been proven. It is believed that the problem lies in structural or operational aspects that are out of the scope of this thesis.

The fine-tuned model is as accurate as the assumptions and the modeling of the rest of the conditions, like loads, water heads, and structural elements' behavior. Therefore, the fine-tuned model's success relies on a well-monitored and organized project. Figure 4.2.8 shows the final deformation plot for the five monitored construction phases.



**Figure 4.2.8:** Comparison of the monitoring measured deformations with the predicted deformations of the Fine Tuned model for five construction phases.



## 4.3 Sensitivity Analysis

One of the most controversial soil layers that significantly impact the behavior of the present retaining structure is the Boom Clay (L15). This layer is present in the general area, but its thickness varies throughout the project. The importance of the geometry for this layer is discussed in Section 4.4. In this thesis's cross-section (L01b), the Boom Clay is located from -21.5 m to -37.6 m NAP. Additionally, the combi-wall piles reach a depth of -34 m NAP; hence their tip exists within the boundaries of this layer, and they interact for 12.5 m. Due to the strong influence of Boom Clay on the response of the entire retaining structure, a proper understanding of its behavior is crucial. Therefore, a sensitivity analysis has been performed to investigate the influence of specific parameters based on the finite element program PLAXIS and the constitutive model Hardening Soil Small Strain (HS-small).

The sensitivity analysis has been performed on stiffness, strength, and small strain properties. As explained in Section 2.1.4, the HS-small constitutive model requires for stiffness input the properties:

- $E_{50}^{ref}$ : Secant stiffness from the triaxial test at reference pressure
- $E_{Oed}^{ref}$ : Tangent stiffness from oedometer test at  $p_{ref}$
- $E_{UR}^{ref}$ : Reference stiffness in unloading / reloading

The relevant strength properties are:

- $\phi'$ : Effective friction angle
- $c'$ : Effective cohesion
- $\psi$ : Angle of dilation

The small strain properties are:

- $G_0^{ref}$ : Reference shear stiffness at small strains
- $\gamma_{07}$ : Shear strain at which  $G$  has reduced to 72.2 %

### 4.3.1 Methodology

To do the sensitivity analysis, each parameter has been investigated separately to determine its influence. However, some of these parameters are interdependent, which has to be considered. Additionally, the finite element program PLAXIS imposes some parameter restrictions for the material to be valid. Those rules had to be respected for the automated model to run all the scenarios continuously. The methodology implemented is to use the Fine Tuned model described in Section 4.2 and change the specific combination of parameters. Then the PLAXIS model is calculated, the results are collected, and the interpretation of the results is performed using the Python Application described in Chapter 2.

Following the instructions of the PLAXIS manual of Brinkgreve et al., 2011 [10], the stiffness properties are interconnected through the equations 4.3.1, 4.3.2, and 4.3.3. These are suggestions of PLAXIS to ensure the validity of the material. Since the change of one stiffness parameter affects the others, only the  $E_{50}^{ref}$  has been chosen for the sensitivity analysis. Regarding the strength parameters of

the material, only the effective friction angle  $\phi'$  and the effective cohesion  $c'$  have been considered because the angle on dilation  $\psi$  is regarded as zero for fine-grained material as the Boom Clay.

$$E_{50}^{ref} = E_{oed}^{ref} \quad (4.3.1)$$

$$E_{ur}^{ref} = E_{oed}^{ref} / 3 \quad (4.3.2)$$

$$E_{ur}^{ref} = E_{50}^{ref} / 3 \quad (4.3.3)$$

Since the constitutive model of choice is the HS-small, the small strain parameters need to be considered. Both the stiffness and strength parameters take place in the derivation of  $G_0^{ref}$  and  $\gamma_{07}$ . The equations 4.3.4, 4.3.5, 4.3.6 and 4.3.7 depict this dependency. Finally, it has been decided to investigate the effective friction angle  $\phi'$ , the effective cohesion  $c'$ , and the Secant stiffness  $E_{50}^{ref}$ . Table 4.3.1 gives an overview of the parameter's interdependencies.

$$E_{stat} = E_{ur} \approx 3 * E_{50} \quad (4.3.4)$$

$$E_0 = (E_{dyn} / E_{stat}) * E_{ur} \quad (4.3.5)$$

$$G_0 = E_0 / (2 * (1 + \nu)) \quad (4.3.6)$$

$$\gamma_{0.7} = (1 / (9 * G_0)) * (2 * c' * (1 + \cos(2 * \phi')) + \sigma'_1 * (1 + k_0) * \sin(2 * \phi')) \quad (4.3.7)$$

**Table 4.3.1:** Interdependent Parameters

Initial Parameter	Dependent Parameter
$E_{50}^{ref}$	$E_{oed}^{ref}$ , $E_{ur}^{ref}$ , $G_0^{ref}$ , $\gamma_{07}$
$E_{oed}^{ref}$	$E_{50}^{ref}$ , $E_{ur}^{ref}$ , $G_0^{ref}$ , $\gamma_{07}$
$E_{ur}^{ref}$	$E_{50}^{ref}$ , $E_{oed}^{ref}$ , $G_0^{ref}$ , $\gamma_{07}$

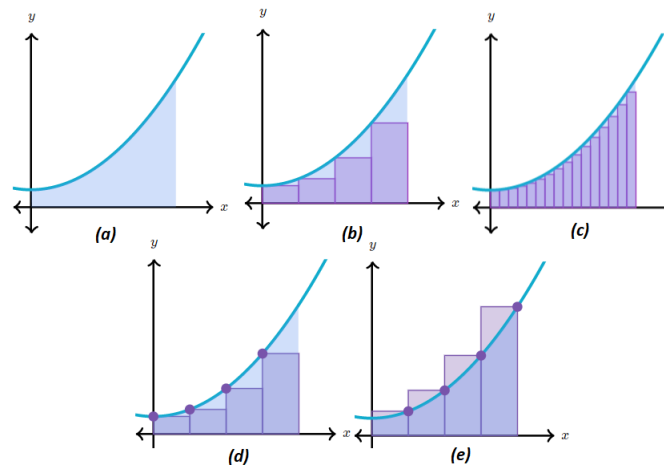
Many scenarios are being considered to perform the sensitivity analysis. A new scenario is created every time the material receives a different value for a parameter. The higher the number of scenarios, the better the accuracy of the predictions. However, each scenario translates to a time-consuming PLAXIS calculation, approximately 35 minutes. Therefore, a reasonable step and range have been chosen depending on the parameter investigated each time. Each parameter under investigation receives values above and below the accurate value used in the Fine Tuned model. This approach will reveal the rate of change in the extreme scenarios and if it remains constant.

Once all the scenarios have been created and stored in a custom library, the interpretation process begins. Firstly, a method was needed to quantify the parameter-induced change in deformations. The most simplified approach would be to investigate the maximum deformation of the combi-wall in each phase. However, not only is the wall not rigid, but it also offsets at the bottom. Hence, such an approach would not represent the total effect of the new scenario on the retaining structure. A better system would be to calculate the average deformation of the wall between scenarios. The accuracy

of this method increase with the increase of the sample deformations along the wall. By utilizing the programming potentials, the application can calculate the "area" between two scenarios using the integration rule of Riemann sums.

### Riemann Sums

The area below a curve is not possible to be calculated precisely in Figure 4.3.1a, but it can be estimated with high accuracy. One approach is the Riemann sums that divide the area below a curve into little rectangles, which are simple to calculate, Figure 4.3.1b. The accuracy of the approximation increases if more rectangles are used, Figure 4.3.1c. The error indicated by the light blue areas decreases as the uniform partitions become smaller. There are two ways of creating rectangles, the left and right Riemann Sums, Figure 4.3.1d, and Figure 4.3.1e, respectively. Depending on the curvature, this method sometimes overestimates, and others underestimate the area under a curve, the so-called error. Equation (4.3.8) gives the area, where  $n$  is the number of partitions,  $f(x_i)$  is the curve's height, and  $\Delta x$  is the thickness of the partitions.

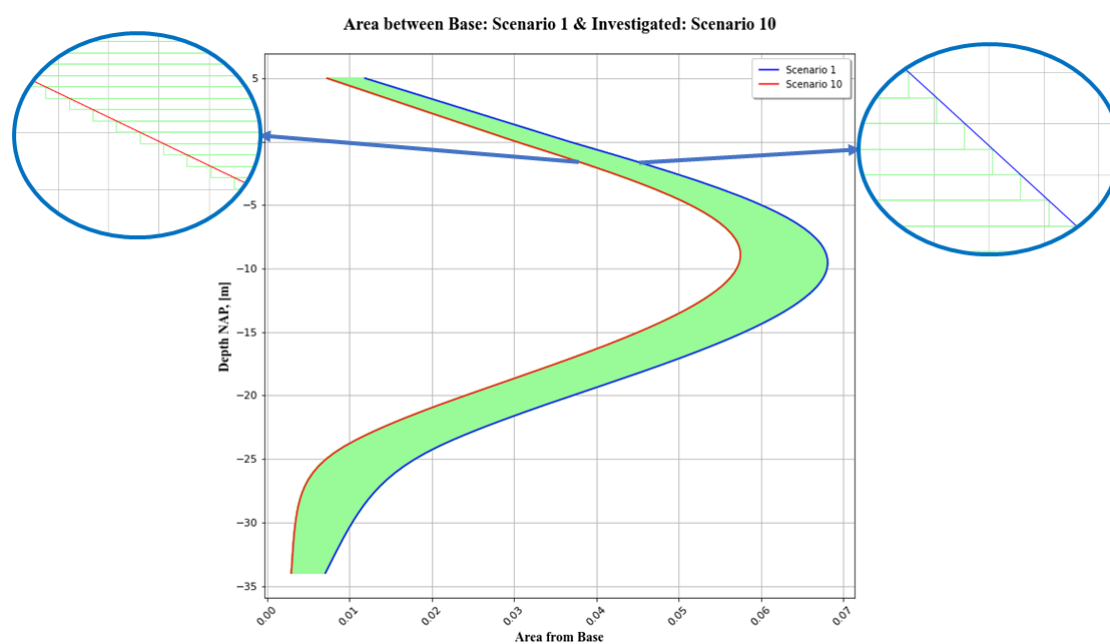


**Figure 4.3.1:** Riemann sums method for the calculation of the area below a curve.

$$\text{Area of rectangles} = \sum_{i=0}^{n-1} f(x_i) * \Delta x \quad (4.3.8)$$

The Riemann method had to be modified slightly for the present case because the area between two curves is now needed. The same logic has been applied but in horizontal orientation. Figure 4.3.2 shows that to reduce the error on the east curve, the "right" Riemann method is used, and on the west curve, the "left" Riemann method is used. Hence, the area is overestimated on the east side and underestimated on the west side. For instance, Figure 4.3.2 shows the area between the hypothetical curves of Scenario 1 and Scenario 10. The zoomed sections present the effect of the right and left Riemann methods mentioned previously. That approach balances the two sides. The spacing that has been decided is 0.01 m. It allows the code to do the calculations in a reasonable amount of time with high accuracy. The calculation time increases exponentially with every power decrease because the total length of the pile is 39 m.

The accuracy provided by the code is essential given the small change between scenarios occasionally. The results produced are the cumulative and incremental differences between scenarios. The cumulative difference shows the percentage of change in the deformations. To create a value that



**Figure 4.3.2:** Example for the calculation of the area between two curves using the Riemann method.

would represent the total behavior of the wall, the deformation of the wall along the depth for the base scenario and the investigated scenario is plotted. Then the area between those two plots is calculated with the Riemann method. This "area" between the two scenarios represents the change in the condition of the wall. It can quantify the effect of each scenario and eventually give the influence of the soil parameter being investigated. From now on, this change will be referred to as "area".

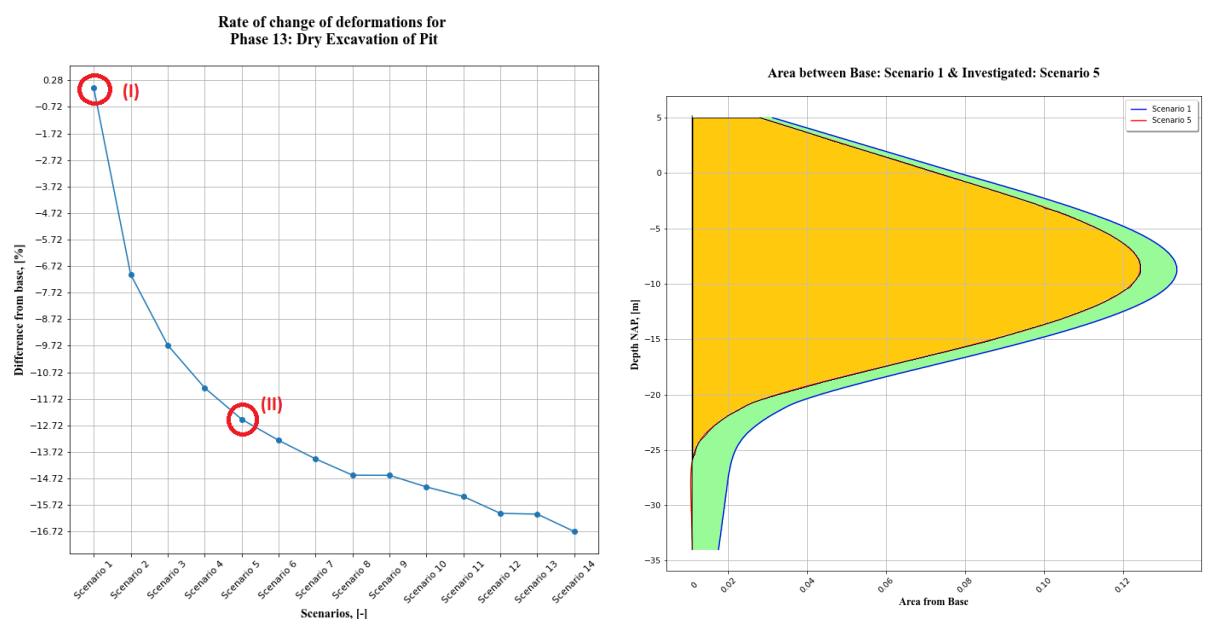
For instance, Figure 4.3.3a plots the area different from the base scenario for construction Phase 13. In this example, each scenario depicts a value of  $E_{50}$  for the Boom Clay. The base scenario is Scenario 1:  $E_{50} = 4000 \text{ kN/m}^2$ ; hence the difference from itself (I) is 0. The effect of Scenario 5:  $E_{50} = 16000 \text{ kN/m}^2$  (II) is a 12.49 % decrease in the total deformation. This number is produced by calculating the area between (green area) and the base area (orange area) in Figure 4.3.3b. Then using Equation 4.3.9, which gives the rate of change (ROC), where  $B$  is the current scenario, and  $A$  is the base scenario, the effect of the new parameter is quantified.

$$\text{Rate of change} = ((B - A) / A) * 100 \quad (4.3.9)$$

The application allows the user to run multiple scenarios simultaneously, save the results in custom libraries, and interpret them. See Section 3.6 of the application.

In contrast, incremental differences are percentages and show the difference between two consecutive scenarios. The cumulative differences are plotted for each scenario to determine the rate of deformation change. When the plot forms a straight line, this parameter's influence remains constant throughout the investigated range. On this occasion, the incremental differences should remain more or less stable. Contrary, when this plot forms a curve, either throughout the whole length or after a point, it means that the influence of the parameter is dropping or increasing. Moreover, the sign depicts the influence of the scenario. A negative sign indicates that the deformations or the area decreases as the scenarios progress, and a positive sign means the contrary.

The sensitivity analysis implemented changes one factor at a time (OTA). For the results of the sensitivity analysis of each parameter to be comparable, a constant range of  $\pm 30\%$  from the mean value



(a) Rate of change for Phase 13 when the secant stiffness  $E_{50}$  of the Boom Clay layer is investigated. (b) Calculation of the "area" between scenario 5 and scenario 10 for the  $E_{50}$  stiffness of Boom Clay

Figure 4.3.3: Example for the explanation of methodology.

of the parameter is investigated. Additionally, that approach will allow the creation of a sample of scenarios that exclude highly unlikely values and make the rate of change more linear with higher correlation. Since the focus is on the Boom Clay layer, two construction phases, Phase 11: The end of the wet excavation, and Phase 8: The end of the dry excavation, are analyzed. The former phase is the most challenging for Boom Clay. The layer is designed undrained and is the only responsible layer for retaining the wall. The latter is another vital construction phase where the Boom Clay is modeled drained and is part of the soil layers retaining the wall. Phase 13, where the pit is set dry, and the highest deformations are monitored, is not that important because, as will be proven in each case, the change of soil parameters has a limited effect due to the existence of the underwater concrete (UWC) floor.

Finally, to assist the comprehension of the total wall behavior throughout all the investigated scenarios, 3D plots are generated to include everything in one figure.

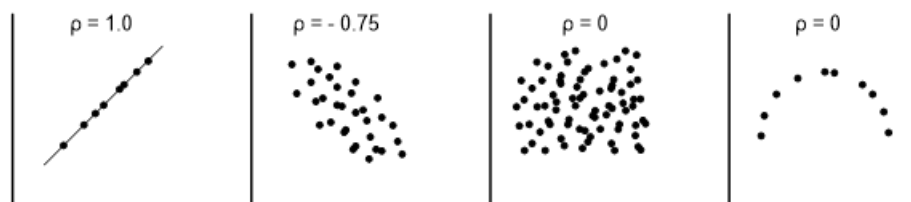
### Linear Correlation

The linear correlation gives the connection between two variables, which can be calculated using simple mathematical equations. The linear correlation equation for two variables, X and Y, is given by Equation 4.3.10. Where COV is the covariance between the two variables and  $\sigma_x$  and  $\sigma_y$  is the standard deviation of variables X and Y. In this case, X is the change in soil parameter, and Y is the change in area.

$$\rho = COV(X, Y) / (\sigma_x * \sigma_y) \quad (4.3.10)$$

In geotechnical engineering is often useful when there are two variables to determine their correlation. In general, the covariance expresses the tendency of the variables to change together. The linear

correlation is a normalized covariance expression defined in the range of  $[-1, 1]$ . When the variables are perfectly connected, the linear correlation  $\rho$  equals  $+1$  (positive correlation) or  $-1$  (negative correlation). On the other hand, when the variables are independent, the  $\rho$  is equal to  $0$ , and every value in between shows an intermediate connection. Example data and the corresponding linear correlation between two variables are shown in Figure 4.3.4.



**Figure 4.3.4:** Example data and the corresponding linear correlation between two variables.

### 4.3.2 Investigation

In this section, the results from the sensitivity analysis are going to be presented. The investigated parameters for the Boom Clay are the secant stiffness  $E_{50}^{ref}$ , the effective friction angle  $\phi'$ , and effective cohesion  $c'$ . For the results to be comparable, each scenario has been calculated based on the Fine Tuned model and a medium-density mesh in the finite element program PLAXIS. Section 2.5 describes the construction phases that will be discussed. Special attention will be given to Phase 8, Phase 11, and Phase 13. The Boom Clay predominately governs the deformations of Phase 11 because it is the only responsible layer for retaining the wall.

#### Rate of Change (ROC)

Firstly, the deformation rate of change (ROC) is being investigated for the three soil properties of Boom Clay. Many iterations for each soil property have been made to acquire a healthy sample. Every time as a base scenario, the accurate value derived by the Fine Tuned model (Section 4.2) is used. All the other scenarios are compared to the base and range from lower to higher values to give a well-rounded influence outcome. The summary of the scenarios considered for each parameter is given in Table 4.3.2. The step chosen for each parameter is representative of the influence. The results are depicted in Figure 4.3.5, where the percentage difference in deformation area from the base scenario is compared to the rest of the scenarios for several construction phases for the three soil properties.

To begin with the interpretation, the rate of change for the  $E_{50}^{ref}$  and  $\phi'$  is not linear, whereas, despite the fluctuations,  $c'$  is relatively linear. When it comes to the non-linear cases, the change in lower values is more rapid, whereas, in the higher end, the impact of the deformations decreases. This behavior is constant throughout all the construction phases plotted. Additionally, The negative sign indicates a decrease in deformations compared to the base scenario. Therefore, all the values lower than the base induce higher deformations, and the higher values are the contrary. Generally, for all the construction phases, the deformation change induced by the variation of effective friction angle is much higher than the other properties. On the other hand, the effective cohesion  $c'$  has a minimal impact, as shown in Figure 4.3.5.

The first observation is the small ROC of Phase 13 for all the parameters. In this phase, the excavation pit is set dry, and the hardened underwater concrete (UWC) functions as a beam and supports the wall. The UWC floor carries most of the load that, otherwise, the Boom Clay at that location would

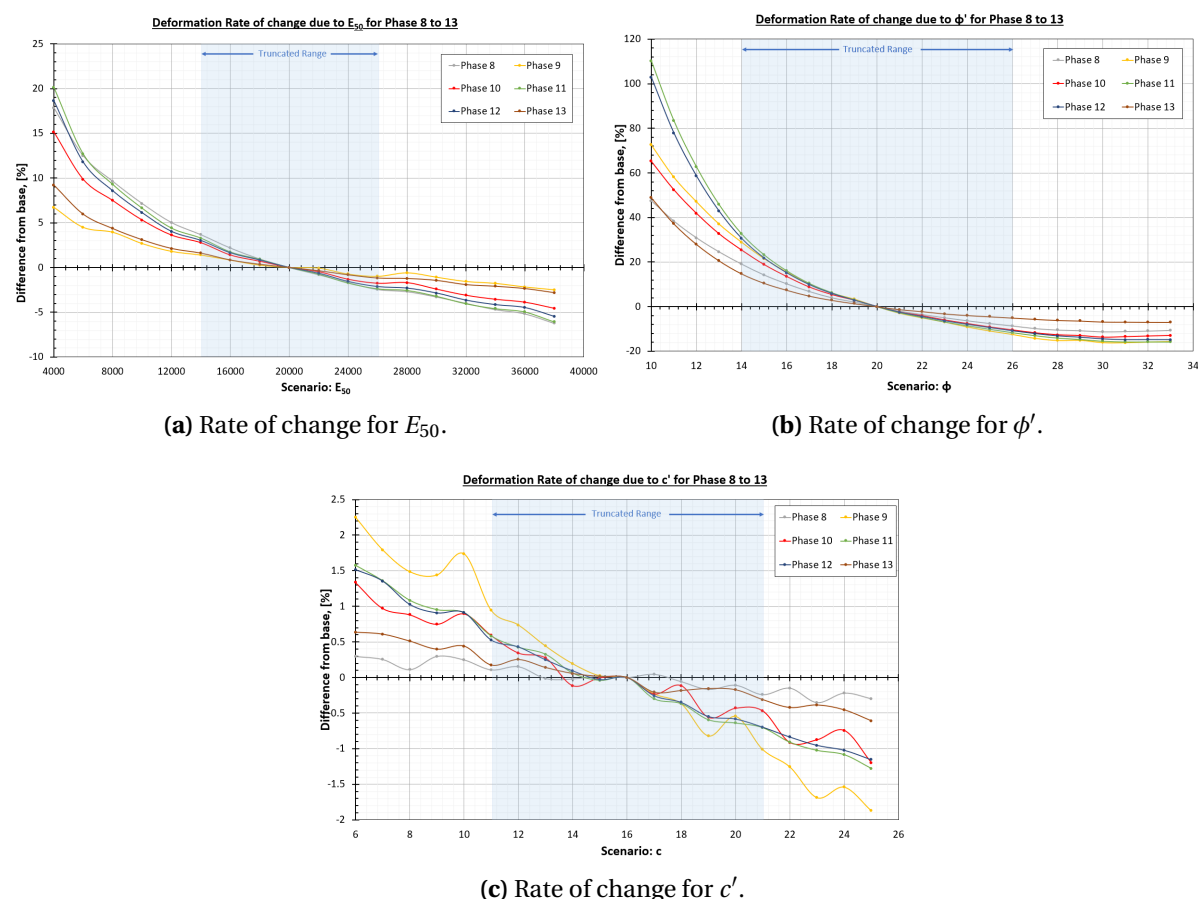
**Table 4.3.2:** Summary of the scenarios investigated for the three soil properties of Boom Clay.

Scenario	$E_{50}^{ref} - [kN/m^2]$	$\phi' - [^\circ]$	$c' - [kN/m^2]$
1	4000	10	6
2	6000	11	7
3	8000	12	8
4	10000	13	9
5	12000	14	10
6	14000	15	11
7	16000	16	12
8	18000	17	13
9	B: 20000	18	14
10	22000	19	15
11	24000	B: 20	B: 16
12	26000	21	17
13	28000	22	18
14	30000	23	19
15	32000	24	20
16	34000	25	21
17	36000	26	22
18	38000	27	23
19		28	24
20		29	25
21		30	
22		31	
23		32	
24		33	

\*B = Base Scenario

be responsible for. Hence, reducing the impact, the Boom Clay properties have on the deformations. In most cases, the Boom Clay properties have the most severe impact on Phase 11. That is to be expected because the Boom Clay is the only soil layer that supports the retaining wall. Additionally, the validity of this investigation can also be confirmed in the comparison of Phase 11 and Phase 12. It is visible that their responses are almost the same. Phase 12 is responsible for the gravel placement and UWC floor pouring. Essentially Phase 12 is the same as Phase 11, except for the weight of the gravel and concrete materials. Phase 10 always has an intermediate behavior and is less influenced by the parameter change than Phase 11. That is because, at that stage of wet excavation, the upper sand layer is still present and contributes to the retaining of the wall.

Contrarily Phase 8 and Phase 9 do not behave similarly for all the soil property sensitivity investigations of the Boom Clay. Phase 8 is the end of dry excavation, where the Boom Clay is modeled as drained. It is influenced the most by the secant stiffness  $E_{50}^{ref}$ , whereas the effective friction angle  $\phi'$  and cohesion  $c'$  affect it the least in comparison to the other phases. This outcome could be attributed to the fact that until Phase 8, the Boom Clay is designed to behave drained. Lastly, the behavior of Phase 9 is different for all three soil properties analyses. It is affected the least when it comes to  $E_{50}^{ref}$ , the most when it comes to  $c'$ , and an intermediate behavior to  $\phi'$ , relative to the rest of construction phases. Phase 9 represents an undrained unloading situation because the water level inside the excavation pit increases, and the wall is pushed in the opposite direction. It can be considered a positive stage for the stability of the retaining wall, and the increase of the stiffness  $E_{50}^{ref}$  appears to have a limited effect. One of the earlier conventions is that the stiffness responsible for unloading  $E_{ur}$  is equal to  $3 * E_{50}$ . Hence, a potential reason for the slight change in Phase 9, where the unloading of the wall is happening, is the high value of  $E_{ur}$ .



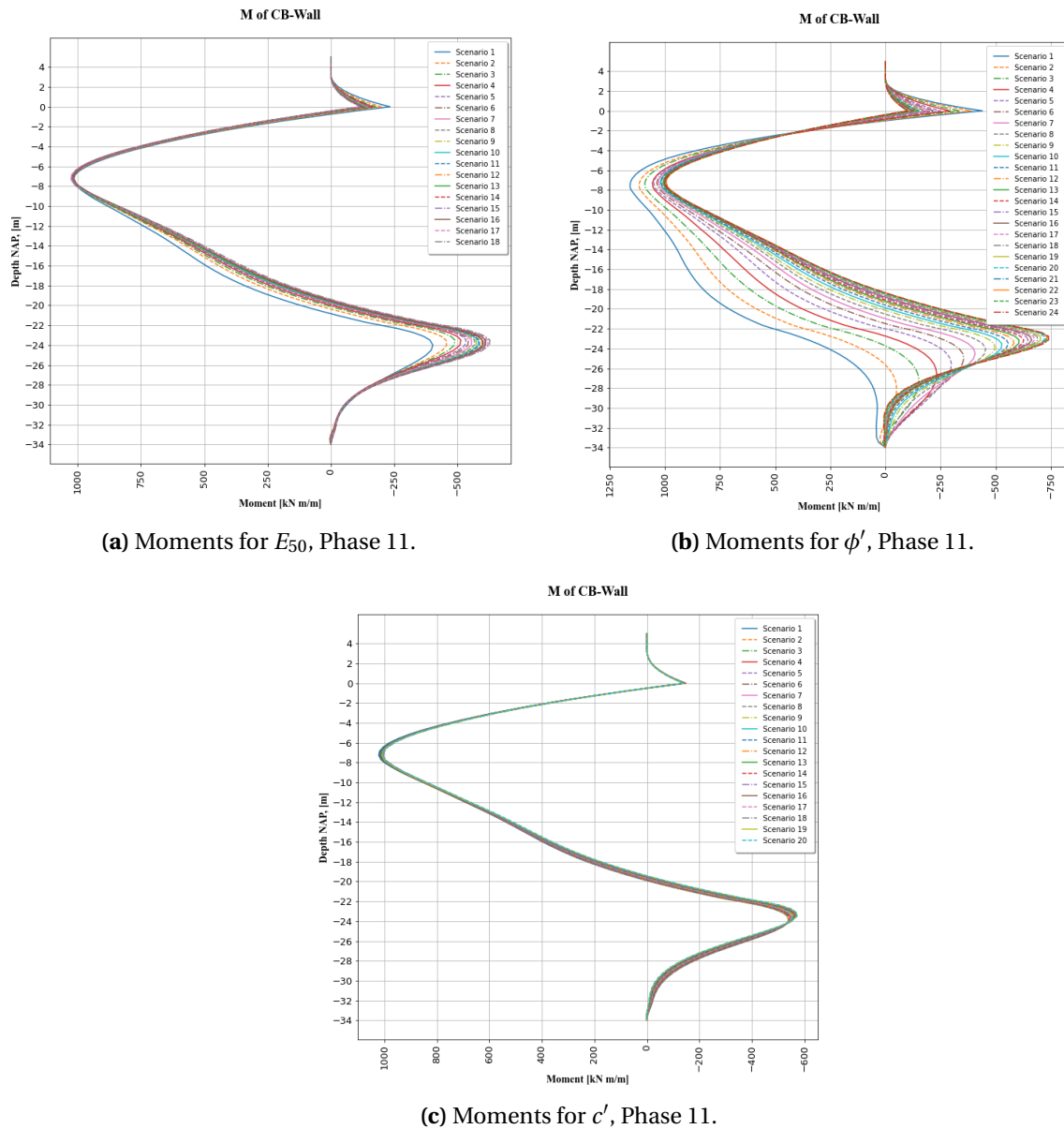
**Figure 4.3.5:** Deformation rate of change due to different  $E_{50}^{ref}$ ,  $\phi'$  and  $c'$  values of the Boom Clay for construction phases 8 to 13. The blue shaded area is the  $\pm 30\%$  change from the base value.

A similar effect as the deformations is found for the moments in the wall. The most impacted phase by the Boom Clay layer is Phase 11; hence it has been chosen for discussion. Figure 4.3.6 shows the effect the different soil properties have on the moments of the wall for construction Phase 11. The moments are significantly affected by the change of  $\phi'$ , and the effect also occurs in higher locations than the Boom Clay layer. The impact of  $E_{50}^{ref}$  and  $c'$  is significantly less. Therefore, uncertainty on the friction angle of the Boom Clay impacts the design of the combi-wall itself.

### Sensitivity to the soil properties

To quantify the sensitivity of the wall to the different Boom Clay soil properties, the rate of change in Figure 4.3.5 is being used. Firstly, the ROC is not linear for  $E_{50}^{ref}$  and  $\phi'$ , which means that the sensitivity is not constant throughout the total investigated range of values. Therefore, a truncated sample of  $\pm 30\%$  from the accurate value has been considered to avoid values that are less likely to occur. This range is depicted in Figure 4.3.5 with a transparent blue area for each soil property. Additionally, the truncated range allows for an almost linear sample and one representative parameter sensitivity. To test the linearity, the correlation of the truncated sample is calculated with the method explained in Paragraph 4.3.1. Table 4.3.3 shows that the truncated ranges are more correlated than the total range. With the average correlation of each truncated range being over 95 %, it is reasonable to assume that the behavior is linear. Only for the effective cohesion, the total range has a higher correlation, which can be attributed to the disturbance in the values.





**Figure 4.3.6:** Moments of the combi-wall for all the scenarios of parameters  $E_{50}^{ref}$ ,  $\phi'$  and  $c'$  for Phase 11.

Table 4.3.4 will focus on two of the most important construction phases of the project, Phases 8 and 11. In the table the range of the parameter values and the area change (AC) for both the total [-100%, +100%] and truncated [-30%, +30%] ranges are given.

Secant Stiffness  $E_{50}^{ref}$

For  $E_{50}^{ref}$  for both Phase 8 and 11, the correlations are over 99%. On the lower end of the truncated range, the  $E_{50}^{ref}$  value is  $14000 \text{ kN/m}^2$  and the area change is 3.67% and 3.29% for Phase 8 and Phase 11, respectively. On the higher end of the truncated range, the  $E_{50}^{ref}$  value is  $26000 \text{ kN/m}^2$  and the area change is -2.45% and -2.37% for Phase 8 and Phase 11, respectively. The negative sign indicates a decrease in the deformations, and the positive the opposite. Both phases show about the same sensitivity to the change of  $E_{50}^{ref}$  stiffness of Boom Clay. Additionally, the same reduction of the parameters leads to a more significant impact on deformations than the same increase.

**Table 4.3.3:** Correlations for each construction phase and each soil property under investigation for the Total and Truncated sample.

Sample	$E_{50}^{ref}$		$\phi'$		$c'$	
	Total	Truncated	Total	Truncated	Total	Truncated
Phase 8	-0.941	-0.992	-0.909	-0.974	-0.943	-0.869
Phase 9	-0.942	-0.983	-0.905	-0.971	-0.989	-0.980
Phase 10	-0.922	-0.988	-0.898	-0.969	-0.980	-0.951
Phase 11	-0.916	-0.994	-0.852	-0.957	-0.994	-0.989
Phase 12	-0.913	-0.993	-0.852	-0.957	-0.992	-0.993
Phase 13	-0.919	-0.992	-0.852	-0.956	-0.986	-0.948
Average	-0.925	-0.990	-0.878	-0.964	-0.981	-0.955

#### Effective Friction Angle $\phi'$

For  $\phi'$  for both Phases 8 and 11, the correlations are over 95 %. On the lower end of the truncated range, the  $\phi'$  value is 10 °, and the area change is 19.05 % and 32.65 % for Phase 8 and Phase 11, respectively. On the higher end of the truncated range, the  $\phi'$  value is 26 °, and the area change is -8.60 % and -11.61 % for Phase 8 and Phase 11, respectively. The negative sign indicates a decrease in the deformations, and the positive the opposite. Phase 11 shows higher sensitivity to the change of  $\phi'$  friction angle of Boom Clay than Phase 8. Additionally, the same reduction of the parameters leads to a more significant impact on deformations than the same increase.

#### Effective Cohesion $c'$

For  $c'$  for both Phase 8 and 11, the correlations are 87 % and 99 %, respectively. The lower value of Phase 8 is due to errors in capturing the small area change between scenarios. On the lower end of the truncated range, the  $c'$  value is 6  $kN/m^2$ , and the area change is 0.11 % and 0.58 % for Phase 8 and Phase 11, respectively. On the higher end of the truncated range, the  $c'$  value is 25 °, and the area change is -0.24 % and -0.71 % for Phase 8 and Phase 11, respectively. The negative sign indicates a decrease in the deformations, and the positive the opposite. Phase 11 shows higher sensitivity to the change of  $\phi'$  friction angle of Boom Clay than Phase 8. Additionally, the same reduction of the parameters leads to a more significant impact on deformations than the same increase.

**Table 4.3.4:** Statistical description of the truncated and total ranges for Phase 8 and 11.

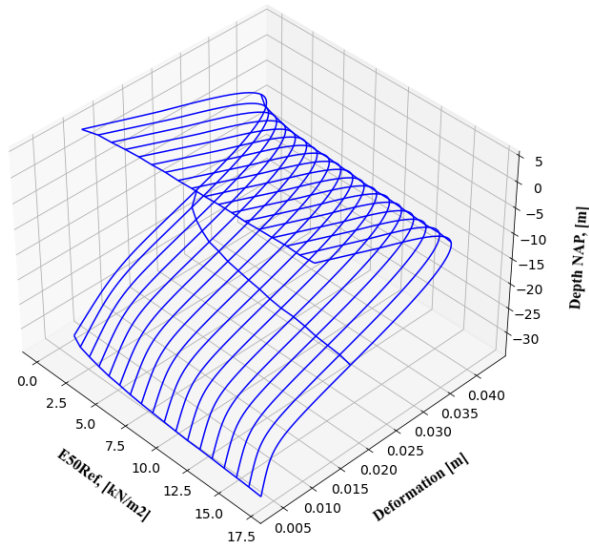
	Mean	St. Dev	COV	-100%	100%	-30 %	+30%
$E_{50}^{ref} - [kN/m^2]$	20000	4320	21.60	4000	38000	14000	26000
AC - Phase 8 - [%]				17.85	-6.23	<b>3.67</b>	<b>-2.45</b>
AC - Phase 11 - [%]				20.13	-6.08	<b>3.29</b>	<b>-2.37</b>
$\phi' - [^\circ]$	20	3.89	19.47	10	33	14	26
AC - Phase 8 - [%]				47.40	110.16	<b>19.05</b>	<b>-8.60</b>
AC - Phase 11 - [%]				-10.60	-15.79	<b>32.65</b>	<b>-11.61</b>
$c' - [kN/m^2]$	16	3.32	20.73	6	25	11.2	20.8
AC - Phase 8 - [%]				0.30	-0.30	<b>0.11</b>	<b>-0.24</b>
AC - Phase 11 - [%]				1.57	-1.28	<b>0.58</b>	<b>-0.71</b>

\* AC = Area change

**Overview of scenario impact**

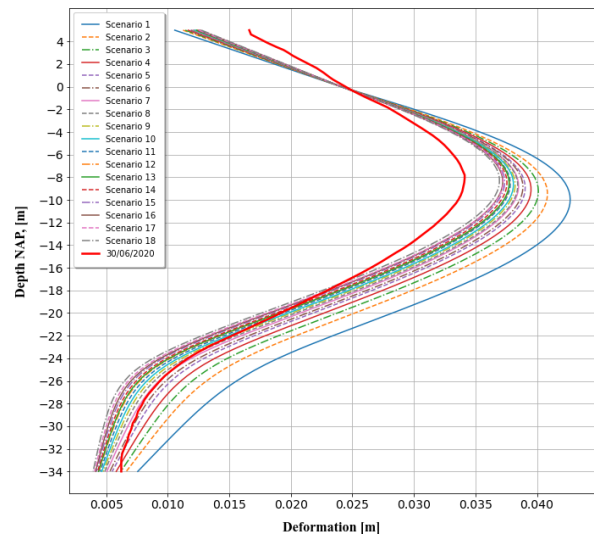
To understand the different scenarios' effects on the deformations of the combi wall, two types of plots have been constructed for the most challenging phase of Boom Clay, Phase 11. The first type is a 3D plot that depicts the change of deformations depending on the soil parameter value over the length of the wall for Phase 11. The second plot is 2D and presents the change of deformations depending on the value of the soil parameter compared to the corresponding monitored deformations (bold red line). The previously mentioned pair of plots are given in Figures 4.3.7, 4.3.8 and 4.3.9 for  $E_{50}^{ref}$ ,  $\phi'$  and  $c'$ , respectively.

3D plot of Depth vs Scenario vs X-Deformation



(a) Horizontal Deformations - 3D

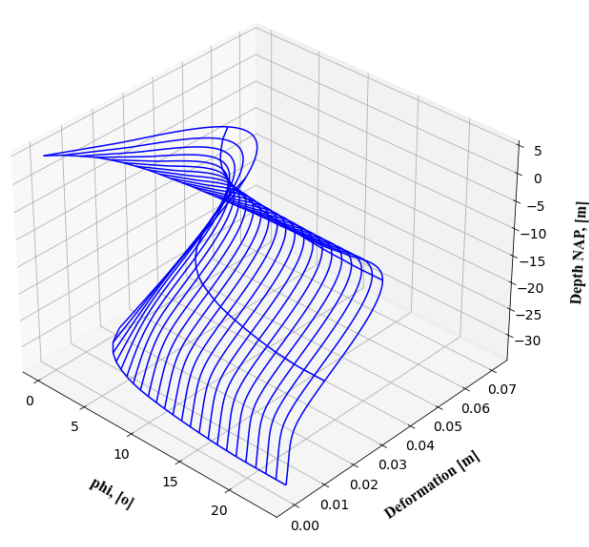
X-Deformation of CB-Wall



(b) Horizontal Deformations & Monitoring - 2D

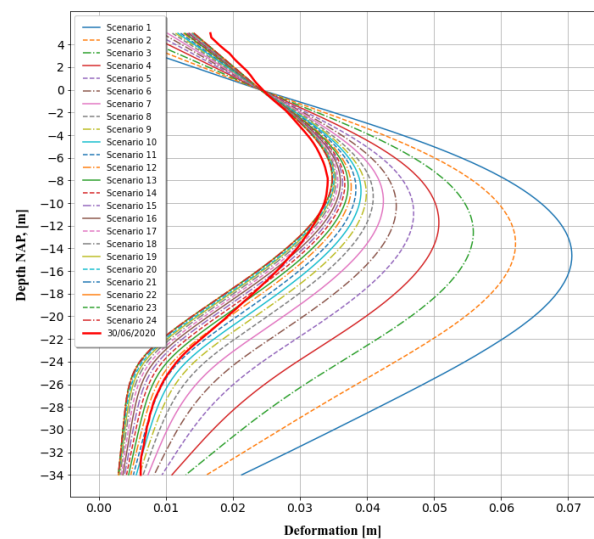
**Figure 4.3.7:** Overview plots of the effects the  $E_{50}^{ref}$  scenarios have on the deformations of the wall.

3D plot of Depth vs Scenario vs X-Deformation



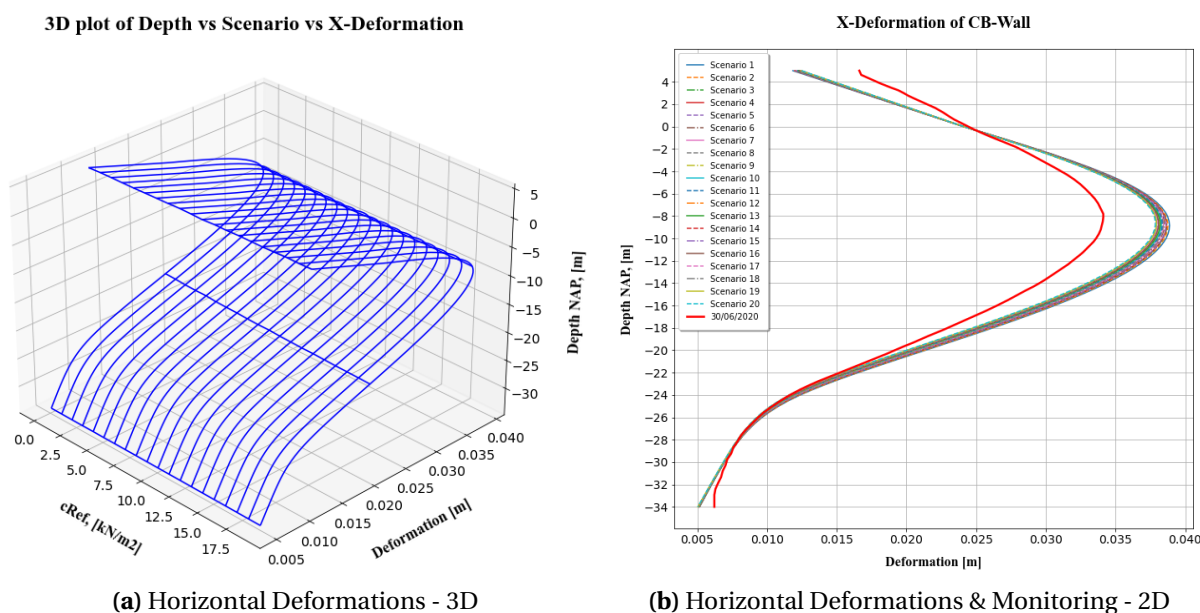
(a) Horizontal Deformations - 3D

X-Deformation of CB-Wall



(b) Horizontal Deformations & Monitoring - 2D

**Figure 4.3.8:** Overview plots of the effects the  $\phi'$  scenarios have on the deformations of the wall.



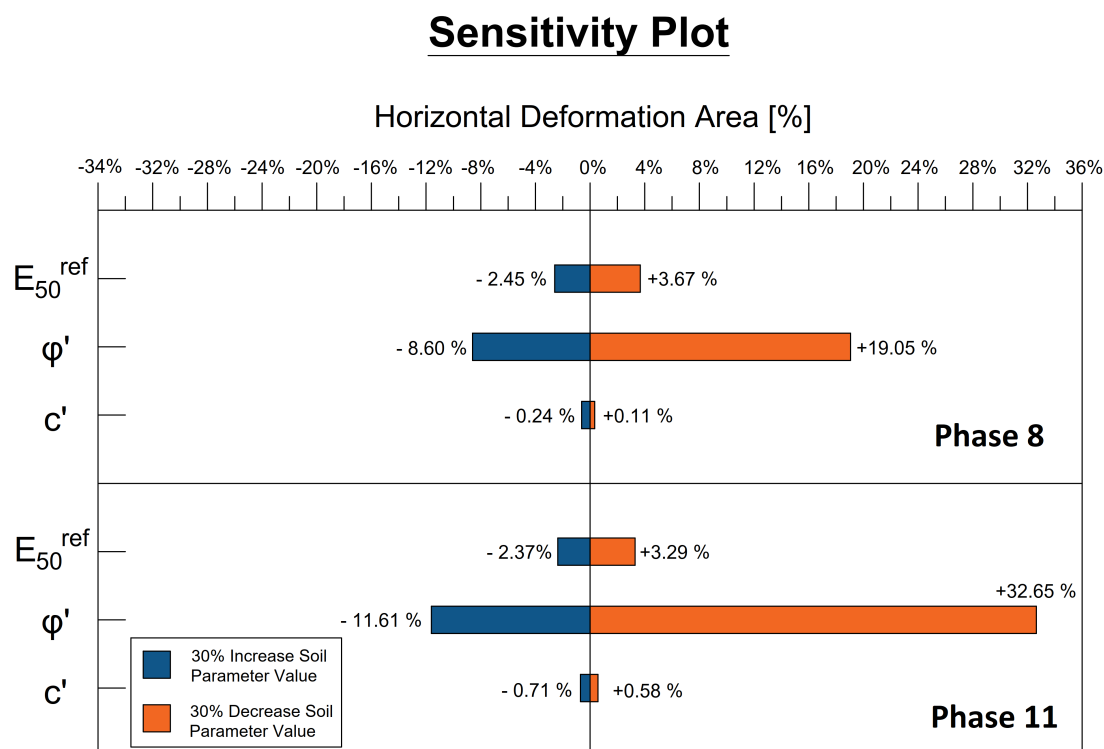
**Figure 4.3.9:** Overview plots of the effects the  $c'$  scenarios have on the deformations of the wall.

The previous plots have been constructed using the Python Application mentioned in Chapter 3. It is also possible for the user to plot the evolution of the vertical deformations, the moments, and the vertical and horizontal forces of the wall.

### 4.3.3 Summary and Discussion

After investigating the secant stiffness  $E_{50}^{ref}$ , effective friction angle  $\phi'$ , and effective cohesion  $c'$ , several conclusions regarding the project's sensitivity to the Boom Clay parameters can be derived. When considering the whole range of scenarios, the rate of change for the stiffness and friction angle is not linear, especially in very low values. On the other hand, the rate of change for cohesion remains almost constant, so it is linear. This behavior is shown in Figures 4.3.5a, 4.3.5b, and 4.3.5c, for  $E_{50}^{ref}$ ,  $\phi'$ , and  $c'$ , respectively. In all cases, the change in deformations is confirmed by the change in moments the wall experiences. Additionally, as seen in the overview 3D and 2D Figures 4.3.7, 4.3.8 and 4.3.9, the deformations and moments are affected the most by low values in effective friction angle. The effective cohesion has limited influence on the deformations and the stiffness, an intermediate effect. Finally, the influence propagates in higher locations than the location of the Boom Clay layer.

The tornado style Figure 4.3.10 summarizes the effect on deformations of the  $\pm 30\%$  change of the soil properties for Phases 8 and 11. In every case, reducing the parameter's values causes an increase in horizontal deformations, and increasing the parameter's values does the opposite. Out of all the parameters, the highest effect is caused by the effective friction angle. Following is the secant stiffness, and lastly, the effective cohesion. When investigating the stiffness individually, Phase 8 and Phase 11 behave similarly. Effective cohesion has a more significant impact on Phase 11. Effective friction angle has more implications for Phase 11 when the parameter increase and a more substantial effect on Phase 8 when the parameter is decreased.

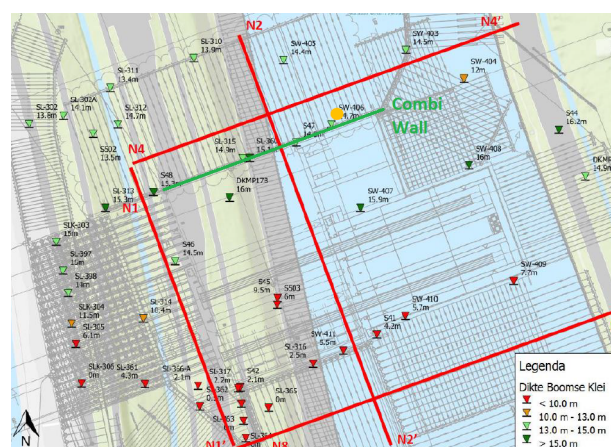


**Figure 4.3.10:** Tornado plot for the percentage of deformation change caused by 30 % change of the soil parameters for the Boom Clay layer.

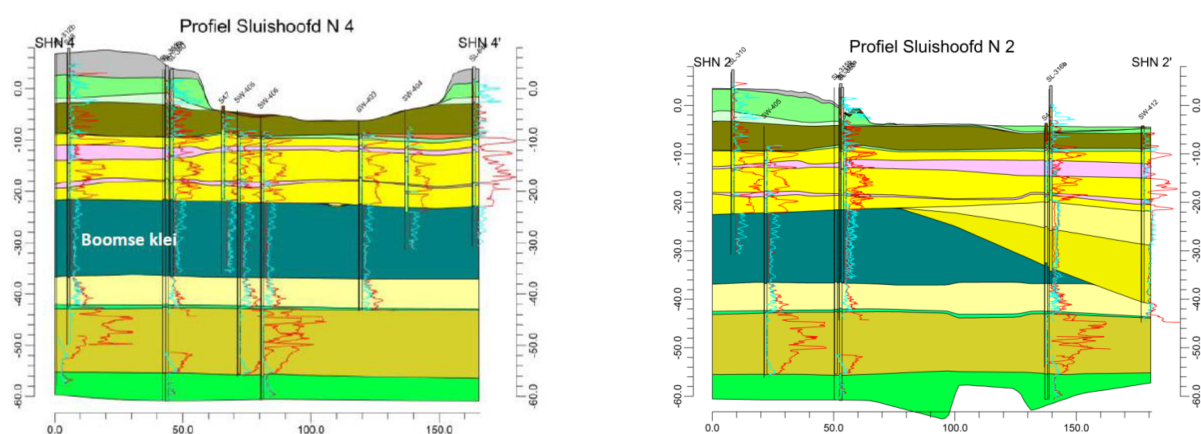
#### 4.4 Impact of the Boom Clay Thickness

The outer lock head, whose general position is given in Figure 4.4.1, is constructed above a wedging layer of Boom Clay. The green line depicts the location of the investigated combi-wall, and the red lines are the locations of soil cross-sections. The cross-section N4-N4' is parallel with the wall and is given in Figure 4.4.2a. The thickness of the Boom Clay layer remains constant in that direction. However, in the soil cross-section N2-N2' perpendicular to the combi-wall given in Figure 4.4.2b, the Boom Clay thickness is reducing. Therefore, investigating the Boom Clay's thickness effect on the behavior of the retaining wall is relevant and important. Moreover, an investigation of the Boom Clay by de Nijs et al., 2015 [28] has shown that the Boom Clay layer is prone to partially cracking when it is unloaded due to swelling. At those locations, the material would behave drained. Therefore, the question is, what is the effect of the Boom Clay thickness on the deformations of the retaining wall, and are the scenarios with a thinner layer more prone to failure due to wrongful consideration of undrained conditions?

The question will be approached by first shortly discussing the theory of drained and undrained modeling and clarifying why it is relevant to the present case study. Then the construction of virtual cross-sections that gradually reduce the thickness of the Boom Clay (L15) layer and replace it with the adjacent upper Sand (L08) layer will be performed. The new cross sections will be generated by adjusting the soil geometry of the Fine Tuned model discussed in Section 4.2. Such geometries can be found in different pit locations, especially towards the southeast side of the outer lock head. Since these new cross-sections are fictional and do not correspond to specific inclinometers, the comparison will be made with the Fine Tuned model to quantify the effect. The effect of the change from drained to the undrained condition will also be investigated for the different Boom Clay thicknesses.



**Figure 4.4.1:** Top view of the outer lock head in the new Terneuzen lock. [Design Documents]



**(a)** Soil Profile of the excavation location in Terneuzen and cross-section N4-N4'.

**(b)** Soil Profile of the excavation location in Terneuzen and cross-section N2-N2'.

**Figure 4.4.2:** Soil cross section at the area of the outer head of the New Terneuzen Lock. [Design Documents]

#### 4.4.1 Undrained versus Drained modeling

There are drained and undrained conditions when it comes to modeling fine-grained soils. A drained calculation assumes that the water can immediately run off the soil layer under load. Therefore, no over- or under-water pressures are being built up. This is the safest model method and is being applied when the material's permeability is relatively high, when the loading rate is slow relative to the permeability, and when the construction phases last relatively long, so the short-term behavior of the layer cannot be counted on. On the other hand, an undrained calculation assumes that when the load increases, the water does not have sufficient time to drain from the layer, so water overpressure builds up. Such conditions increase the strength of fine-grained soil layers. Contrary to the drained conditions, it can be applied when the permeability is relatively low, when the loading conditions are changing quickly and when the construction phases last for a short period.

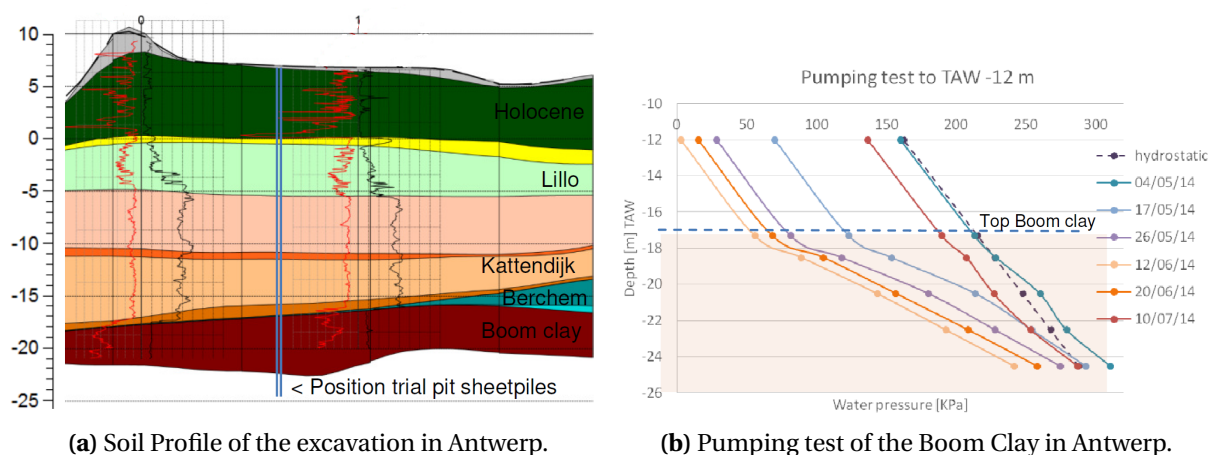
For deep excavations, Vermeer and Meier, 1998 [32], deduced that when:

- $T < 0.1$  ( $U < 10\%$ ) → Use undrained conditions
- $T > 0.4$  ( $U > 70\%$ ) → Use drained conditions

Where  $T$  is a dimensionless time factor and  $U$  is the degree of consolidation. The  $T$  is given by Equation 4.4.1 and shows that the undrained soil behavior depends on the permeability  $k$ , the oedometer modulus  $E_{oed}$ , the unit weight of water  $\gamma_w$ , the drainage length  $D$ , and construction time  $t$ .

$$T = \frac{k * E_{oed}}{\gamma_w * D^2} * t \quad (4.4.1)$$

A novel endeavor was the construction and monitoring of a trial pit excavation in Antwerp, focusing on the behavior of Boom Clay. That layer is located at a depth of -20 m NAP, similar to the project this thesis investigates. Additionally, the two projects have similar geological profiles, as shown in Figure 4.4.3a and Figure 4.4.2a for the Antwerp and Terneuzen project, respectively. In the trial pit, they deliberately created conditions by pumping and excavating to measure the pore water pressures of the Boom Clay, among others. A paper on the topic has been written by de Nijs et al., 2015 [28]. It concludes that the top two meters of the Boom Clay layer indicate a much higher permeability according to piezometers, whereas the lower levels have much lower permeability (Figure 4.4.3b). The higher permeability can be attributed to the formation of cracks at the upper part of the layer due to swelling and is shown in the pumping test of the Boom Clay (Figure 4.4.3b).



**Figure 4.4.3:** Soil cross-section and pumping test of the Boom Clay from the Antwerp trial pit. [de Nijs et al., 2015 [28]]

Therefore, the formation of cracking can affect the permeability  $k$  and the drainage path length  $D$ , which according to Vermeer and Meier, 1998 [32] are parameters that regulate whether the layer can be considered drained or undrained. The risk is increasing for locations where the Boom Clay thickness is insufficient. Therefore, the cross-sections with lower Boom Clay thickness will also be examined in drained conditions to quantify the effects on the retaining wall.

#### 4.4.2 Thickness Investigation

When calculating the equilibrium of a construction pit retaining wall, the behavior of the passive zone is usually calculated as drained in the Netherlands. This is a safe approach because estimating the period over which the passive zone reacts undrained usually cannot be accurately determined in advance. Permeability is an important parameter in whether the fine-grained material is drained or undrained. In the project under investigation, some of the construction phases required the design of the Boom Clay as undrained due to economic significance. However, it was a decision that imposed many time and construction constraints due to the unknowns in Boom Clay's behavior.

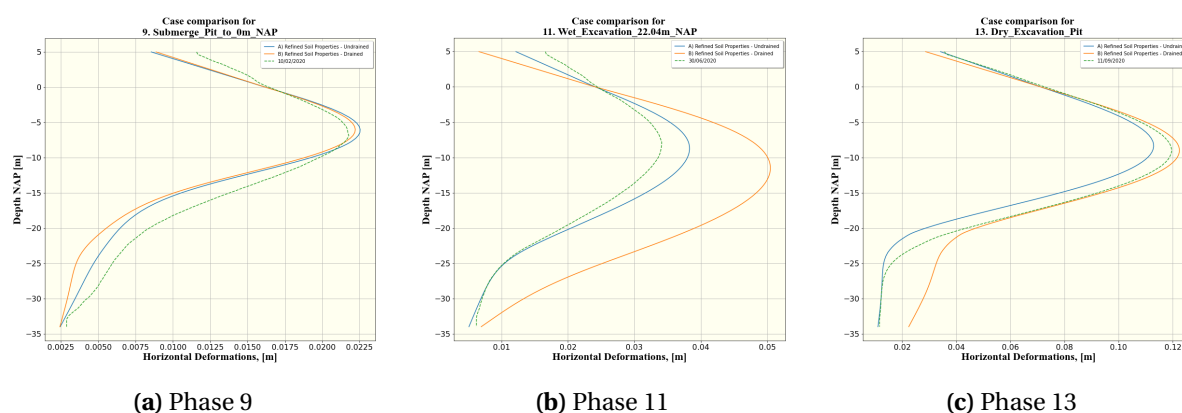
Further investigation is deemed necessary considering that:

- The Boom Clay thickness is not constant throughout the project
- The need to design undrained for certain phases of the present project
- The not uniform permeability throughout the Boom Clay layer according to de Nijs et al., 2015 [28].

Utilizing the monitoring data from the inclinometers that captured the actual behavior of the combi-wall and allowed the creation of the Fine Tuned model, four extra scenarios will be run with different Boom Clay thicknesses to investigate the effect. The thickness of the Boom Clay layer in the original location is 16.1 m. The new models will have thicknesses of 13, 10, and 7 m of Boom Clay.

### Finetuned model in partially undrained and drained conditions

The Fine Tuned model is discussed in Section 4.2 and simulated the Boom Clay with the HS-small model, considering undrained conditions from Phase 9 till the end (Partially undrained approach). This decision has been made to agree with the undrained stages the actual design followed. The scenario where the Boom Clay is undrained from the beginning is investigated in Appendix I.2, and the effect is minimal. A comparison of the Fine Tuned model and a model where the Boom Clay is drained through all the stages is given in Figure 4.4.4. Since the models are the same until Phase 8, only the following stages will be considered.



**Figure 4.4.4:** Comparison of partially undrained and drained Fine tuned model for 3 phases.

The fully drained model (orange line) fits worse with the monitoring deformations (dashed line) in all three construction stages. Especially in the most crucial Phase 11, where the behavior of the Boom Clay is essential, it significantly overestimates the deformations. Therefore, it is proven that the drainage conditions are undrained in reality until Phase 13 and the consideration of drained conditions is over-conservative. The difference is quantified in Table 4.4.1. Specifically, for Phase 11, the Partially undrained Boom Clay model has 83 % higher accuracy than the fully drained model.

### Effect of Boom Clay thickness to the deformations of the wall

This paragraph will investigate the effect of deformations when the Boom Clay thickness varies. Figure 4.4.5a compares deformations of models for Phase 11 that consist of different Boom Clay layer

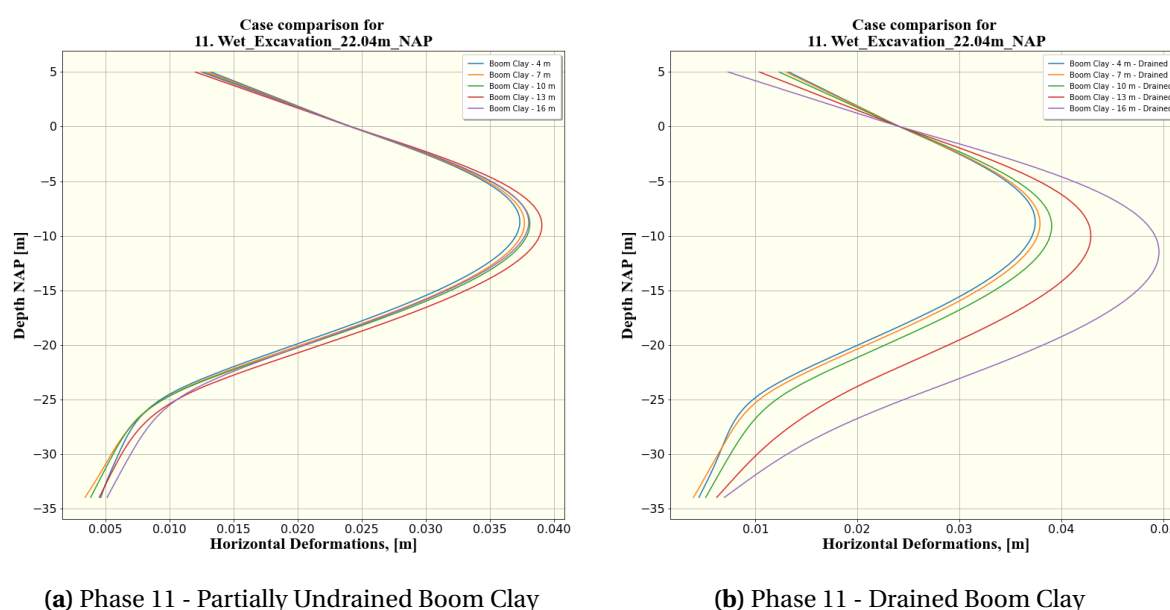


**Table 4.4.1:** Area in  $m^2$  from the monitoring data of the Partially undrained Boom Clay model and the fully drained Boom Clay model.

	Phase 9	Phase 11	Phase 13
Partially Undrained Boom Clay model	0.067	0.078	0.226
Fully Drained Boom Clay model	0.053	0.468	0.246

thicknesses and consider Partially Undrained Boom Clay. As explained in the previous paragraph, Partially Undrained Boom Clay means that the layer is simulated in drained conditions until Phase 8, and the following phase uses undrained conditions. On the other hand, Figure 4.4.5b compares deformations for models with different Boom Clay on Phase 11 but with fully drained conditions. Fully drained conditions mean that throughout all the construction phases, the Boom Clay is kept at drained conditions.

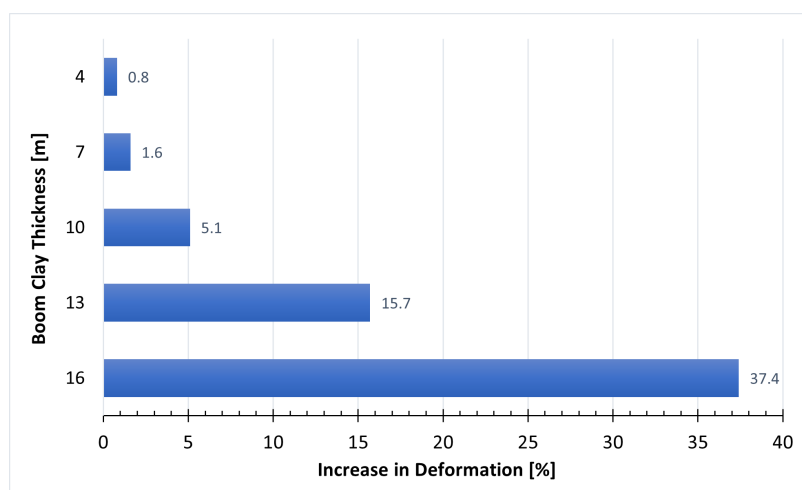
By interpreting Figure 4.4.5 many conclusions can be drawn. In Figure 4.4.5a, thinner Boom Clay (L15) layers are replaced by the adjacent upper Sand (L08) layer, and partially undrained conditions are considered. The comparison does not show a significant change in deformations; as a matter of fact, a slight decrease is noticed. On the other hand, Figure 4.4.5b shows that the difference in deformations is significant for the various Boom Clay thicknesses when drained conditions are being considered. The models that have thinner Boom Clay layers cause fewer deformations. Therefore, the locations with thinner Boom Clay layers are less susceptible to deformations if undrained conditions are wrongfully considered. The quantified effect of transitioning from Partially Undrained to Fully Drained Boom Clay conditions for the different layer thicknesses is given in Table ??.



**Figure 4.4.5:** Deformation comparison for different Boom Clay thicknesses in partial undrained and drained Boom Clay conditions.

### 4.4.3 Summary and discussion

The effect on the thinner Boom Clay layers' deformations depends on the drainage conditions considered. If the *Partially Undrained* conditions are considered, the deformations remain relatively the same throughout the scenarios (Figure 4.4.5a). On the other hand, if the *Fully Drained* conditions



**Figure 4.4.6:** Percentage increase in deformations when transitioning from Partiality Undrained to Fully Drained Boom Clay for different thicknesses.

are considered, the thickness of the layer imposes greater influence on the horizontal deformations of the wall. More specifically, the thinner the layer, the fewer the deformations. That is a logical outcome because when the Boom Clay is drained has weaker retaining properties, so reducing this weaker layer and using a stronger sand layer positively impacts the deformations. Therefore to answer the second part of the question, the case of wrongfully considering undrained conditions for the Boom Clay layer is less severe at the location where the layer is thinner.

However, the results are relevant for this specific case. A limitation that is imposed on the approach is the fictional scenarios. The effect the thickness will have in the other locations would be determined more accurately if they had been analyzed with their geometries and unique features. For instance, an assumption that is generally true but not exact is that in every location, all the Boom Clay is replaced only by layer L08. Unfortunately, the complete analysis of other locations would significantly exceed the time frame of the present thesis.

## 4.5 Model Prediction

The conventional project design methods consist of very conservative designs to increase safety and overcome all the uncertainties. However, such a design is rather costly and often prohibits project construction. Therefore, the observation method, whose advantages have been discussed by Nicholson et al., 1999 [27], has become more popular in recent years. It allows the engineers to adjust their design during construction based on monitoring data from the field. As a result, the project is not heavily over-designed, and to reduce the risk factor, mitigating measures are decided and applied in case the field data mandate it. However, due to the nature of this application of utilizing monitoring information efficiently as produced, it can be beneficial for the observational method as well.

The application developed in the present thesis follows the idea of the observation method but is different. It will use the monitoring data as being produced, but it will not suggest mitigating measures. However, the goal is for the tool to be used alongside the conventional design and improve its certainty by adding information. Additionally, it can be used in site engineering to investigate solutions to problems using the actual conditions applied in the project rather than those predicted during the design. An example will be investigated to prove whether utilizing information from early

construction stages can improve the designer's confidence for future stages.

### 4.5.1 Investigation

In this section, an investigation of how the monitoring data can be used to improve the project's original design will be conducted. The focus of the present section will be only on the parameters of the soil layers. All the models will have the same structural elements, loads, heads, and geometries as decided in Chapter 2, with the only variable being the soil properties. In this section, three models will be considered locally to perform the investigation: the Initial, the Base, and the Improved models. Because such an investigation requires many calculations, the sensitivity analysis tool introduced in Chapter 3 will be used.

The first model discussed is the Initial model. It uses the soil properties used in the original design for the cross-section L01b. These values are characteristic and are summarised in Table 2.8.2 under the Design values section. One of the most influential soil layers for the present retaining wall is the Boom Clay (L15), spanning from -21.5 m NAP to -37.6 m NAP. Due to uncertainties of the Boom Clay behavior, a rather simplistic constitutive model has been used for the design, the Mohr-Coulomb. This constitutive model uses one stiffness property to represent the material's behavior. According to the project report, Boom Clay was expected to be in unloading reloading conditions; hence the stiffness  $E'$  used by the designers is the un-/reloading stiffness  $E_{ur}$ . Additionally, to simulate the undrained condition after Phase 8, it uses a method called Quasi approach that keeps the drainage conditions of the layer drained but doubles the cohesion. Based on this method, the properties of the undrained Boom Clay (L15b) are given in Table 2.8.2 under the Design values.

Firstly, parametric research in this thesis has shown that using Mohr-Coulomb for the Boom Clay, no optimum convergence with the monitoring deformations can be achieved. Secondly, the quasi-method for designing undrained conditions is not universally accepted. For these reasons, it has been decided to change the constitutive soil model to the Hardening Soil Small Strain, the most appropriate model for the present Boom Clay as discussed in Section 4.1. The new properties HS-small model demands are created based on the methods described in Chapter 2. Similarly, using the Undrained method A, the new model will keep the undrained condition after Phase 8. This new model, the Base model, will be used to research the prediction capabilities. The Boom Clay layer properties of the Initial and Base model are summarized in Table 4.5.1. The difference in deformations produced using these models for Phases 8, and 11 is depicted in Figure 4.5.1a and 4.5.1b, respectively. The improvement in deformations just by changing from the MC (green line) model to the HS-small (blue line) for the Boom Clay is noticeable.

The first construction phase monitored in the design is Phase 8: End of dry excavation to -11 m NAP. It will act as the first stage, where the project's engineers have information from monitoring that can be utilized to prove or improve their design for the later stages. Therefore, this section will investigate how much better the prediction of the deformations for Phase 11: End of wet excavation to -22 m NAP is if the soil properties are updated in Phase 8 utilizing the monitoring compared to the original design. Phase 11 has been chosen as a point of reference because it is one of the most crucial construction phases of the project. At that phase, the excavation reaches the highest depth, and the only material supporting the combi-wall are the anchors at 0 NAP and the controversial Boom Clay.

In Figures 4.5.1a and 4.5.1c the deformations and the moments of the wall are given for Phase 8, respectively. Focusing on the Base model (blue line), the difference with the monitoring prediction (dashed line) is noticeable. Following the same methodology as Section 4.2, the moment's plot is being considered to determine which soils interact with the wall at a particular construction phase. It can be concluded that the Sand (L08) [-12, -21.5] m NAP and Boom Clay (L15) [-21.5, -37.6] m

**Table 4.5.1:** Boom Clay properties for the initial, base and improved model in drained and undrained conditions.

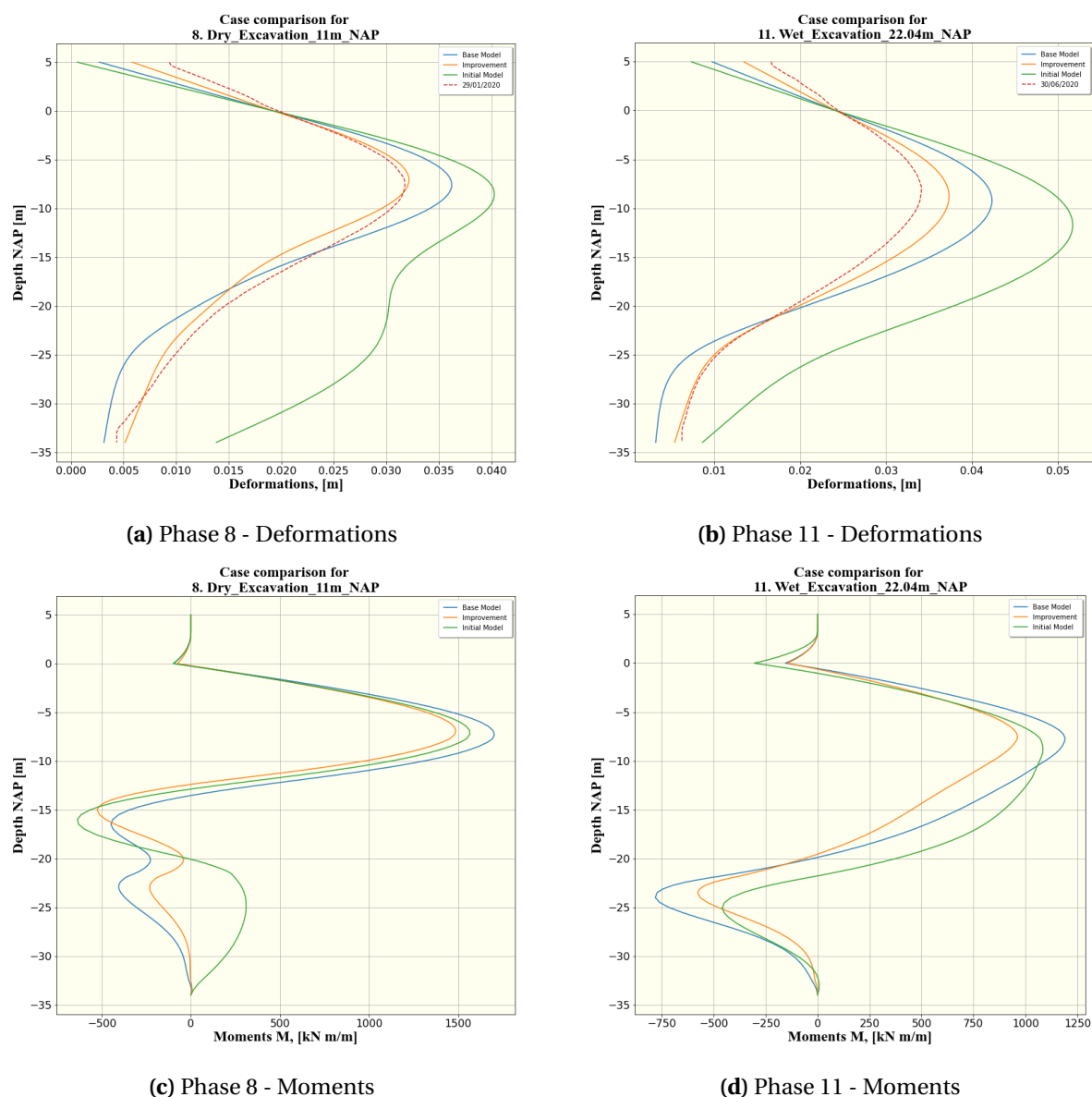
Name	Initial Model			Base Model			Improved Model		
	L15	L15b	L08	L15	L15b	L08	L15	L15b	L08
<b>Model</b>	MC	MC	HSS	HSS	HSS	HSS	HSS	HSS	HSS
<b>Drain.</b>	Drai.	Drai.	Drai.	Drai.	Undr. A	Drai.	Drai.	Undr. A	Drai.
$\gamma_{dry}$	19.2	19.2	18	19.2	19.2	18	19.2	19.2	18
$\gamma_{sat}$	19.2	19.2	20	19.2	19.2	20	19.2	19.2	20
$\phi'$	22	22	35.8	22	22	35.8	<b>20</b>	<b>20</b>	<b>42</b>
$c'$	15	30	0	15	<b>15</b>	0	<b>16</b>	<b>16</b>	0
$\psi$	0	0	2.8	0	0	2.8	0	0	10
$E^{ref}$	52000	52000	-	-	-	-	-	-	-
$E_{50}^{ref}$	-	-	<b>50000</b>	<b>17300</b>	<b>17300</b>	<b>50000</b>	<b>20000</b>	<b>20000</b>	<b>60000</b>
$E_{oed}^{ref}$	-	-	<b>37700</b>	<b>17300</b>	<b>17300</b>	<b>37700</b>	<b>20000</b>	<b>20000</b>	<b>60000</b>
$E_{ur}^{ref}$	-	-	<b>200000</b>	<b>52000</b>	<b>52000</b>	<b>200000</b>	<b>40000</b>	<b>40000</b>	<b>180000</b>
$v$	0.3	0.3	-	-	-	-	-	-	-
$v_{ur}$	-	-	0.15	0.3	0.3	0.15	0.3	0.3	0.15
$m$	-	-	0.5	0.8	0.8	0.5	0.8	0.8	0.5
$G_0^{ref}$	-	-	201000	93400	93400	201000	78462	78462	223500
$\gamma_{07}$	-	-	1.0E-4	4.07E-4	4.07E-4	0.0001	4.68E-4	4.68E-4	9.7E-5

NAP are responsible for retaining the wall in the active side at Phase 8. Therefore, the parameters that are meaningful to adjust are those soil layers. Many scenarios can be run automatically using the sensitivity analysis tool for the improved soil properties to be selected. The Improved model contains the refined soil properties for layers L15 and L08. The values of the properties are given in Table 4.5.1, the deformations and moments of the Improved model (orange line) are depicted in Figure 4.5.1a and 4.5.1b for Phase 8, respectively.

To examine the prediction method benefits Figure 4.5.1b and 4.5.1d are examined for the deformations and moments of Phase 11, respectively. The deformations of the improved model (orange line) fit better the monitoring data (dashed line) than the base model (blue line) in Phase 11. The quantified improvement of deformations is given in Table 4.5.2. The improved accuracy in Phase 11 is 66 % because from 0.169  $m^2$  area difference of the Base model from the monitoring data became 0.058  $m^2$  with the Improved model. The area between curves has been calculated using the Reimann Sums described in Paragraph 4.3.1.

**Table 4.5.2:** Area difference between the three models deformations from the monitoring deformations, for Phase 8 and Phase 11.

Area Difference [ $m^2$ ]	Initial Model	Base Model	Improved Model
Phase 8	0.414	0.107	0.049
Phase 11	0.463	0.169	0.058



**Figure 4.5.1:** Comparison of the initial, base and improved model predictions for Phases 8 and 11.

## 4.5.2 Summary and discussion

To conclude, the model can be improved as the project is being constructed and monitoring data are produced. In the specific example, by utilizing information in Phase 8, 66 % more accuracy was achieved in Phase 11. To improve the soil or other parameters, many scenarios must be calculated in the finite element program PLAXIS and then interpreted. The automation and the interpretation tools provided by the Python Application of Chapter 3 make this process viable at the prospect of time and data management. This case altered only the stiffness and strength properties of the materials through twenty repetitions. When more parameters are tested with more repetitions, higher accuracy is possible. However, more repetitions were not viable time-wise in the present thesis; hence the twenty repetitions are also a limitation of the analysis conducted. Therefore, an automated approach is suggested as a topic of future research in Section 5.2.

Additionally, it is important that the project this tool will be used on to have frequent monitoring of the deformations and the operations in the project. The New Terneuzen project, even though it had

sufficient monitoring for this tool to be applied other aspects like the external loads applied or exact timelines were not perfectly logged. Therefore, educated guesses and assumptions had to be made, as explained in Chapter 2.

Nevertheless, conducting this investigation would confirm or improve the existing model of the project and, by providing more information, would reduce the risk factor and uncertainty for future phases. Finally, the prediction of future construction phases is favored when there is a predominant retaining layer like the Boom Clay. Hence, this can be considered another limitation of the tool.

## 4.6 Design Improvement

This thesis attempted to simulate the actual design used in the project by creating the Design model. The actual and the Design model have the same soil layer modeling aspects (properties, constitutive models, drainage). However, they differ on other design elements like the applied loads, structural elements, and aquifer heads. The Design model will use the previously mentioned parameters as performed in reality. The orange line in Figures 4.6.2, 4.6.3 and 4.6.4 depicts the deformation predictions of the Design model for Phases 8, 11 and 13, respectively. This orange line is the closest simulation of the actual design this thesis has to offer.

Early on, it was observed that the Design model had poor predictions compared to the monitoring for the entire wall. The Mean and Fine Tuned models discussed previously were able to improve the prediction in the lower location of the wall using more advanced constitutive models for the important Boom Clay layer and mean soil properties for all the layers. However, the problem with the predicted deformations at the anchor level remained. Therefore, the assumption of prescribed deformations of the combi wall at the anchor level has been made.

This section will focus on the aspects that could improve the predictions of the actual design. Firstly, the outcome of the Fine Tuned model, discussed in Section 4.2, will be compared with the outcome of the Design model. Then the assumption of prescribed deformations will be investigated along with a potential solution to the problematic simulation of the anchoring system. Lastly, attention will be given to the effect the Design and Fine Tuned model with the different fixity methods have on the combi wall safety by performing each time the unity check (UC).

The results from all the investigations of the present section are summarized in Figure 4.6.2, 4.6.3 and 4.6.4 for the deformations and the moments. Table 4.6.1 contains the quantified comparison of the model predictions with the monitoring deformations for all the investigations.

### 4.6.1 Improvement of the Design Model with the Fine Tuned model.

Figures 4.6.2, 4.6.3 and 4.6.4 present the deformations of the Design (orange line) and Fine Tuned (purple line) model without the deformation restrains for the construction Phases 8, 11 and 13, respectively. Both models predict poorly the deformations at the anchor level for all the construction phases. Moreover, the Design model does not predict the deformations at the lower part of the wall where the Boom Clay is located. Whereas the Fine Tuned model with the more advanced constitutive model, discussed in Section 4.1, and the refined soil properties through the iterative method, discussed in Section 4.2, can provide a much more accurate prediction for the lower part of the wall. More specifically, the accuracy of the predictions has improved by 72 %, 75 %, and 60 % for Phases 8, 11, and 13, respectively. Quantification of the improvement has been performed with the area change calculation through the Riemann method (Paragraph 4.3.1); the results are given in Table 4.6.1.

Additionally, Figures 4.6.2, 4.6.3 and 4.6.4 present the moments of the Design (orange line) and Fine Tuned (purple line) model without the deformation restrains for the construction Phases 8, 11 and 13. Even though there is a difference in the moments between the Design and Fine Tuned model for Phases 8 and 11, it does not matter. These moments are covered either way by the moments of the governing Phase 11 that determine the retaining wall's design and will be discussed for every scenario in Paragraph 4.6.4.

#### 4.6.2 *Fixed versus Free approach retaining wall modeling*

Despite improving the prediction in the lower part of the wall using the Fine Tuned model, the prediction at the anchor location is still unsatisfying. Firstly, a parametric investigation of the layers concerning the anchoring system has been conducted to investigate this effect. The properties of the responsible layers for the anchor system were improved, and significant reductions in the external loads were performed. None of these changes allowed for a better match with the monitoring. Furthermore, the analysis was conducted for a different wall location, monitored by a different inclinometer to rule out faulty data. The results showed the same over predictions of wall deformations at the anchor level. Therefore, to reduce the uncertainties and focus on the Boom Clay location of the wall, the assumption had been made that the deformation of the wall at the anchor level should follow the monitoring deformations. To achieve this, the wall in the finite element program PLAXIS had pre-described horizontal movement at the anchor level. With this assumption, the Fine Tuned model was created. In this section, the effect of this decision will be investigated. The terms *Fixed approach* will refer to prescribed deformations at the anchor level of the wall, and the term *Free approach* will refer to no deformations restrains at all.

Initially, the Design model with *Fixed* (blue line) and *Free* (orange line) deformations are going to be compared (Figures 4.6.2, 4.6.3 and 4.6.4). In the project's actual design, the engineers could not fix the deformation of the wall at the anchor level because, at that point, the construction of the wall had not started yet. Therefore, they overpredicted by 84 %, 114 %, and 78 % the deformations for Phases 8, 11, and 13, respectively. The moments of the wall for Phases 8 and 11 of the Fine Tuned model are slightly different from the Design model. However, this does not influence the design of the wall because Phases 8 and 11 are not governing. The safety of the wall will be discussed in Paragraph 4.6.4 for the governing construction phase.

Even though a better match in deformations is produced at the top part of the wall when *Fixing* the movement, the bottom is still problematic in the Design model. That is why the better constitutive model has been chosen and proven in Section 4.1 for the Boom Clay. Additionally, the refined soil properties have been used to create the Fine Tuned model with Hs-small for the Boom Clay to be comparable with the monitoring deformations. Using the more realistic Fine Tuned model, the design choice of *Fixed* versus *Free* deformations will be investigated. The horizontal deformations and moments for the *Fixed* (red line) and *Free* (purple line) Fine Tuned model are compared in Figures 4.6.2, 4.6.3 and 4.6.4. Similarly to the Design model comparison made in the previous paragraph, the deformations were significantly reduced. The moments have differences for Phase 8 and Phase 11 but are still less than the governing Phase 13.

The deformation predictions have improved when comparing the *Fixed* approach of the Fine Tuned and Design model. However, the moments of Phase 13 that dictate the design of the wall are relatively similar for both models and all the fixity approaches. Therefore, the design choice of fitting the deformations at the anchor level would not have changed the calculation of the wall stiffness. In case the settlements behind the wall were relevant, they would have to spend more on a stiffer pile to deform less, even though, in reality, the wall would have never reached these deformations. The axial and shear forces figures are summarized in Appendix I.3.

Ultimately, no matter the decision of using mean soil properties or characteristic soil properties, HS-small or Mohr-Coulomb for the Boom Clay layer, the problem of predicting the deformations at the anchor level remains and affects the stiffness of the wall when the settlements are of significance.

### 4.6.3 Potential solution with shaft friction on the anchor rods

It is speculated that the problem originates from the fact that PLAXIS does not provide the option to include an interface to the Node-to-Node plates that are used to simulate anchor rods. As described in Section 2.4, the anchor rods used have a significant length (45 m) and significant diameter (110 cm), and they are made out of steel, a material that is considered to be relatively rough. Therefore, the shaft friction developed on them is not irrelevant. Consequently, it will be attempted to simulate the shaft friction of the anchor rod.

The shaft friction capacity  $Q_s$  of the anchor rod is derived by the Equation 4.6.1, where  $P$  is the perimeter,  $L$  the length of the anchor rod, and  $\tau_f$  is the unit shear friction. The  $\tau_f$  is derived by the Equation 4.6.2, where  $K_f$  is the coefficient of lateral earth pressure,  $\delta$  is the interface friction angle, and  $\sigma'_v$  is the effective vertical stress.

$$Q_s = P * L * \tau_f \quad (4.6.1)$$

$$\tau_f = K_f * \tan(\delta) * \sigma'_v \quad (4.6.2)$$

$$\sigma'_v = \gamma_{dry} * z \quad (4.6.3)$$

$$K_0 = 1 - \sin(\phi') \quad (4.6.4)$$

$$\delta = \begin{cases} x = \phi' - 2.5, & \text{if } x \leq 27.5 \\ 27.5, & \text{otherwise} \end{cases}$$

Considering that the anchor rod is located inside a sand layer (LX02) with effective friction angle,  $\phi'$  equal to  $37.5^\circ$ , dry unit weight  $\gamma_{dry}$  equal to 18.75 at a depth  $z$  of 3.5 m the effective vertical stress  $\sigma'_v$  according to Equation 4.6.3 is  $65.63 \text{ kN/m}^2$ . The interface friction angle  $\delta$  and the coefficient of lateral earth pressure  $K_0$  are  $27.5^\circ$  and 0.391, respectively. Therefore, through Equation 4.6.2, the unit shear friction is 13.36 kPa. However, because there is an external uniformly distributed load on top of approximately 10 kPa, the  $\tau_f$  equals 15.35 kPa. Finally, the shaft friction capacity  $Q_s$  of the anchor rod according to Equation 4.6.1 is 239 kN. Therefore, the force is applied as a concentrated horizontal load on the anchor wall (pink arrow) of Figure 4.6.1 to simulate the shaft friction of the rod.

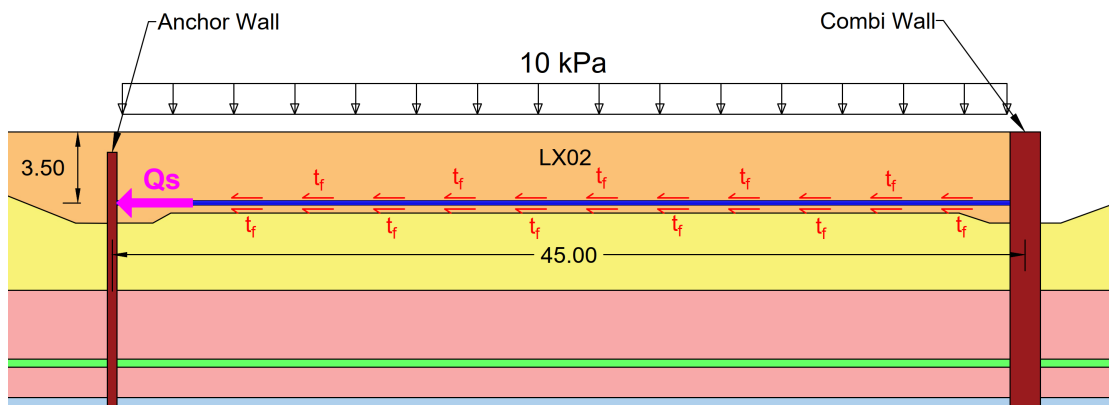


Figure 4.6.1: Anchor rod - shaft friction



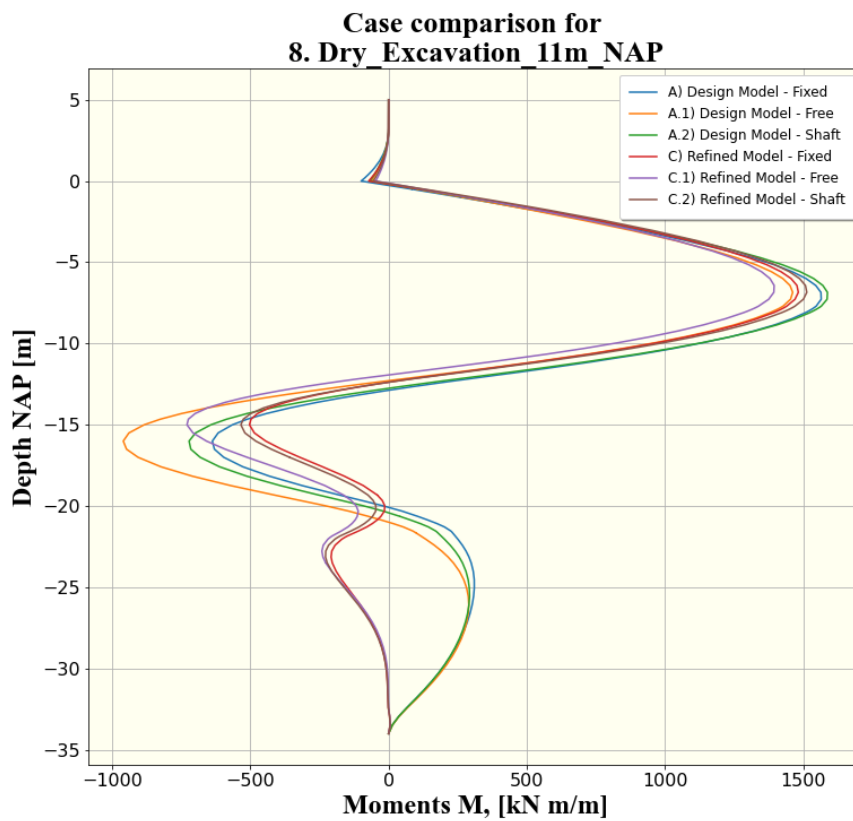
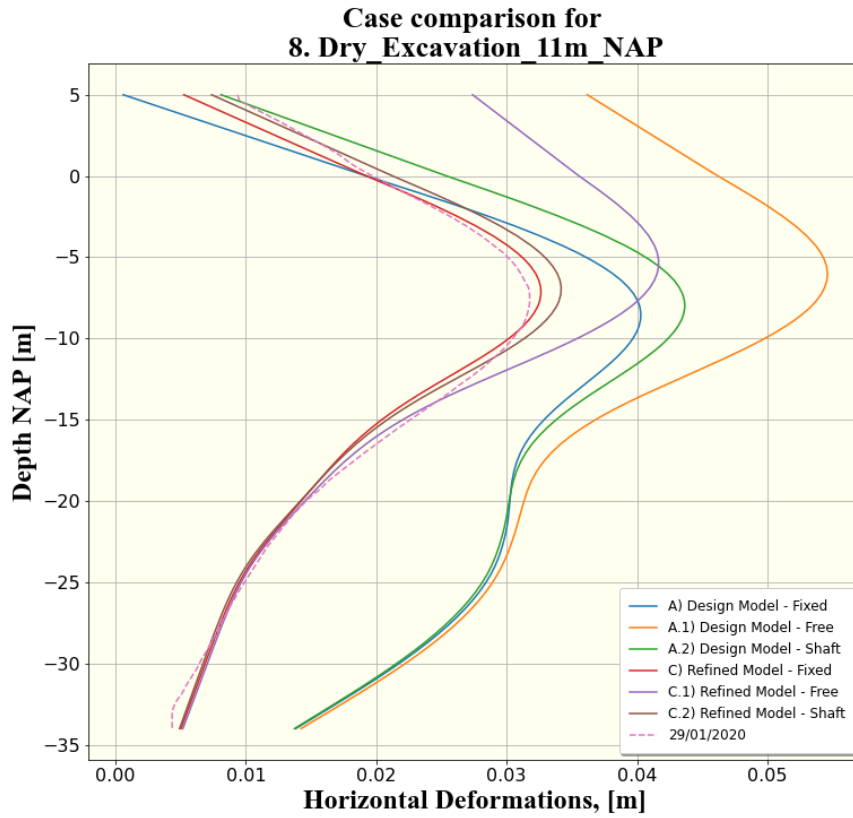
The results are remarkable, as shown in Figures 4.6.2, 4.6.3 and 4.6.4 with a green line for the Design model and brown line for the Fine Tuned model. The deformations at the anchor level, both for the Design and Fine Tuned model, for both construction phases, are almost the same as when they were *Fixed*. Therefore, the shaft friction of the anchor rod significantly affects the wall's deformations.

This method applied to the Fine Tuned model represents the reality as accurately as possible without the artificial restraints on the deformations. Table 4.6.1 present the quantified results of all the methods for the three models. It uses the area change of each model with the corresponding monitoring deformations, as analyzed in Paragraph 4.3.1. The proximity of the Shaft and Fixed values for all three models indicated the effectiveness of the shaft friction consideration. Additionally, it would allow the project's designer to better predict the deformations at the anchor level without the knowledge of the monitoring deformations.

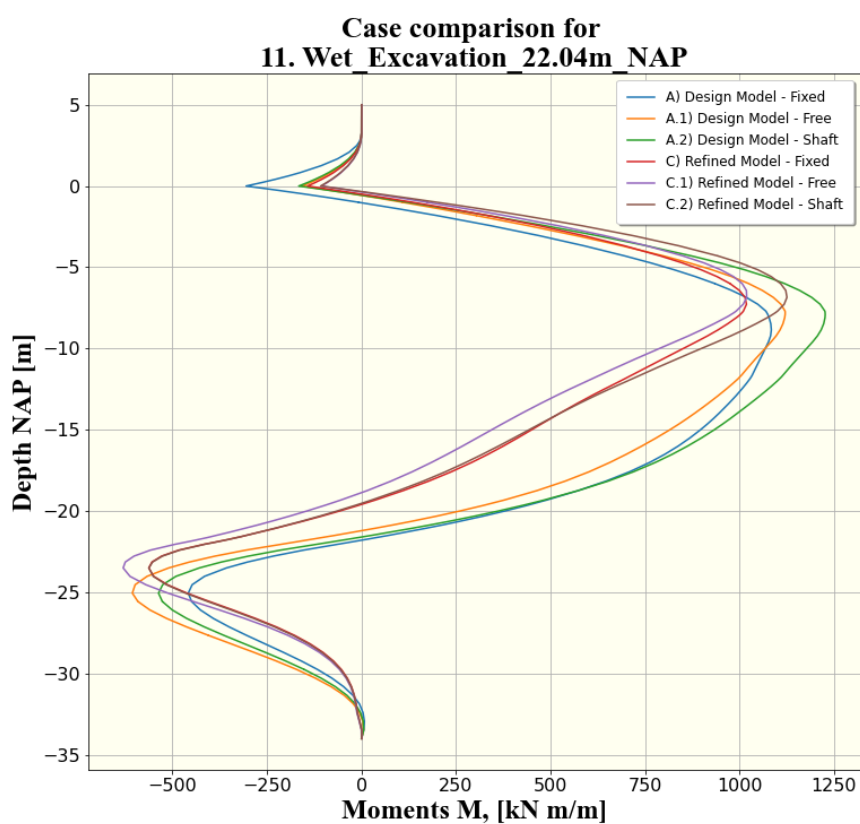
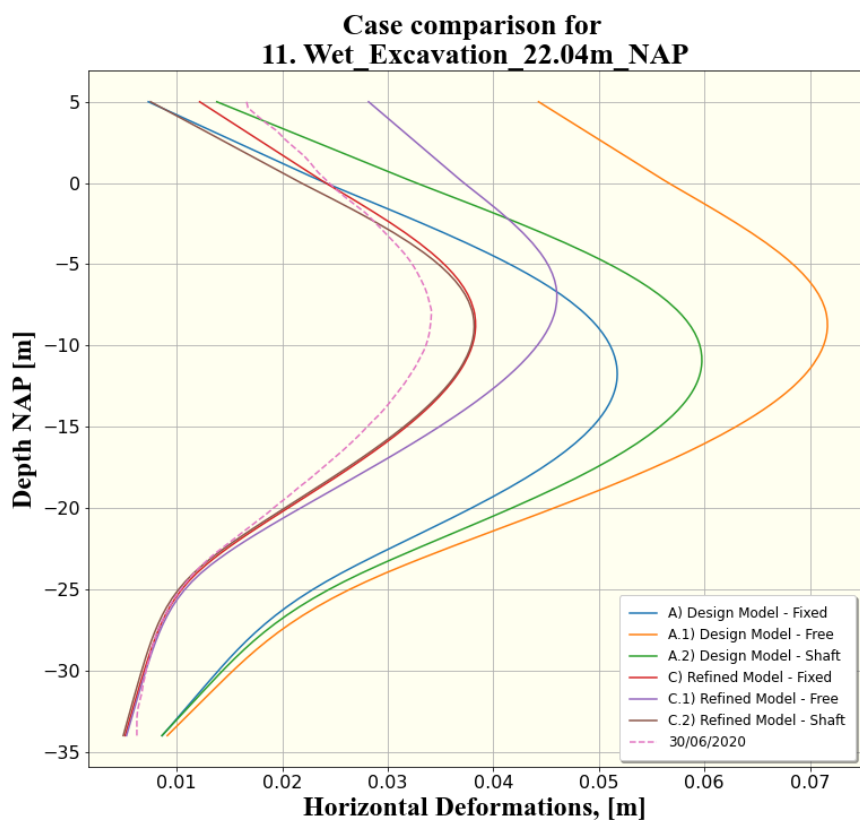
However, despite the excellent results of the *Shaft friction* approach, some assumptions were made, and some limitations were met. Starting with the orientation of the concentrated load, which always remains in the same direction. In reality, the wall has a stage (Phase 9) where the wall moves in the opposite direction away from the excavation pit because the free water level inside is increased. Theoretically, the local shaft friction would change direction if the anchor rod is pushed by the combi wall relative to the soil surrounding it. Moreover, constant consideration of this force assumes that the rod is moving and the soil surrounding it remains stationary. This is not always the case because the soil also deforms. Therefore, such a force is not developed when they move as a system. Additionally, it has been assumed that the external loads are constantly 10 kPa, but that is not entirely accurate. The last assumption is that the rod is in complete contact with the soil at any time, with its length and diameter remaining constant. Further investigation is needed on how this rod can be adequately simulated in PLAXIS to accurately capture the effect of shaft friction with the evolution of the construction phases.

**Table 4.6.1:** Summary of the area difference in  $m^2$  of the three models with the three anchor simulations for the five construction phases of the project that are monitored.

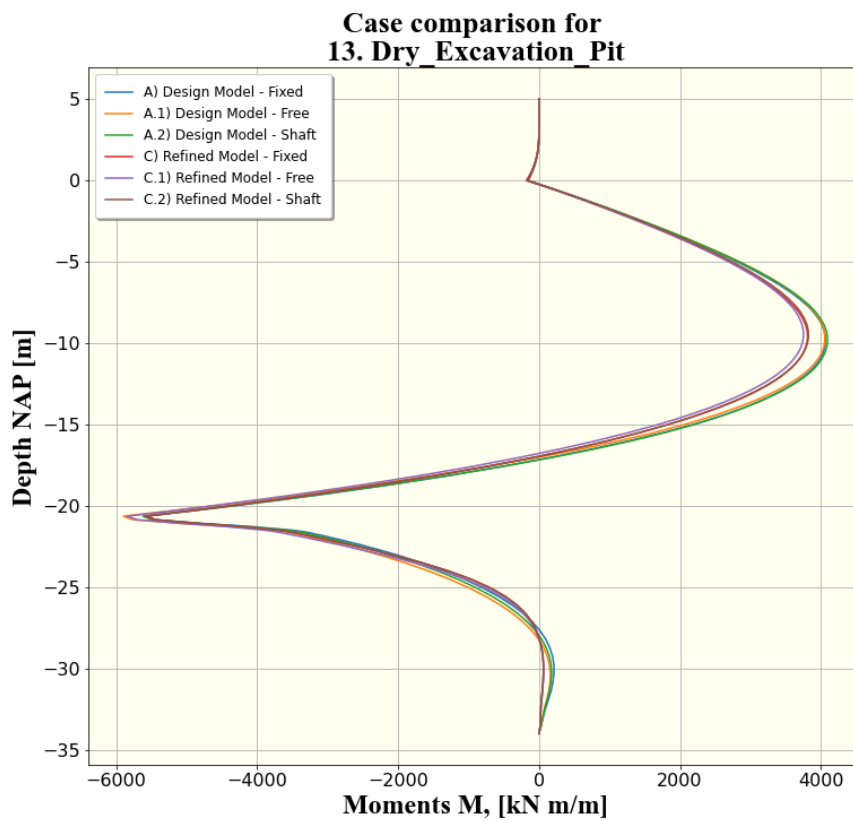
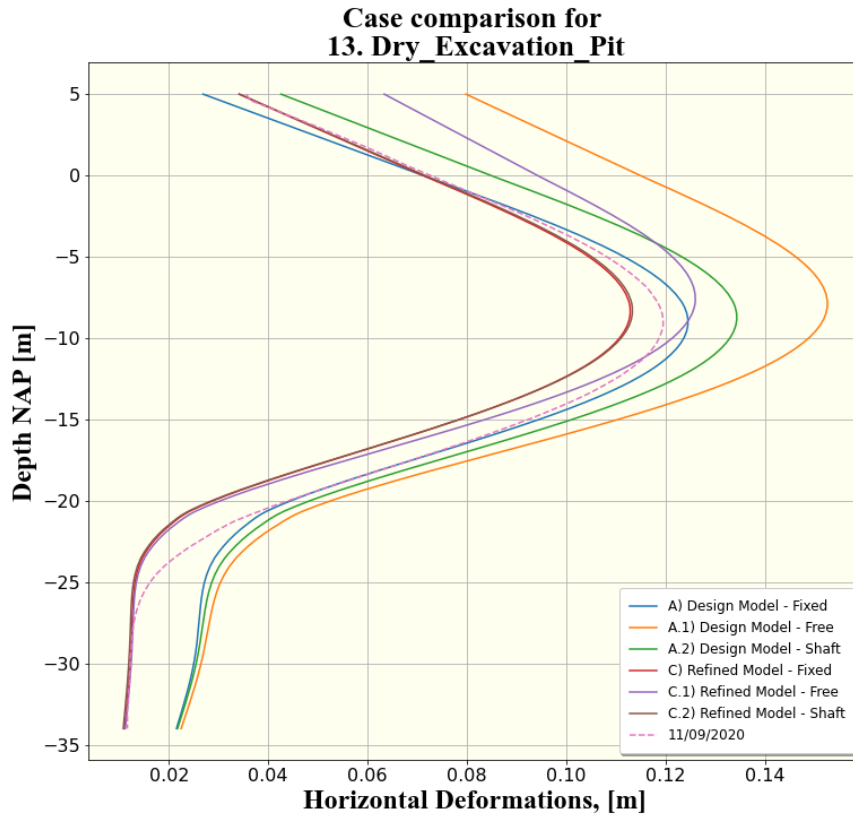
	Monitoring Date	Design Model			Mean Model			Fine Tuned Model		
		Free	Fixed	Shaft	Free	Fixed	Shaft	Free	Fixed	Shaft
P. 8	29/01/2020	0.761	0.414	0.456	0.339	0.097	0.149	0.215	0.038	0.044
P. 9	10/02/2020	0.299	0.070	0.110	0.297	0.117	0.142	0.171	0.053	0.083
P. 10	08/05/2020	0.454	0.145	0.179	0.285	0.087	0.115	0.167	0.035	0.069
P. 11	30/06/2020	1.035	0.463	0.063	0.351	0.139	0.161	0.261	0.078	0.092
P. 13	11/09/2020	0.958	0.215	0.441	0.478	0.315	0.298	0.381	0.226	0.225



**Figure 4.6.2:** Deformations and moments comparison of the Design and Fine Tuned model with the *Free*, the *Fixed* and the *Shaft* approaches at the anchor level of the combi wall, for Phases 8.



**Figure 4.6.3:** Deformations and moments comparison of the Design and Fine Tuned model with the *Free*, the *Fixed* and the *Shaft* approaches at the anchor level of the combi wall, for Phases 11.



**Figure 4.6.4:** Deformations and moments comparison of the Design and Fine Tuned model with the *Free*, the *Fixed* and the *Shaft* approaches at the anchor level of the combi wall, for Phases 13.

#### 4.6.4 Effects of the fixity methods to the safety of the combi wall

So far, three fixity methods of the retaining wall at the anchor level have been discussed, the *Fixed*, the *Free*, and the *Shaft friction* approach. The traditional design approached the model and determined the dimensions of the combi wall with the *Free* approach. Therefore, the effect on the safety of the wall, as a structural element, will be investigated by changing between the three fixity methods for both the Design and Fine Tuned models.

The unity check has been used to compare the effect of the different fixity approaches and models on the combi wall. The unity check is the ratio between actual and allowable stress. The values of these unity checks should be less or equal to 1.0 to comply with the requirements. The models use the same exact wall but differ in the moments and forces produced. Therefore, the models with values closer to 1 exert higher strain on the wall.

Two categories of input are required to calculate the unity check (UC). The first contains the properties of the steel piles and sheet piles of the combi wall. Additionally, it considers that the piles are filled with cement bentonite. The second category includes every model's moments and forces applied to the wall, as well as the effective horizontal stress in the passive and active sides applied by the soil. The effective stresses have been derived from PLAXIS from 5 cm on the left and right sides of the wall (Appendix I.4). The unity check has been performed for both ULS and SLS conditions. In the ULS conditions, according to the Eurocode NEN 9997-1, 2016, the moments and axial loads applied to the pile are increased by 1.2. Finally, this calculation has been performed for the four different sections of the wall predetermined from the design. The moments and forces considered are derived by the governing construction phase that produces the highest moments. In the present models, Phase 13, when the pit is set dry, and the UWC takes the loads, is always the governing phase (Figure 4.6.4). The results are presented in Table 4.6.2. The excel tool used to derive the UC originated from the project, and an example screenshot of the input is shown in Appendix I.4.

Several conclusions can be derived by interpreting Table 4.6.2. As was expected, the UC for the SLS conditions is always lower than the ULS conditions because smaller loads are considered, and safety factors do not reduce the steel strength. Section one has extremely low values of UC because very small moments are applied at that wall level. The highest UCs are met in Section 3, where the wall is in contact with the UWC floor, which induces high moments. In every case, the UC of the Fine Tuned models is slightly lower than the UC of the corresponding Design models despite the considerable difference in deformations shown in the previous paragraphs. It should be noted that the UC for the different sections of the design is relatively low. In the actual project, especially for the section that is in contact with the UWC floor, the UC was very close to 1. The Design model used to simulate the actual design differs in the external loads and aquifers heads that are less severe than predicted in the design; hence lower UC values are produced.

#### 4.6.5 Summary and discussion

To summarize, this thesis has created the Design Model to simulate the actual design under the new conditions applied during the project construction. However, it is proven that the prediction of the deformations compared to the corresponding monitoring deformations is poor. The inaccuracy exists both at the top (anchor system region) and bottom (boom clay region) part of the wall. Using the Fine Tuned model in combination with the *Fixed* deformations, the prediction accuracy has increased by 95 %, 92 %, and 76 % for Phases 8, 11, and 13, respectively. Similar improvements are noticed if the Fine Tuned model is combined with the *Shaft* approach instead of the *Fixed* approach. Even though the *Shaft* approach produces promising results in accuracy and allows the designer to use it before the generation of the monitoring data, it still requires further investigation. Finally, it

**Table 4.6.2:** Unity check of the combi wall for the Design and Fine Tuned model over the different fixity methods of the combi wall at the anchor level.

			Fixed		Free		Shaft Friction		
			Fine Tuned	Design	Fine Tuned	Design	Fine Tuned	Design	
<b>Section 1</b> (1420 x 15.8) [+5, -0.5] m NAP Sheet Pile + Bent.	ULS	$M_{max}$	250	497	184	226	190	240	
		$N_{ed}$	142	210	215	146	217	205	
		<b>U.C.</b>	<b>0.059</b>	<b>0.117</b>	<b>0.044</b>	<b>0.054</b>	<b>0.046</b>	<b>0.057</b>	
	SLS	$M_{max}$	208	414	153	188	158	200	
		$N_{ed}$	118	175	179	122	181	171	
		<b>U.C.</b>	<b>0.045</b>	<b>0.09</b>	<b>0.034</b>	<b>0.041</b>	<b>0.035</b>	<b>0.044</b>	
	<b>Section 2</b> (1420 x 27.7) [-0.5, -12] m NAP Sheet Pile + Bent.	ULS	$M_{max}$	4573	4877	4501	4868	4588	4910
			$N_{ed}$	682	644	664	607	680	634
			<b>U.C.</b>	<b>0.556</b>	<b>0.592</b>	<b>0.547</b>	<b>0.591</b>	<b>0.557</b>	<b>0.596</b>
SLS		$M_{max}$	3811	4064	3751	4057	3823	4092	
		$N_{ed}$	568	537	553	506	567	528	
		<b>U.C.</b>	<b>0.423</b>	<b>0.451</b>	<b>0.417</b>	<b>0.450</b>	<b>0.425</b>	<b>0.454</b>	
<b>Section 3</b> (1420 x 25.8) [-12, -23.5] m NAP Sheet Pile + Bent.		ULS	$M_{max}$	6686	6697	7016	7079	6718	6745
			$N_{ed}$	1306	1219	1294	1210	1297	1214
			<b>U.C.</b>	<b>0.879</b>	<b>0.878</b>	<b>0.922</b>	<b>0.927</b>	<b>0.883</b>	<b>0.883</b>
	SLS	$M_{max}$	5572	5581	5847	5899	5598	5621	
		$N_{ed}$	1088	1016	1078	1008	1081	1012	
		<b>U.C.</b>	<b>0.669</b>	<b>0.668</b>	<b>0.701</b>	<b>0.705</b>	<b>0.681</b>	<b>0.672</b>	
	<b>Section 4</b> (1420 x 15.8) [-23.5, -34] m NAP Bentonite	ULS	$M_{max}$	1995	2004	2126	2280	1994	2113
			$N_{ed}$	659	721	646	734	649	739
			<b>U.C.</b>	<b>0.526</b>	<b>0.481</b>	<b>0.508</b>	<b>0.546</b>	<b>0.477</b>	<b>0.507</b>
SLS		$M_{max}$	1662	1670	1772	1900	1662	1761	
		$N_{ed}$	549	601	538	612	541	616	
		<b>U.C.</b>	<b>0.363</b>	<b>0.366</b>	<b>0.387</b>	<b>0.415</b>	<b>0.363</b>	<b>0.421</b>	

has been proven that the Fined Tuned model with the different fixity approaches has minimum effect on the safety of the pile. Because even though it predicts fewer deformations, the moments and axial forces for the governing phase remain relatively the same. Moving from the Design model with *Free* approach to the Fined Tuned with *Fixed* or *Shaft* approach, the UC reduces only 5 %. Therefore, the Fine Tuned model would be helpful for the design, if the deformations behind the wall have a significant impact (like in urban areas), but it will not help reduce the wall's stiffness significantly. However, it confirms that the actual design, despite the simplicity of the constitutive model used for the Boom Clay and the poor match of the deformations at the anchor level, did not over-designed the combi wall.

## Conclusions and Recommendations

The case study of the outer lock head of the New Terneuzen Lock is considered to investigate the behavior of the Boom Clay and to develop an automated method for improving the deformation predictions in a deep excavation format. The investigation is conducted using a Python-Plaxis application and monitoring data from the field. In this chapter, the main conclusions of this study are summarized based on the investigation and observations presented in Chapter 4. Subsequently, recommendations for future studies are given.

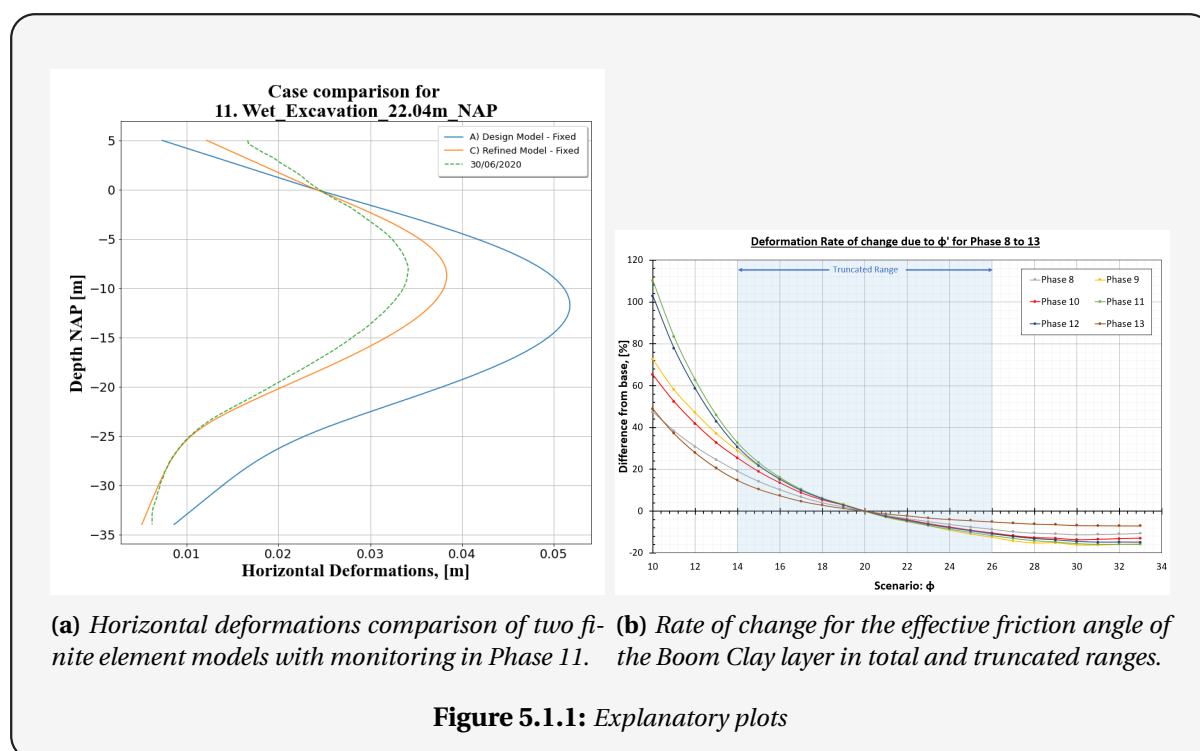
### 5.1 Conclusions

The research questions for the present thesis were investigated through the Python Application (Chapter 3) and three finite element models (Design, Mean, Fine Tuned). All three models share the same as-built structural elements, aquifers heads, and external loads but differ in the soil modeling. The Design model has been created to represent the actual design of the project; hence it uses characteristic soil properties. The Mean model represents the soil layers with mean (most probable) soil properties. Lastly, the Fine Tuned model uses refined soil properties based on the information from the monitoring deformations.

*In this background information section, two explanatory plots (Figure 5.1.1) are given to assist in interpreting the results and conclusions discussed in this chapter.*

*Many conclusions will use the term "percentage improvement in horizontal deformations prediction". To explain this term, an example in Figure 5.1.1a is used. The continuous lines depict the deformations of two Plaxis models, and the dashed line the monitoring deformations for construction Phase 11. The quality of the predictions is quantified using the area change between the models and the monitored horizontal deformations along the height of the combi wall. The area is calculated in  $m^2$  using the Riemann sums, and the smaller it is, the better the match. For instance, the area between the Fine Tuned model (orange line) and the dashed line is 83 %, smaller than the area between the Design model (blue line) and the dashed line. Hence, the Fine Tuned model produces 83 % more accurate deformation predictions than the Design model. Equivalent figures can be found in Chapter 4 for most of the research questions.*

*Figure 5.1.1b depicts the rate of change (ROC) of the effective friction angle  $\phi'$ . It refers to the sensitivity analysis research question 2 and aims to visualize the parameter ranges used. This plot shows how much the total horizontal deformations of the wall change for the soil property ranges for several construction phases. Similar figures have been created for the rest of the soil properties investigated and can be found in the report.*



**(a)** Horizontal deformations comparison of two finite element models with monitoring in Phase 11. **(b)** Rate of change for the effective friction angle of the Boom Clay layer in total and truncated ranges.

**Figure 5.1.1:** Explanatory plots

Following, the main conclusions of this work, derived from the investigation in Chapter 4, are presented by answering the research questions posed in the introduction. The answer includes a small summary of the methodology used, then the main conclusions are presented, and potential limitations are acknowledged.

1. Which constitutive soil model approaches more accurately the behavior of Boom Clay and how is it compared with the one used in the design?

To answer this question, three constitutive models have been tested. The implemented PLAXIS models differ with regard to the constitutive models used for the Boom Clay and the assumed drainage conditions. The constitutive models tested were the Hardening Soil (HS) and Hardening Soil Small Strain (HS-small) with Undrained A conditions and the Mohr-Coulomb (MC) for two stiffnesses and two drainage approaches, the Quasi and Undrained A. The results were evaluated through comparison with the corresponding monitoring deformations for five important construction phases. The investigation was conducted in Section 4.1 and the main conclusions are:

- The HS and HS-small constitutive models had better accuracy in comparison to the MC models;
- The Quasi drainage approach in every case examined produces fewer deformations than the corresponding Undrained A approach for the MC constitutive soil models;
- All the MC models over-predict the deformations. However, the decision of the actual design to use as stiffness  $E'$  the un-/reloading stiffness  $E_{ur}$  with the Quasi approach for the undrained conditions was in the right direction;
- The HS-small constitutive model produces the best overall prediction of retaining wall's horizontal deformations;
- Phase 11 was the end of wet excavation to -22 m NAP, where the Boom Clay had the most crucial role since it is the only soil layer that retains the wall, and the underwater concrete floor has not yet been constructed. For this phase the HS-small model provided 68 % more accuracy in the total deformations than the approach used in the actual design.



### 1.1) Fine Tuned Model

By having the best constitutive model for the Boom Clay, an iterative method was applied using the Python Application and PLAXIS. This process aimed to fit the model deformations to the monitoring deformations by altering the relevant soil properties until a  $\pm 10\%$  convergence is achieved. These new soil properties are considered the actual ones that best represent the true behavior of the material. The Fine Tuned model concluded in Section 4.2 that:

- The fine tuned strength and stiffness parameters of the sand layers L09 and L08 are higher than the mean values. For the densely packed sand layer (L08):
  - $\phi'$ :  $37.8 \rightarrow 42^\circ$ ,  $E_{50}^{ref}$ :  $43127 \rightarrow 60000 \text{ kN/m}^2$  and  $E_{ur}^{ref}$ :  $172508 \rightarrow 180000 \text{ kN/m}^2$
 For the moderately packed clay or loamy sand layer (L09):
  - $\phi'$ :  $32 \rightarrow 35^\circ$ ,  $E_{50}^{ref}$ :  $20285 \rightarrow 30000 \text{ kN/m}^2$ , and  $E_{ur}^{ref}$ :  $81140 \rightarrow 90000 \text{ kN/m}^2$
- The fine tuned strength and stiffness parameters of the Boom clay layer (L15) are lower than the mean values; More specifically:
  - $\phi'$ :  $24.4 \rightarrow 20^\circ$ ,  $c'$ :  $18.5 \rightarrow 16 \text{ kPa}$ ,  $E_{50}^{ref}$ :  $23200 \rightarrow 20000 \text{ kN/m}^2$ , and  $E_{ur}^{ref}$ :  $46400 \rightarrow 40000 \text{ kN/m}^2$
- The model using the fine tuned soil properties achieved 25 % to 65 % more accuracy in the prediction than the Mean model. More specifically, for Boom Clay's most challenging construction phase, Phase 11, the Fine Tuned model provided 46 % better accuracy than the Mean model;
- A side investigation proved that the bentonite of the combi-wall has an insignificant effect on the deformations of the wall. Specifically, the change is 7 %, 5%, and 10 % for the construction Phase 8, 11, and 13.

It should be noted that the Fine Tuned Model is as accurate as the assumptions made about all the aspects of the model. The previously mentioned values are only true for the assumptions of the current project. Also, the number of soil properties altered, and the repetition applied affected the outcome. Finally, the results are limited by using a 2D modeling approach that does not allow for capturing the 3D effects of reality.

## 2. What is the sensitivity of the retaining wall to the different soil properties of the Boom Clay?

To answer this question, three soil properties of the Boom Clay have been investigated separately ( $E_{50}^{ref}$ ,  $\phi'$ ,  $c'$ ). The Fine Tuned model with the HS-small constitutive model has been used to run the different scenarios in PLAXIS. Two value ranges have been created for each parameter. The first is the *Total range* that considers exceptionally high and low values compared to the base case. The second range is enveloped within the first and is called *Truncated range*, indicated with a blue shade in Figure 5.1.1b, that considers properties within  $\pm 30\%$  from the base value. A custom tool calculates the change in deformations between scenarios by calculating the area change. Hence, a rate of change (ROC) plot showing how much the wall's total horizontal deformations change for the soil property ranges for several construction phases is created. The investigation has been performed in Section 4.3, and the main conclusions are:

- When considering the *Total range* the ROC for  $E_{50}^{ref}$  and  $\phi'$  is not linear especially in low values. Contrary the ROC for the  $c'$  remains linear;
- When considering the *Truncated range*, the ROC of all three soil properties is linear. It is proven by the linear correlation  $\rho$  of the soil parameter change and the area change with a negative correlation of over 95 % for all the soil properties considered;
- By increasing the value of each of the three soil properties causes a reduction in horizontal deformations, and by reducing it, the contrary;

- Using the *Truncated range*, it has been concluded that for almost all the properties decreasing the value by 30 % induces a higher impact than increasing it by 30 %;
- The higher deformation impact is caused by  $\phi'$ , the lowest by  $c'$  and an intermediate by  $E_{50}^{ref}$ .

3. *What is the effect of the Boom Clay thickness on the deformations and safety of the retaining wall, with special attention to the consideration of drained or undrained behaviour?*

To examine this research question, four virtual cross-sections have been formed, each with a reducing thickness of Boom Clay from the top to follow the wedging behavior of the Boom Clay in the project area. The layer was replaced by the upper adjacent sand layer (L08). Additionally, these four new geometries were tested both in *Partially Undrained* and *Fully Drained* conditions. The *Partially Undrained* conditions in this thesis refer to the Boom Clay layer behaving undrained only after Phase 8. Whereas the *Fully Drained* conditions consider the Boom Clay layer drained throughout all the construction phases. Finally, all the new geometries were used in the Fine Tuned model, considered the most accurate since the monitoring data have calibrated it. The investigation took place in Section 4.4, and the main conclusions are:

- When *Partially Undrained* conditions are considered, the deformations for every thickness scenario remain almost the same;
- When *Fully Drained* conditions are considered, the thinner the Boom Clay layer, the less the deformations;
- For the real thickness (16.1 m) of the Boom Clay layer, it is proven to behave undrained over the period of the monitoring/ excavation considered. More specifically, when the layer is considered undrained, in the crucial Phase 11, it provides 83 % more accurate predictions than when it is considered drained;
- As a result, in the case of wrongfully considering undrained conditions for the Boom Clay layer, the impact is less severe as the thickness reduces or the soil behaves undrained during the project.

It should be noted that the results are relevant to the particular project. A limiting factor is the fictional cross-sections used over the actual ones due to time constraints.

4. *Is there an improvement in the accuracy of the prediction of the following construction stages by updating the parameters of the previous stages with an iterating process?*

For this question to be answered, three models have been considered, the Initial, the Base, and the Improved model. The investigation will consider as variables only the soil properties. The remaining aspects of the model (loads, heads, structural elements, geometry) will stay the same in all models. The Initial model used the soil conditions the actual design uses. The Base model uses the same soil conditions but with the improved HS-small constitutive soil model for the Boom Clay. Finally, the Improved model uses the soil properties derived by an iteration process to match the monitoring deformations. "Phase 8: End of dry excavation to -11 m NAP" will be used to improve the prediction, and "Phase 11: End of wet excavation to -22 m NAP" will be used to evaluate the improvement achieved. The investigation was conducted in Section 4.5, and the main conclusions are:

- The outcome horizontal deformations of the Initial model that includes the soil properties used in the actual design disagrees with the monitoring deformations;
- The Base model just by changing the constitutive model of the Boom Clay layer from Mohr-Coulomb to the more advanced HS-small improved the prediction of Phase 8 by 74 %;

- The Improved model that has been created by the iterating method for Phase 8 has 88 % and 54 % more accuracy than the Initial and Base model, respectively;
- By adjusting the soil properties with the iterating method in Phase 8, 87 % more accuracy is achieved in Phase 11 compared to the outcome of the Initial model. In other words, by using the prediction method in Phase 8, the prediction of Phase 11 improved by 87 % in comparison with the predictions of the original design.

The prediction method, in this case, was very beneficial. However, the success of the prediction is heavily determined by the predominant influence the Boom Clay has on the present retaining wall for all stages. In different geometries, the prediction effect could be smaller.

5. *How can the current design be improved using the iterating method with the python application and monitoring data during the construction of the project? Are these benefits worth the extra analysis on top of the conventional design?*

To approach this research question, a Design model has been created that considers the same soil layer modeling aspects (properties, constitutive models, drainage) as the actual model but uses the "as-build" data regarding the external loads, the aquifer heads, and structural elements. Different methods of fixity at the anchoring system (*Free*, *Fixed*, *Shaft friction*) have been investigated to improve the deformation prediction at that level. The *free fixity* considers no restrains other than the anchoring system at 0 m NAP on the combi wall. The actual design uses this fixity method. The *Fixed fixity* imposes prescribed deformations in PLAXIS at 0 m NAP of the combi wall based on the corresponding horizontal deformations at that level from the monitoring. Lastly, the *Shaft friction fixity* considers the shaft capacity of the anchor rods by translating it into a horizontal force applied on the anchor wall at the anchor rod/wall connection location.

Furthermore, the Fine Tuned model has been used to improve predictions around the region of the Boom Clay at the lower part of the wall. Lastly, the safety of the wall under the new models and fixity methods has been evaluated. The deformations have been quantified by the area change calculation, and the safety of the wall by the unity check. The investigation was conducted in Section 4.6, and the main conclusions are:

- The Design model has an inferior prediction accuracy of the deformations throughout the total wall length for every construction phase;
- The Fine Tuned model with the more sophisticated constitutive model and the refined soil properties through the iterating method increased the deformation prediction accuracy of the Design model. More specifically, the accuracy improved by 72 %, 75% and 60 % for the construction the Phases 8, 11, and 13, respectively. However, by itself was only able to improve the deformations at the Boom Clay region of the wall;
- The fixity approaches (*Fixed* and *Shaft friction*) of the combi wall at the anchor level investigated allow for an improvement of deformation prediction at the top part of the combi wall. This methodology improved both the prediction of the Design and Fine Tuned model. The problem has been attributed to the inability of PLAXIS to consider the shaft friction of the anchor rod from the anchoring system;
- Comparing the Design model with the *Free* approach at the anchoring level of the wall and the Fine Tuned model with the *Fixed* or *Shaft friction* approach, the improvement in the prediction of the deformations reached the impressive numbers of 95 %, 92 % and 76 % for the Phases 8, 11 and 13, respectively;
- The unity check on bending moment difference between the two previously mentioned models for the most severe part of the wall (Section 3) is only 5 %. This is attributed to the fact that despite the important difference in deformations, the moments and axial forces that dictate the dimensioning of the wall are relatively similar in governing Phase 13;

- For the particular case, the Fine Tuned Model and the fixity methods are worth the extra investigation when the deformations behind the wall are relevant. Otherwise, they have confirmed the design of the combi wall from the actual project because the phase with the UWC floor is dominant and covers all the differences in moments and forces from the previous phases.

It should be mentioned that despite the promising results, the *Shaft friction* approach requires further investigation since several assumptions have been made for its use. Similarly to previous research questions where the Fine Tuned model has been used, its accuracy depends on the validity of the assumptions and the number of repetitions.

The results have been produced for the specific configurations of the outer lock head of the New Terneuzen Lock. Care must be taken with extrapolating the results to other cases. Additionally, various assumptions have been made whose accuracy influences the results.

## 5.2 Recommendations

This research covered a broad range of aspects of the retaining wall. Therefore, the investigation came across points that required further research that was out of the scope of the present thesis. In those occasions, assumptions have been made, or limitations have been set.

In the present study, an attempt was made using the monitoring data to simulate the actual behavior of the wall. The present wall uses an anchoring system comprised of anchor walls and horizontal anchor rods at 0 m NAP. The present cross-section (L01b) anchoring system interacts with backfield sand layers LX02 and LX01. Early in the research, it was observed that the model deformations did not agree with the monitoring deformations at the upper part of the wall where the anchoring system is located. Therefore, the deformations of the entire wall were affected. An assumption was made to reduce the variables and focus on the interesting for the thesis locations. Every model in PLAXIS had prescribed movement at the anchor level according to the monitoring. The effect of this assumption is shown in Figures 4.6.2, 4.6.3 and 4.6.4, where the Fine Tuned model has been solved with three anchoring approaches. It is believed that one mechanism that could cause the difference between the *Fixed* and *Free* approach is the shaft friction on the anchor rod. Anchor rods in PLAXIS are simulated with Node-to-Node elements that do not have the capabilities for interface; hence do not consider shaft friction. Because the length and diameter of these rods are substantial, the skin friction could create a relevant resisting force. In a brief investigation, the shaft friction of the anchor rod has been translated to a horizontal force resisting the movement of the wall. The results were very promising. However, further research on this mechanism is essential because the applied solution with force is based on many assumptions and simplifications. Therefore, on what occasions should the anchor rod shaft friction be considered, and how can it be simulated appropriately in PLAXIS?

Furthermore, a three-dimensional numerical simulation of the excavation is likely important. The 3D effect could be significant, especially in locations like the present cross-section close to one of the corners of the excavation pit. It is interesting to see how accurate the soil properties derived by the Fine Tuned model are and if they still match the monitoring deformations when the retaining wall is simulated in a three-dimensional environment.

The consolidation and swelling could also be investigated for the Boom Clay behavior. The consolidation investigation would provide even more information about the settlements and undrained behavior of the Boom Clay. It would be interesting for the construction phases considered in this thesis to see if consolidation is included how the outcome of the Fine Tuned model would change.

The present thesis encountered some problems with the lab tests on Boom Clay soil samples. Further investigation could be conducted on handling soil samples with swelling potential and how the disturbed samples can be used to derive useful information.

Creating the Fine Tuned model required an iterative process, visualized in the flow chart of Section 1.4. The python application provided tools to help the users decide when the convergence is not enough and what is the appropriate change of the parameters based on the sensitivity analysis. The constant human-code interaction creates delays, and eventually, it allows for only a limited amount of iterations and soil combinations that can be tested. Therefore, an automated process would allow for more iterations and, theoretically, more accurate predictions. The code could be structured based on conditions or even trained on results. The code needed for the loop exists in the sensitivity analysis tool, but the interpretation mechanism is missing.

The Python application aims to work as a central hub that allows the user to collect monitoring data, perform model calculations in PLAXIS and make interpretations. This application is intended to be used during the project's construction to assure the project's designers and increase confidence in the safety of the original design. In the input, there is a vital scheduling aspect. Several inputs of the model are directly related to the operations performed in the field, and the scheduling followed. In the management aspect, this application could be extended to retrieve input information for the model by scheduling software used in projects, improving efficiency.

# Bibliography

- [1] I Alpan. "The geotechnical properties of soils". In: *Earth-Science Reviews* 6.1 (1970), pp. 5–49.
- [2] Patrick Arnold et al. "A numerical and reliability-based investigation into the technical feasibility of a Dutch radioactive waste repository in Boom Clay". In: (2015).
- [3] J Atkinson and G Salfors. "Experimental determination of soil properties (stress-strain-time)". In: *Proc. 10th Eur. Conf: Soil Mech., Florence*. Vol. 3. 1991, p. 915.
- [4] John Herbert Atkinson and PL Bransby. "The mechanics of soils: an introduction to critical state soil mechanics". In: (1978).
- [5] G Baldi. "Interpretation of CPT's and CPTU's. 2nd Part: Drained penetration of sands". In: *Proc. IV Int. Geotech. Sem., Singapore* (1986).
- [6] Steven F Bartlett, Bret N Lingwall, and Jan Vaslestad. "Methods of protecting buried pipelines and culverts in transportation infrastructure using EPS geof foam". In: *Geotextiles and Geomembranes* 43.5 (2015), pp. 450–461.
- [7] T Benz and PA Vermeer. "Zuschrift zum Beitrag" "Über die Korrelation der oedometrischen und der" dynamischen" Steifigkeit nichtbindiger Boden" von T. Wichtmann und Th. Triantafyllidis (Bautechnik 83, No. 7, 2006)". In: *Bautechnik* 84.5 (2007), pp. 361–364.
- [8] Laurits Bjerrum. "Engineering geology of Norwegian normally-consolidated marine clays as related to settlements of buildings". In: *Geotechnique* 17.2 (1967), pp. 83–118.
- [9] JE Bowles. *Foundation analysis and design. Int. Student Edition*. 1968.
- [10] RBJ Brinkgreve, WM Swolfs, and E Engin. "PLAXIS 2D 2010 material models manual". In: *PLAXIS BV* (2011).
- [11] Vladimir Buljak and Gianluca Ranzi. *Constitutive Modeling of Engineering Materials: Theory, Computer Implementation, and Parameter Identification*. Academic Press, 2021.
- [12] R Carpentier. *Relationship between the cone resistance and the undrained shear strength of stiff fissured clays*. AA Balkema, 1982.
- [13] YF Deng et al. "Laboratory hydro-mechanical characterisation of Boom Clay at Essen and Mol". In: *Physics and Chemistry of the Earth, Parts A/B/C* 36.17-18 (2011), pp. 1878–1890.
- [14] Erwin Gartung and Hermann K Neff. "Empfehlungen des Arbeitskreises" Geotechnik der Deponiebauwerke" der Deutschen Gesellschaft für Geotechnik e. V.(DGGT)". In: *Bautechnik* 78.9 (2001), pp. 609–614.
- [15] Jacob Gerrit de Gijt and ML Broeken. *Quay walls*. CRC Press, 2013.
- [16] Bobby O Hardin and Vincent P Drnevich. "Shear modulus and damping in soils: design equations and curves". In: *Journal of the Soil mechanics and Foundations Division* 98.7 (1972), pp. 667–692.
- [17] ST Horseman, MG Winter, and DC Entwistle. "Geotechnical characterization of Boom clay in relation to the disposal of radioactive waste". In: (1987).
- [18] Jozsef JAKY. "The coefficient of earth pressure at rest". In: *J. of the Society of Hungarian Architects and Engineers* (1944), pp. 355–358.
- [19] MA Op de Kelder. "2D FEM analysis compared with the in-situ deformation measurements: A small study on the performance of the HS and HSsmall model in a design". In: *Plaxis Bulletin, Issue 38* (2015), pp. 10–17.

- [20] Charles Cushing Ladd and T William Lambe. "The strength of "undisturbed" clay determined from undrained tests". In: *Laboratory shear testing of soils*. ASTM International, 1964.
- [21] T William Lambe and Robert V Whitman. *Soil mechanics*. Vol. 10. John Wiley & Sons, 1991.
- [22] Kenneth Lester Lee. *Triaxial compressive strength of saturated sand under seismic loading conditions*. University of California, Berkeley, 1965.
- [23] T Lunne, T Berre, and SI Strandvik. "Sample disturbance effects in soft low plastic Norwegian clay". In: *Symposium on Recent Developments in Soil and Pavement Mechanics* CAPES-Fundacao Coordenacao do Aperfeicoamento de Pessoal de Nivel Superior; CNPq-Conselho Nacional de Desenvolvimento Cientifico e Tecnologico; FAPERJ-Fundacao de Ampora a Pesquisa do Estado do Rio de Janeiro; FINEP-Financiadora de Estudos e Projetos. 1997.
- [24] Tom Lunne and Hans Peter Christoffersen. "Interpretation of cone penetrometer data for offshore sands". In: *Offshore Technology Conference*. OnePetro. 1983.
- [25] Michail Miliouritsas. "Geotechnical modelling of a deep tunnel excavation in the Boom Clay formation". In: (2014).
- [26] Alan D Moore. *Python GUI Programming with Tkinter: Develop responsive and powerful GUI applications with Tkinter*. Packt Publishing Ltd, 2018.
- [27] Duncan Nicholson et al. "The observational method in ground engineering: principles and applications". In: *REPORT-CONSTRUCTION INDUSTRY RESEARCH AND INFORMATION ASSOCIATION* 185 (1999).
- [28] Richard de Nijs et al. "Geotechnical monitoring of a trial pit excavation toward the Boom clay in Antwerp (Belgium)". In: *Geotechnical Safety and Risk V*. IOS Press, 2015, pp. 577–582.
- [29] Peter K Robertson. "Soil behaviour type from the CPT: an update". In: *2nd International symposium on cone penetration testing*. Vol. 2. 56. Cone Penetration Testing Organizing Committee. 2010, p. 8.
- [30] T Schanz. "Formulation and verification of the Hardening-Soil Model". In: *RBJ Brinkgreve, Beyond 2000 in Computational Geotechnics* (1999), pp. 281–290.
- [31] T Schanz and PA Vermeer. "Angles of friction and dilatancy of sand". In: *Geotechnique* 46.1 (1996), pp. 145–151.
- [32] PA Vermeer and CP Meier. "Stability and deformations in deep excavations in cohesive soils". In: *Proceedings of International Conference on Soil-Structure Interaction in Urban Civil Engineering, Darmstadt Geotechnics*. Vol. 1. 4. 1998.
- [33] Pieter A Vermeer and R De Borst. "Non-associated plasticity for soils, concrete and rock". In: *HERON*, 29 (3), 1984 (1984).
- [34] GJ Vis and JM Verweij. "Geological and geohydrological characterization of the Boom Clay and its overburden". In: *COVRA NV Report OPERA-PU-TNO411 (Utrecht)* (2014).
- [35] Torsten Wichtmann and Theodor Triantafyllidis. "On the correlation of "static" and "dynamic" stiffness moduli of non-cohesive soils". In: *Bautechnik* 86.S1 (2009), pp. 28–39.

# **Appendices**





# References to codes

## A.1 Table 2.b - NEN9997

target caption

Grondsoort			Karakteristieke waarde* van grondeigenschap																						
Hoofd-naam	Bijmengeele	Consolententie <sup>b</sup>	$\gamma^a$	$\gamma_{sat}$	$q_u^{c,d}$	$C_p^{e,f}$	$C_s^g$	$C_d/(1+e_0)^h$	$C_a^i$	$C_{sw}/(1+e_0)^j$	$E_{100}^{k,h}$	$\phi^{l,m}$	$c^l$	$c_u$											
			kN/m <sup>3</sup>	kN/m <sup>3</sup>	MPa			[-]	[-]	[-]	MPa	Graden	kPa	kPa											
Grind	Zwak siltig	Los	17	19	15	500	$\infty$	0,004 6	0	0,001 5	45	32,5	0												
		Matig	18	20	25	1 000	$\infty$	0,002 3	0	0,000 8	75	35,0	0	N.v.t.											
		Vast	19	20	22	30	1 200	1 400	$\infty$	0,001 9	0,001 6	90	105	37,5	40,0	0									
	Sterk siltig	Los	18	20	10	400	$\infty$	0,005 8	0	0,001 9	30	30,0	0												
		Matig	19	21	15	600	$\infty$	0,003 8	0	0,001 3	45	32,5	0	N.v.t.											
		Vast	20	21	22	25	1 000	1 500	$\infty$	0,002 3	0,001 5	75	110	35,0	40,0	0									
Zand	Schoon	Los	17	19	5	200	$\infty$	0,011 5	0	0,003 8	15	30,0	0												
		Matig	18	20	15	600	$\infty$	0,003 8	0	0,001 3	45	32,5	0	N.v.t.											
		Vast	19	20	22	25	1 000	1 500	$\infty$	0,002 3	0,001 5	75	110	35,0	40,0	0									
	Zwak siltig, kleiig	Los	18	19	20	21	12	450	650	$\infty$	0,005 1	0,003 5	0	0,001 7	0,001 2	35	50	27,0	32,5	0	N.v.t.				
		Matig	18	19	20	21	8	200	400	$\infty$	0,011 5	0,005 8	0	0,003 8	0,001 9	15	30	25,0	30,0	0	N.v.t.				
		Vast	18	19	20	21	8	200	400	$\infty$	0,011 5	0,005 8	0	0,003 8	0,001 9	15	30	25,0	30,0	0	N.v.t.				
Leem*	Zwak zandig	Slap	19	19	1	25	650	0,092 0	0,003 7	0,002 0	2	27,5	30,0	0	50										
		Matig	20	20	2	45	1 300	0,051 1	0,002 0	0,017 0	3	27,5	32,5	1	100										
		Vast	21	22	3	70	1 900	2 500	0,032 9	0,023 0	0,001 3	0,000 9	5	7	27,5	35,0	2,5	3,8	200	300					
	Sterk zandig	Slap	19	20	19	20	2	45	70	1 300	2 000	0,051 1	0,032 9	0,002 0	0,001 3	0,017 0	0,011 0	3	5	27,5	35,0	0	1	50	100
		Matig	14	14	0,5	7	80	0,328 6	0,013 1	0,109 5	1	17,5	0	25											
		Vast	17	17	1,0	15	160	0,153 3	0,006 1	0,051 1	2	17,5	5	50											
Klei	Zwak zandig	Slap	15	15	0,7	10	110	0,230 0	0,009 2	0,076 7	1,5	22,5	0	40											
		Matig	18	18	1,5	20	240	0,115 0	0,004 6	0,038 3	3	22,5	5	80											
		Vast	20	21	2,5	30	50	400	600	0,076 7	0,046 0	0,003 1	0,001 8	0,025 6	0,015 3	5	10	22,5	27,5	13	15	120	170		
	Sterk zandig	Slap	18	20	1,0	25	140	320	1 880	0,092 0	0,016 4	0,003 7	0,000 7	0,030 7	0,005 5	2	5	27,5	32,5	0	1	0	10		
		Matig	13	13	0,2	7,5	30	60	0,306 7	0,015 3	0,102 2	0,5	15,0	0	1	10									
		Vast	15	16	0,5	10	15	40	60	0,230 0	0,153 3	0,011 5	0,007 7	0,076 7	0,051 1	1,0	2,0	15,0	0	1	25	30			
Veen	Niet voorbelast	Slap	10	12	10	12	0,1	5	7,5	20	30	0,460 0	0,306 7	0,023 0	0,015 3	0,153 3	0,102 2	0,2	0,5	15,0	1	2,5	10	20	
		Matig	12	13	12	13	0,2	7,5	10	30	40	0,306 7	0,230 0	0,015 3	0,011 5	0,102 2	0,076 7	0,5	1,0	15,0	2,5	5	20	30	
Variatiecoëfficiënt v			0,05			-			0,25			0,10			0,20										

### Comments

- The table shows the low and high characteristic values of averages for the relevant soil type. Within an area defined by the admixture row and the parameter column (a cell):
  - If an increase in the value of one of the soil properties leads to a more unfavorable situation than the application of the lower characterization value presented in the table, the right value on the same line must be used. If no value is stated to the right, the value must be applied directly below;

NOTE: This is the case, for example, with negative adhesive on a pole where a higher value of  $\phi'$ ,  $c'$  and  $c_u$  also gives a higher value of the negative adhesive.

  - For  $C_c/(1+e_0)$ ,  $C_a$  and  $C_{sw}/(1+e_0)$  the high characteristic mean values are listed in the table.
- Los:  $0 < R_n < 0,33$   
 Matig:  $0,33 \leq R_n \leq 0,67$   
 Vast:  $0,67 < R_n < 1,00$
- The  $\gamma$ -values apply to a natural moisture content.

- The  $q_c$  values (cone resistance) given here should be considered as an entry in the table and should not be used in the calculations.
- The  $C_a$  values are valid for a voltage increase range of at most 100 %. For gravel, sand, and to a limited extent also for loam and heavily sandy clay,  $q_c$ ,  $E_{100}$ ,  $\phi'$ , and the compression parameters,  $C_p'$ ,  $C_c/(1 + e_0)$  and  $C_{sw}/(1 + e_0)$  have been standardized for an effective vertical ground stress  $\sigma_v'$  of 100 kPa. In order to obtain a correct entry in the table for the values of  $q_c$  measured in the field, these values must be converted to the level of the effective vertical ground tension  $\sigma_v'$  of 100 kPa. In that context, the formula  $q_{c, \text{table}} = q_{c, \text{measured}} * C_{q_c}$  must be used, where  $C_{q_c}$  must be derived from  $C_{q_c} = (100/\sigma_v')^{0.67}$ . The angle of effective friction  $\phi'$  and the cohesion  $c'$  depend on the consistency of the soil. This means that this conversion is also needed for  $\phi'$  and  $c'$ . If  $q_{c, \text{table}}$  becomes larger than the value given in the table, the lower rule applies for the relevant soil type.
- The values refer to saturated loam.
- The modulus of elasticity loop at load repetitions may be assumed as side three times the declared value.

## A.2 Table 9.b - NEN9997

Tabel 9.b — Wandrijvingshoek voor klei, leem, zand en grind

Relatieve ruwheidsbenaming van het wandoppervlak	Nadere definitie van de ruwheid van de wand	Wandrijvingshoek ( $\delta$ )	
		Recht glijvlak	Gekromd glijvlak
Getand	$> 10 d_{50}$	$0,67 \phi'_k$	$\leq \phi'_k$
Ruw	$0,5 d_{50} - 10 d_{50}$	$0,67 \phi'_k$	$\leq \phi'_k - 2,5^\circ$ met een maximum van $27,5^\circ$
Half ruw	$0,1 d_{50} - 0,5 d_{50}$	$0,33 \phi'_k$	$0,5 \phi'_k$
Glad	$< 0,1 d_{50}$	$0^\circ$	$0^\circ$

## A.3 Table 3.1 - CUR 2003 - 7

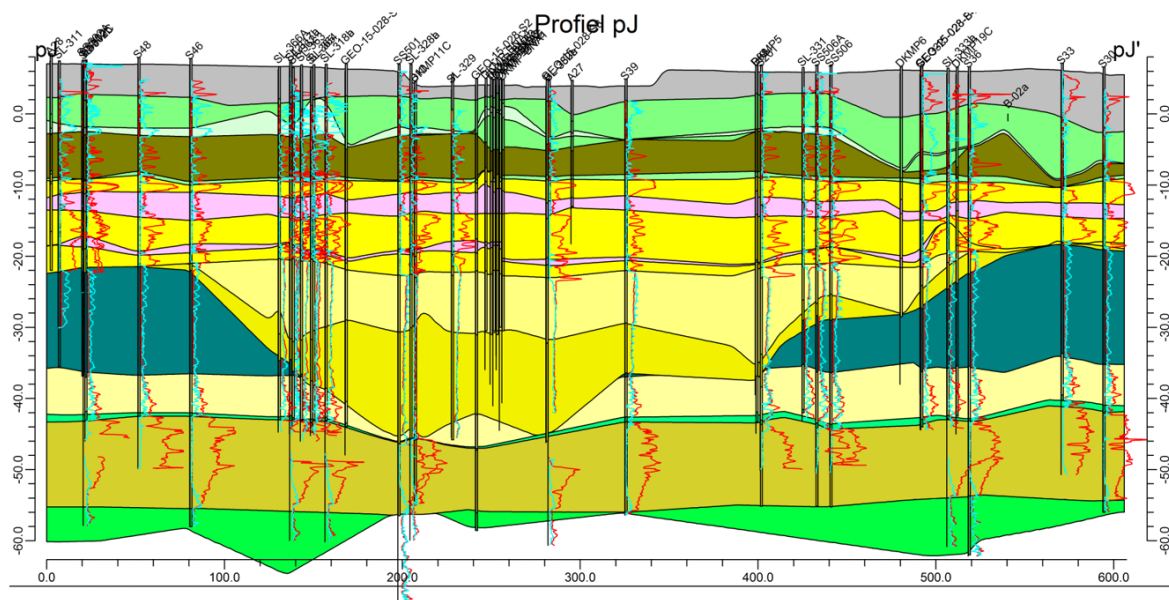
Tabel 31. Richtlijnen voor E waarden (vuistregels) ten behoeve van het Hardening Soil Model.







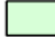
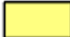



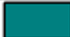

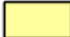





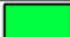
	$E_{oed,ref}$	$E_{50,ref}$	$E_{nr,ref}$
klei (OCR = 1)	$< 5$ $\approx 50000 / (w_L - 10)$ $\approx 50000 / I_p$ $\approx 100/\lambda^*$	$\approx 2E_{oed,ref}$	$\approx 8 E_{50,ref}$ $\geq 5 E_{50,ref}$ (klei/ silt)
klei (OCR > 1) en silt	$10 - 25$ $\approx 50000 / (w_L - 10)$ $\approx 50000 / I_p$	$\approx E_{oed,ref}$	$\approx 4 E_{50,ref}$
zand (OCR = 1)	$20 - 60$ $\approx 3q_c \sqrt{p_{ref}/\sigma_{v0}}$	$\approx E_{oed,ref}$ $\approx 60000 R_c$	$\approx 4 - 5 E_{50,ref}$

# B

## Soil Investigation

### B.1 Soil Cross Section



	L00 Slib		L10 ZAND, matig tot dichtgepakt, zwak siltig
	L01 Aanvulling		L11 ZAND, sterk kleihoudend of leemhoudend
	L02 KLEI, licht tot matig zandig, zacht		L12 ZAND, matig tot dichtgepakt, zwak siltig
	L03 VEEN		L13 glauconiethoudend ZAND 1
	L04 KLEI, licht tot matig zandig, zacht		L14 glauconiethoudend ZAND 2
	L05 ZAND, los tot matig gepakt met klei- en leemlenzen		L15 Boomse KLEI
	L06 ZAND, (zeer) los tot matig gepakt, zwak siltig		L16 ZAND, licht glauconiethoudend
	L07 VEEN/KLEI		L17 LEEM/KLEI, sterk siltig
	L08 ZAND, matig tot dichtgepakt, zwak siltig		L18 ZAND, zeer dichtgepakt
	L09 ZAND, sterk kleihoudend of leemhoudend		L19 LEEM/KLEI, zandig

## B.2 Oedometer Test - Lab report

Opdracht : 1702832

Plaats : nvt

Project : Laboratoriumonderzoek

### SAMENDRUKKINGSPROEF

Taylor (NEN5118)

Boring : BL-791

Startdatum : 19-09-2017

Diepte : NAP -1.60 / -1.65 m.

Monster : 11

Einddatum : 29-09-2017

Initieel vol.gew.  $\gamma$  : 16.11 kN/m<sup>3</sup>

Bus : 22855

Hoogte monster : 19.00 mm

Droog vol.gew.  $\gamma_{dr}$  : 10.26 kN/m<sup>3</sup>

Apparaat : 22

Zetting (24u) : 0.885 mm

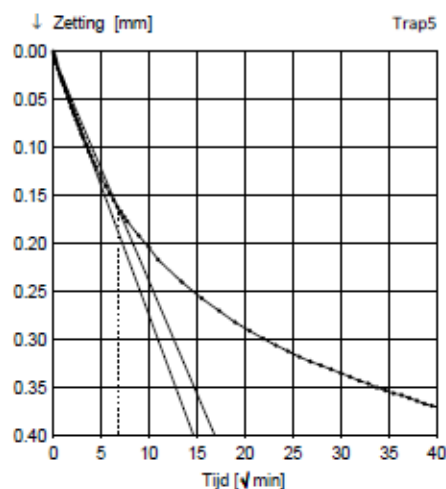
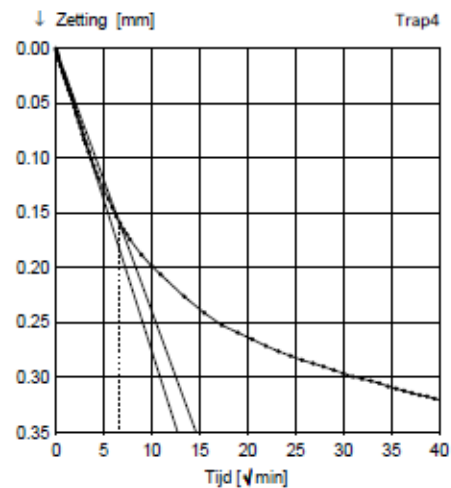
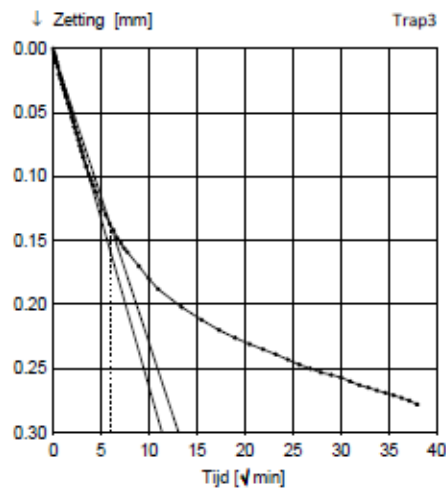
Watergehalte W : 57 %

Soort monster : Ongeroerd

h (24u) : 18.115 mm

Grondsoort : Klei, matig siltig, zwak humeus gr.

Belastingtrappen:	Trap1	Trap2	Trap3	Trap4	Trap5	Trap6	Trap7
Belasting [kN/m <sup>2</sup> ]	43	60	84	116	161	116	161
$\Delta p$ [kN/m <sup>2</sup> ]	43	17	24	32	45	-45	45
$c_v$ [10 <sup>-9</sup> m <sup>2</sup> /s] (wortel-t)			2.37	1.87	1.72		
$m_v$ [1/MPa]			0.35	0.31	0.23		
$k_{10}$ [10 <sup>-11</sup> m/s]			8.17	5.71	3.81		
$c_v$ [10 <sup>-9</sup> m <sup>2</sup> /s] (log-t)			1.92	1.18			20.45
$C_{\alpha}$ [10 <sup>-3</sup> ]			4.466	5.363			0.6242



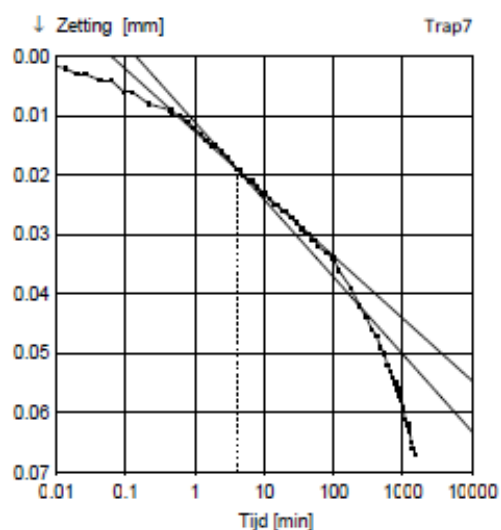
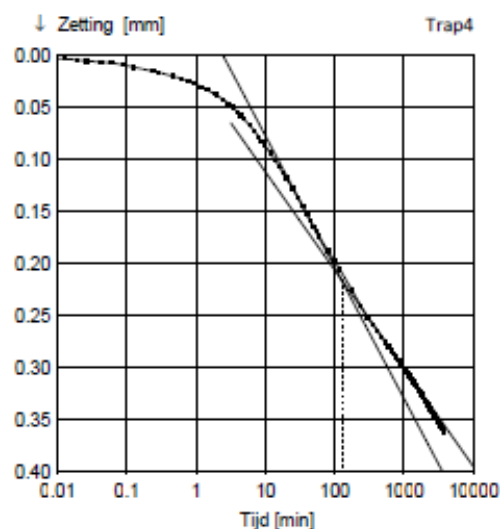
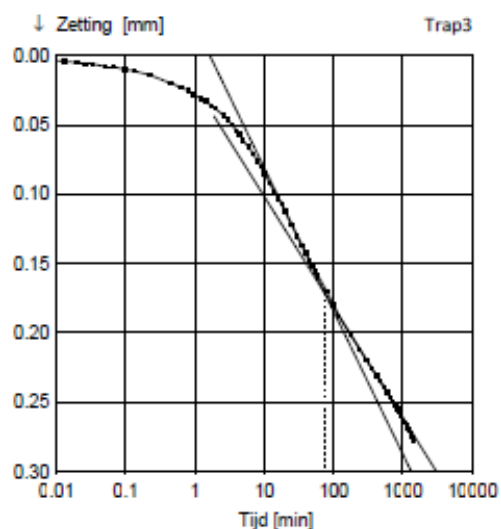
Opdracht : 1702832  
 Plaats : nvt  
 Project : Laboratoriumonderzoek

**SAMENDRUKKINGSPROEF**

Casagrande (NEN5118)

Boring : BL-791                      Startdatum : 19-09-2017                      Diepte :                      NAP -1.60 / -1.65 m.  
 Monster : 11                              Einddatum : 29-09-2017                      Initieel vol.gew.                       $\gamma$  : 16.11 kN/m<sup>3</sup>  
 Bus : 22855                              Hoogte monster : 19.00 mm                      Droog vol.gew.                       $\gamma_{dr}$ : 10.26 kN/m<sup>3</sup>  
 Apparaat : 22                              Zetting (24u) : 0.885 mm                      Watergehalte                      W : 57 %  
 Soort monster : Ongeroerd                      h (24u) : 18.115 mm                      Grondsoort :                      Klei, matig siltig, zwak humeus gr.

Belastingtrappen:	Trap1	Trap2	Trap3	Trap4	Trap5	Trap6	Trap7
Belasting [kN/m <sup>2</sup> ]	43	60	84	116	161	116	161
$\Delta p$ [kN/m <sup>2</sup> ]	43	17	24	32	45	-45	45
$c_v$ [10 <sup>-3</sup> m <sup>2</sup> /s] (wortel-t)			2.37	1.87	1.72		
$m_v$ [1/MPa]			0.35	0.31	0.23		
$k_{10}$ [10 <sup>-11</sup> m/s]			8.17	5.71	3.81		
$c_v$ [10 <sup>-3</sup> m <sup>2</sup> /s] (log-t)			1.92	1.18			20.45
$C_{\alpha}$ [10 <sup>-3</sup> ]			4.466	5.363			0.6242



Opdracht : 1702832  
 Plaats : nvt  
 Project : Laboratoriumonderzoek

**SAMENDRUKKINGSPROEF**

Totaaloverzicht proefresultaten

Boring	: BL-791	Startdatum	: 19-09-2017	Diepte	: NAP -1.60 / -1.65 m.
Monster	: 11	Einddatum	: 29-09-2017	Initieel vol.gew.	$\gamma$ : 16.11 kN/m <sup>3</sup>
Bus	: 22855	Hoogte monster	: 19.00 mm	Droog vol.gew.	$\gamma_{dr}$ : 10.26 kN/m <sup>3</sup>
Apparaat	: 22	Zetting (24u)	: 0.885 mm	Watergehalte	W : 57 %
Soort monster	: Ongeroid	$e_0$	: 1.44	Grondsoort	: Klei, matig siltig, zwak humeus gr.

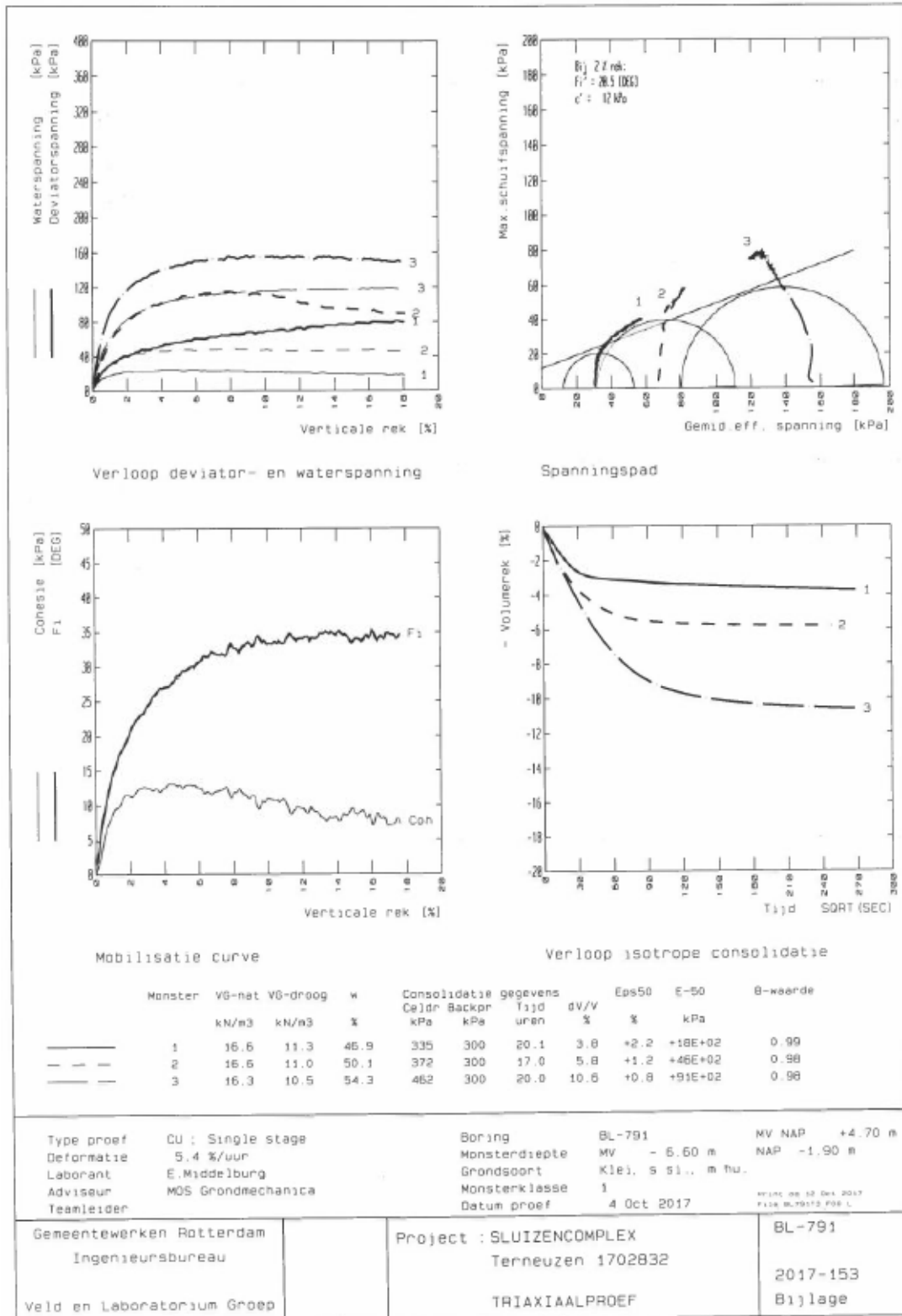
**Bepaling parameters per trap**

Belasting p [kPa]	43	60	84	116	161	116	161
<b>NEN / Bjerrum</b>	<b>Trap 1</b>	<b>2</b>	<b>3</b>	<b>4</b>	<b>5</b>	<b>6</b>	<b>7</b>
$C_{c(r)/sw} = \Delta e / \Delta \log p$	0.1732	0.2445	0.2897	0.3285	0.0325	0.0596	
$CR/RR/SR = C_c / (1 + e_0)$	0.0709	0.1001	0.1186	0.1346	0.0133	0.0244	
$C_{\alpha} = \Delta e / \Delta \log t$			0.0045	0.0054			0.0006
<b>KoppeJan</b>	<b>Trap 1</b>	<b>2</b>	<b>3</b>	<b>4</b>	<b>5</b>	<b>6</b>	<b>7</b>
$C_p$	33.8	22.3	19.2	16.5	85.7	88.6	
$C_s$	193.0	97.9	123.9	57.8	130.7	239.3	
$C_{10^4}$	19.9	11.7	11.8	7.7	23.7	35.7	
<b>Taylor / Casagrande</b>	<b>Trap 1</b>	<b>2</b>	<b>3</b>	<b>4</b>	<b>5</b>	<b>6</b>	<b>7</b>
$c_v$ [10 <sup>-8</sup> m <sup>2</sup> /s] (Taylor)			2.37	1.87	1.72		
$m_v$ [1/MPa]			0.35	0.31	0.23		
$k_{10}$ [10 <sup>-11</sup> m/s]			8.17	5.71	3.81		
$c_v$ [10 <sup>-8</sup> m <sup>2</sup> /s] (Casagrande)			1.92	1.18			20.45
<b>Isotachen</b>	<b>Trap 1</b>	<b>2</b>	<b>3</b>	<b>4</b>	<b>5</b>	<b>6</b>	<b>7</b>
a, b	0.0325	0.0465	0.0561	0.0652	0.0065	0.0120	
c			0.0024	0.0034			

**Bepaling  $P_g$  en parameters op basis van geselecteerde trappen**

NEN / Bjerrum	Trap 6 - 7	Trap 4 - 5	Trap 5 - 6	Trap 4
$P_g = 83.1$	$C_r = 0.0596$ $RR = 0.0244$	$C_c = 0.3285$ $CR = 0.1346$	$C_{sw} = 0.0325$ $SR = 0.0133$	$C_{\alpha} = 0.0054$
<b>KoppeJan</b>	<b>Trap 1 - 2</b>	<b>Trap 4 - 5</b>	<b>Trap 5 - 6</b>	<b>Trap 6 - 7</b>
$P_g = 79.7$	$C_p = 33.8$ $C_s = 193.0$ $C_{10^4} = 19.9$	$C_p' = 16.5$ $C_s' = 57.8$ $C_{10^4}' = 7.7$	$A_p = 85.7$ $A_s = 130.7$ $A_{10^4} = 23.7$	$C_{p(r)} = 88.6$ $C_{s(r)} = 239.3$ $C_{10^4(r)} = 35.7$
<b>Isotachen</b>	<b>Trap 6 - 7</b>	<b>Trap 4 - 5</b>	<b>Trap 5</b>	
$P_g = 84.1$	a = 0.0120	b = 0.0652	c = 0.0034	

### B.3 Triaxial Test - Lab Report



BISGEO\_TRIAX : 1  
 Boring : BL-791  
 Diepte NAP : -1.9  
 Terrein sp : 0  
 Datum : 4 Oct 2017  
 Grondcode : Ks3h2  
 Grondsoort : Klei, s si., m hu.  
 Gn-gem kN/m3 : 16.5  
 Gdr-gem kN/m3 : 11.0  
 W-gem % : 50.4  
 Type proef : CU Uitvoering : S Cohesie 0 : N  
 Deelproeven : 3 Monsterklasse : 1 Procedure : -  
 Deformatie : 5.4 %/uur  
 Bestand : BL791T3.A00

## MOBILISATIE GEGEVENS

EA	FI	Coh	P1	Q1	dV1	P2	Q2	dV2	P3	Q3	dV3
%	Deg	kPa	kPa	kPa	%	kPa	kPa	%	kPa	kPa	%
0.0	0.0	0.0	35.0	0.0	0.00	72.0	0.0	0.00	162.0	0.0	0.00
.1	2.2	1.1	31.1	2.0	0.00	67.0	4.1	0.00	153.1	7.0	0.00
.2	3.7	2.0	31.0	4.2	0.00	67.2	6.2	0.00	154.0	12.1	0.00
.3	6.1	2.4	31.4	6.2	0.00	67.6	8.8	0.00	155.1	19.1	0.00
.4	7.7	3.9	31.4	8.3	0.00	68.0	12.6	0.00	154.6	24.7	0.00
.5	9.0	5.4	31.3	10.0	0.00	68.1	16.4	0.00	152.9	29.2	0.00
.6	10.3	6.6	31.6	11.6	0.00	68.2	19.4	0.00	151.3	33.3	0.00
.7	11.5	7.2	31.8	12.6	0.00	68.3	21.8	0.00	150.4	36.7	0.00
.8	12.6	7.8	31.8	13.5	0.00	68.8	24.1	0.00	149.4	39.6	0.00
.9	13.7	8.4	31.6	14.4	0.00	69.2	26.2	0.00	148.1	42.6	0.00
1.0	14.6	8.9	31.7	15.0	0.00	69.5	28.4	0.00	146.8	44.9	0.00
1.1	15.2	9.6	32.3	16.0	0.00	69.9	30.2	0.00	145.7	46.6	0.00
1.2	15.9	9.9	32.4	16.5	0.00	70.6	31.9	0.00	144.8	48.3	0.00
1.3	16.8	9.9	32.0	16.6	0.00	70.9	33.2	0.00	143.9	50.0	0.00
1.4	17.6	10.1	32.1	17.2	0.00	70.9	34.3	0.00	143.1	51.8	0.00
1.5	18.0	10.6	32.8	18.3	0.00	70.6	35.0	0.00	142.3	53.1	0.00
1.6	18.4	11.2	33.1	19.1	0.00	70.5	36.0	0.00	141.6	54.3	0.00
1.7	18.8	11.6	33.2	19.5	0.00	70.9	37.1	0.00	140.6	55.1	0.00
1.8	19.3	11.8	33.3	20.1	0.00	71.6	38.2	0.00	140.3	56.5	0.00
1.9	20.0	11.7	33.3	20.3	0.00	71.7	38.8	0.00	139.7	57.6	0.00
2.0	20.5	11.7	33.3	20.3	0.00	71.9	39.8	0.00	138.9	58.3	0.00
3.0	24.3	12.9	35.9	23.9	0.00	74.9	46.9	0.00	134.9	65.6	0.00
4.0	27.2	12.7	38.1	26.1	0.00	77.0	51.0	0.00	132.3	70.0	0.00
5.0	29.0	13.1	39.4	28.3	0.00	78.3	53.3	0.00	130.3	72.9	0.00
6.0	30.6	12.9	41.5	30.5	0.00	80.0	55.0	0.00	128.8	75.4	0.00
7.0	32.0	12.3	43.3	31.3	0.00	80.9	56.9	0.00	127.5	76.3	0.00
8.0	33.0	11.9	44.6	32.5	0.00	81.5	57.5	0.00	126.9	77.6	0.00
9.0	33.4	11.4	47.0	34.0	0.00	80.7	56.3	0.00	126.3	78.0	0.00
10.0	33.3	11.3	47.3	34.3	0.00	80.8	55.8	0.00	125.5	77.5	0.00
11.0	33.5	11.1	49.4	35.8	0.00	79.4	54.4	0.00	123.7	77.0	0.00
12.0	34.1	9.8	50.5	36.5	0.00	77.0	51.3	0.00	124.1	77.8	0.00
13.0	34.5	9.0	52.2	37.2	0.00	75.1	49.7	0.00	122.7	77.1	0.00
14.0	34.6	8.7	53.1	37.9	0.00	73.7	48.0	0.00	122.5	76.9	0.00
15.0	33.8	9.6	54.0	38.6	0.00	72.5	47.5	0.00	122.0	76.0	0.00

## PARAMETERS PER DEELPROEF

Gnat	Gdrg	W	Peff	E50	Eps50	nu	Psi
kN/m3	kN/m3	%	kPa	kPa	%	-	Deg
16.6	11.3	46.9	35	175.3E+1	2.2	.50	0.0
16.6	11.0	50.1	72	455.5E+1	1.2	.50	0.0
16.3	10.5	54.3	162	905.5E+1	.8	.50	0.0

EINDE BESTAND



## B.4 Soil Parameter Determination - Unit Weight

**Table B.4.1:** Statistical profile for the dry and saturated unit weight of layer L05.

Unit Weight	Units	Average	St.dev	Min	Max	Mean
$\gamma_{sat}$	$kN/m^3$	18.56	1.72	12.30	20.70	18.80
$\gamma_{dry}$	$kN/m^3$	14.71	2.44	6.40	17.60	14.80

**Table B.4.2:** Statistical profile for the dry and saturated unit weight of layer L07.

Unit Weight	Units	Average	St.dev	Min	Max	Mean
$\gamma_{sat}$	$kN/m^3$	14.85	2.67	11.60	19.36	13.99
$\gamma_{dry}$	$kN/m^3$	9.24	3.64	5.40	15.20	8.48

**Table B.4.3:** Statistical profile for the dry and saturated unit weight of layer L08, L10 & L12.

Unit Weight	Units	Average	St.dev	Min	Max	Mean
$\gamma_{sat}$	$kN/m^3$	18.74	1.27	14.63	20.13	19.03
$\gamma_{dry}$	$kN/m^3$	15.55	0.90	12.80	17.17	15.67

**Table B.4.4:** Statistical profile for the dry and saturated unit weight of layer L09 & L11.

Unit Weight	Units	Average	St.dev	Min	Max	Mean
$\gamma_{sat}$	$kN/m^3$	18.53	0.74	17.20	19.70	18.60
$\gamma_{dry}$	$kN/m^3$	14.66	0.89	13.20	16.30	14.75

**Table B.4.5:** Statistical profile for the dry and saturated unit weight of layer L15.

Unit Weight	Units	Average	St.dev	Min	Max	Mean
$\gamma_{sat}$	$kN/m^3$	19.25	1.10	16.90	20.90	19.35
$\gamma_{dry}$	$kN/m^3$	15.18	1.11	13.00	16.80	15.35

**Table B.4.6:** Statistical profile for the dry and saturated unit weight of layer L16.

Unit Weight	Units	Average	St.dev	Min	Max	Mean
$\gamma_{sat}$	$kN/m^3$	19.13	0.43	17.80	19.80	19.10
$\gamma_{dry}$	$kN/m^3$	15.53	0.40	14.60	16.30	15.650

**Table B.4.7:** Statistical profile for the dry and saturated unit weight of layer L17.

Unit Weight	Units	Average	St.dev	Min	Max	Mean
$\gamma_{sat}$	$kN/m^3$	19.13	0.21	18.90	19.40	19.10
$\gamma_{dry}$	$kN/m^3$	15.60	0.14	15.50	15.80	15.50

**Table B.4.8:** Statistical profile for the dry and saturated unit weight of layer L18.

Unit Weight	Units	Average	St.dev	Min	Max	Mean
$\gamma_{sat}$	$kN/m^3$	18.61	0.60	17.30	19.50	18.80
$\gamma_{dry}$	$kN/m^3$	15.21	0.52	14.20	16.00	15.40

## B.5 Soil Parameter Determination - Small Strain

**Table B.5.1:** Calculation of small strain shear stiffness  $G_0^{ref}$  for soil layers L05a and L05b using Alpan, 1970 [1] and Benz & Vermeer, 2007 [7] methods.

Par.	Units	Alpan L05a	Alpan L05b	Benz L05a	Benz L05b	Average L05a	Average L05b
$E_{stat}$	$kPa$	121392	184856	121392	184856	121392	184856
$E_{stat}/E_{dyn}$	-	2.90	2.40	4.00	3.60	3.45	3.00
$E_0^{ref}$	$kPa$	352038	443654	485570	665482	418804	554568
$G_0^{ref}$	$kPa$	146683	184856	202321	277284	174502	231070

**Table B.5.2:** Calculation of small strain shear stiffness  $G_0^{ref}$  for layer L07 using Alpan, 1970 and Benz & Vermeer, 2007 [7] methods.

Par.	Units	Alpan	Benz	Average
$E_{stat}$	$kPa$	2336	2336	2336
$E_{stat}/E_{dyn}$	-	19	24	21.5
$E_0^{ref}$	$kPa$	44384	56064	50224
$G_0^{ref}$	$kPa$	19297	24376	21837

**Table B.5.3:** Calculation of small strain shear stiffness  $G_0^{ref}$  for the layer L08 with Alpan, 1970 and Benz & Vermeer, 2007 [7] methods.

Par.	Units	Alpan	Benz	Average
$E_{stat}$	$kPa$	172508	172508	152508
$E_{stat}/E_{dyn}$	-	2.6	3.6	3.1
$E_0^{ref}$	$kPa$	448520	621028	534774
$G_{0ref}$	$kPa$	195009	270012	232511

**Table B.5.4:** Calculation of small strain shear stiffness  $G_0^{ref}$  for layer L09 with Alpan, 1970 and Benz & Vermeer, 2007 [7] methods.

Par.	Units	Alpan	Benz	Average
$E_{stat}$	<i>kPa</i>	81140	81140	81140
$E_{stat}/E_{dyn}$	-	3.2	4.6	3.9
$E_0$	<i>kPa</i>	259649	373245	316447
$E_{stat}$	<i>kPa</i>	112891	162280	137586

**Table B.5.5:** Calculation of small strain shear stiffness  $G_0^{ref}$  for layer L15 with Alpan, 1970 and Benz & Vermeer, 2007 methods.

Par.	Units	Alpan	Benz	Average
$E_{stat}$	<i>kPa</i>	42278	42278	42278
$E_{stat}/E_{dyn}$	-	4.05	5.90	4.98
$E_0^{ref}$	<i>kPa</i>	171226	249440	210333
$G_0^{ref}$	<i>kPa</i>	65856	95939	80897

**Table B.5.6:** Calculation of small strain shear stiffness  $G_0^{ref}$  for layer L16 with Alpan, 1970 and Benz & Vermeer, 2007 methods.

Par.	Units	Alpan	Benz	Average
$E_{stat}$	<i>kPa</i>	131789	131789	131789
$E_{stat}/E_{dyn}$	-	2.8	3.9	3.35
$E_0^{ref}$	<i>kPa</i>	369011	513979	441495
$G_0^{ref}$	<i>kPa</i>	153754	214158	183956

**Table B.5.7:** Calculation of small strain shear stiffness  $G_0^{ref}$  for layer L17 with Alpan, 1970 and Benz & Vermeer, 2007 methods.

Par.	Units	Alpan	Benz	Average
$E_{stat}$	<i>kPa</i>	58128	58128	58128
$E_{stat}/E_{dyn}$	-	3.8	5.2	4.5
$E_0^{ref}$	<i>kPa</i>	220885	302263	261574
$G_0^{ref}$	<i>kPa</i>	92035	125943	108989

**Table B.5.8:** Calculation of small strain shear stiffness  $G_0^{ref}$  for Alpan, 1970 and Benz & Vermeer, 2007 methods.

Par.	Units	Alpan LX02	Alpan LX01	Benz LX02	Benz LX01	Average LX02	Average LX01
$E_{stat}$	<i>kPa</i>	156000	84000	156000	84000	156000	84000
$E_{stat}/E_{dyn}$	-	2.5	2.1	5.8	6.8	4.15	4.45
$E_0^{ref}$	<i>kPa</i>	390000	176400	904800	571200	647400	373800
$G_0^{ref}$	<i>kPa</i>	162500	73500	377000	238000	269750	155750

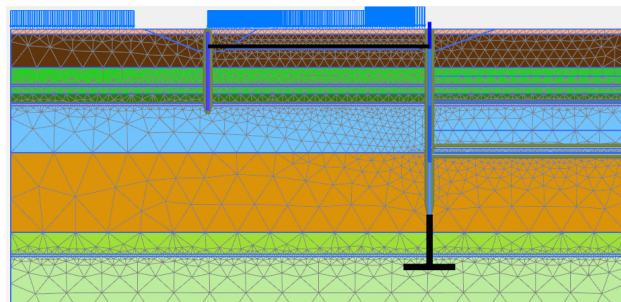
# C

## Construction Phases

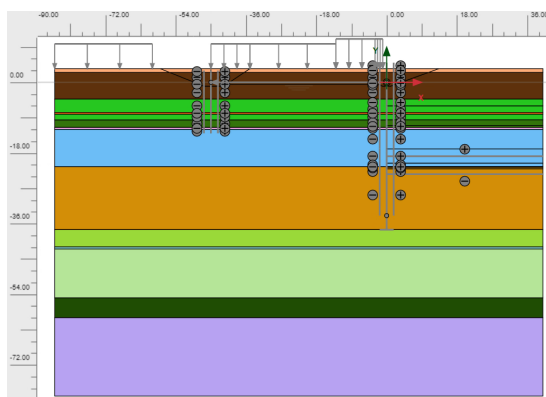
This Appendix provides screenshots of PLAXIS input regarding the medium-density generated mesh and the geometry used in each phase. Additionally, CAD drawings have been made that depict the project's soil layers, dimensions, and elements for the construction phases.

### C.1 PLAXIS mesh

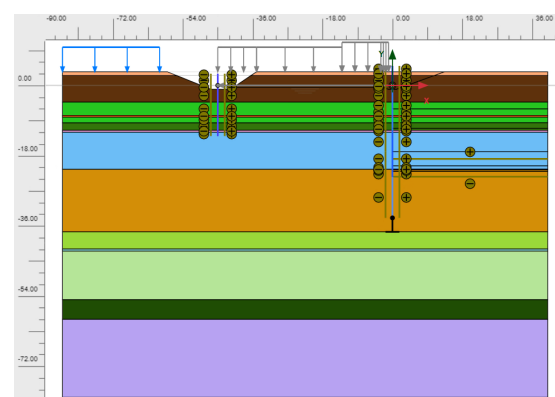
Medium density mesh has been used for all the scenarios in the present thesis.



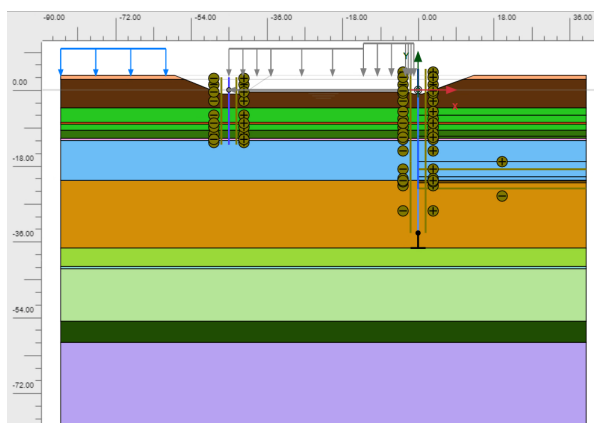
### C.2 PLAXIS input screenshots



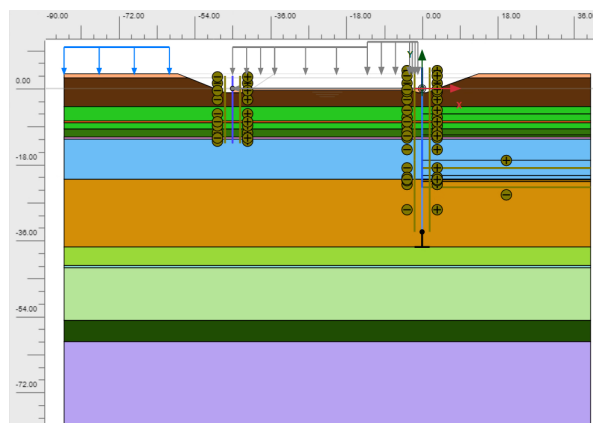
(a) Phase 0



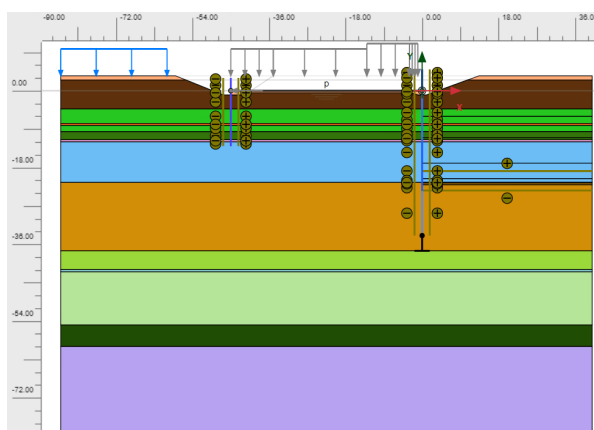
(b) Phase 1



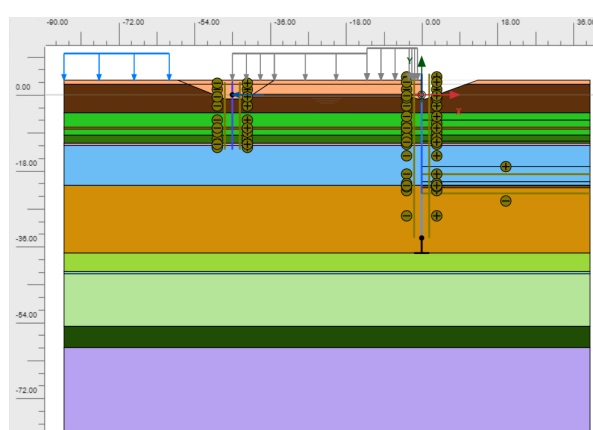
(a) Phase 2



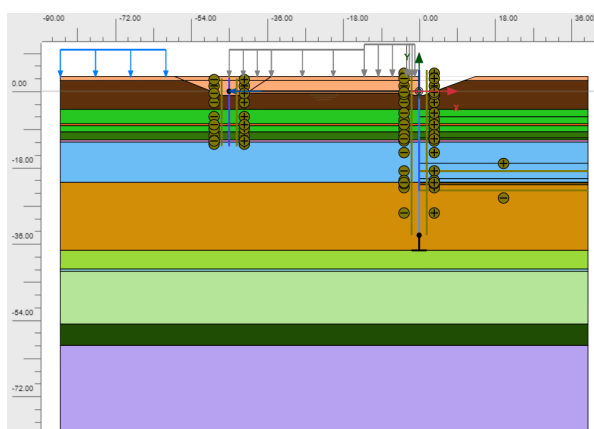
(b) Phase 3



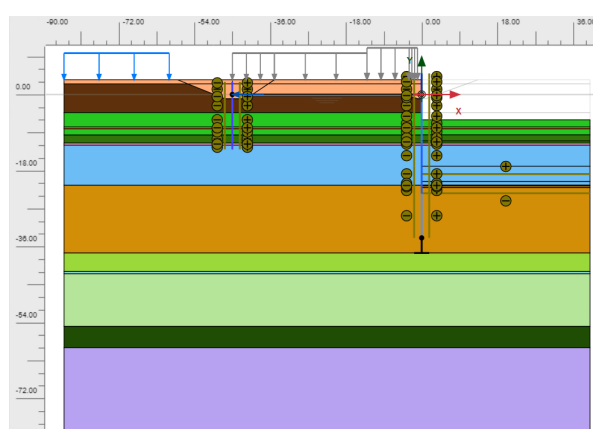
(c) Phase 4



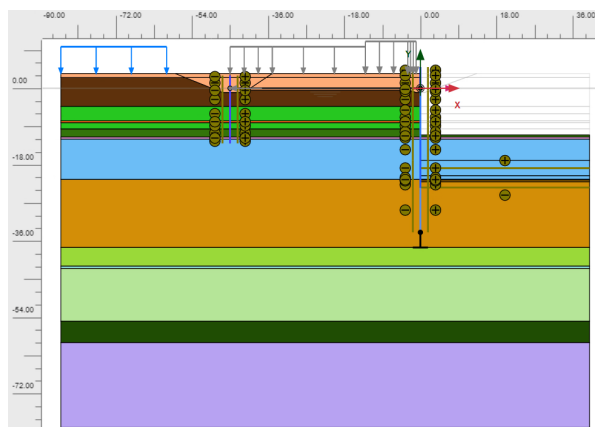
(d) Phase 5



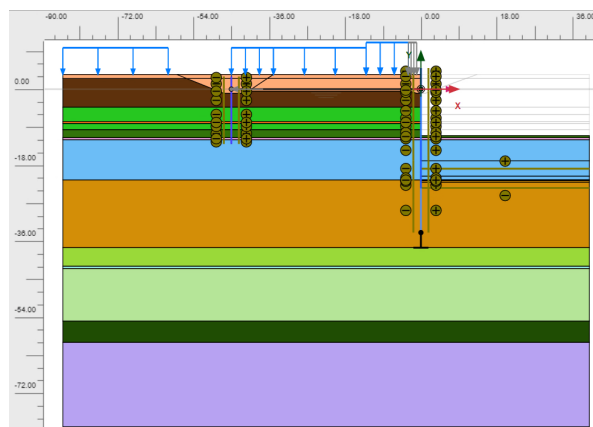
(e) Phase 6



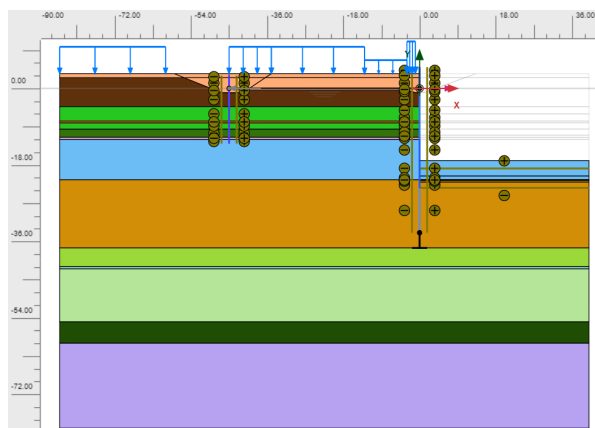
(f) Phase 7



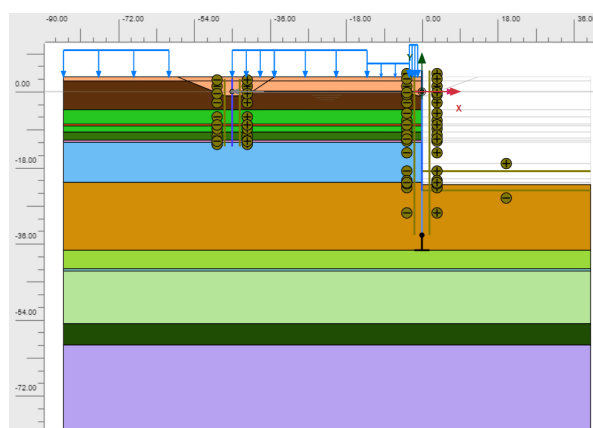
(a) Phase 8



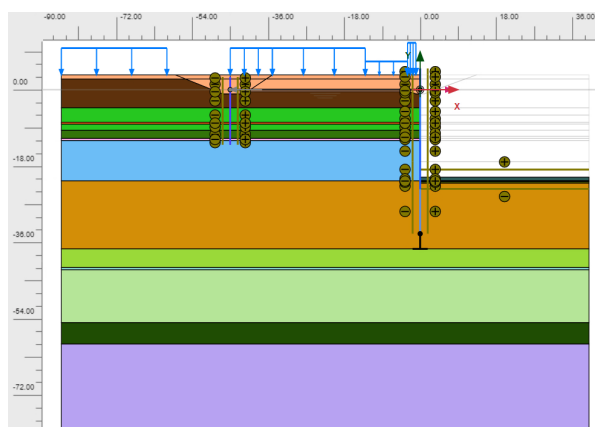
(b) Phase 9



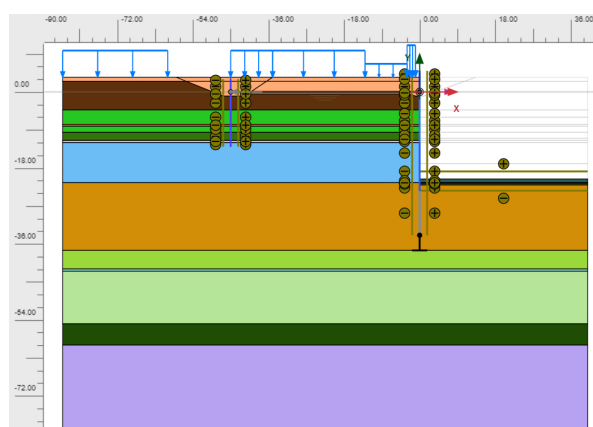
(c) Phase 10



(d) Phase 11



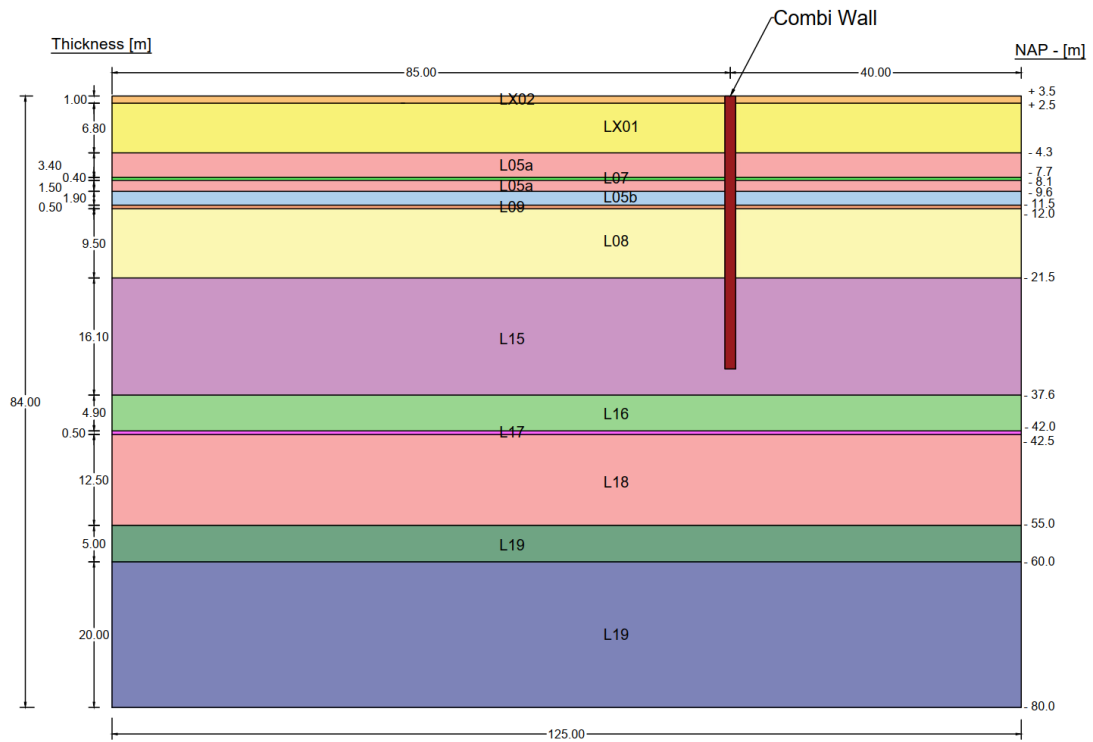
(e) Phase 12



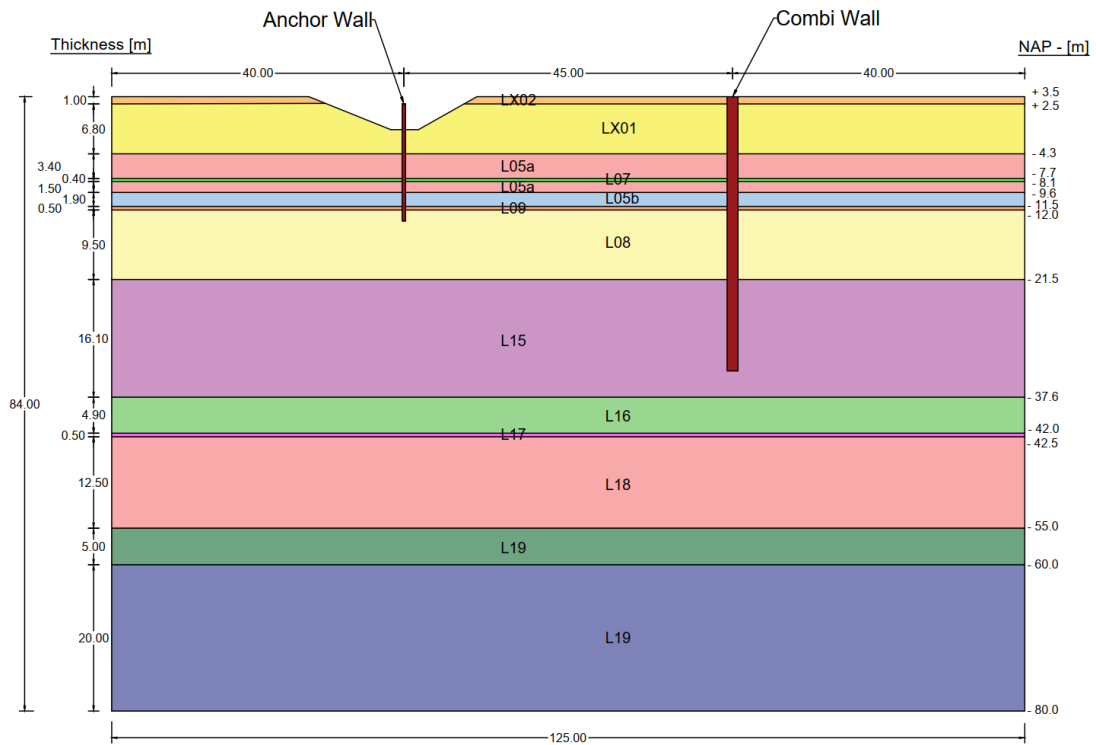
(f) Phase 13

### C.3 CAD drawings

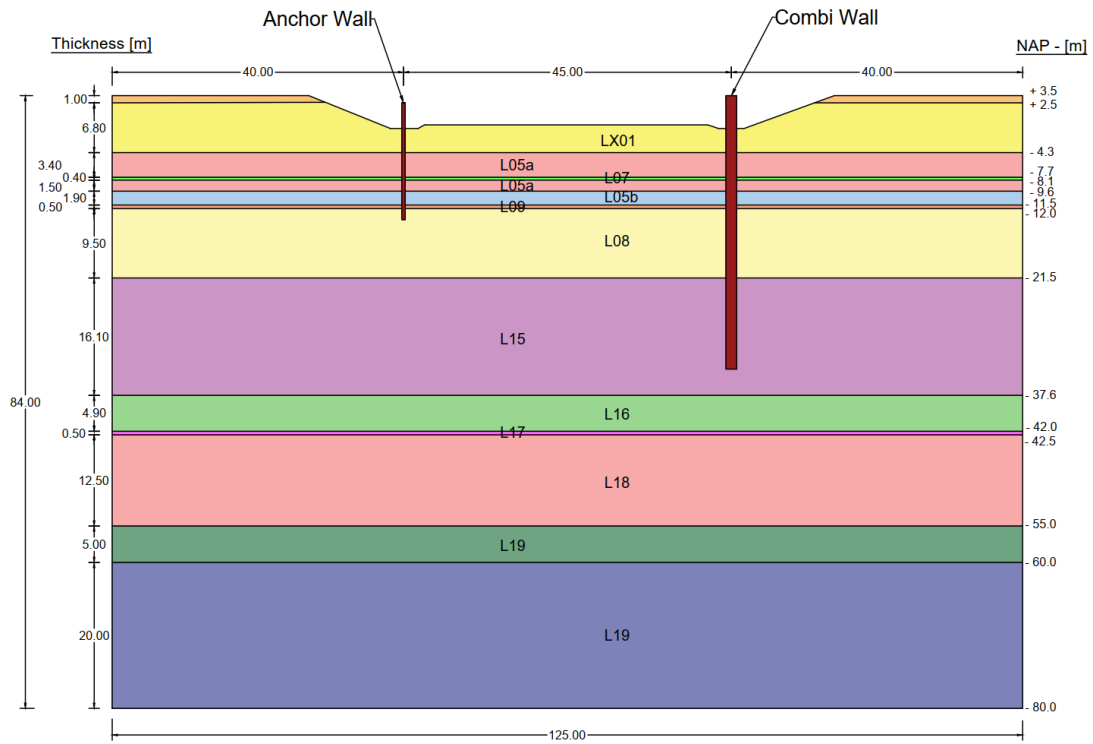
#### 0. Initial Conditions



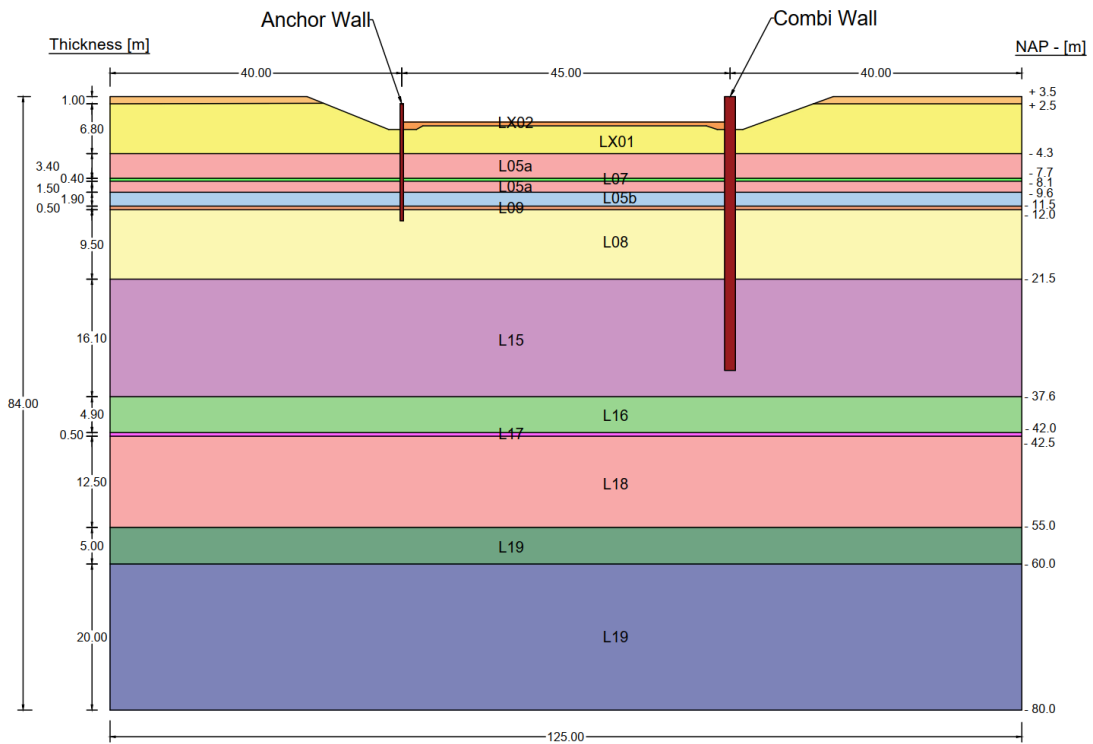
#### 1. Anchor Wall Excavation



### 2. Excavation for Anchor Wall Installation

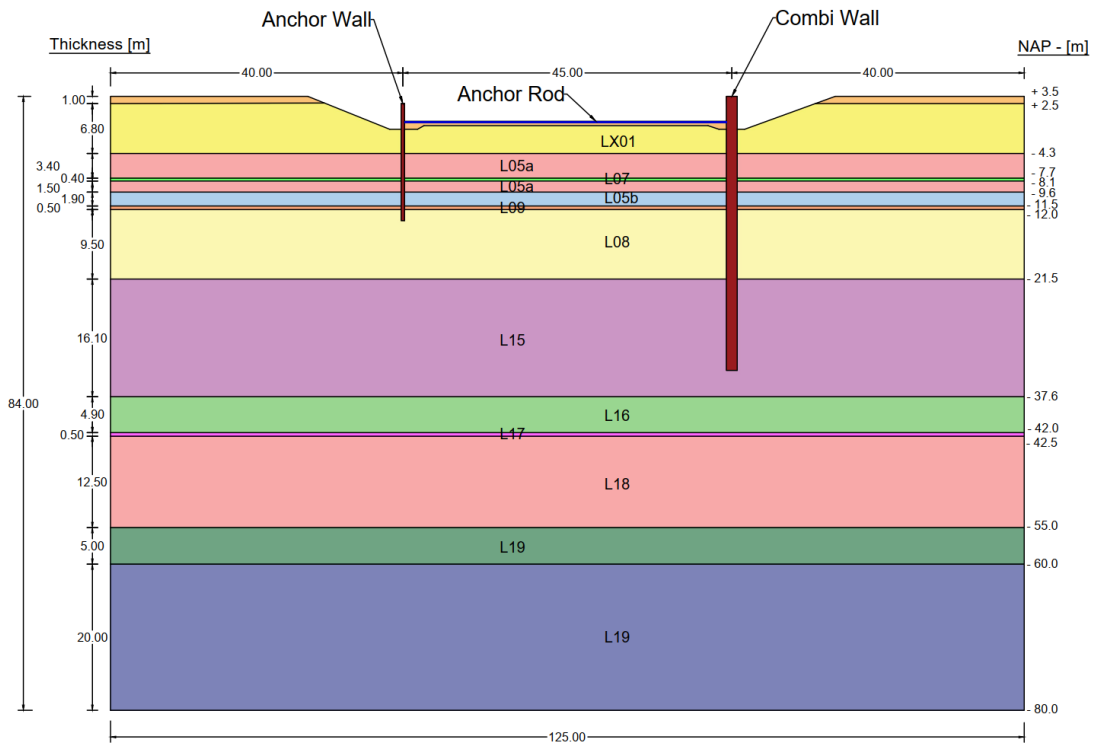


### 3. Replenish to Anchor Level with Soil

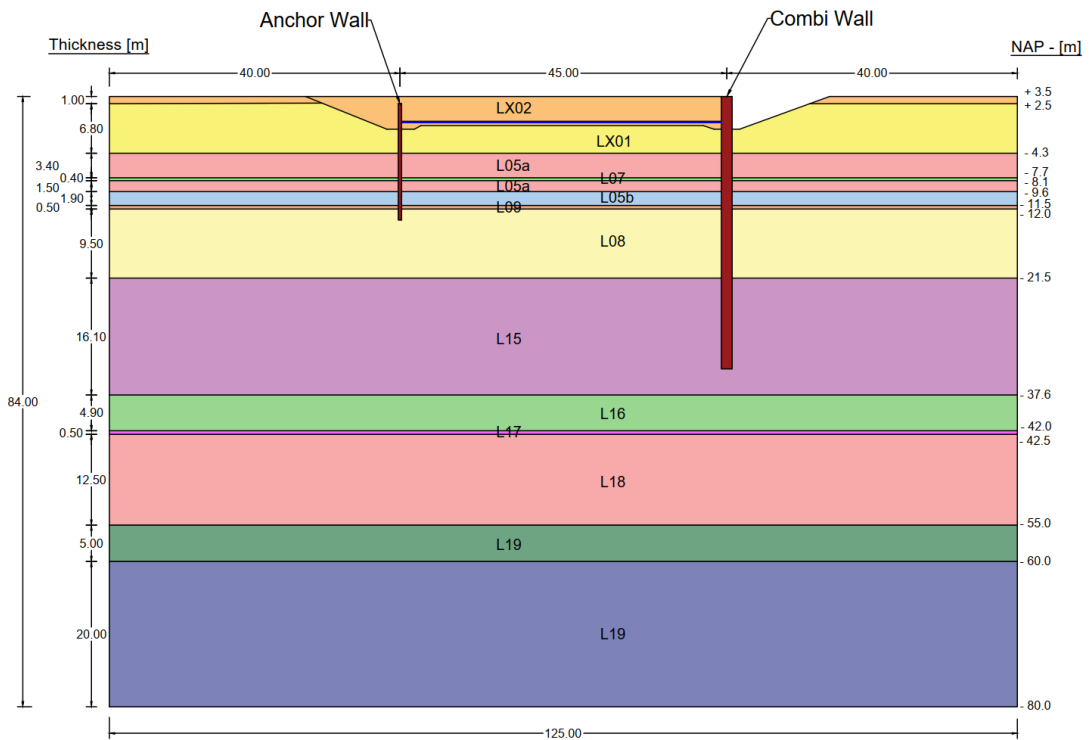




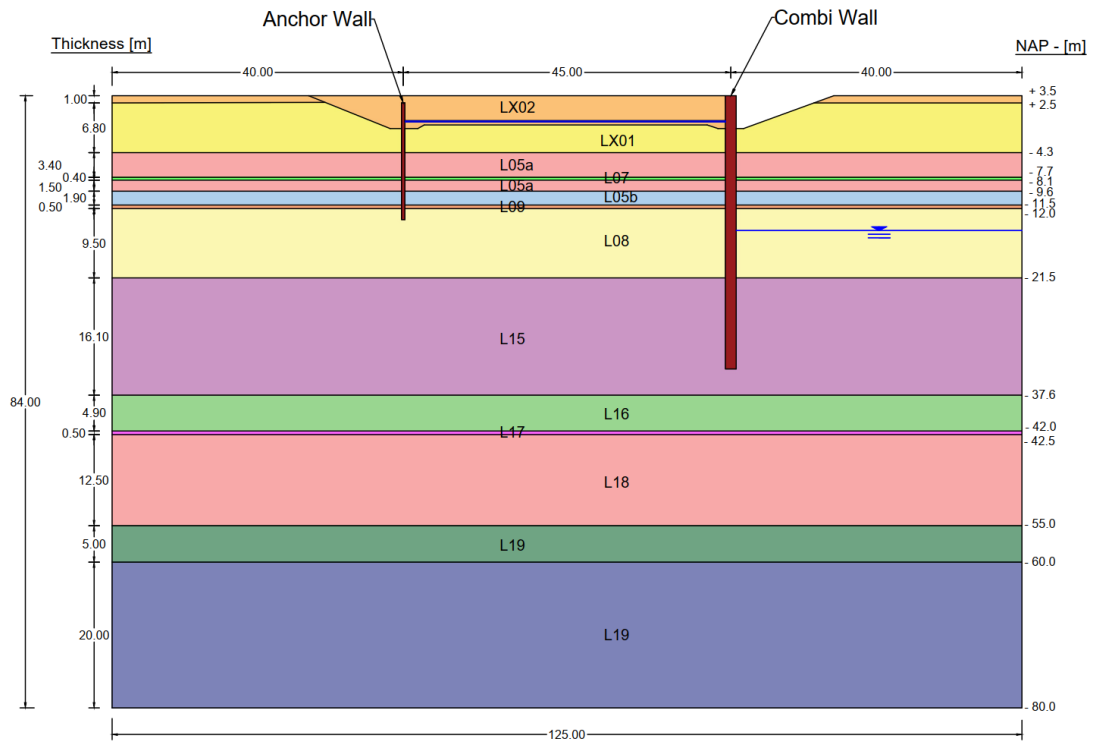
### 4. Installation and Pre-tension of Anchors



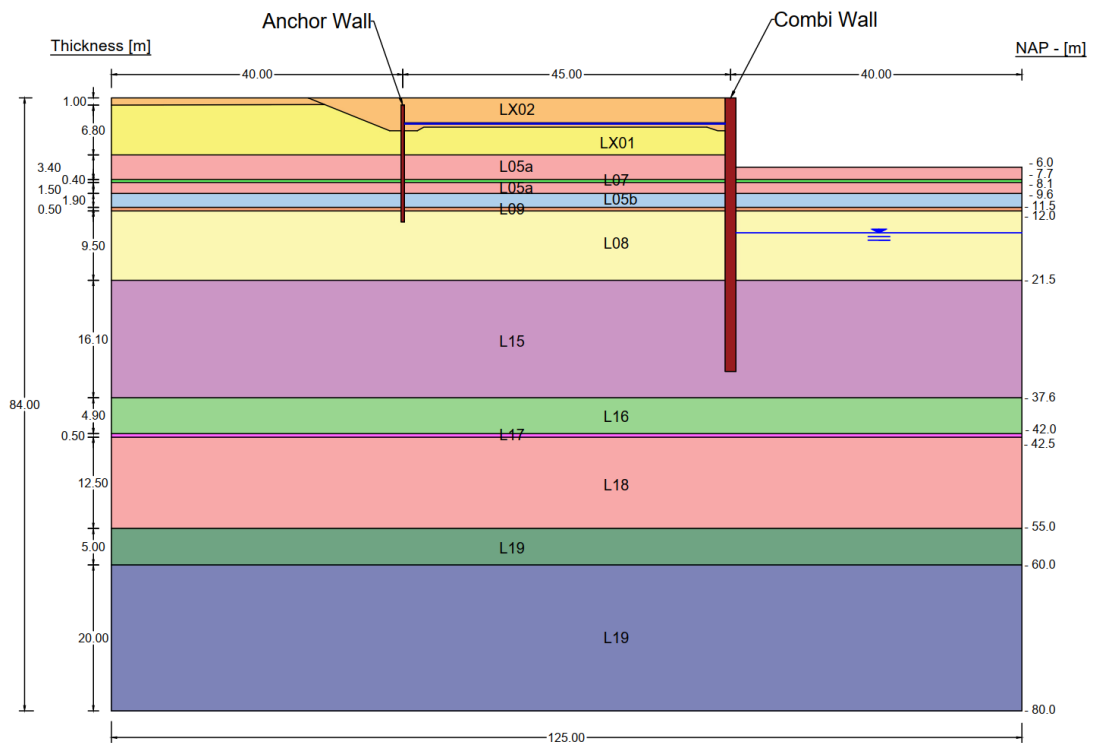
### 5. Soil Replenish to Surface



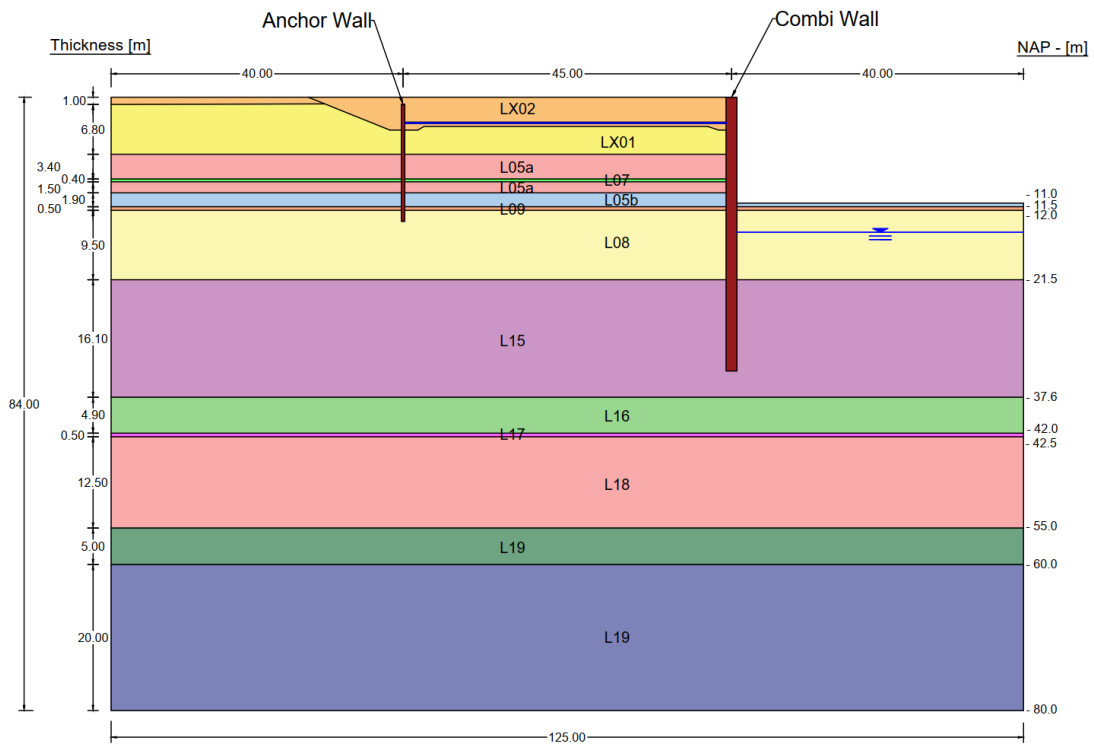
### 6. Lower Water Level in Pit to -15 m NAP



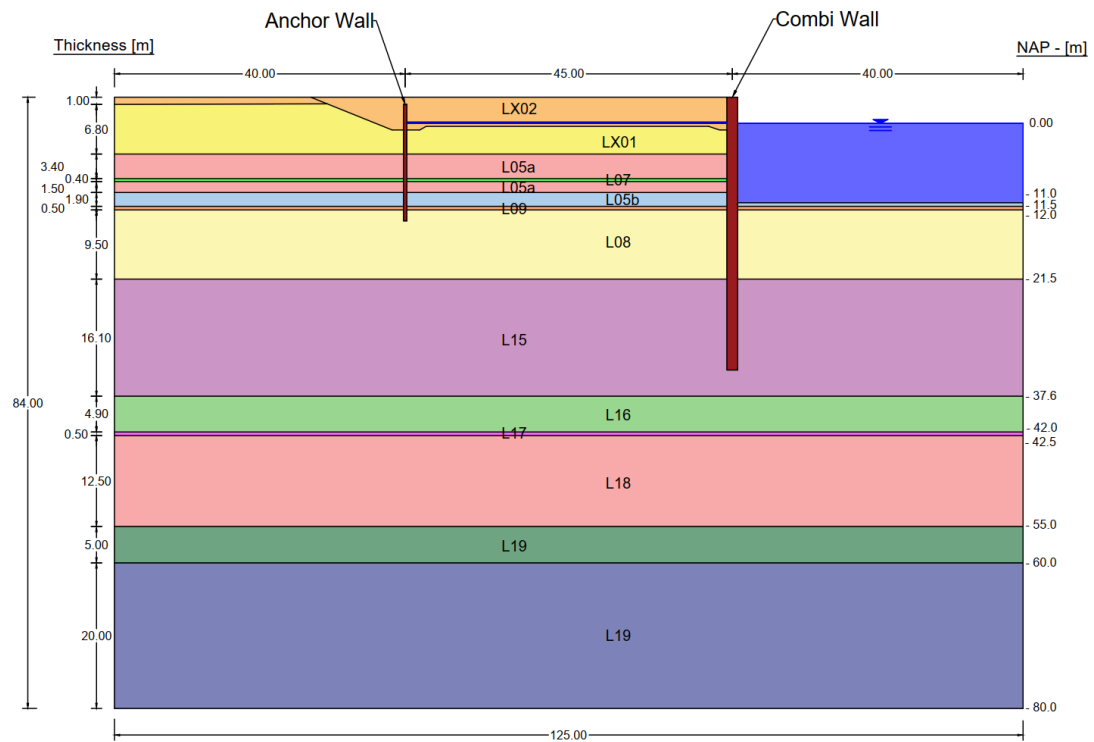
### 7. Dry Excavation to -6 m NAP



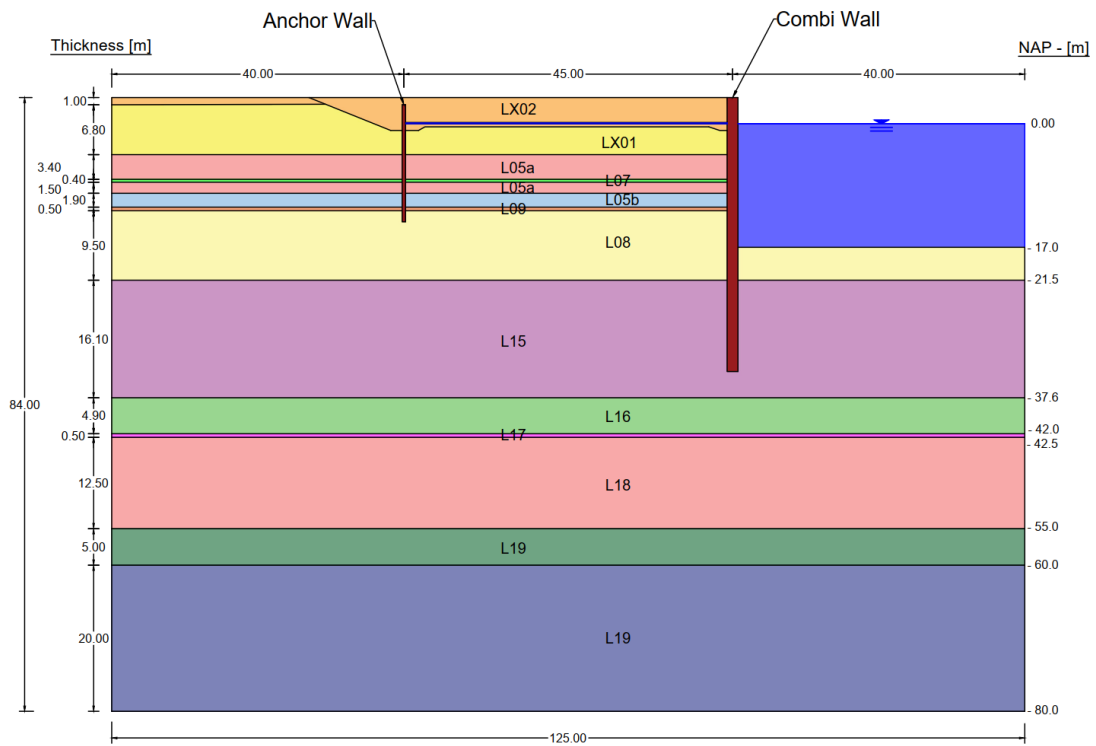
### 8. Dry Excavation to - 11 m NAP



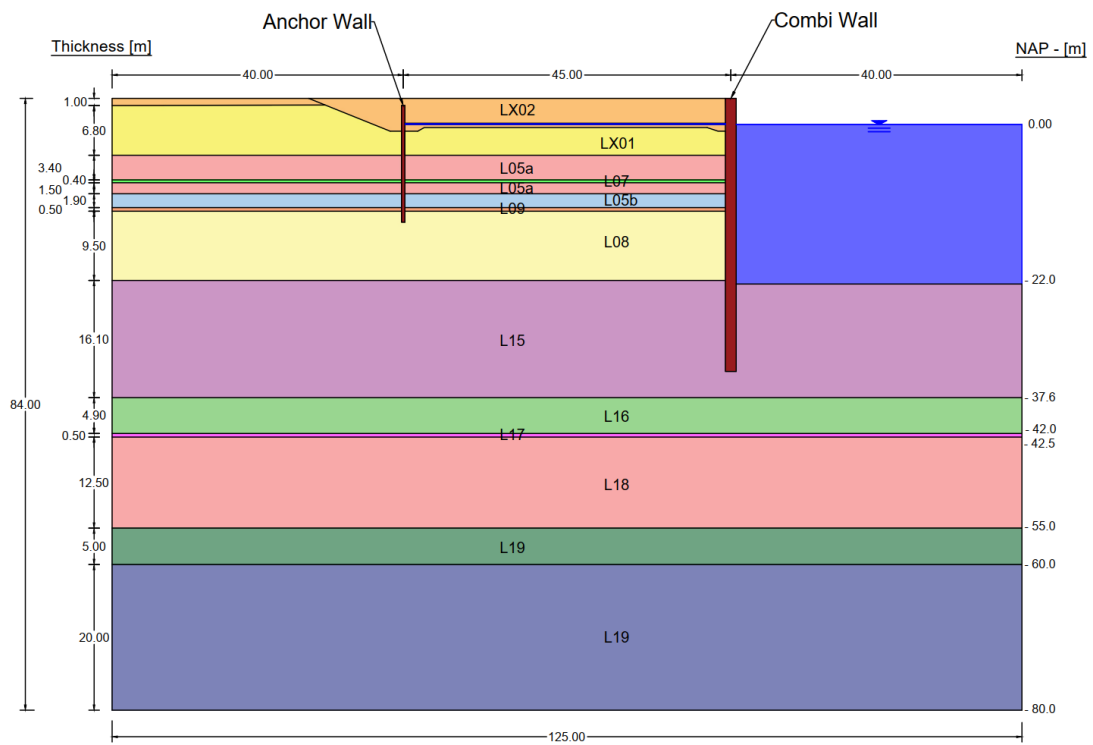
### 9. Submerge Pit to 0 m NAP



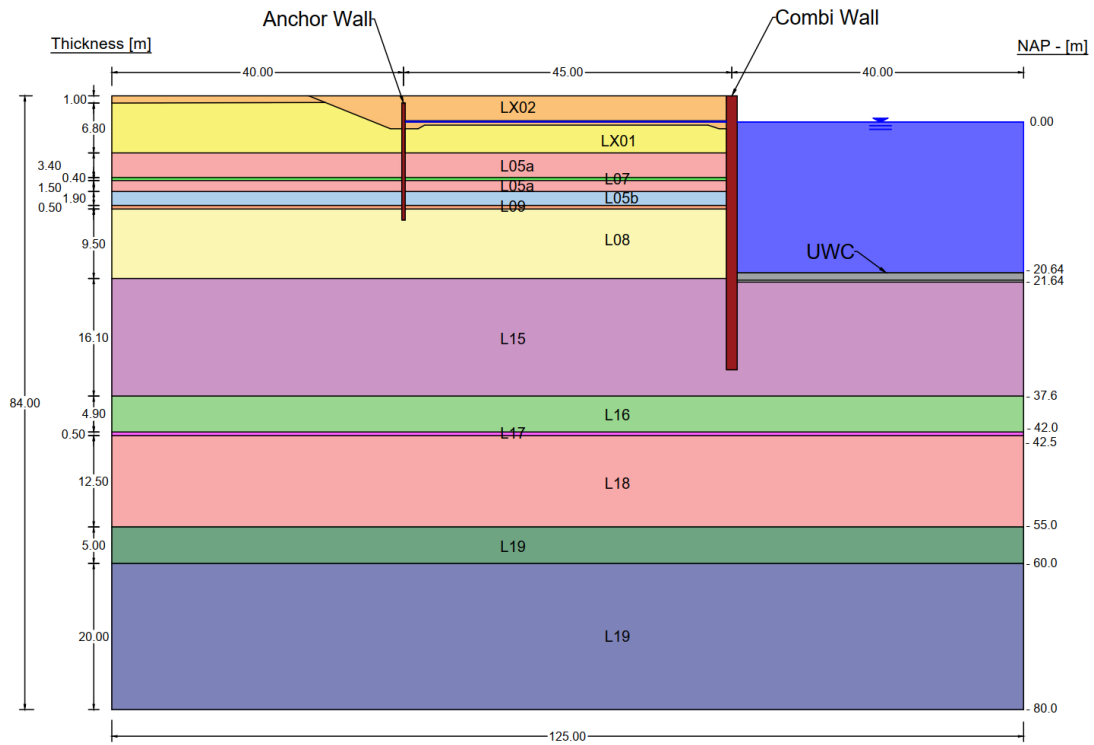
### 10. Dry Excavation to - 17 m NAP



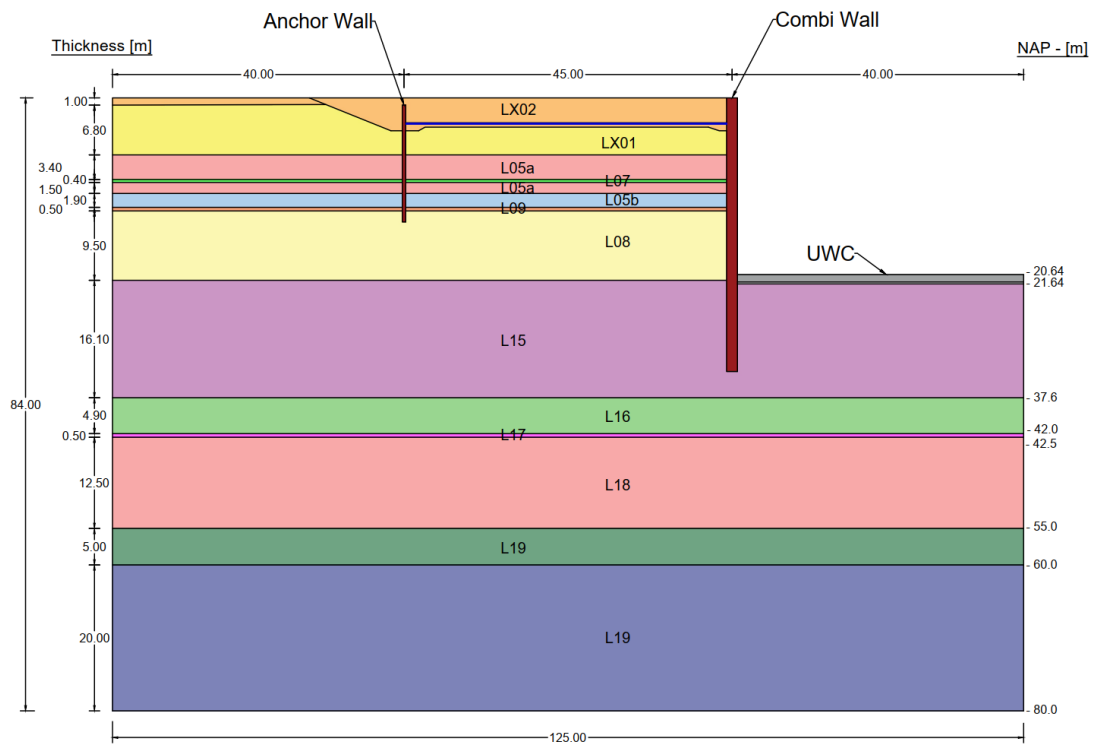
### 11. Dry Excavation to - 22 m NAP



### 12. Dumping Gravel and Pouring UWC



### 13. Set Excavation Pit Dry



# D

## Project Loads

**Photo 1: 09-09-2019**



**Photo 2: 23-10-2019**



**Photo 3: 17-01-2020**

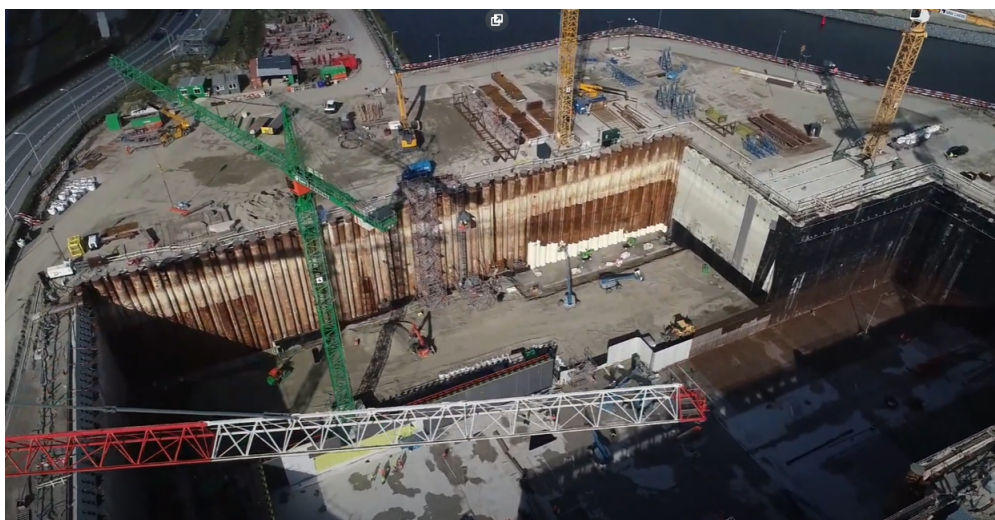


**Photo 4: 10-02-2020**



**Photo 5: 23-04-2020**



**Photo 6: 16-06-2020****Photo 7: 19-10-2020****Photo 8: 20-08-2020**



## Aquifer Heads

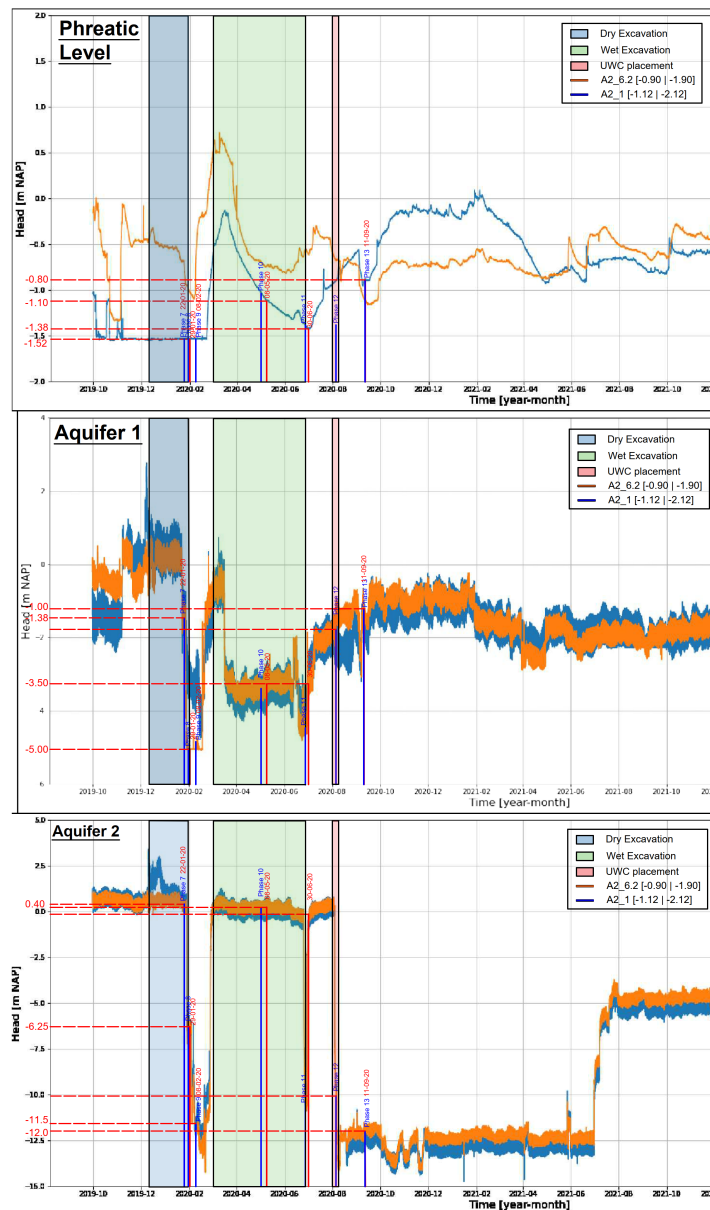


Figure E.0.1: Aquifer heads from the field. [Project Data]

## Boom Clay Lab Tests

### F.1 Samples Location

Extensive soil lab testing has been performed to derive the soil parameters for the various layers. Specifically, for the investigated layer (Boom Clay), 18 Triaxial isotopically consolidated undrained compression tests (CIU) and nine oedometer tests have been performed. Table F.1.1 summarizes the location and type of tests done for the Boom Clay Layer. The location of the boreholes is depicted in Figure F.1.1.

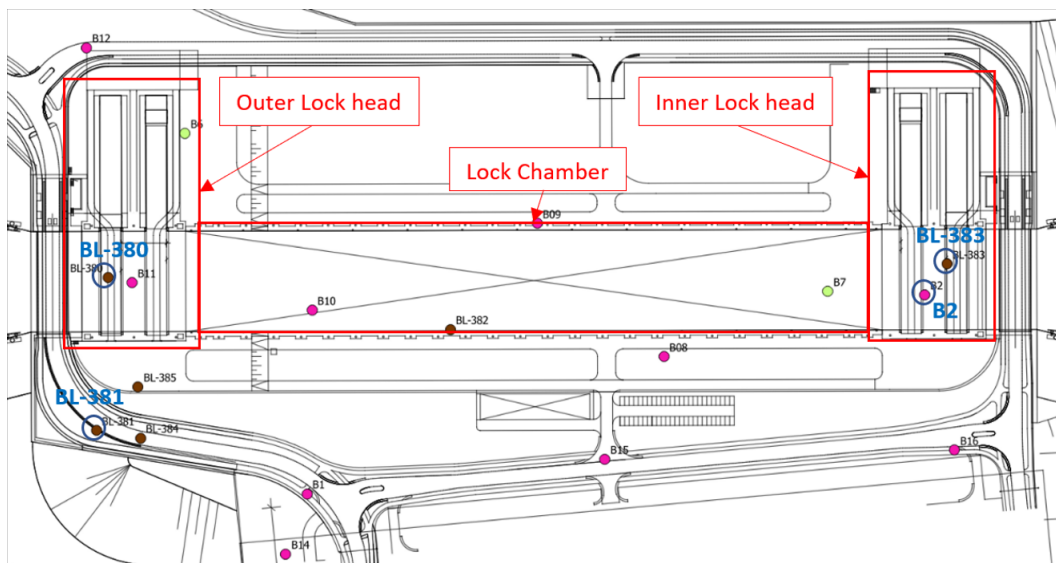


Figure F.1.1: Locations of the boreholes.

### F.2 Stiffness Determination Methodology

For the determination of the Boom Clay mechanical properties, four samples have been chosen that had been tested both in triaxial and oedometer apparatus. These samples were B2 – St.10, B2 – St.12, B2 – St.17, and B2 – St.19.

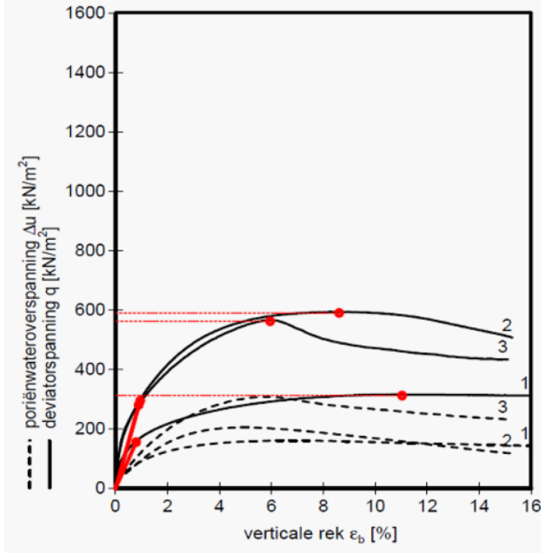
The secant stiffness  $E_{50}$  is derived from the triaxial tests. Figure F.2.1a depicts the deviatoric stress  $q$  versus vertical strain  $\epsilon_b$  example plot from the triaxial lab tests for three different confining stresses.

**Table F.1.1:** Lab tests for the Boom Clay layer.

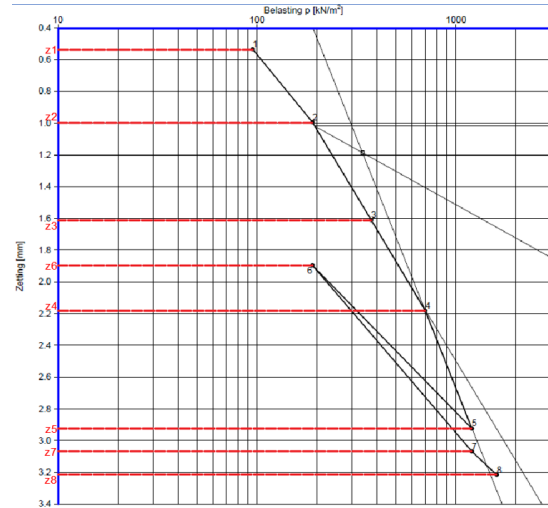
N.	Borehole	Sample	Average NAP Depth (m)	Test Type
1	BL – 380	St-15	-30.63	CIU, Triaxial
2	BL – 380	St-22	-33.43	CIU, Triaxial
3	BL – 380	St-26	-35.03	CIU, Triaxial
4	BL – 381	St-13	-29.93	CIU, Triaxial
5	BL – 381	St-18	-31.9	CIU, Triaxial
6	BL – 381	St-22	-33.53	CIU, Triaxial
7	BL – 383	St-15	-25.26	CIU, Triaxial
8	BL – 383	St-21	-27.81	CIU, Triaxial
8 9	BL – 383	St-25	-29.51	CIU, Triaxial
10	B2	St-6	-20.51	CIU, Triaxial
11	B2	St-8	-21.36	CIU, Triaxial
12	B2	St-10	-22.76	CIU, Triaxial
13	B2	St-12	-24.26	CIU, Triaxial
14	B2	St-14	-25.26	CIU, Triaxial
15	B2	St-17	-27.31	CIU, Triaxial
16	B2	St-19	-29.36	CIU, Triaxial
17	B2	St-21	-30.06	CIU, Triaxial
18	B2	St-24	-34.76	CIU, Triaxial
19	B2	St-7	-21.06	Oedometer Test
20	B2	St-10	-23.06	Oedometer Test
21	B2	St-12	-24.51	Oedometer Test
22	B2	St-15	-26.31	Oedometer Test
23	B2	St-16	-27.06	Oedometer Test
24	B2	St-17	-27.41	Oedometer Test
25	B2	St-19	-29.26	Oedometer Test
26	B2	St-20	-29.96	Oedometer Test
27	B2	St-23	-33.46	Oedometer Test

Firstly, a horizontal line is drawn at the maximum deviatoric stress. A second parallel line to the previous one at half deviatoric stress is sketched for each confining stress. At the location where the second line intersects the curve, a point is created. The inclination of the line connecting the point and the beginning of the axis with the horizontal axis is the secant stiffness  $E_{50}$ .

The oedometer stiffness  $E_{oed}$  and the un-/reloading stiffness  $E_{ur}$  have been derived from the plot vertical pressures versus settlements, as shown in Figure F.2.1b. The initial height of the sample is known; hence it can be transformed into a plot of pressures versus strains, Figure F.2.2a. At every new curve point, the tangent line is the oedometer stiffness at that specific stress condition. Since this test also includes unloading/reloading cycles, the calculation of  $E_{ur}$  is possible with the same method in the corresponding sections of the curve.

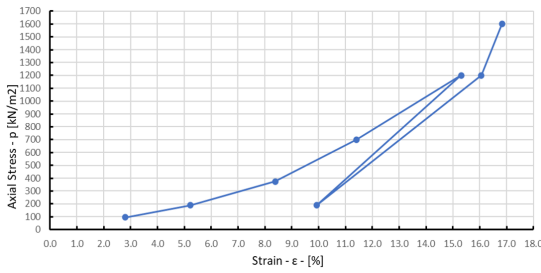


(a) Deviatoric vs vertical strain of a sample for three confining stress, form a triaxial test.

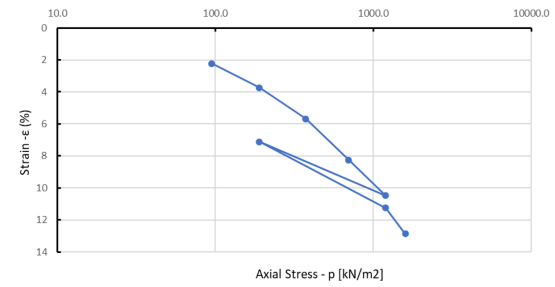


(b) Axial stress vs vertical settlement for a soil sample in an oedometer apparatus.

Figure F.2.1: Triaxial and Oedometer lab test output plots.



(a) Axial stress vs vertical strain of a soil sample in an oedometer apparatus.



(b) Log Axial stress vs vertical strain of a soil sample in an oedometer apparatus.

Figure F.2.2: Oedometer lab test output process.

### F.3 Stiffness Determination of the Samples

Applying these processes to the four Boom Clay samples, the stiffness is being derived. The effective cell pressures from the triaxial tests are given in Table F.3.1 and the deviatoric stress  $q$  versus the vertical strain  $\epsilon_b$  for the four samples is given in Figure F.3.1. The calculated values using the methodology described before are given from Table F.3.2 to Table F.3.5 for the four Boom Clay samples.

The secant stiffness needs to be converted to a reference level of 100 kPa, as the Plaxis manual suggests. The equation used for this purpose is Equation F.3.1. The  $E_{oed}^{ref}$  and  $E_{ur}^{ref}$  can be directly derived by deriving the stiffnesses directly at the reference stress. The rate of stress dependency  $m$  is given by Equation F.3.2.

$$E_{50}^{ref} = E_{50} * \left( \frac{\sigma_3'}{p_{ref}} \right)^m \tag{F.3.1}$$

$$\frac{E_{50}^{(1)}}{E_{50}^{(2)}} = \left( \frac{\sigma_3^{(1)}}{\sigma_3^{(2)}} \right)^m \tag{F.3.2}$$

**Table F.3.1:** Effective cell pressures used for the triaxial tests of the four Boom Clay samples.

		Step 1	Step 2	Step 3
B2 - St. 10	Back Pressure	300	300	300
	Horizontal Consolidation Stress	375	563	750
	Effective Cell Pressure	75	263	450
B2 - St. 12	Back Pressure	300	300	300
	Horizontal Consolidation Stress	385	578	770
	Effective Cell Pressure	85	278	470
B2 - St. 17	Back Pressure	300	300	300
	Horizontal Consolidation Stress	405	608	810
	Effective Cell Pressure	105	308	510
B2 - St. 19	Back Pressure	300		300
	Horizontal Consolidation Stress	420		840
	Effective Cell Pressure	120		540

In the oedometer test, un-reloading cycles have been performed. Following the procedure explained previously, the Eoed at reference stress level  $p_{ref} = 100$  kPa is being calculated. Similarly, the un-/reloading stiffness at the reference level is derived from the corresponding sections of the test. The plot of axial stress  $p$  vs the strain  $\epsilon$  for the four samples of Boom Clay is given in Figure F.3.2.

The calculated results are summarized in Table F.3.6. The final un-/reloading stiffness is the average value of the unloading and reloading branch.

**Table F.3.2:** Secant stiffness  $E_{50}$  calculation for Boom Clay sample B2 - St.10.

B2 - St.10	Step 1	Step 2	Step 3	Unit
$\sigma'_3$	227	383	442	$kN/m^2$
$\sigma'_3$ (ini)	75	263	450	$kN/m^2$
$q_f$	313.7	593.1	566.4	$kN/m^2$
$q_f/2$	156.9	296.6	283.2	$kN/m^2$
$\epsilon$	0.794	0.953	0.895	%
$E_{50}$	19756	31118	31642	$kN/m^2$
$s_u$	156.9	296.6	283.2	$kN/m^2$
$p_{ref}$	100	100	100	$kN/m^2$
$E_{50}^{ref}$	24868.9	14356.2	9499.5	$kN/m^2$
Average $E_{50}^{ref}$			16242	$kN/m^2$
$m$	$m_{1-2}$	$m_{2-3}$	$m_{1-3}$	Average m
	0.868	0.117	0.707	0.564

**Table F.3.3:** Secant stiffness  $E_{50}$  calculation for Boom Clay sample B2 - St.12.

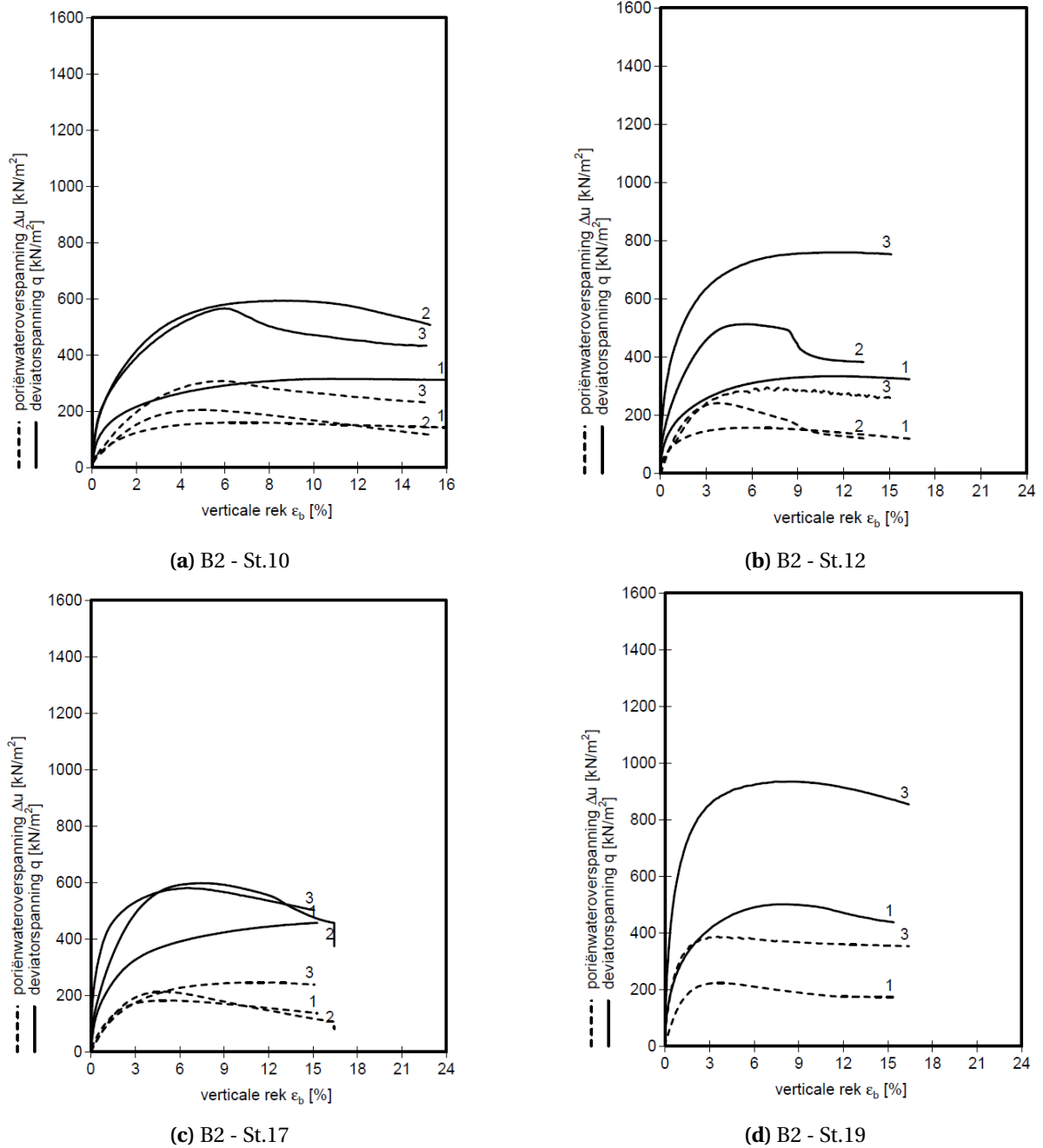
B2 - St.12	Step 1	Step 2	Step 3	Unit
$\sigma'_3$	246	358	494	$kN/m^2$
$\sigma'_3$ (ini)	85	278	470	$kN/m^2$
$q_f$	334.0	512.0	760.0	$kN/m^2$
$q_f/2$	167.0	256.0	380.0	$kN/m^2$
$\epsilon$	0.794	0.953	0.895	%
$E_{50}$	21033	26863	42458	$kN/m^2$
$s_u$	167.0	256.0	380.0	$kN/m^2$
$p_{ref}$	100	100	100	$kN/m^2$
$E_{50}^{ref}$	23953.1	11855.3	42458	$kN/m^2$
Average $E_{50}^{ref}$			16040	$kN/m^2$
$m$	$m_{1-2}$	$m_{2-3}$	$m_{1-3}$	Average m
	0.652	1.422	1.008	1.027

**Table F.3.4:** Secant stiffness  $E_{50}$  calculation for Boom Clay sample B2 - St.17.

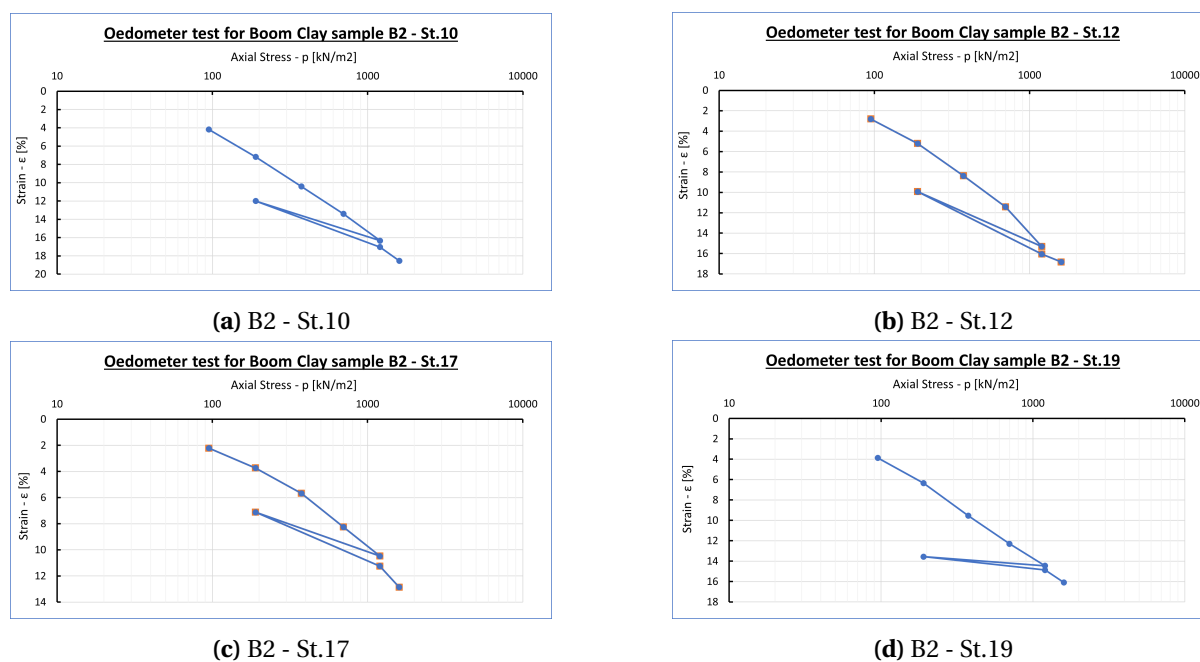
B2 - St.17	Step 1	Step 2	Step 3	Unit
$\sigma'_3$	105	308	510	$kN/m^2$
$\sigma'_3$ (ini)	105	308	510	$kN/m^2$
$q_f$	456.0	598.0	580.0	$kN/m^2$
$q_f/2$	228.0	299.0	290.0	$kN/m^2$
$\epsilon$	0.794	0.953	0.895	%
$E_{50}$	28715	31375	32402	$kN/m^2$
$s_u$	228.0	299.0	290.0	$kN/m^2$
$p_{ref}$	100	100	100	$kN/m^2$
$E_{50}^{ref}$	27616.1	12756.7	8800.7	$kN/m^2$
Average $E_{50}^{ref}$			16391.2	$kN/m^2$
$m$	$m_{1-2}$	$m_{2-3}$	$m_{1-3}$	Average m
	0.0082	0.064	0.076	0.074

**Table F.3.5:** Secant stiffness  $E_{50}$  calculation for Boom Clay sample B2 - St.19.

B2 - St.19	Step 1	Step 2	Step 3	Unit
$\sigma'_3$	223		468	$kN/m^2$
$\sigma'_3$ (ini)	120		540	$kN/m^2$
$q_f$	500.0		934.0	$kN/m^2$
$q_f/2$	250.0		467.0	$kN/m^2$
$\epsilon$	0.794		0.895	%
$E_{50}$	31486		52179	$kN/m^2$
$s_u$	250.0		467.0	$kN/m^2$
$p_{ref}$	100		100	$kN/m^2$
$E_{50}^{ref}$	27212.9		13538.8	$kN/m^2$
Average $E_{50}^{ref}$			20375.8	$kN/m^2$
$m$	$m_{1-2}$	$m_{2-3}$	$m_{1-3}$	Average m
	-	-	0.681	0.681



**Figure E.3.1:** Deviatoric stress  $q$  versus vertical strain  $\epsilon$  for the four Boom Clay triaxial samples under three confining stresses each.



**Figure E.3.2:** Axial stress  $p$  versus Strain  $\epsilon$  for the four oedometer tests on the Boom Clay samples.

**Table F.3.6:** Summary of the oedometer stiffness  $E_{oed}$  and the unloading reloading stiffness  $E_{ur}$  derived from the oedometer tests of the four Boom Clay samples.

Parameters	Units	B2 - St.10	B2 - St.12	B2 - St.17	B2 - St.19
$E_{oed}^{ref}$	$kN/m^2$	3200	3900	6300	3900
$E_{unloading}^{ref}$	$kN/m^2$	23300	18800	30100	113500
$E_{reloading}^{ref}$	$kN/m^2$	20100	16500	24400	77100
$E_{ur}^{ref}$	$kN/m^2$	21700	17600	27300	95300



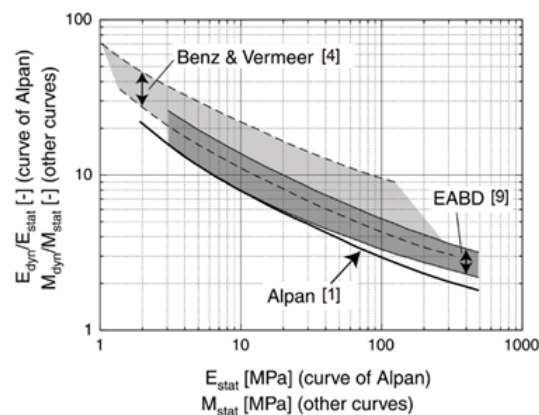
# Small Strain Parameter Determination

In this appendix, an investigation will be conducted on the effect of the different small strain parameter determination methods on the retaining wall's deformation. Firstly, the different methods are discussed, then a generalized investigation of all the soil layers is performed.

## G.1 Small Strain Correlations

The Hardening Soil Small Strain soil constitutive model uses two extra parameters to consider the small strains. Due to the absence of experimental data, the determination of small strain shear stiffness  $G_0^{ref}$  and the shear strain at which  $G$  has reduced to 72.2 %  $\gamma_{07}$  is being performed through correlations. One of the most common and used in the project's current design is the [1] method. A more recent investigation has been performed [7]. However, there is controversy on what stiffness Alpan refers to when he mentions the static modulus. That has been investigated by both [7] and [35], who concluded that Alpan's  $E_{stat}$  is the apparent elastic Young's modulus in conventional soil testing. However, both authors found that if Alpan's correlation is fitted with  $E_{stat} = 3 * E_{50}$ , the stiffness predictions are reasonable. Additionally, [7] provided an alternative correlation between  $M_{dyn}/M_{stat}$  and  $M_{stat}$ . To summarize in the original approach Alpan considers  $E_{stat} = E_{50}$  and Benz & Vermeer  $E_{stat} = E_{ur} = 3 * E_{50}$ .

The correlations [1], [7] and [14] are presented in Figure G.1.1, and as can be seen, there are differences between them, most probably that is due to a different interpretation of  $E_{stat}$ .



**Figure G.1.1:** Different methods to calculate the small strain parameters.

Considering all the investigations above, the  $E_{stat}$  or  $M_{stat}$  is determined from Equation G.1.1. The small strain modulus  $G_0$  can be calculated if Poisson's ratio  $\nu$  is known by the Equation G.1.3 of [35], where  $E_0$  is the static Young's modulus at very small strains and is essentially the  $E_{stat}$ . The shear strain  $\gamma_{0.7}$ , for which the secant shear modulus is reduced to 70 % of the value  $G_0$ , is being calculated using Equation G.1.4 of [16]. Where  $c'$  is the effective drained cohesion,  $\phi'$  is the effective drained friction angle,  $K_0$  is the neutral earth pressure coefficient, and  $\sigma'_1$  is the effective vertical stress.

$$E_{stat} = E_{ur} \approx 3 * E_{50} \quad (G.1.1)$$

$$E_0 = \frac{E_{dyn}}{E_{stat}} * E_{ur} \quad (G.1.2)$$

$$G_0 = \frac{E_0}{2 * (1 + \nu)} \quad (G.1.3)$$

$$\gamma_{0.7} = \frac{1}{9 * G_0} * (2 * c' * (1 + \cos(2 * \phi')) + \sigma'_1 * (1 + k_0) * \sin(2 * \phi')) \quad (G.1.4)$$

## G.2 Small Strain effect on all the soil layers

The correlations for small strains will be examined using the model described in Chapter 2 with the mean soil parameters and the HS-small strain constitutive model for all the soil layers. Because the [7] method has an upper and a lower limit, the average of those is being used. Table G.2.1 describes the determination of  $G_0^{ref}$  for the Alpan, Benz & Vermeer methods and the average value of those. Table G.2.2 describes the  $\gamma_{0.7}$  determination for the Alpan, the Benz & Vermeer methods, and the average approach. All the values have been calculated using Figure G.1.1 and Equations G.1.1 to G.1.4. The outcome of the investigations is presented in Figure G.2.1 for five different construction phases.

**Table G.2.1:**  $G_0^{ref}$  determination for all the soil layers of cross-section L01b using Alpan's, Benz & Vermeer's methods and the average.

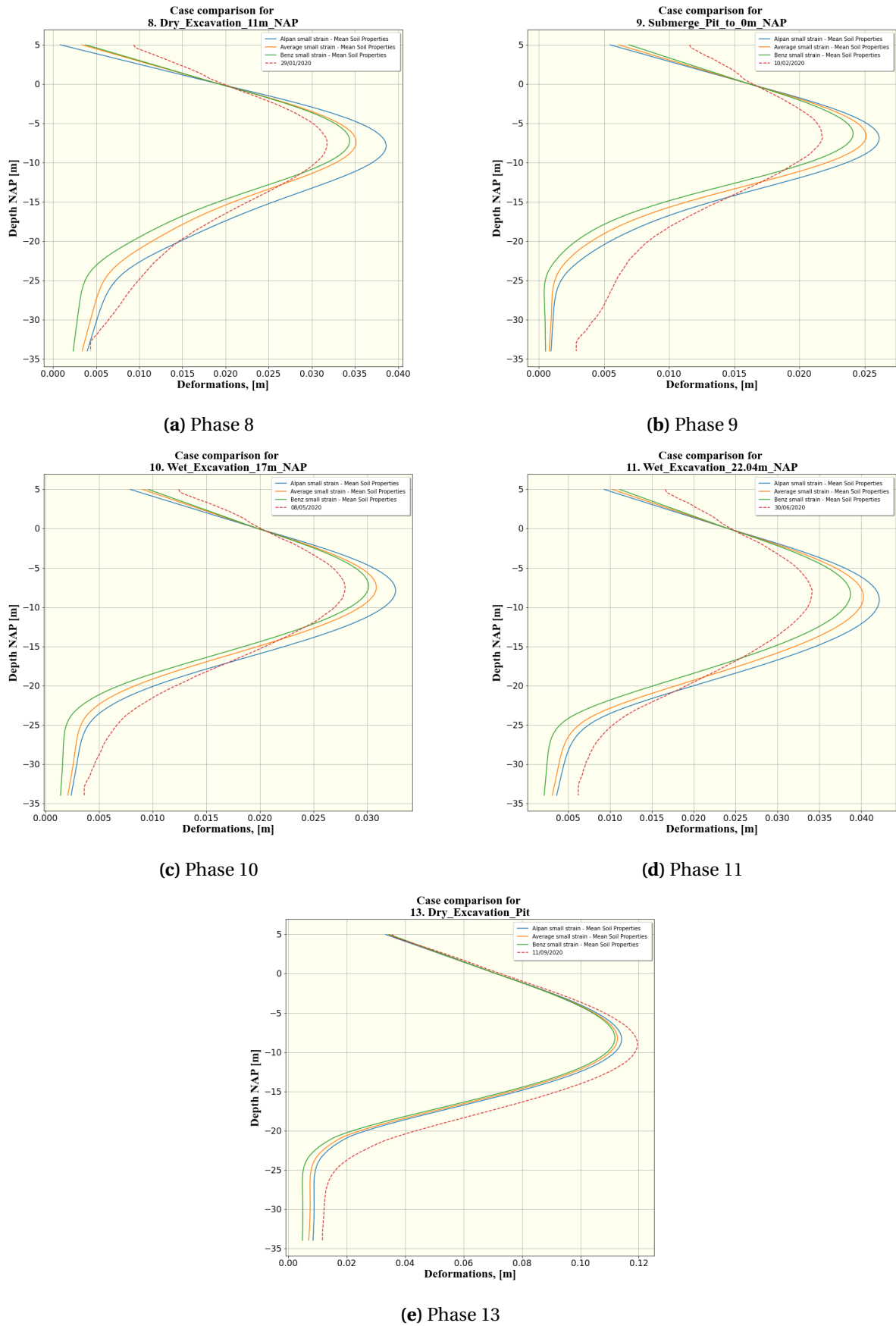
L01b	$E_{ur}^{ref}$	$\nu_{ur}$	Alpan			Benz & Vermeer			Average		
			$\frac{E_i}{E_{ur}}$	$E_0^{ref}$	$G_0^{ref}$	$\frac{E_i}{E_{ur}}$	$E_0^{ref}$	$G_0^{ref}$	$\frac{E_i}{E_{ur}}$	$E_0^{ref}$	$G_0^{ref}$
LX2	156000	0.2	2.5	390000	162500	5.8	904800	377000	4.15	647400	269750
LX01	84000	0.2	2.1	176400	73500	6.8	571200	238000	4.45	373800	155750
L05a	125000	0.2	1.7	212500	88542	6	750000	312500	3.85	481250	200521
L07	15000	0.2	6.5	97500	40625	14	210000	87500	10.25	153750	64063
L05a	121392	0.2	6	728352	303480	6	728352	303480	6	728352	303480
L05b	184856	0.2	2.3	425169	177154	5.7	1053679	439033	4	739424	308093
L09	81140	0.15	3.1	251534	109363	6.6	535524	232837	4.85	393529	171100
L08	172508	0.15	2.4	414019	180008	5.8	1000546	435020	4.1	707283	307514
L15	46400	0.3	4	185600	71385	8	371200	142769	6	278400	107077
L16	131789	0.2	2.8	369009	153754	5.9	777555	323981	4.35	573282	238868
L17	58128	0.2	3.6	209261	87192	7.6	441773	184072	5.6	325517	135632
L18	123266	0.2	6	739596	308165	6	739596	308165	6	739596	308165
L19	58128	0.2	3.6	209261	87192	7.6	441773	184072	5.6	325517	135632
L19	58128	0.2	3.6	209261	87192	7.6	441773	184072	5.6	325517	135632

**Table G.2.2:**  $\gamma_{0.7}$  small strain parameters determination for all soil layers of cross-section L01b using Alpan's, Benz & Vermeer's method and the average.

Layer	$c'$	$\phi'$	$\sigma'_1$	$K_0$	Alpan	Benz & Vermeer	Average
LX2	0	37.5	9.355	0.391	0.00000859	0.0000037	0.00000518
LX1	0	33.5	44.074	0.391	0.00008531	0.00002635	0.00004026
L05a	0	29.1	71.036	0.537	0.00011645	0.00003299	0.00005142
L07	6.63	20.3	74.346	0.686	0.00028691	0.00013321	0.00018194
L05a	0	29.1	79.6955	0.537	0.00003812	0.00003812	0.00003812
L05b	0	37.8	91.465	0.395	0.00007751	0.00003128	0.00004457
L09	0	32	102.347	0.486	0.00013888	0.00006523	0.00008877
L08	0	40	146.612	0.395	0.00012433	0.00005145	0.00007278
L15	18.55	24.4	256.7935	0.839	0.00064885	0.00032442	0.00043257
L16	0	37.8	345.81	0.559	0.00037736	0.00017908	0.0002429
L17	17.4	26.2	368.4425	0.93	0.00078935	0.0003739	0.00050744
L18	0	43.6	427.7875	0.375	0.00021183	0.00021183	0.00021183
L19	17.44	26.2	506.375	0.868	0.00102659	0.00048628	0.00065995
L19	17.44	26.2	619.2	0.868	0.00123938	0.00058707	0.00079674

The investigations concluded that the [1] method always produces higher deformations than the [7] method. These results are confirmed by a similar investigation of [19], where the excavation of Vijzelhof Amsterdam has a model in PLAXIS with the different small strain methods and is compared with inclinometer measurements.

When compared with the monitoring deformations the Alpan method fit the deformations better than the other model at lower level but worse on higher locations of the wall. The average approach as expected lays in the middle between the other two methods. Therefore, it is considered the best approach overall to be followed.



**Figure G.2.1:** Comparison of the wall deformations derived with Alpan's, Benz & Vermeer's and average small strain methods.

# H

## Python Application

### H.1 Python Libraries used

**Listing H.1:** Python libraries used for the Application

---

```
from itertools import chain
import pandas as pd
import numpy as np
import sys
import matplotlib.pyplot as plt
import matplotlib
from itertools import cycle
from tkinter import filedialog as fd
from tkinter.filedialog import asksaveasfile
import time
import xlswriter
import openpyxl
from openpyxl import load_workbook
import os.path
from glob import glob
import os
from tkinter import *
import tkinter as tk
from tkinter import ttk
import tkinter
from PIL import ImageTk, Image
from tkinter import messagebox
from tkinter import filedialog
from pathlib import Path
import shutil
import re
import pyperclip
from bisect import bisect_left
from shapely.geometry.polygon import LinearRing, Polygon
from matplotlib.backends.backend_tkagg import FigureCanvasTkAgg, NavigationToolbar2Tk
import scipy.interpolate
from plxscripting.easy import *
```

---

## H.2 Monitoring Input File Structure

Inclinometer Data											
A	B	C	D	E	F	G	H	I	J	K	L
N	Date	Time	Surf. A	N.A.P.	Absolute A	Absolute B	Cumulative A	Cumulative B	Incremental A	Incremental B	
1	15/10/2019	8:43	0	5.2	0.0008	0.1144	0	0	0	0	15/10/2019
2	15/10/2019	9:15	-0.5	4.7	0.0008	0.1144	0	0	0	0	
3	20/11/2019	1:37	-1	4.2	0	0.1105	0	0	0	0	
4	24/01/2020	11:30	-1.5	3.7	-0.001	0.1084	0	0	0	0	
5	29/01/2020	11:33	-2	3.2	-0.0021	0.1058	0	0	0	0	
6	10/02/2020	4:13	-2.5	2.7	-0.003	0.1034	0	0	0	0	
7	18/03/2020	21:59	-3	2.2	-0.0041	0.1042	0	0	0	0	
8	06/04/2020	10:13	-3.5	1.7	-0.0045	0.1023	0	0	0	0	
9	23/04/2020	10:36	-4	1.2	-0.0041	0.102	0	0	0	0	
10	08/05/2020	14:58	-4.5	0.7	-0.0032	0.0998	0	0	0	0	
11	11/06/2020	10:34	-5	0.2	-0.0038	0.0976	0	0	0	0	
12	30/06/2020	14:33	-5.5	-0.3	-0.0048	0.0973	0	0	0	0	
13	31/07/2020	09:31	-6	-0.8	-0.005	0.0959	0	0	0	0	
14	11/08/2020	3:24	-6.5	-1.3	-0.0058	0.0947	0	0	0	0	
15	04/09/2020	3:53	-7	-1.8	-0.0067	0.0925	0	0	0	0	
16	06/09/2020	3:20	-7.5	-2.3	-0.0083	0.0899	0	0	0	0	
17	08/09/2020	5:06	-8	-2.8	-0.0095	0.087	0	0	0	0	
18	09/09/2020	9:17	-8.5	-3.3	-0.0101	0.0851	0	0	0	0	
19	11/09/2020	10:24	-9	-3.8	-0.0102	0.0835	0	0	0	0	
20	14/09/2020	09:06	-9.5	-4.3	-0.0097	0.0825	0	0	0	0	
21	15/10/2020	4:34	-10	-4.8	-0.0087	0.0818	0	0	0	0	
22	12/11/2020	11:19	-10.5	-5.3	-0.0085	0.0808	0	0	0	0	
23	17/12/2020	2:57	-11	-5.8	-0.0078	0.0797	0	0	0	0	
24	18/02/2021	12:11	-11.5	-6.3	-0.0077	0.08	0	0	0	0	
25			-12	-6.8	-0.0078	0.08	0	0	0	0	
26			-12.5	-7.3	-0.0059	0.0789	0	0	0	0	
27			-13	-7.8	-0.0042	0.0777	0	0	0	0	
28			-13.5	-8.3	-0.0033	0.0767	0	0	0	0	
29			-14	-8.8	-0.0027	0.0758	0	0	0	0	
30			-14.5	-9.3	-0.0017	0.075	0	0	0	0	
31			-15	-9.8	-0.0012	0.0739	0	0	0	0	
32			-15.5	-10.3	-0.001	0.0731	0	0	0	0	
33			-16	-10.8	-0.0004	0.0717	0	0	0	0	
34			-16.5	-11.3	-0.0007	0.0706	0	0	0	0	
35			-17	-11.8	-0.0007	0.0688	0	0	0	0	
36			-17.5	-12.3	-0.0013	0.0678	0	0	0	0	
37			-18	-12.8	-0.0015	0.0662	0	0	0	0	
38			-18.5	-13.3	-0.0019	0.0649	0	0	0	0	
39			-19	-13.8	-0.0023	0.0632	0	0	0	0	
40			-19.5	-14.3	-0.0027	0.0617	0	0	0	0	
41			-20	-14.8	-0.0032	0.06	0	0	0	0	
42			-20.5	-15.3	-0.0033	0.0579	0	0	0	0	
43			-21	-15.8	-0.0039	0.0563	0	0	0	0	
44			-21.5	-16.3	-0.0039	0.0544	0	0	0	0	
45			-22	-16.8	-0.0041	0.053	0	0	0	0	
46			-22.5	-17.3	-0.0042	0.051	0	0	0	0	
47			-23	-17.8	-0.0038	0.0493	0	0	0	0	
48			-23.5	-18.3	-0.0035	0.0477	0	0	0	0	
49			-24	-18.8	-0.0033	0.046	0	0	0	0	
50			-24.5	-19.3	-0.0027	0.0448	0	0	0	0	
51			-25	-19.8	-0.001	0.0434	0	0	0	0	
52			-25.5	-20.3	0	0.0428	0	0	0	0	
53			-26	-20.8	0.0011	0.0419	0	0	0	0	
54			-26.5	-21.3	0.002	0.0415	0	0	0	0	
55			-27	-21.8	0.0033	0.0407	0	0	0	0	
56			-27.5	-22.3	0.0015	0.038	0	0	0	0	
57			-28	-22.8	0.0008	0.0351	0	0	0	0	
58			-28.5	-23.3	0.0001	0.0331	0	0	0	0	
59			-29	-23.8	0	0.0313	0	0	0	0	
60			-29.5	-24.3	0.0009	0.0299	0	0	0	0	
61			-30	-24.8	0.0015	0.0296	0	0	0	0	
62			-30.5	-25.3	0.0029	0.0288	0	0	0	0	
63			-31	-25.8	0.0037	0.0292	0	0	0	0	
64			-31.5	-26.3	0.0052	0.0294	0	0	0	0	
65			-32	-26.8	0.006	0.0273	0	0	0	0	
66			-32.5	-27.3	0.0057	0.0247	0	0	0	0	
67			-33	-27.8	0.0049	0.0215	0	0	0	0	
68			-33.5	-28.3	0.0043	0.0187	0	0	0	0	
69			-34	-28.8	0.0033	0.0167	0	0	0	0	
70			-34.5	-29.3	0.0022	0.0154	0	0	0	0	
71			-35	-29.8	0.0019	0.0132	0	0	0	0	
72			-35.5	-30.3	0.0003	0.013	0	0	0	0	
73			-36	-30.8	0.0002	0.0112	0	0	0	0	
74			-36.5	-31.3	-0.0008	0.0087	0	0	0	0	
75			-37	-31.8	-0.0003	0.005	0	0	0	0	
76			-37.5	-32.3	-0.001	0.0038	0	0	0	0	
77			-38	-32.8	-0.0006	0.0015	0	0	0	0	
78			0	5.2	0.0006	0.115	-0.0002	0.0006	0	0	15/10/2019
79			-0.5	4.7	0.0006	0.115	-0.0002	0.0006	0	0	
80			-1	4.2	-0.0002	0.111	-0.0002	0.0005	0	0	
81			-1.5	3.7	-0.0012	0.109	-0.0002	0.0005	0	0	
82			-2	3.2	-0.0023	0.1063	-0.0002	0.0005	0	0	
83			-2.5	2.7	-0.0032	0.1039	-0.0002	0.0005	0	0	
84			-3	2.2	-0.0043	0.1047	-0.0002	0.0005	0	0	
85			-3.5	1.7	-0.0047	0.1028	-0.0002	0.0005	0	0	
86			-4	1.2	-0.0043	0.1025	-0.0002	0.0005	0	0	
87			-4.5	0.7	-0.0034	0.1003	-0.0002	0.0005	0	0	
88			-5	0.2	-0.004	0.0981	-0.0002	0.0005	0	0	
89			-5.5	-0.3	-0.0051	0.0978	-0.0002	0.0005	0	0	
90			-6	-0.8	-0.0052	0.0964	-0.0002	0.0005	0	0.0001	
91			-6.5	-1.3	-0.006	0.0951	-0.0002	0.0003	0	0	
92			-7	-1.8	-0.0069	0.0929	-0.0002	0.0003	0	0	
93			-7.5	-2.3	-0.0084	0.0902	-0.0002	0.0003	0	0	

(a) Inclinometer Data

	A	B	C	D
1	Total Station			
2	N	Inclinometer	Total Station	Calculated
3	1	Dates	Dates	Difference
4	2	15/10/2019		0
5	3	20/11/2019	11/20/2019	0
6	4	24/01/2020	1/22/2020	4.449
7	5	29/01/2020	1/29/2020	3.862
8	6	10/02/2020	2/10/2020	2.484
9	7	18/03/2020	3/19/2020	7.678
10	8	06/04/2020	4/6/2020	7.373
11	9	23/04/2020	4/22/2020	8.473
12	10	08/05/2020	5/8/2020	3.428
13	11	11/06/2020	6/10/2020	4.617
14	12	30/06/2020	7/2/2020	6.022
15	13	31/07/2020	7/31/2020	-4.465
16	14	11/08/2020	8/11/2020	-1.995
17	15	04/09/2020	9/4/2020	1.826
18	16	06/09/2020	9/6/2020	-5.057
19	17	08/09/2020	9/7/2020	6.069
20	18	09/09/2020	9/9/2020	7.314
21	19	11/09/2020	9/11/2020	11.448
22	20	14/09/2020	9/15/2020	7.681
23	21	15/10/2020	10/15/2020	8.569
24	22	12/11/2020		0
25	23	17/12/2020		0
26	24	18/02/2021		0

(b) Total Station Data

Figure H.2.1: Monitoring Input File

## H.3 Plaxis Model Input File Structure

### Soil Properties

A	B	C	D	E	F	G	H	I	J	K	L	M	N	O	P	Q	R	S	T	U	V	
1	Name	Constitutive model	Drainage Type	Colour	v <sub>unsat</sub>	v <sub>sat</sub>	φ	c <sub>ref</sub>	ψ	E <sub>ref</sub>	E <sub>50_ref</sub>	E <sub>oed_ref</sub>	E <sub>ur_ref</sub>	v <sub>u</sub>	v <sub>ur</sub>	m	p <sub>ref</sub>	G <sub>0_ref</sub>	y <sub>D</sub>	K <sub>0-Default</sub>	Tensile CutOff	Dilatancy CutOff
2	Ident/location	Soil/soil	Drainage Type	Colour	gmm/m <sup>3</sup>	gmm/m <sup>3</sup>	kg/m <sup>3</sup>	kg/m <sup>3</sup>	kg/m <sup>3</sup>	kg/m <sup>3</sup>	kg/m <sup>3</sup>	kg/m <sup>3</sup>	kg/m <sup>3</sup>	kg/m <sup>3</sup>	kg/m <sup>3</sup>	kg/m <sup>3</sup>	kg/m <sup>3</sup>	kg/m <sup>3</sup>	kg/m <sup>3</sup>	kg/m <sup>3</sup>	kg/m <sup>3</sup>	kg/m <sup>3</sup>
3	str	str	str	str	float	float	float	float	float	float	float	float	float	float	float	float	float	float	float	float	float	float
4	str	str	str	str	float	float	float	float	float	float	float	float	float	float	float	float	float	float	float	float	float	float
5	LX02	hssmall	Drained	8038394	18.71	20	37.5	0	7.5	39000	39000	156000		0.2	0.5	100	208000	0.000023	TRUE	TRUE	TRUE	
6	LX01	hssmall	Drained	864345	17	19	33.5	0	2.6	21000	21000	84000		0.2	0.5	100	1.12E+05	1.00E-04	TRUE	TRUE	TRUE	
7	L05a	hssmall	Drained	2548531	18.56	18.56	29.1	0	0	30348	30348	125000		0.2	0.5	100	174502	0.0001	TRUE	TRUE	TRUE	
8	L07	hssmall	Drained	2252535	14.85	14.85	20.3	6.63	0	2703	2703	8200		0.15	0.8	100	21837	0.00089	TRUE	TRUE	TRUE	
9	L05a_low	hssmall	Drained	2548531	18.56	18.56	29.1	0	0	30348	30348	121392		0.2	0.5	100	174502	0.0001	TRUE	TRUE	TRUE	
10	L05b	hssmall	Drained	885304	21	21	37.8	0	7.8	46214	46214	184856		0.2	0.5	100	231070	0.00011	TRUE	TRUE	TRUE	
11	L09/L11	hssmall	Drained	14785263	18.74	18.74	35	0	5	30000	30000	90000		0.15	0.5	100	139688	0.000109	TRUE	TRUE	TRUE	
12	L08/L10/L12	hssmall	Drained	15909235	18.53	18.53	42	0	10	60000	60000	180000		0.15	0.5	100	223500	0.000097	TRUE	TRUE	TRUE	
13	L15	hssmall	Drained	1020108	19.25	19.25	20	16	0	20000	20000	40000		0.3	0.8	100	78462	0.000468	TRUE	TRUE	TRUE	
14	L16	hssmall	Drained	4123295	19.13	19.13	37.8	0	7.8	32947	32947	131789		0.2	0.5	100	183956	0.00036	TRUE	TRUE	TRUE	
15	L17	hssmall	Drained	15003546	19.13	19.13	26.2	17.4	0	11626	11626	58128		0.2	0.8	100	108989	0.00064	TRUE	TRUE	TRUE	
16	L18	hssmall	Drained	10153913	18.61	18.61	43.6	0	13.6	61600	53000	123266		0.2	0.5	100	343152	0.00023	TRUE	TRUE	TRUE	
17	L19	hssmall	Drained	415267	19.13	19.13	26.2	17.44	0	11626	11626	58128		0.2	0.8	100	108989	0.00075	TRUE	TRUE	TRUE	
18	L19_low	hssmall	Drained	1570710	19.13	19.13	26.2	17.44	0	11626	11626	58128		0.2	0.8	100	108989	0.00075	TRUE	TRUE	TRUE	
19	Gravel	Linear Elastic	Non-porous	5792561	23	20	35	0	5	40000	29330	160000		0.2	0.5	100	83250	0.00014	TRUE	TRUE	TRUE	
20	UWC	Linear Elastic	Non-porous	5792561	23	20	35	0	5	40000	29330	160000		0.2	0.5	100	83250	0.00014	TRUE	TRUE	TRUE	
21	L15b	hssmall	Undrained A	1020108	19.25	19.25	20	16	0	20000	20000	40000		0.3	0.8	100	78462	0.000468	TRUE	TRUE	TRUE	

Figure H.3.1: Plaxis Model Input File - Soil Properties Section

### Borehole

A	B	C	D
1	Soil Name	Depth	X-Location
2	Initial	m	m
3	LX02	3.5	0
4	LX01	2.5	
5	L05a	-4.3	
6	L07	-7.7	
7	L05a_low	-8.1	
8	L05b	-9.6	
9	L09/L11	-11.5	
10	.08/L10/L12	-12	
11	L15	-21.5	
12	L16	-37.6	
13	L17	-42	
14	L18	-42.5	
15	L19	-55	
16	L19_low	-60	
17		-80	

Figure H.3.2: Plaxis Model Input File - Borehole Section

### Heads

B	C	D	E	F	G	H	I	J	K	L	M	N	O	P	Q	R
1	heral	Impermeable General			Phase	Discription			Aquifer Values			Impermeable Values				
2	4	Number of Imperm.	3		N.	Discription	Condition	Phreatic	Aquifer 1	Aquifer 2	Aquifer 3	Condition	Impermeable 1	Impermeable 2	Impermeable 3	Free Water
3	top	bottom	Name	Top	Bottom	0	Initial Phase	Head	2.30	1.20	1.20	0.68	Interpolate			-
4	3.5	-7.7	Impermeable 1	-7.7	-8.1	1	Anchor Wall Excavation	Head	-1.52	-0.5	0.62	0.68	Interpolate			-
5	-8.1	-21.5	Impermeable 2	-21.5	-37.6	2	Layed Anchor Excavation	Head	-1.52	-0.5	0.62	0.68	Interpolate			-
6	-37.6	-55	Impermeable 3	-55	-60	3	Replenish Soil to Anchor Level	Head	-1.52	-0.5	0.62	0.68	Interpolate			-
7	-60	-80				4	Install and Pre-tension Anchor	Head	-1.52	-0.5	0.62	0.68	Interpolate			-
8						5	Full Soil Replenish with LX02	Head	-1.52	-0.5	0.62	0.68	Interpolate			-
9						6	Lower Water Level in Pit	Head	-1.52	-0.5	0.62	0.68	Interpolate			-
10						7	Dry Excavation to -6 m NAP	Head	-1.52	-1.5	0.4	0.68	Interpolate			-
11						8	Dry Excavation to -11 m NAP	Head	-1.52	-5	-6.25	0.68	Interpolate			-
12						9	Submerge Pit to 0 m NAP	Head	-1.52	-5	-11.5	0.68	Interpolate			0
13						10	Wet Excavation to -17 m NAP	Head	-1.38	-3.5	0.3	0.68	Interpolate			0
14						11	Wet Excavation to -22.04 m NAP	Head	-1.38	-3.5	0.3	0.68	Interpolate			0
15						12	Dumping Gravel & Pouring OWB	Head	-0.8	-2	-12	0.68	Interpolate			0
16						13	Dry Excavation Pit	Head	-0.8	-1	-12	0.68	Interpolate			-

Figure H.3.3: Plaxis Model Input File - Heads Section

**Plates**

	A	B	C	D	E	F	G	H
1	<b>Name</b>	<b>Type</b>	<b>CB Type 1</b>	<b>CB Type 2</b>	<b>CB Type 3</b>	<b>CB Type 4</b>	<b>Anchor Wall</b>	<b>UWC</b>
2	<b>Identification</b>	<i>str</i>	CB1_1420x15.7	CB2_1420x25.8	CB3_1420x27.7	CB4_1420x15.7	AW_AZ_26x700	OWB
3	<b>MaterialType</b>	<i>str</i>	Elastic	Elastic	Elastic	Elastic	Elastoplastic	Elastic
4	<b>PreventPunching</b>	<i>bool</i>	FALSE	FALSE	FALSE	FALSE	FALSE	FALSE
5	<b>w</b>	<i>float</i>	19.65	20.81	20.63	18.88	1.47	0.01
6	<b>Isotropic</b>	<i>bool</i>	FALSE	FALSE	FALSE	FALSE	FALSE	TRUE
7	<b>EA1</b>	<i>float</i>	7941352	11764385	11158419	5830000	3927000	10
8	<b>EA2</b>	<i>float</i>	7941352	11764385	11158419	5830000	196400	
9	<b>EI</b>	<i>float</i>	1467535	2373065	2231623	1380000	125400	1
10	<b>StructNu</b>	<i>float</i>						0
11	<b>Mp</b>	<i>float</i>					1320	
12	<b>Np1</b>	<i>float</i>					8041	
13	<b>Np2</b>	<i>float</i>					402.1	
14	<b>X top</b>	-	0	0	0	0	-45	
15	<b>Y top</b>	-	5	-0.5	-12	-23.5	3	
16	<b>X bot</b>	-	0	0	0	0	-45	
17	<b>Y bot</b>	-	-0.5	-12	-23.5	-34	-13	

Figure H.3.4: Plaxis Model Input File - Plates Section

**Node to Node**

	A	B	C
1	<b>Name</b>	<b>Type</b>	<b>N2N Rod</b>
2	<b>Identification</b>	<i>str</i>	Anchor Rod
3	<b>MaterialType</b>	<i>str</i>	Elastoplastic
4	<b>Colour</b>	<i>int</i>	197378
5	<b>Lspacing</b>	<i>float</i>	2.73
6	<b>EA</b>	<i>float</i>	1818390
7	<b>FMaxTens</b>	<i>float</i>	5715
8	<b>FMaxComp</b>	<i>float</i>	0.001

Figure H.3.5: Plaxis Model Input File - Node to Node Section

**Fixed End Anchors**

	A	B	C
1	<b>Name</b>	<b>Type</b>	<b>Fixed End</b>
2	<b>Identification</b>	<i>str</i>	Strut
3	<b>MaterialType</b>	<i>str</i>	Elastoplastic
4	<b>Colour</b>	<i>int</i>	197378
5	<b>Lspacing</b>	<i>float</i>	1
6	<b>EA</b>	<i>float</i>	12000
7	<b>FMaxTens</b>	<i>float</i>	0.01
8	<b>FMaxComp</b>	<i>float</i>	1000000000000

Figure H.3.6: Plaxis Model Input File - Fixed End Anchors Section



### Phases

	A	B
1	N.	Phase Name
2	0	Initial Phase
3	1	Anchor Wall Excavation
4	2	Excavation for Anchor Installation
5	3	Replenish to Anchor Level with Soil
6	4	Install and Pre-tension anchors
7	5	Soil Replenish to Surface
8	6	Lower Water Level in Pit to -15 m NAP
9	7	Dry Excavation to -6 m NAP
10	8	Dry Excavation to -11 m NAP
11	9	Submerge Pit to 0 m NAP
12	10	Wet Excavation to -17 m NAP
13	11	Wet Excavation to -22 m NAP
14	12	Dumping Gravel and Pouring UWC
15	13	Dry Excavation of Pit

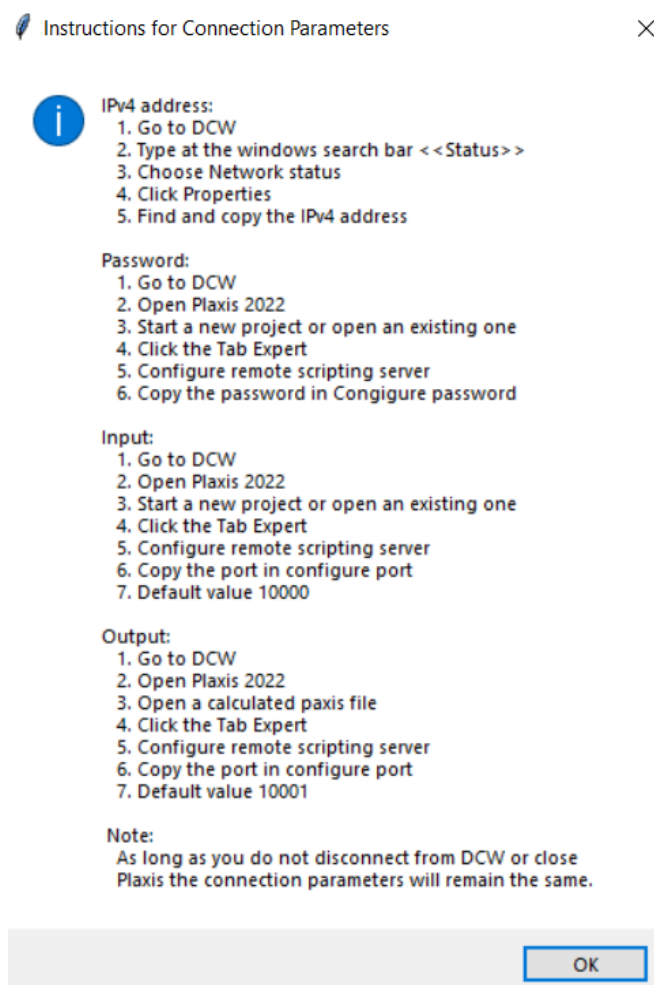
Figure H.3.7: Plaxis Model Input File - Phases Section

### Soil Stresses

	A	B	C	D	E	F	G	H	I	J	K	L	M	N
1	Layer	Top	Bottom	Thickness	Water Level	Dry/Wet	$\gamma_{dry}$	$\gamma_{sat}$	$\sigma_v$ (bot)	$\sigma_v$ (mid)	u bot	u mid	$\sigma'_v$ bot	$\sigma'_v$ mid
2	LX02	3.5	2.5	1	2.5	Dry	18.71	18.71	19	9	0	0	19	9
3	LX01	2.5	-4.3	6.8		Wet	17.46	17.46	137	78	68	34	69	44
4	L05a	-4.3	-7.7	3.4		Wet	10.94	10.94	175	156	102	85	73	71
5	L07	-7.7	-8.1	0.4		Wet	18.56	18.56	182	178	106	104	76	74
6	L05a_low	-8.1	-9.6	1.5		Wet	14.85	14.85	204	193	121	114	83	80
7	L05b	-9.6	-11.5	1.9		Wet	18.56	18.56	240	222	140	131	100	91
8	L09/L11	-11.5	-12	0.5		Wet	21	21	250	245	145	143	105	102
9	L08/L10/L1	-12	-21.5	9.5		Wet	18.74	18.74	428	339	240	193	188	147
10	L15	-21.5	-37.6	16.1		Wet	18.53	18.53	726	577	401	321	325	257
11	L16	-37.6	-42	4.4		Wet	19.25	19.25	811	769	445	423	366	346
12	L17	-42	-42.5	0.5		Wet	19.13	19.13	821	816	450	448	371	368
13	L18	-42.5	-55	12.5		Wet	19.13	19.13	1060	940	575	513	485	428
14	L19	-55	-60	5		Wet	18.61	18.61	1153	1106	625	600	528	506
15	L19_low	-60	-80	20		Wet	19.13	19.13	1536	1344	825	725	711	619
16	L15b	-21.5	-37.6	16.1		Wet	18.53	18.53	726.46	577.2935	401	320.5	325.46	256.7935

Figure H.3.8: Plaxis Model Input File - Soil Stresses Section

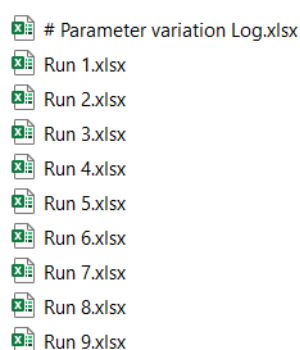
## H.4 Plaxis - Python Remote Connection Instructions



**Figure H.4.1:** Remote Connection Instructions

## H.5 Sensitivity Analysis File Structure

The format the folder created by the sensitivity analysis tool of the python application is shown in Figure H.5.1.



**Figure H.5.1:** Sensitivity Analysis File Structure

# Parameter variation Log

	A	B	C	D	E	F	G	H	I	J	K
1	N.	Soil Layer	Parameter	Value	Unit		N.	Soil Layer	Parameter	Value	Unit
2		1 L15	E50Ref	4000	kN/m2			1 L15	E50Ref	4000	kN/m2
3		2 L15	E50Ref	8000	kN/m2			2 L15	E50Ref	8000	kN/m2
4		3 L15	E50Ref	12000	kN/m2			3 L15b	E50Ref	12000	kN/m2
5		4 L15	E50Ref	16000	kN/m2			4 L15b	E50Ref	16000	kN/m2
6		5 L15	E50Ref	20000	kN/m2			5 L15b	E50Ref	20000	kN/m2
7		6 L15	E50Ref	24000	kN/m2			6 L15b	E50Ref	24000	kN/m2
8		7 L15	E50Ref	28000	kN/m2			7 L15b	E50Ref	28000	kN/m2
9		8 L15	E50Ref	32000	kN/m2			8 L15b	E50Ref	32000	kN/m2
10		9 L15	E50Ref	36000	kN/m2			9 L15b	E50Ref	36000	kN/m2

(a) Log - Tab

	A	B	C	D	E
1	Phases				
2	Phase 1: Anchor Wall Excavation				
3	Phase 2: Excavation for Anchor Installation				
4	Phase 3: Replenish to Anchor Level with Soil				
5	Phase 4: Install and Pre-tension anchors				
6	Phase 5: Soil Replenish to Surface				
7	Phase 6: Lower Water Level in Pit to -15 m NAP				
8	Phase 7: Dry Excavation to -6 m NAP				
9	Phase 8: Dry Excavation to -11 m NAP				
10	Phase 9: Submerge Pit to 0 m NAP				
11	Phase 10: Wet Excavation to -17 m NAP				
12	Phase 11: Wet Excavation to -22 m NAP				
13	Phase 12: Dumping Gravel and Pouring UWC				
14	Phase 13: Dry Excavation of Pit				

(b) Phases - Tab

	A	B	C	D	E	F	G	H	I	J	K	L	M	N	O	P	Q	R	S	T	U	V	W	X	Y	Z	AA	AB	AC
1	New Parameters																												
2	1 Identification	L15	SoilModel	hssmall	DrainageType	Drained	Colour	1020108	gammaUns	19.25	gammaSat	19.25	phi	20	cRef	16	psi	0	E50Ref	4000	EOedRef	4000	EURRef	12000	nuUR	0.3	PowerM	0.8	
3	2 Identification	L15	SoilModel	hssmall	DrainageType	Drained	Colour	1020108	gammaUns	19.25	gammaSat	19.25	phi	20	cRef	16	psi	0	E50Ref	6000	EOedRef	6000	EURRef	18000	nuUR	0.3	PowerM	0.8	
4	3 Identification	L15	SoilModel	hssmall	DrainageType	Drained	Colour	1020108	gammaUns	19.25	gammaSat	19.25	phi	20	cRef	16	psi	0	E50Ref	8000	EOedRef	8000	EURRef	24000	nuUR	0.3	PowerM	0.8	
5	4 Identification	L15	SoilModel	hssmall	DrainageType	Drained	Colour	1020108	gammaUns	19.25	gammaSat	19.25	phi	20	cRef	16	psi	0	E50Ref	10000	EOedRef	10000	EURRef	30000	nuUR	0.3	PowerM	0.8	
6	5 Identification	L15	SoilModel	hssmall	DrainageType	Drained	Colour	1020108	gammaUns	19.25	gammaSat	19.25	phi	20	cRef	16	psi	0	E50Ref	12000	EOedRef	12000	EURRef	36000	nuUR	0.3	PowerM	0.8	
7	6 Identification	L15	SoilModel	hssmall	DrainageType	Drained	Colour	1020108	gammaUns	19.25	gammaSat	19.25	phi	20	cRef	16	psi	0	E50Ref	14000	EOedRef	14000	EURRef	42000	nuUR	0.3	PowerM	0.8	
8	7 Identification	L15	SoilModel	hssmall	DrainageType	Drained	Colour	1020108	gammaUns	19.25	gammaSat	19.25	phi	20	cRef	16	psi	0	E50Ref	16000	EOedRef	16000	EURRef	48000	nuUR	0.3	PowerM	0.8	
9	8 Identification	L15	SoilModel	hssmall	DrainageType	Drained	Colour	1020108	gammaUns	19.25	gammaSat	19.25	phi	20	cRef	16	psi	0	E50Ref	18000	EOedRef	18000	EURRef	54000	nuUR	0.3	PowerM	0.8	
10	9 Identification	L15	SoilModel	hssmall	DrainageType	Drained	Colour	1020108	gammaUns	19.25	gammaSat	19.25	phi	20	cRef	16	psi	0	E50Ref	20000	EOedRef	20000	EURRef	60000	nuUR	0.3	PowerM	0.8	
11	10 Identification	L15	SoilModel	hssmall	DrainageType	Drained	Colour	1020108	gammaUns	19.25	gammaSat	19.25	phi	20	cRef	16	psi	0	E50Ref	22000	EOedRef	22000	EURRef	66000	nuUR	0.3	PowerM	0.8	
12	11 Identification	L15	SoilModel	hssmall	DrainageType	Drained	Colour	1020108	gammaUns	19.25	gammaSat	19.25	phi	20	cRef	16	psi	0	E50Ref	24000	EOedRef	24000	EURRef	72000	nuUR	0.3	PowerM	0.8	
13	12 Identification	L15	SoilModel	hssmall	DrainageType	Drained	Colour	1020108	gammaUns	19.25	gammaSat	19.25	phi	20	cRef	16	psi	0	E50Ref	26000	EOedRef	26000	EURRef	78000	nuUR	0.3	PowerM	0.8	
14	13 Identification	L15	SoilModel	hssmall	DrainageType	Drained	Colour	1020108	gammaUns	19.25	gammaSat	19.25	phi	20	cRef	16	psi	0	E50Ref	28000	EOedRef	28000	EURRef	84000	nuUR	0.3	PowerM	0.8	
15	14 Identification	L15	SoilModel	hssmall	DrainageType	Drained	Colour	1020108	gammaUns	19.25	gammaSat	19.25	phi	20	cRef	16	psi	0	E50Ref	30000	EOedRef	30000	EURRef	90000	nuUR	0.3	PowerM	0.8	
16	15 Identification	L15	SoilModel	hssmall	DrainageType	Drained	Colour	1020108	gammaUns	19.25	gammaSat	19.25	phi	20	cRef	16	psi	0	E50Ref	32000	EOedRef	32000	EURRef	96000	nuUR	0.3	PowerM	0.8	
17	16 Identification	L15	SoilModel	hssmall	DrainageType	Drained	Colour	1020108	gammaUns	19.25	gammaSat	19.25	phi	20	cRef	16	psi	0	E50Ref	34000	EOedRef	34000	EURRef	102000	nuUR	0.3	PowerM	0.8	
18	17 Identification	L15	SoilModel	hssmall	DrainageType	Drained	Colour	1020108	gammaUns	19.25	gammaSat	19.25	phi	20	cRef	16	psi	0	E50Ref	36000	EOedRef	36000	EURRef	108000	nuUR	0.3	PowerM	0.8	
19	18 Identification	L15	SoilModel	hssmall	DrainageType	Drained	Colour	1020108	gammaUns	19.25	gammaSat	19.25	phi	20	cRef	16	psi	0	E50Ref	38000	EOedRef	38000	EURRef	114000	nuUR	0.3	PowerM	0.8	
20																													
21																													
22	1 Identification	L15b	SoilModel	hssmall	DrainageType	Undrained A	Colour	1020108	gammaUns	19.25	gammaSat	19.25	phi	20	cRef	16	psi	0	E50Ref	4000	EOedRef	4000	EURRef	12000	nuUR	0.3	PowerM	0.8	
23	2 Identification	L15b	SoilModel	hssmall	DrainageType	Undrained A	Colour	1020108	gammaUns	19.25	gammaSat	19.25	phi	20	cRef	16	psi	0	E50Ref	6000	EOedRef	6000	EURRef	18000	nuUR	0.3	PowerM	0.8	
24	3 Identification	L15b	SoilModel	hssmall	DrainageType	Undrained A	Colour	1020108	gammaUns	19.25	gammaSat	19.25	phi	20	cRef	16	psi	0	E50Ref	8000	EOedRef	8000	EURRef	24000	nuUR	0.3	PowerM	0.8	
25	4 Identification	L15b	SoilModel	hssmall	DrainageType	Undrained A	Colour	1020108	gammaUns	19.25	gammaSat	19.25	phi	20	cRef	16	psi	0	E50Ref	10000	EOedRef	10000	EURRef	30000	nuUR	0.3	PowerM	0.8	
26	5 Identification	L15b	SoilModel	hssmall	DrainageType	Undrained A	Colour	1020108	gammaUns	19.25	gammaSat	19.25	phi	20	cRef	16	psi	0	E50Ref	12000	EOedRef	12000	EURRef	36000	nuUR	0.3	PowerM	0.8	
27	6 Identification	L15b	SoilModel	hssmall	DrainageType	Undrained A	Colour	1020108	gammaUns	19.25	gammaSat	19.25	phi	20	cRef	16	psi	0	E50Ref	14000	EOedRef	14000	EURRef	42000	nuUR	0.3	PowerM	0.8	
28	7 Identification	L15b	SoilModel	hssmall	DrainageType	Undrained A	Colour	1020108	gammaUns	19.25	gammaSat	19.25	phi	20	cRef	16	psi	0	E50Ref	16000	EOedRef	16000	EURRef	48000	nuUR	0.3	PowerM	0.8	
29	8 Identification	L15b	SoilModel	hssmall	DrainageType	Undrained A	Colour	1020108	gammaUns	19.25	gammaSat	19.25	phi	20	cRef	16	psi	0	E50Ref	18000	EOedRef	18000	EURRef	54000	nuUR	0.3	PowerM	0.8	

(c) Parameters - Tab

Figure H.5.2: Structure of the # Parameter variation Log excel file from the sensitivity analysis of the python application.

Run i

	A	B	C	D	E	F	G	H	I	J	K	L	M	N	O	P	Q	R	S	T	U	V	W	X	Y	Z
1	Phase 1 : Anchor Wall Excavation									Phase 2 : Excavation for Anchor Installation									Phase 3 : Replenish to Anchor Level with Soil							
2	N	X	Y	dx	dy	N	Q	M		N	X	Y	dx	dy	N	Q	M	N	Q	M	N	Q	M	N	Q	M
3	m	m	m	m	m	kN/m	kN/m	kN/m		m	m	m	m	m	kN/m	kN/m	kN/m	kN/m	kN/m	kN/m	kN/m	kN/m	kN/m	kN/m	kN/m	kN/m
4	1	0	5	0.00076	-0.0048	-0.0018	3.6E-13	-4E-13		1	0	5	0.00244	0.00133	-0.0018	-2E-13	-3E-13		1	0	5	0.00256	0.0007	-0.0018	3.6E-13	1E-1
5	2	0	4.625	0.00075	-0.0048	-7.3668	1.5E-09	2.8E-10		2	0	4.625	0.00236	0.00133	-7.3668	1.5E-09	2.8E-10		2	0	4.625	0.00248	0.0007	-7.3668	1.5E-09	2.8E-1
6	3	0	4.25	0.00074	-0.0048	-14.737	3E-09	1.1E-09		3	0	4.25	0.00229	0.00133	-14.737	3E-09	1.1E-09		3	0	4.25	0.0024	0.0007	-14.737	3E-09	1.1E-0
7	4	0	3.875	0.00073	-0.0048	-22.107	4.5E-09	2.6E-09		4	0	3.875	0.00222	0.00133	-22.107	4.5E-09	2.6E-09		4	0	3.875	0.00232	0.0007	-22.107	4.5E-09	2.6E-0
8	5	0	3.5	0.00072	-0.0048	-29.455	0.00934	4.5E-09		5	0	3.5	0.00215	0.00133	-29.472	6E-09	4.5E-09		5	0	3.5	0.00225	0.0007	-29.472	6E-09	4.5E-0
9	6	0	3.5	0.00072	-0.0048	-29.472	6E-09	4.5E-09		6	0	3.5	0.00215	0.00133	-29.475	6E-09	4.5E-09		6	0	3.5	0.00225	0.0007	-29.475	6E-09	4.5E-0
10	7	0	3.25	0.00072	-0.0048	-34.593	-0.0096	-0.0007		7	0	3.25	0.0021	0.00133	-34.385	7.1E-09	6.2E-09		7	0	3.25	0.00219	0.0007	-34.385	7.1E-09	6.2E-0
11	8	0	3	0.00071	-0.0048	-40.052	-0.0077	-0.0029		8	0	3	0.00205	0.00133	-39.299	8.1E-09	8.1E-09		8	0	3	0.00214	0.0007	-39.299	8.1E-09	8.1E-0
12	9	0	2.75	0.0007	-0.0048	-45.897	0.00385	-0.0037		9	0	2.75	0.002	0.00133	-44.212	9.1E-09	1E-08		9	0	2.75	0.00209	0.0007	-44.212	9.1E-09	1E-0
13	10	0	2.5	0.0007	-0.0048	-52.189	0.01388	-0.0013		10	0	2.5	0.00196	0.00134	-49.122	1E-08	1.3E-08		10	0	2.5	0.00204	0.0007	-49.122	1E-08	1.3E-0
14	11	0	2.5	0.0007	-0.0048	-52.562	0.00915	-0.0013		11	0	2.5	0.00196	0.00134	-49.126	1E-08	1.3E-08		11	0	2.5	0.00204	0.0007	-49.126	1E-08	1.3E-0
15	12	0	2.08333	0.00068	-0.0048	-63.748	-0.0053	-0.0003		12	0	2.08333	0.00188	0.00134	-57.309	1.2E-08	1.7E-08		12	0	2.08333	0.00195	0.00071	-57.309	1.2E-08	1.7E-0
16	13	0	1.66667	0.00067	-0.0048	-75.267	-0.0248	-0.0064		13	0	1.66667	0.0018	0.00134	-65.498	1.3E-08	2.2E-08		13	0	1.66667	0.00187	0.00071	-65.498	1.3E-08	2.2E-0
17	14	0	1.25	0.00066	-0.0048	-87.092	-0.0496	-0.0217		14	0	1.25	0.00172	0.00134	-73.687	1.5E-08	2.8E-08		14	0	1.25	0.00178	0.00071	-73.687	1.5E-08	2.8E-0
18	15	0	0.83333	0.00065	-0.0048	-99.159	-0.0787	-0.0485		15	0	0.83333	0.00164	0.00135	-81.871	1.7E-08	3.5E-08		15	0	0.83333	0.00169	0.00072	-81.871	1.7E-08	3.5E-0
19	16	0	0.83333	0.00065	-0.0048	-99.195	0.08	-0.0485		16	0	0.83333	0.00164	0.00135	-81.874	1.7E-08	3.5E-08		16	0	0.83333	0.00169	0.00072	-81.874	1.7E-08	3.5E-0
20	17	0	0.625	0.00065	-0.0048	-105.25	-0.0949	-0.0665		17	0	0.625	0.0016	0.00135	-85.965	1.8E-08	3.9E-08		17	0	0.625	0.00165	0.00072	-85.965	1.8E-08	3.9E-0
21	18	0	0.41667	0.00064	-0.0048	-111.36	-0.1115	-0.0881		18	0	0.41667	0.00156	0.00135	-90.06	1.8E-08	4.2E-08		18	0	0.41667	0.00161	0.00072	-90.06	1.8E-08	4.2E-0
22	19	0	0.20833	0.00063	-0.0048	-117.47	-0.1281	-0.113		19	0	0.20833	0.00152	0.00136	-94.154	1.9E-08	4.6E-08		19	0	0.20833	0.00156	0.00073	-94.154	1.9E-08	4.6E-0
23	20	0	0	0.00063	-0.0048	-123.58	-0.1445	-0.1414		20	0	0	0.00147	0.00136	-98.246	2E-08	5E-08		20	0	0	0.00152	0.00073	-98.246	0.00705	5E-0
24	21	0	0	0.00063	-0.0048	-123.59	-0.1447	-0.1414		21	0	0	0.00147	0.00136	-98.248	2E-08	5E-08		21	0	0	0.00152	0.00073	-98.246	2E-08	5E-0
25	22	0	-0.125	0.00063	-0.0048	-127.24	-0.1538	-0.1601		22	0	-0.125	0.00145	0.00136	-100.7	2.1E-08	5.3E-08		22	0	-0.125	0.0015	0.00073	-100.75	-0.0651	-0.002
26	23	0	-0.25	0.00062	-0.0048	-130.88	-0.1627	-0.1799		23	0	-0.25	0.00143	0.00136	-103.16	2.1E-08	5.6E-08		23	0	-0.25	0.00147	0.00073	-103.32	-0.2388	-0.020
27	24	0	-0.375	0.00062	-0.0048	-134.51	-0.1714	-0.2008		24	0	-0.375	0.0014	0.00136	-105.62	2.2E-08	5.8E-08		24	0	-0.375	0.00144	0.00073	-105.96	-0.4994	-0.065
28	25	0	-0.5	0.00062	-0.0048	-138.11	-0.1798	-0.2227		25	0	-0.5	0.00138	0.00136	-108.07	2.2E-08	6.1E-08		25	0	-0.5	0.00142	0.00073	-108.62	-0.7976	-0.148
29	26	0	-0.5	0.00062	-0.0048	-138.12	-0.1802	-0.2227		26	0	-0.5	0.00138	0.00136	-108.07	2.2E-08	6.1E-08		26	0	-0.5	0.00142	0.00073	-108.65	-0.8323	-0.148
30	27	0	-0.625	0.00061	-0.0048	-141.84	-0.1883	-0.2457		27	0	-0.625	0.00135	0.00137	-110.67	2.3E-08	6.4E-08		27	0	-0.625	0.00139	0.00074	-111.56	-1.2815	-0.277
31	28	0	-0.75	0.00061	-0.0048	-145.54	-0.1975	-0.2698		28	0	-0.75	0.00133	0.00137	-113.27	2.3E-08	6.7E-08		28	0	-0.75	0.00137	0.00074	-114.49	-1.7742	-0.469
32	29	0	-0.875	0.00061	-0.0048	-149.2	-0.2077	-0.2952		29	0	-0.875	0.00131	0.00137	-115.88	2.4E-08	7E-08		29	0	-0.875	0.00134	0.00074	-117.37	-2.2288	-0.719
33	30	0	-1	0.0006	-0.0048	-152.81	-0.2182	-0.3218		30	0	-1	0.00128	0.00137	-118.57	2.4E-08	7.3E-08		30	0	-1	0.00131	0.00074	-120.19	-2.5985	-1.022
34	31	0	-1	0.0006	-0.0048	-152.82	-0.2189	-0.3218		31	0	-1	0.00128	0.00137	-118.48	-0.2071	7.3E-08		31	0	-1	0.00131	0.00074	-120.44	-3.1786	-1.022
35	32	0	-1.2051	0.0006	-0.0048	-158.66	-0.2381	-0.3686		32	0	-1.2051	0.00124	0.00137	-116.7	-1.9577	-0.2285		32	0	-1.2051	0.00127	0.00074	-119.57	-7.4486	-2.158
36	33	0	-1.4101	0.00059	-0.0048	-164.35	-0.2587	-0.4195		33	0	-1.4101	0.0012	0.00137	-115.22	-3.3708	-0.7793		33	0	-1.4101	0.00123	0.00074	-118.84	-9.5519	-3.92
37	34	0	-1.6152	0.00059	-0.0048	-169.88	-0.2797	-0.4747		34	0	-1.6152	0.00116	0.00138	-113.91	-4.4985	-1.5918		34	0	-1.6152	0.00119	0.00075	-118.22	-10.052	-5.967

Figure H.5.3: Run excel file structure from the sensitivity analysis of the python application.

## Extra Material Chapter 4

### I.1 Bentonite effect to the stiffness of the combi wall

In this section the effect of the bentonite to the horizontal deformations of the wall is being tested. When considering only the steel pipes and the sheet pile walls of the combi wall the properties of the wall for all four sections is are given in Table I.1.1.

**Table I.1.1:** Properties for each section of the retaining wall without bentonite consideration.

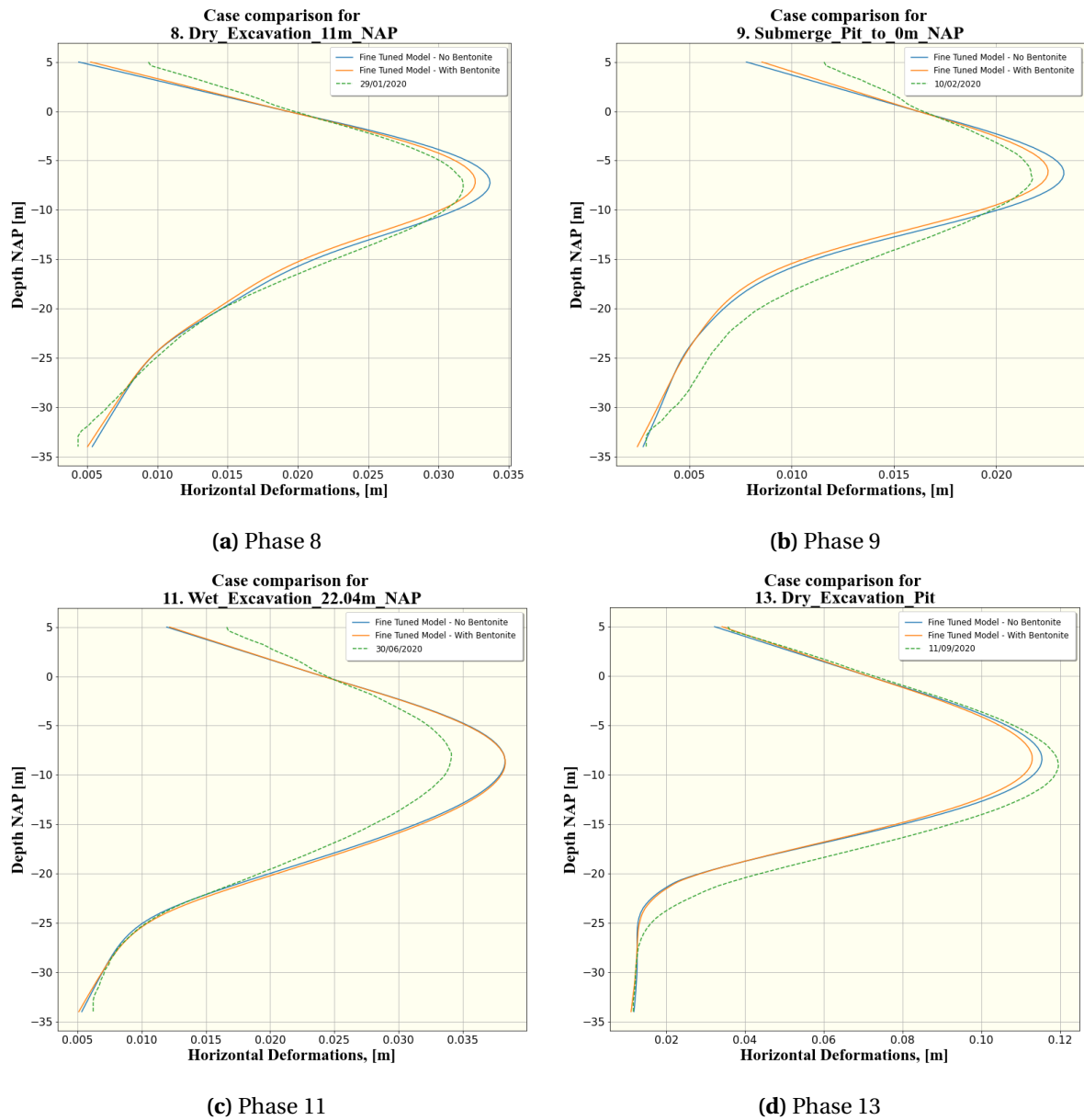
Name	Section 1	Section 2	Section 3	Section 4	Units
<b>w</b>	2.68	4.08	3.86	1.90	kN/m/m
<b>EA</b>	7300577	11132733	10525321	5190463	kN/m/m
<b>EI</b>	1365381	2273072	2131292	1279467	$kN * m^2 / m$

Using the Fine Tuned model the cases of Bentonite and No Bentonite are compared in Figure I.1.1 for four construction phases. The total area between the models and the corresponding monitoring deformations are given in Table I.1.2.

**Table I.1.2:** Area change in  $m^2$  for the case on Bentonite and no bentonite in comparison to the corresponding monitoring deformations for 5 construction phases.

Phase	Bentonite	No Bentonite
<b>Phase 8</b>	0.038	0.041
<b>Phase 9</b>	0.053	0.053
<b>Phase 10</b>	0.035	0.037
<b>Phase 11</b>	0.078	0.074
<b>Phase 13</b>	0.226	0.204

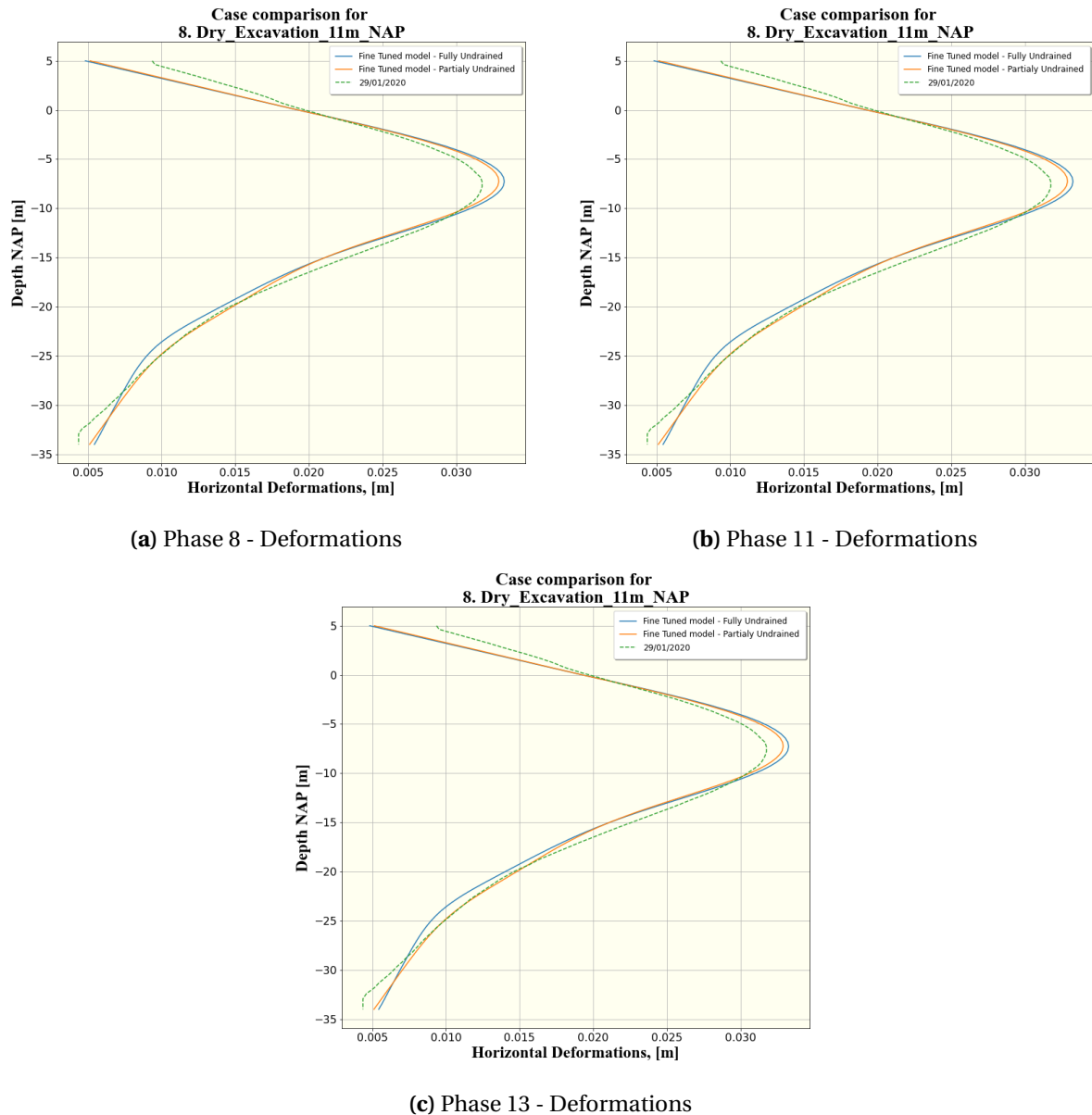
It can be concluded that the the effect the cement Bentonite have to the horizontal deformations of the wall is insignificant.



**Figure I.1.1:** Investigation of the effect of the bentonite to the horizontal deformations of the combi wall for four contraction phases.

## I.2 Fully Undrained approach

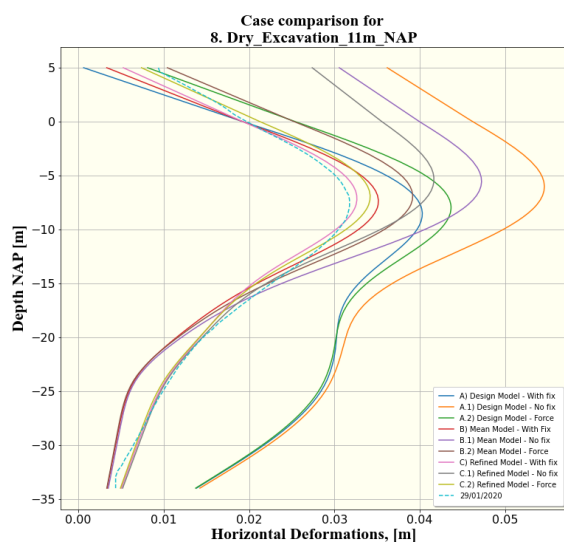
In this section, the partially undrained and fully undrained scenarios are compared. The partially undrained scenario models the Boom Clay Undrained after Phase 8, following the approach of the actual design. The fully undrained approach models the Boom Clay in undrained conditions from Phase 1. The comparison for Phases 8, 11 and 13 is given in Figure I.2.1. It is concluded that the effect in minimum and the approach of the actual design will be used for the models to be comparable.



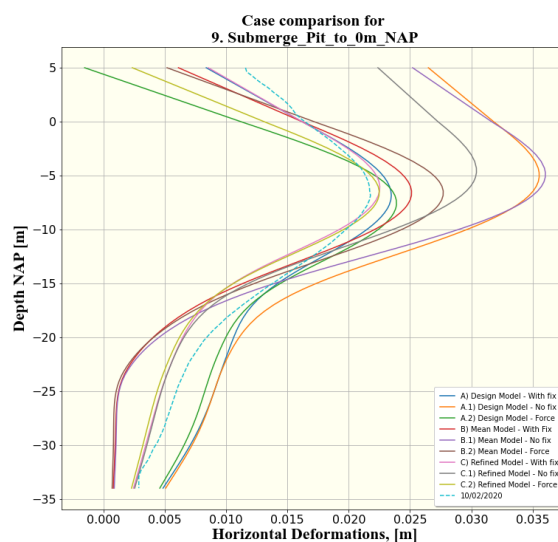
**Figure I.2.1:** Partially vs fully undrained Boom Clay conditions for the construction Phases 8, 11 and 13.

### I.3 Design Improvement

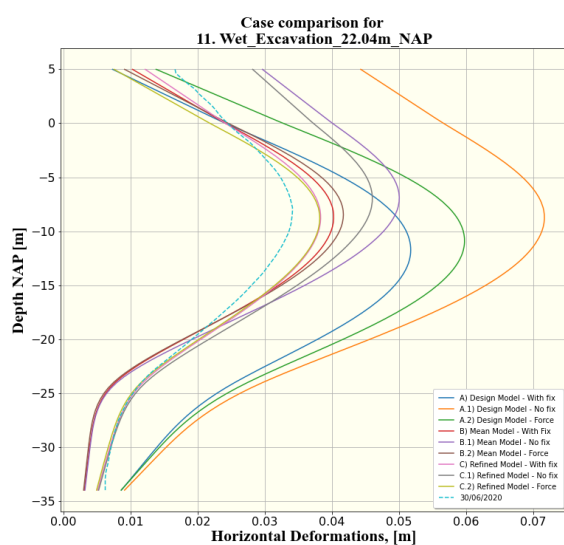
In this Appendix the full comparison of the Design, Mean and Fine Tuned model for the three methods of anchor rod simulation (Free, Fixed, Shaft Friction) are presented. Four construction phases are investigated for the Deformation (Figure I.3.1), Moments (Figure I.3.2), Force Q (Figure I.3.3) and Force N (Figure I.3.4) comparison.



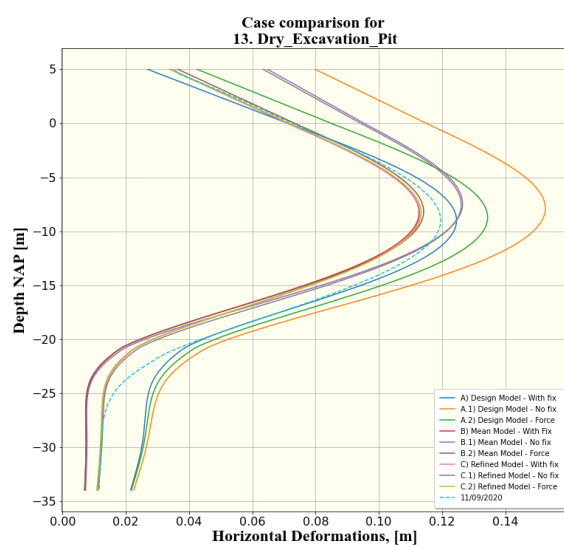
(a) Phase 8 - Deformations



(b) Phase 9 - Deformations



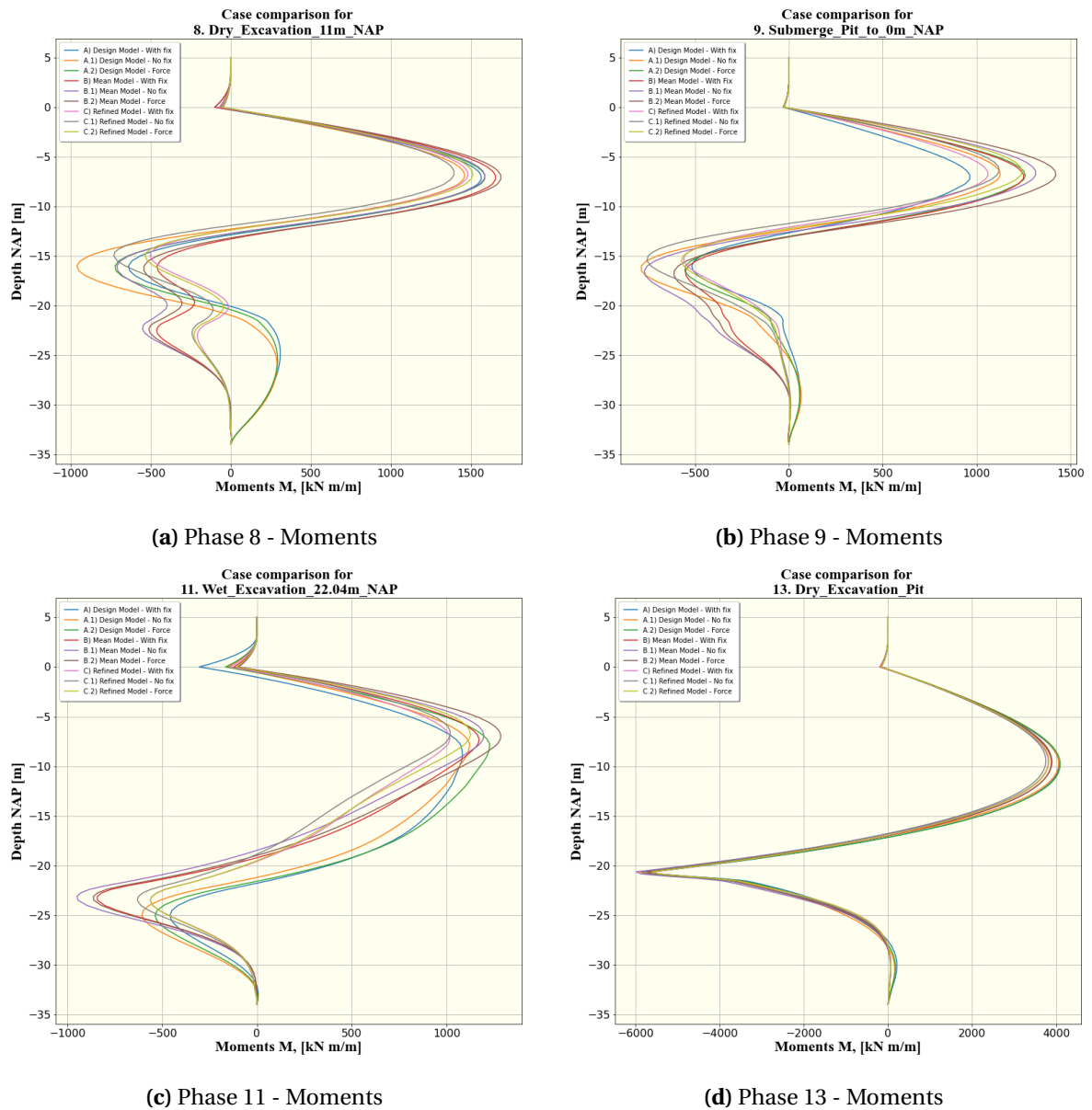
(c) Phase 11 - Deformations



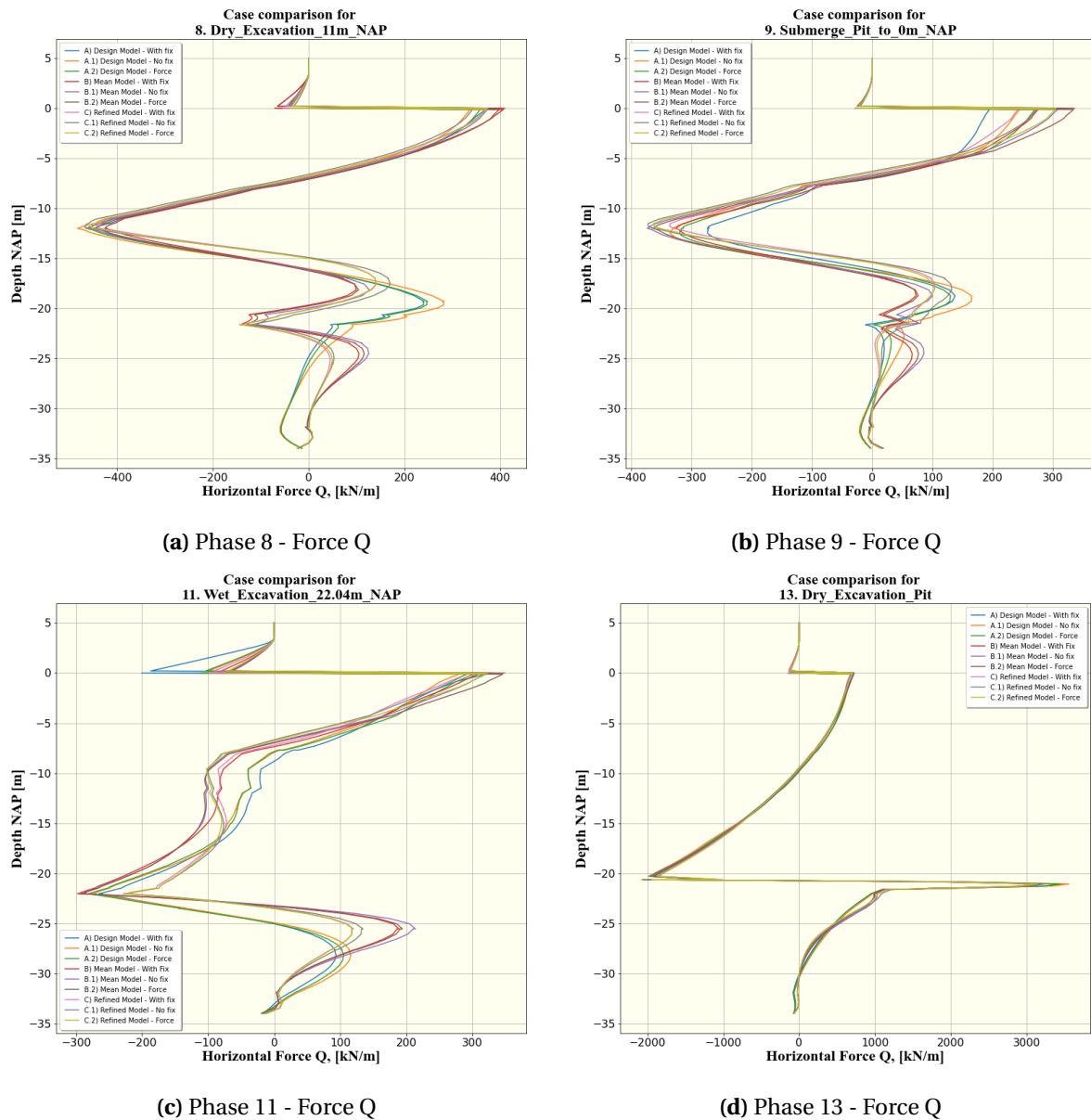
(d) Phase 9 - Deformations

**Figure I.3.1:** Deformations comparison for the Design, Mean and Fine Tuned models for the three anchor rod assumption (free, fixed, shaft friction) for four construction phases. The corresponding monitoring deformations are also included.

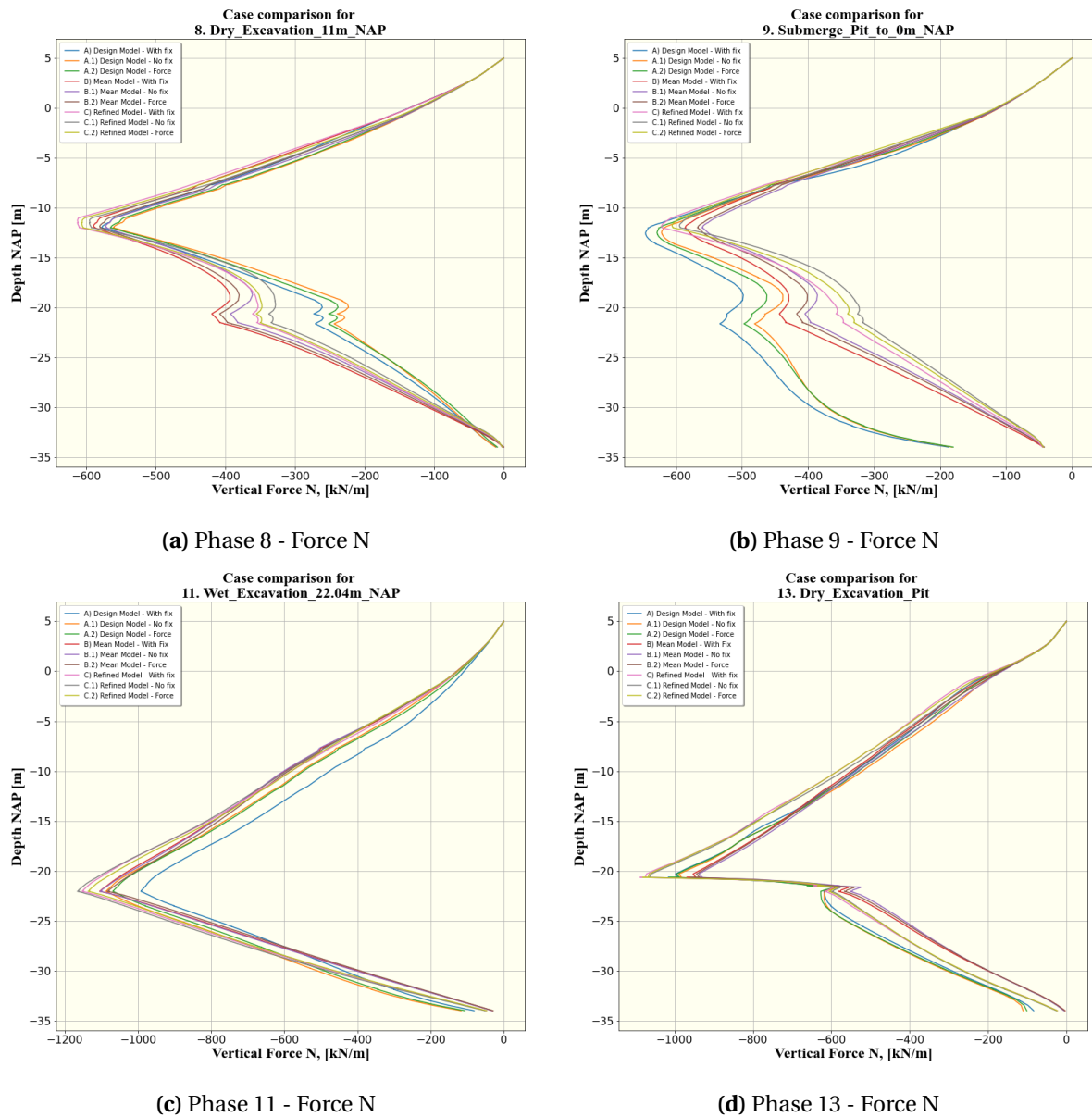




**Figure I.3.2:** Moments comparison for the Design, Mean and Fine Tuned models for the three anchor rod assumption (free, fixed, shaft friction) for four construction phases.



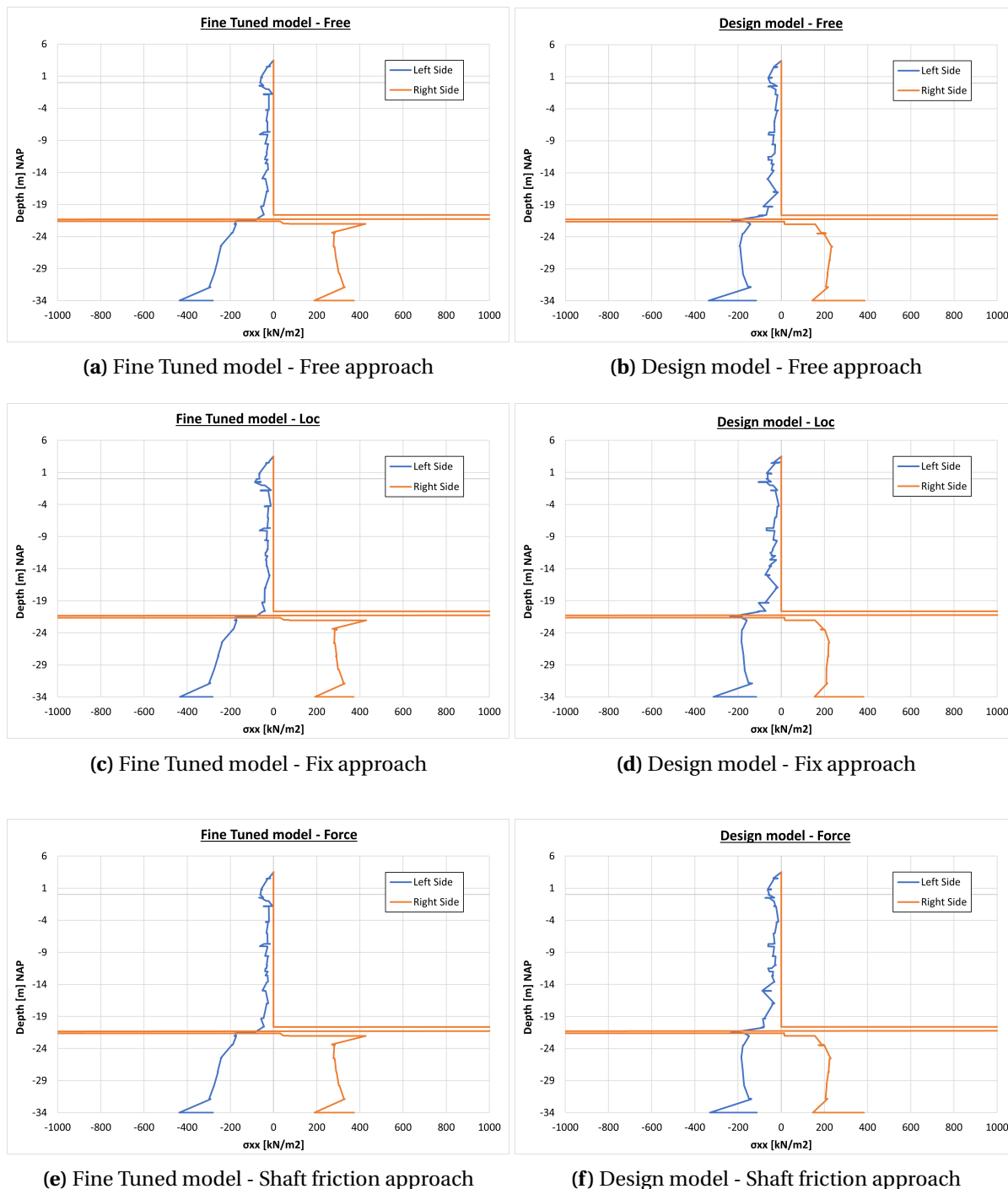
**Figure I.3.3:** Force Q comparison for the Design, Mean and Fine Tuned models for the three anchor rod assumption (free, fixed, shaft friction) for four construction phases.




**Figure I.3.4:** Force N comparison for the Design, Mean and Fine Tuned models for the three anchor rod assumption (free, fixed, shaft friction) for four construction phases.

### I.4 Horizontal Effective stress

In Figure I.4.1 the horizontal effective stress  $\sigma'_{xx}$  for the Design and Fine Tuned model for all the fixity approaches are given. It has been derive from the PLAXIS models 5cm left and right form the retaining wall for the governing Phase 13.



**Figure I.4.1:** Horizontal effective stress  $\sigma'_{xx}$  for the Design and Fine Tuned model under the three different fixity approaches.

Project:	Nieuwe Sluis Terneuzen	Date:	12/19/2017	 VOORTVAREND EN DOORDACHT																																																																																																																																																																																																																								
Projectnummer:		Name:	APO																																																																																																																																																																																																																									
Description:	berekening buispaal	Version:	1.0																																																																																																																																																																																																																									
<b>Calculation of capacity of the bending moments for combiwalls According to Handbook Quay walls CUR 211 second edition §6.6.6</b>																																																																																																																																																																																																																												
<b>Limitations</b>				Program "Gresnigt" versie 1.0 Opsteller: M van der Veer																																																																																																																																																																																																																								
For empty piles: <ul style="list-style-type: none"> <li>The ENV 1993-5 respects a limitation of the steel grade of S430.</li> <li>Testing of piles by the committee of the CUR211 has been performed up to a yield stress of 500 MPa. This may be considered as provisional evidence to use this method for X70 steel also fy = 483 MPa</li> <li>The formula are valid for water head differences less than 4 m.</li> </ul> For sand filled piles: <ul style="list-style-type: none"> <li>Sand shall be present in the area of the section subject to evaluation of the resistance.</li> <li>Sand may be loose or medium dense, if naturally available.</li> <li>In actively filled piles the sand fill shall be compacted, obtaining 70% relative density or qc values &gt; 10 MPa.</li> <li>Clay filled piles shall be considered as empty piles. Sand filled piles with thin (&lt; 0.5 D) intermediate clay layers may be considered as sand filled piles.</li> <li>EN 1993-5 clause 5.5.4 (8) and (9) suggests that filling the pile with well compacted non cohesive material contributes to avoiding local buckling. Fill requirements and achieved tube resistance are not given.</li> <li>Please note that the effect of the sand fill is not addressed in any of the models in the presently valid Eurocodes.</li> <li>This provides a basis for using the paragraph design by testing in the Eurocode.</li> <li>The results of this work should not be used for dolphin piles or for other applications where plastic deformation capacity is required. The effect of use of the recommendations for these type of structures may result in choosing larger D/t* values, which is not recommendable.</li> </ul>																																																																																																																																																																																																																												
<b>Notes</b> Enable iterative calculations (File>Options>Formulas), otherwise manual iteration required in row 32 (green cell) If both active and passive soil pressure are present, combine Case 2 and Case 3 This sheet will calculate the capacity of the Bending moment and Normal forces. For that reason the ovalization by second order effect of the tube's (formula (6.7) and (6.8)) is calculated with the maximum allowable kappa and not with the actual kappa. This gives a lower U.C. but the same M <sub>Ed</sub> when M <sub>Ed</sub> = M <sub>Ed</sub> For calculated the initial out of roundness U <sub>o,init</sub> , the internal diameter is used according to the NEN EN 1993-1-6 §8.4.2 For E <sub>o,init</sub> < 10 MPa, formula 6.1 and 6.12 will be used. For E <sub>o,init</sub> ≥ 10 MPa formula 6.17 and 6.18 are used. The recommended safe value E <sub>o,init</sub> = 10 MPa When pile is out of the range of formula 6.17, formula 6.1 will be used It is assumed that also the local bending moment will be reduced by the sand filling. The reduction of the local bending moment is taken the same as for the displacement.																																																																																																																																																																																																																												
<table border="1"> <thead> <tr> <th>Parameter</th> <th>Symbol</th> <th>Unit</th> <th>Value</th> </tr> </thead> <tbody> <tr> <td colspan="4"><b>Input variables</b></td> </tr> <tr> <td>outer diameter</td> <td>D<sub>nom</sub></td> <td>[mm]</td> <td>1420</td> </tr> <tr> <td>wall thickness</td> <td>t<sub>nom</sub></td> <td>[mm]</td> <td>15.8</td> </tr> <tr> <td>steel grade</td> <td></td> <td>[-]</td> <td>S 480 M H M L H</td> </tr> <tr> <td>Yield stress</td> <td>f<sub>y</sub></td> <td>[N/mm<sup>2</sup>]</td> <td>460</td> </tr> <tr> <td>tube class according to EN 1993-1-6</td> <td></td> <td>[-]</td> <td>C</td> </tr> <tr> <td>Calculation check</td> <td></td> <td>[-]</td> <td>ULS</td> </tr> <tr> <td>Material factor</td> <td>γ<sub>M0</sub></td> <td>[-]</td> <td>1.10</td> </tr> <tr> <td>Compression moduli of sand</td> <td>E<sub>o,init</sub></td> <td>[MPa]</td> <td>500</td> </tr> <tr> <td>Calculated as sand filled or empty</td> <td></td> <td>[-]</td> <td>Sand filled</td> </tr> <tr> <td colspan="4">Using formula right hand side for calculation capacity of bending moment</td> </tr> <tr> <td>Corrosion in ner side</td> <td>C<sub>in</sub></td> <td>[mm]</td> <td>0.00</td> </tr> <tr> <td>Corrosion outer side</td> <td>C<sub>out</sub></td> <td>[mm]</td> <td>0.00</td> </tr> <tr> <td>Corrosion sheet pile</td> <td>C<sub>sheet</sub></td> <td>[mm]</td> <td>0.00</td> </tr> <tr> <td>Total width of both clutch</td> <td>b<sub>clutch</sub></td> <td>[mm]</td> <td>48</td> </tr> <tr> <td>Total width intermediated sheets</td> <td>b<sub>sheet</sub></td> <td>[mm]</td> <td>1400</td> </tr> <tr> <td>Height single intermediated sheet</td> <td>h<sub>sheet n=1</sub></td> <td>[mm]</td> <td>501</td> </tr> <tr> <td>Total height intermediated sheets</td> <td>h<sub>sheet</sub></td> <td>[mm]</td> <td>501</td> </tr> <tr> <td>Total second inertia moment intermediated sheets (welded), now</td> <td>I<sub>sheet</sub></td> <td>[cm<sup>4</sup>]</td> <td>0</td> </tr> <tr> <td>Total second inertia moment intermediated sheets (welded), cor</td> <td>I<sub>sheet cor</sub></td> <td>[cm<sup>4</sup>]</td> <td>115370</td> </tr> <tr> <td>Total area of the intermediated sheets</td> <td>A<sub>sheet</sub></td> <td>[cm<sup>2</sup>]</td> <td>0</td> </tr> <tr> <td>Yield stress of the sheets</td> <td>f<sub>y, sheet</sub></td> <td>[N/mm<sup>2</sup>]</td> <td>390</td> </tr> <tr> <td>Thickness of web</td> <td>t<sub>w</sub></td> <td>[mm]</td> <td>20.0</td> </tr> <tr> <td>Thickness of flange</td> <td>t<sub>f</sub></td> <td>[mm]</td> <td>16.0</td> </tr> <tr> <td>Considered neutral axis of sheets</td> <td>Z<sub>sheet</sub></td> <td>[mm]</td> <td>0.0</td> </tr> <tr> <td colspan="4"><b>Results 2d calculation (D sheet/Plates)</b></td> </tr> <tr> <td>Horizontal effective soil pressure active side</td> <td>P<sub>a</sub></td> <td>[kN/m<sup>2</sup>]</td> <td>189</td> </tr> <tr> <td>Horizontal effective soil pressure passive side</td> <td>P<sub>p</sub></td> <td>[kN/m<sup>2</sup>]</td> <td>292</td> </tr> <tr> <td>Bending moment</td> <td>M<sub>Ed</sub></td> <td>[kNm/m]</td> <td>1995</td> </tr> <tr> <td>Normal force</td> <td>N<sub>Ed</sub></td> <td>[kN/m]</td> <td>659</td> </tr> <tr> <td colspan="4"><b>Output variables</b></td> </tr> <tr> <td>plastic resistance of bending moment of sheets</td> <td>M<sub>pl, sheet, plastic</sub></td> <td>[kNm/m]</td> <td>24.96</td> </tr> <tr> <td>Curvature of tube = curvature of sheet</td> <td>κ</td> <td>[m<sup>-1</sup>]</td> <td>4.79E-06</td> </tr> <tr> <td>strain of sheet</td> <td>ε</td> <td>[-]</td> <td>1.20E-03</td> </tr> <tr> <td>allowable stress</td> <td>σ<sub>sheet</sub></td> <td>[N/mm<sup>2</sup>]</td> <td>252.1</td> </tr> <tr> <td>Elastic section modulus</td> <td>W<sub>sheet</sub></td> <td>[cm<sup>3</sup>]</td> <td>4606</td> </tr> <tr> <td>Additional bending moment by sheets</td> <td>M<sub>sheet</sub></td> <td>[kNm]</td> <td>1181</td> </tr> <tr> <td></td> <td>c<sub>tc</sub></td> <td>[m]</td> <td>2.87</td> </tr> <tr> <td></td> <td>A<sub>sheet</sub></td> <td>[cm<sup>2</sup>/m]</td> <td>243</td> </tr> <tr> <td></td> <td>W<sub>sheet</sub></td> <td>[cm<sup>3</sup>/m]</td> <td>8532</td> </tr> <tr> <td></td> <td>E<sub>sheet</sub></td> <td>[kN/m<sup>2</sup>]</td> <td>1342529</td> </tr> <tr> <td></td> <td>m<sub>sheet</sub></td> <td>[kNm/m]</td> <td>4286</td> </tr> <tr> <td>tensile force</td> <td>F<sub>1</sub></td> <td>[kN/m]</td> <td>49.8</td> </tr> <tr> <td>effective soil pressure one side</td> <td>q<sub>2</sub></td> <td>[kPa]</td> <td>208</td> </tr> <tr> <td>effective soil pressure two sides</td> <td>q<sub>3</sub></td> <td>[kPa]</td> <td>381.7</td> </tr> <tr> <td>bending moment</td> <td>M<sub>Ed</sub></td> <td>[kNm]</td> <td>5722</td> </tr> <tr> <td>normal force</td> <td>N<sub>Ed</sub></td> <td>[kN]</td> <td>1890</td> </tr> <tr> <td>bending moment capacity</td> <td>M<sub>Ed, combi</sub></td> <td>[kNm]</td> <td>12234</td> </tr> <tr> <td>normal force capacity</td> <td>N<sub>Ed</sub></td> <td>[kN]</td> <td>29093</td> </tr> <tr> <td>Unity Check</td> <td>U.C.</td> <td>[-]</td> <td>0.477</td> </tr> <tr> <td>Unity Check local stresses</td> <td>U.C.</td> <td>[-]</td> <td>0.01</td> </tr> <tr> <td>Check if iteration is done</td> <td></td> <td></td> <td>Ok</td> </tr> <tr> <td>Check combiwall capacity</td> <td></td> <td></td> <td>Ok</td> </tr> </tbody> </table>					Parameter	Symbol	Unit	Value	<b>Input variables</b>				outer diameter	D <sub>nom</sub>	[mm]	1420	wall thickness	t <sub>nom</sub>	[mm]	15.8	steel grade		[-]	S 480 M H M L H	Yield stress	f <sub>y</sub>	[N/mm <sup>2</sup> ]	460	tube class according to EN 1993-1-6		[-]	C	Calculation check		[-]	ULS	Material factor	γ <sub>M0</sub>	[-]	1.10	Compression moduli of sand	E <sub>o,init</sub>	[MPa]	500	Calculated as sand filled or empty		[-]	Sand filled	Using formula right hand side for calculation capacity of bending moment				Corrosion in ner side	C <sub>in</sub>	[mm]	0.00	Corrosion outer side	C <sub>out</sub>	[mm]	0.00	Corrosion sheet pile	C <sub>sheet</sub>	[mm]	0.00	Total width of both clutch	b <sub>clutch</sub>	[mm]	48	Total width intermediated sheets	b <sub>sheet</sub>	[mm]	1400	Height single intermediated sheet	h <sub>sheet n=1</sub>	[mm]	501	Total height intermediated sheets	h <sub>sheet</sub>	[mm]	501	Total second inertia moment intermediated sheets (welded), now	I <sub>sheet</sub>	[cm <sup>4</sup> ]	0	Total second inertia moment intermediated sheets (welded), cor	I <sub>sheet cor</sub>	[cm <sup>4</sup> ]	115370	Total area of the intermediated sheets	A <sub>sheet</sub>	[cm <sup>2</sup> ]	0	Yield stress of the sheets	f <sub>y, sheet</sub>	[N/mm <sup>2</sup> ]	390	Thickness of web	t <sub>w</sub>	[mm]	20.0	Thickness of flange	t <sub>f</sub>	[mm]	16.0	Considered neutral axis of sheets	Z <sub>sheet</sub>	[mm]	0.0	<b>Results 2d calculation (D sheet/Plates)</b>				Horizontal effective soil pressure active side	P <sub>a</sub>	[kN/m <sup>2</sup> ]	189	Horizontal effective soil pressure passive side	P <sub>p</sub>	[kN/m <sup>2</sup> ]	292	Bending moment	M <sub>Ed</sub>	[kNm/m]	1995	Normal force	N <sub>Ed</sub>	[kN/m]	659	<b>Output variables</b>				plastic resistance of bending moment of sheets	M <sub>pl, sheet, plastic</sub>	[kNm/m]	24.96	Curvature of tube = curvature of sheet	κ	[m <sup>-1</sup> ]	4.79E-06	strain of sheet	ε	[-]	1.20E-03	allowable stress	σ <sub>sheet</sub>	[N/mm <sup>2</sup> ]	252.1	Elastic section modulus	W <sub>sheet</sub>	[cm <sup>3</sup> ]	4606	Additional bending moment by sheets	M <sub>sheet</sub>	[kNm]	1181		c <sub>tc</sub>	[m]	2.87		A <sub>sheet</sub>	[cm <sup>2</sup> /m]	243		W <sub>sheet</sub>	[cm <sup>3</sup> /m]	8532		E <sub>sheet</sub>	[kN/m <sup>2</sup> ]	1342529		m <sub>sheet</sub>	[kNm/m]	4286	tensile force	F <sub>1</sub>	[kN/m]	49.8	effective soil pressure one side	q <sub>2</sub>	[kPa]	208	effective soil pressure two sides	q <sub>3</sub>	[kPa]	381.7	bending moment	M <sub>Ed</sub>	[kNm]	5722	normal force	N <sub>Ed</sub>	[kN]	1890	bending moment capacity	M <sub>Ed, combi</sub>	[kNm]	12234	normal force capacity	N <sub>Ed</sub>	[kN]	29093	Unity Check	U.C.	[-]	0.477	Unity Check local stresses	U.C.	[-]	0.01	Check if iteration is done			Ok	Check combiwall capacity			Ok
Parameter	Symbol	Unit	Value																																																																																																																																																																																																																									
<b>Input variables</b>																																																																																																																																																																																																																												
outer diameter	D <sub>nom</sub>	[mm]	1420																																																																																																																																																																																																																									
wall thickness	t <sub>nom</sub>	[mm]	15.8																																																																																																																																																																																																																									
steel grade		[-]	S 480 M H M L H																																																																																																																																																																																																																									
Yield stress	f <sub>y</sub>	[N/mm <sup>2</sup> ]	460																																																																																																																																																																																																																									
tube class according to EN 1993-1-6		[-]	C																																																																																																																																																																																																																									
Calculation check		[-]	ULS																																																																																																																																																																																																																									
Material factor	γ <sub>M0</sub>	[-]	1.10																																																																																																																																																																																																																									
Compression moduli of sand	E <sub>o,init</sub>	[MPa]	500																																																																																																																																																																																																																									
Calculated as sand filled or empty		[-]	Sand filled																																																																																																																																																																																																																									
Using formula right hand side for calculation capacity of bending moment																																																																																																																																																																																																																												
Corrosion in ner side	C <sub>in</sub>	[mm]	0.00																																																																																																																																																																																																																									
Corrosion outer side	C <sub>out</sub>	[mm]	0.00																																																																																																																																																																																																																									
Corrosion sheet pile	C <sub>sheet</sub>	[mm]	0.00																																																																																																																																																																																																																									
Total width of both clutch	b <sub>clutch</sub>	[mm]	48																																																																																																																																																																																																																									
Total width intermediated sheets	b <sub>sheet</sub>	[mm]	1400																																																																																																																																																																																																																									
Height single intermediated sheet	h <sub>sheet n=1</sub>	[mm]	501																																																																																																																																																																																																																									
Total height intermediated sheets	h <sub>sheet</sub>	[mm]	501																																																																																																																																																																																																																									
Total second inertia moment intermediated sheets (welded), now	I <sub>sheet</sub>	[cm <sup>4</sup> ]	0																																																																																																																																																																																																																									
Total second inertia moment intermediated sheets (welded), cor	I <sub>sheet cor</sub>	[cm <sup>4</sup> ]	115370																																																																																																																																																																																																																									
Total area of the intermediated sheets	A <sub>sheet</sub>	[cm <sup>2</sup> ]	0																																																																																																																																																																																																																									
Yield stress of the sheets	f <sub>y, sheet</sub>	[N/mm <sup>2</sup> ]	390																																																																																																																																																																																																																									
Thickness of web	t <sub>w</sub>	[mm]	20.0																																																																																																																																																																																																																									
Thickness of flange	t <sub>f</sub>	[mm]	16.0																																																																																																																																																																																																																									
Considered neutral axis of sheets	Z <sub>sheet</sub>	[mm]	0.0																																																																																																																																																																																																																									
<b>Results 2d calculation (D sheet/Plates)</b>																																																																																																																																																																																																																												
Horizontal effective soil pressure active side	P <sub>a</sub>	[kN/m <sup>2</sup> ]	189																																																																																																																																																																																																																									
Horizontal effective soil pressure passive side	P <sub>p</sub>	[kN/m <sup>2</sup> ]	292																																																																																																																																																																																																																									
Bending moment	M <sub>Ed</sub>	[kNm/m]	1995																																																																																																																																																																																																																									
Normal force	N <sub>Ed</sub>	[kN/m]	659																																																																																																																																																																																																																									
<b>Output variables</b>																																																																																																																																																																																																																												
plastic resistance of bending moment of sheets	M <sub>pl, sheet, plastic</sub>	[kNm/m]	24.96																																																																																																																																																																																																																									
Curvature of tube = curvature of sheet	κ	[m <sup>-1</sup> ]	4.79E-06																																																																																																																																																																																																																									
strain of sheet	ε	[-]	1.20E-03																																																																																																																																																																																																																									
allowable stress	σ <sub>sheet</sub>	[N/mm <sup>2</sup> ]	252.1																																																																																																																																																																																																																									
Elastic section modulus	W <sub>sheet</sub>	[cm <sup>3</sup> ]	4606																																																																																																																																																																																																																									
Additional bending moment by sheets	M <sub>sheet</sub>	[kNm]	1181																																																																																																																																																																																																																									
	c <sub>tc</sub>	[m]	2.87																																																																																																																																																																																																																									
	A <sub>sheet</sub>	[cm <sup>2</sup> /m]	243																																																																																																																																																																																																																									
	W <sub>sheet</sub>	[cm <sup>3</sup> /m]	8532																																																																																																																																																																																																																									
	E <sub>sheet</sub>	[kN/m <sup>2</sup> ]	1342529																																																																																																																																																																																																																									
	m <sub>sheet</sub>	[kNm/m]	4286																																																																																																																																																																																																																									
tensile force	F <sub>1</sub>	[kN/m]	49.8																																																																																																																																																																																																																									
effective soil pressure one side	q <sub>2</sub>	[kPa]	208																																																																																																																																																																																																																									
effective soil pressure two sides	q <sub>3</sub>	[kPa]	381.7																																																																																																																																																																																																																									
bending moment	M <sub>Ed</sub>	[kNm]	5722																																																																																																																																																																																																																									
normal force	N <sub>Ed</sub>	[kN]	1890																																																																																																																																																																																																																									
bending moment capacity	M <sub>Ed, combi</sub>	[kNm]	12234																																																																																																																																																																																																																									
normal force capacity	N <sub>Ed</sub>	[kN]	29093																																																																																																																																																																																																																									
Unity Check	U.C.	[-]	0.477																																																																																																																																																																																																																									
Unity Check local stresses	U.C.	[-]	0.01																																																																																																																																																																																																																									
Check if iteration is done			Ok																																																																																																																																																																																																																									
Check combiwall capacity			Ok																																																																																																																																																																																																																									

For μ ≤ 1: β<sub>o, sand-filled</sub> = 0.90  
 For 1 ≤ μ ≤ 3: β<sub>o, sand-filled</sub> = 0.85 + 0.0  
 For μ ≥ 3: β<sub>o, sand-filled</sub> = 1.0

(not used in the calculation)  
 (no intermediated sheets)

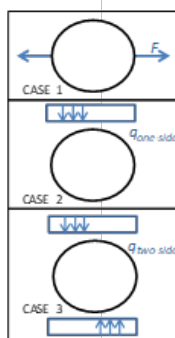


Figure I.4.2: Unity check excel example.